Acoustic imaging in enclosed spaces

Antonio Pereira

To cite this version:

Antonio Pereira. Acoustic imaging in enclosed spaces. Acoustics [physics.class-ph]. INSA de Lyon, 2013. English. NNT : 2013ISAL0066 . tel-00984347v2

HAL Id: tel-00984347

https://theses.hal.science/tel-00984347v2

Submitted on 7 May 2015

THÈSE

ACOUSTIC IMAGING IN ENCLOSED SPACES

présentée devant
l'Institut National des Sciences Appliquées de Lyon

par
Antonio PEREIRA
Ingénieur diplômé de l'INSA de Lyon

pour obtenir
le GRADE DE DOCTEUR

école doctorale :
Mécanique, énergétique, Génie Civil, Acoustique
Spécialité : **Acoustique**

Thèse préparée au Laboratoire Vibrations Acoustique

jury

QUENTIN LECLÈRE (Maître de Conférences)	INSA de Lyon	Directeur de Thèse
ALI MOHAMMAD-DJAFARI (Professeur)	CNRS-SUPELEC	Rapporteur
MANUEL MELON (Maître de Conférences)	CNAM	Rapporteur
JEAN-CLAUDE PASCAL (Professeur)	LAUM	Examinateur
JÉRÔME ANTONI (Professeur)	INSA de Lyon	Examinateur

Année 2013

INSA Direction de la Recherche - Ecoles Doctorales – Quinquennal 2011-2015

SIGLE	ECOLE DOCTORALE	NOM ET COORDONNEES DU RESPONSABLE
CHIMIE	**CHIMIE DE LYON** **http://www.edchimie-lyon.fr** Insa : R. GOURDON	M. Jean Marc LANCELIN Université de Lyon – Collège Doctoral Bât ESCPE 43 bd du 11 novembre 1918 69622 VILLEURBANNE Cedex Tél : 04.72.43 13 95 directeur@edchimie-lyon.fr
E.E.A.	**ELECTRONIQUE, ELECTROTECHNIQUE, AUTOMATIQUE** **http://edeea.ec-lyon.fr** Secrétariat : M.C. HAVGOUDOUKIAN eea@ec-lyon.fr	M. Gérard SCORLETTI Ecole Centrale de Lyon 36 avenue Guy de Collongue 69134 ECULLY Tél : 04.72.18 60 97 Fax : 04 78 43 37 17 Gerard.scorletti@ec-lyon.fr
E2M2	**EVOLUTION, ECOSYSTEME, MICROBIOLOGIE, MODELISATION** **http://e2m2.universite-lyon.fr** Insa : H. CHARLES	Mme Gudrun BORNETTE CNRS UMR 5023 LEHNA Université Claude Bernard Lyon 1 Bât Forel 43 bd du 11 novembre 1918 69622 VILLEURBANNE Cédex Tél : 04.72.43.12.94 e2m2@biomserv.univ-lyon1.fr
EDISS	**INTERDISCIPLINAIRE SCIENCES-SANTE** **http://ww2.ibcp.fr/ediss** Sec : Safia AIT CHALAL Insa : M. LAGARDE	M. Didier REVEL Hôpital Louis Pradel Bâtiment Central 28 Avenue Doyen Lépine 69677 BRON Tél : 04.72.68 49 09 Fax :04 72 35 49 16 Didier.revel@creatis.uni-lyon1.fr
INFOMATHS	**INFORMATIQUE ET MATHEMATIQUES** http://infomaths.univ-lyon1.fr	M. Johannes KELLENDONK Université Claude Bernard Lyon 1 INFOMATHS Bâtiment Braconnier 43 bd du 11 novembre 1918 69622 VILLEURBANNE Cedex Tél : 04.72. 44.82.94 Fax 04 72 43 16 87 infomaths@univ-lyon1.fr
Matériaux	**MATERIAUX DE LYON** Secrétariat : M. LABOUNE PM : 71.70 –Fax : 87.12 Bat. Saint Exupéry Ed.materiaux@insa-lyon.fr	M. Jean-Yves BUFFIERE INSA de Lyon MATEIS Bâtiment Saint Exupéry 7 avenue Jean Capelle 69621 VILLEURBANNE Cédex Tél : 04.72.43 83 18 Fax 04 72 43 85 28 Jean-yves.buffiere@insa-lyon.fr
MEGA	**MECANIQUE, ENERGETIQUE, GENIE CIVIL, ACOUSTIQUE** Secrétariat : M. LABOUNE PM : 71.70 –Fax : 87.12 Bat. Saint Exupéry mega@insa-lyon.fr	M. Philippe BOISSE INSA de Lyon Laboratoire LAMCOS Bâtiment Jacquard 25 bis avenue Jean Capelle 69621 VILLEURBANNE Cedex Tél :04.72.43.71.70 Fax : 04 72 43 72 37 Philippe.boisse@insa-lyon.fr
ScSo	**ScSo*** M. OBADIA Lionel Sec : Viviane POLSINELLI Insa : J.Y. TOUSSAINT	M. OBADIA Lionel Université Lyon 2 86 rue Pasteur 69365 LYON Cedex 07 Tél : 04.78.69.72.76 Fax : 04.37.28.04.48 Lionel.Obadia@univ-lyon2.fr

*ScSo : Histoire, Geographie, Aménagement, Urbanisme, Archéologie, Science politique, Sociologie, Anthropologie

Résumé

Ce travail de recherche porte sur le problème de l'identification des sources de bruit en espace clos. La motivation principale était de proposer une technique capable de localiser et quantifier les sources de bruit à l'intérieur des véhicules industriels, d'une manière efficace en temps. Dans cette optique, la méthode pourrait être utilisée par les industriels à des fins de réduction de bruit, et donc construire des véhicules plus silencieux.

Un modèle simplifié basé sur la formulation par sources équivalentes a été utilisé pour résoudre le problème. Nous montrerons que le problème est mal conditionné, dans le sens où il est très sensible face aux erreurs de mesure, et donc des techniques dites de régularisation sont nécessaires. Une étude détaillée de cette question, en particulier le réglage de ce qu'on appelle de paramètre de régularisation, a été important pour assurer la stabilité de la solution. En particulier, un critère de régularisation basé sur une approche bayésienne s'est montré très robuste pour ajuster le paramètre de régularisation de manière optimale.

L'application cible concernant des environnements intérieurs relativement grands, nous a imposé des difficultés supplémentaires, à savoir: (a) le positionnement de l'antenne de capteurs à l'intérieur de l'espace; (b) le nombre d'inconnues (sources potentielles) beaucoup plus important que le nombre de positions de mesure. Une formulation par pondération itérative a ensuite été proposé pour surmonter les problèmes ci-dessus de manière à: (1) corriger pour le positionnement de l'antenne de capteurs dans l'habitacle ; (2) obtenir des résultats corrects en terme de quantification des sources identifiées. Par ailleurs, l'approche itérative nous a conduit à des résultats avec une meilleure résolution spatiale ainsi qu'une meilleure dynamique. Plusieurs études numériques ont été réalisées afin de valider la méthode ainsi que d'évaluer sa sensibilité face aux erreurs de modèle. En particulier, nous avons montré que l'approche est affectée par des conditions non-anéchoïques, dans le sens où les réflexions sont identifiées comme des vraies sources. Une technique de post-traitement qui permet de distinguer entre les chemins directs et réverbérants a été étudiée.

La dernière partie de cette thèse porte sur des validations expérimentales et applications pratiques de la méthode. Une antenne sphérique constituée d'une sphère rigide et 31 microphones a été construite pour les tests expérimentaux. Plusieurs validations académiques ont été réalisées dans des environnements semi-anéchoïques, et nous ont illustré les avantages et limites de la méthode. Enfin, l'approche a été testé dans une application pratique, qui a consisté à identifier les sources de bruit ou faiblesses acoustiques à l'intérieur d'un bus.

Mots clés : imagerie acoustique identification de sources problèmes inverses, antennes sphériques, méthode des sources equivalentes, régularisation, holographie acoustique de champ proche, régularisation par approche Bayésienne.

Abstract

This thesis is concerned with the problem of noise source identification in closed spaces. The main motivation was to propose a technique which allows to locate and quantify noise sources within industrial vehicles, in a time-effective manner. In turn, the technique might be used by manufacturers for noise abatement purposes such as to provide quieter vehicles.

A simplified model based on the equivalent source formulation was used to tackle the problem. It was shown that the problem is ill-conditioned, in the sense that it is very sensitive to errors in measurement data, thus regularization techniques were required. A detailed study of this issue, in particular the tuning of the so-called *regularization parameter*, was of importance to ensure the stability of the solution. In particular, a Bayesian regularization criterion was shown to be a very robust approach to optimally adjust the regularization parameter in an automated way.

The target application concerns very large interior environments, which imposes additional difficulties, namely: (a) the positioning of the measurement array inside the enclosure; (b) a number of unknowns (“candidate” sources) much larger than the number of measurement positions. An iterative weighted formulation was then proposed to overcome the above issues by: first correct for the positioning of the array within the enclosure and second iteratively solve the problem in order to obtain a correct source quantification. In addition, the iterative approach has provided results with an enhanced spatial resolution and dynamic range. Several numerical studies have been carried out to validate the method as well as to evaluate its sensitivity to modeling errors. In particular, it was shown that the approach is affected by non-anechoic conditions, in the sense that reflections are identified as “real” sources. A post-processing technique which helps to distinguish between direct and reverberant paths has been discussed.

The last part of the thesis was concerned with experimental validations and practical applications of the method. A custom spherical array consisting of a rigid sphere and 31 microphones has been built for the experimental tests. Several academic experimental validations have been carried out in semi-anechoic environments, which illustrated the advantages and limits of the method. Finally, the approach was tested in a practical application, which consisted in identifying noise sources inside a bus at driving conditions.

Keywords: acoustical imaging, noise source identification, inverse methods, acoustical holography, spherical arrays, equivalent source method, iterative weighted approach, regularization, L-curve, Bayesian regularization.

Résumé détaillé

Le bruit et les vibrations sont des paramètres importants pour l'évaluation du confort des passagers et des utilisateurs des véhicules de transport, ainsi que pour l'environnement sonore urbain. Dans ce contexte, les collectivités locales commencent à s'inquiéter de la pollution sonore et de son impact sur la qualité de vie. Cela conduit les autorités à imposer de nouvelles réglementations dans le but de contrôler les émissions de bruit.

C'est dans cette optique, qui s'inscrit ce travail de recherche dans le cadre du projet ACOUBUS, financé par l'Agence de l'Environnement et de la Maîtrise de l'Energie (ADEME). L'un des objectifs principaux de ce projet est d'intégrer l'acoustique dans le développement des nouveaux véhicules industriels, notamment les bus urbains, et par conséquent de donner lieu à des véhicules moins bruyants et un environnement sonore urbain plus calme. Des véhicules de transport en commun plus silencieux sont importants à l'égard des communautés pour, entre autres:

(a) motiver les citadins à utiliser les transports en commun;

(b) offrir de meilleures conditions de travail aux opérateurs;

(c) diminuer le bruit environnemental dans les grandes agglomérations, etc.

Actuellement, les ingénieurs disposent d'un grand nombre de moyens expérimentaux pour la caractérisation de sources. Quelques uns de ces moyens sont entre autres : l'analyse modale, les méthodes d'analyse de voies de transfert (TPA,OPA), les méthodes d'imagerie acoustique, etc. C'est particulièrement ce troisième groupe de méthodes qui va nous intéresser dans cette thèse. D'une manière générale, le but des méthodes d'imagerie acoustique est de reconstruire, localiser ou quantifier des sources de bruit, à partir de mesures du champ acoustique (typiquement délivrées par des antennes de capteurs).

L'étude réalisée au cours de ce travail de recherche, s'inscrit dans la partie du projet ACOUBUS dédiée à la performance acoustique à l'intérieur des bus. L'objectif principal est de proposer des techniques d'imagerie acoustique capables de localiser et quantifier les sources contribuant au niveau de bruit à l'intérieur de ces véhicules. En outre, il est important pour la technique d'être suffisamment rapide de manière à réduire le temps de mise au point acoustique.

Le premier chapitre de cette thèse est consacré à une synthèse bibliographique des méthodes existantes pour l'identification de sources, plus précisément les méthodes appliquées aux espaces clos. Nous avons vu que, selon la façon de résoudre ce problème, les différentes méthodes sont classées en trois groupes, à savoir: 1) les méthodes des formation de voies; 2) l'holographie acoustique de champ proche; 3) les méthodes inverses. Nous discutons de quelques extensions sur ces méthodes afin de les appliquer aux espaces fermés.

Une partie de la synthèse bibliographique concerne également les méthodes dites de séparation de champ. Ces méthodes sont basées sur la mesure de la pression acoustique et de la vitesse particulaire soit en champ proche, soit autour de la source étudiée. L'idée est de séparer les différentes contributions du champ acoustique, par exemple, le champ direct rayonné par la source, le champ réverbéré, le champ dû aux sources secondaires, ou le champ diffracté par la surface source. Nous discutons également des approches expérimentales, qui sont basées sur la mesure des chemins de propagation au lieu de les calculer par des modèles analytiques. L'avantage de ces approches est la représentation correcte de la propagation à l'intérieur des habitacles, l'inconvénient majeur étant le protocole expérimental assez coûteux en temps de mesure.

Dans une dernière partie, nous présentons une synthèse des développements sur l'antennerie acoustique, afin de mieux s'adapter à ce type d'environnement. Une partie est consacrée aux antennes sphériques rigides et transparentes. Nous verrons que dû a leur symétrie 3D, les sphères sont bien adaptées aux mesures dans les espaces fermés.

Parmi les méthodes présentées dans la synthèse bibliographique, nous nous intéressons particulièrement à la méthode des sources équivalentes (ESM). Des facteurs comme simplicité, rapidité de calcul et la possibilité d'obtenir des résultats de localisation ainsi que de quantification ont motivé ce choix.

Le deuxième chapitre est donc consacré à l'étude de la méthode des sources équivalentes, en particulier son application aux espaces clos. Pour ce faire, nous utilisons un modèle de potentiel de simple couche pour représenter les surfaces de l'habitacle. L'idée est donc de trouver la densité de ce potentiel qui représente aux mieux l'information mesurée par une antenne de capteurs, placée à l'intérieur de l'habitacle. Nous remarquons que cette approche simplifiée du problème entraînera des avantages mais aussi des inconvénients, notamment pour avoir négligé l'effet des réflexions. Ensuite, nous avons vu que cette approche est basée sur un problème inverse et donc sensible aux difficultés liées a ce type de problème, en particulier, la sensibilité des solutions face aux erreurs de mesure et/ou de modèle. Des techniques dites de régularisation, sont donc nécessaires pour assurer la stabilité de la solution. L'aspect de la régularisation est brièvement introduit dans le Chapitre 2 (une étude plus détaillée est présentée au chapitre suivant).

La deuxième partie du Chapitre 2 est consacrée aux modèles de propagation acoustique, qui vont relier les sources équivalentes aux capteurs de mesure. En particulier, nous nous intéressons aux modèles de propagation entre sources élémentaires (monopoles) et microphones sur l'antenne de mesure. Etant donné que nous nous sommes intéressés aux antennes sphériques rigides, une partie de ce chapitre est dédiée à l'étude de quelques particularités de ce type d'antenne. La rigidité de la sphère va engendrer la diffraction des ondes acoustiques qui arrivent sur celle-ci. La prise en compte de la diffraction autour de la sphère, par le modèle de propagation, est possible grâce à la solution de l'équation de Helmholtz en coordonnées sphériques. Ceci est l'objet de la troisième partie du Chapitre 2. Finalement, nous concluons ce chapitre par l'étude d'une approche d'analyse de causalité, proposée afin de mieux comprendre les résultats d'identification, notamment la distinction entre les vraies sources et leurs réflexions.

Le chapitre 3 est entièrement consacré à l'étude de la régularisation du problème inverse. Nous commençons par introduire quelques aspects préliminaires sur la régularisation. Notamment nous utilisons la condition de Picard afin d'expliquer l'instabilité inhérente des problèmes inverses face aux erreurs de mesure. Ensuite, nous faisons une synthèse bibliographique des différentes méthodes de régularisation existantes dans la littérature, avec une précision sur la méthode de décomposition en valeurs singulières tronquée (TSVD) et la régularisation de Tikhonov. Par la suite nous discutons du problème inverse sur un point de vue Bayésien. Dans le cadre Bayésien nous considérons les variables et inconnues du problème comme des variables aléatoires et leur nature d'incertitudes est codée par des densités de probabilité (ddp). L'application de cette approche aux problèmes inverses donne lieu à deux parties, à savoir:

1. un *modèle de vraisemblance* qui relie les observations (mesures) aux inconnues du problème, à partir d'un modèle physique de propagation;

2. un *modèle a priori*, incorporant des informations disponibles sur les inconnues du problème, avant de réaliser les mesures.

La règle de Bayes nous montre comment rassembler ces deux modèles afin de trouver la densité de probabilité *a posteriori*, qui nous donne la probabilité inverse des inconnues (champ source) sachant les mesures. Celle-ci est la solution du problème inverse, d'où nous pouvons obtenir plusieurs estimateurs, le maximum a posteriori (MAP) étant un choix typique. Plus précisément, l'estimateur MAP nous donne la valeur la plus probable des inconnues (e.g. champ source) sachant les mesures.

Ensuite nous remarquons que selon nos choix pour les ddp *a priori* et de *vraisemblance*, nous obtenons naturellement des mécanismes de régularisation particuliers. En plus, nous notons que des choix particuliers donnent lieu à une régularisation du type Tikhonov. En revanche, la difficulté majeure des diverses techniques de régularisation est le réglage d'un paramètre que l'on appelle le *paramètre de régularisation*.

Cela est l'objet de la deuxième partie du Chapitre 3, consacrée au problème de réglage automatique du paramètre de régularisation. Dans ce contexte, nous montrons que le cadre Bayésien nous ouvre des nouvelles voies pour répondre à cette question. Des critères pour estimer ce paramètre directement à partir des données mesurées et du modèle direct, vont découler de cette approche.

Ensuite nous étudions une méthode assez répandue dans la littérature, la courbe en L (L-curve). Nous expliquons le principe de cette méthode et plus particulièrement les difficultés rencontrées quand appliquée aux problèmes étudiés dans cette thèse. Plus précisément, le critère de la courbe en L génère des discontinuités dans la sélection du paramètre de régularisation en fonction de la fréquence. Cela introduit des discontinuités non-physiques sur le spectre de puissance de la source. Nous analysons ensuite une extension du critère de la Courbe en L afin d'éliminer ces inconvénients.

La troisième partie du Chapitre 3 est dédiée à une comparaison des différentes méthodes pour la sélection du paramètre de régularisation. Nous comparons, par le moyen de simulations numériques et d'une validation expérimentale, le critères de la Courbe en L, la validation croisée généralisée (ou GCV pour Generalized Cross-Validation) et le critère Bayésien présenté précédemment. La performance de ces trois méthodes par rapport a un grand nombre de paramètres a été étudiée, notamment: (a) le niveau de bruit; (b) la fréquence d'étude; (c) le nombre d'inconnues du problème; (d) la distance entre surface source et surface de mesure, directement liée au nombre de conditionnement de la matrice à inverser. Cette étude nous a permis de tirer des conclusions importantes pour la suite de ce projet. Nous avons vu que les approches GCV et courbe en L présentent des performances qui varient considérablement en fonction des différents paramètres étudiés. En revanche, le critère Bayésien s'est montré très robuste face aux différents paramètres, avec l'erreur la plus petite par rapport à la solution optimale. Une validation expérimentale nous a conduit à des résultats similaires, avec toujours le critère Bayésien le plus robuste. Ceci est illustré sur la Figure 1, où nous comparons la puissance acoustique estimée par différentes méthodes de sélection du paramètre de régularisation. Nous observons que la méthode GCV surestime largement la puissance dans certaines bandes de fréquence. En plus, nous constatons les discontinuités introduites par la Courbe en L, notamment autour des fréquences de 950 Hz et 650 Hz. Nous espérons que les résultats issus de cette comparaison seront utiles non seulement pour la régularisation des problèmes traités dans cette thèse, mais aussi pour ceux qui travaillent sur des problèmes inverses en acoustique.

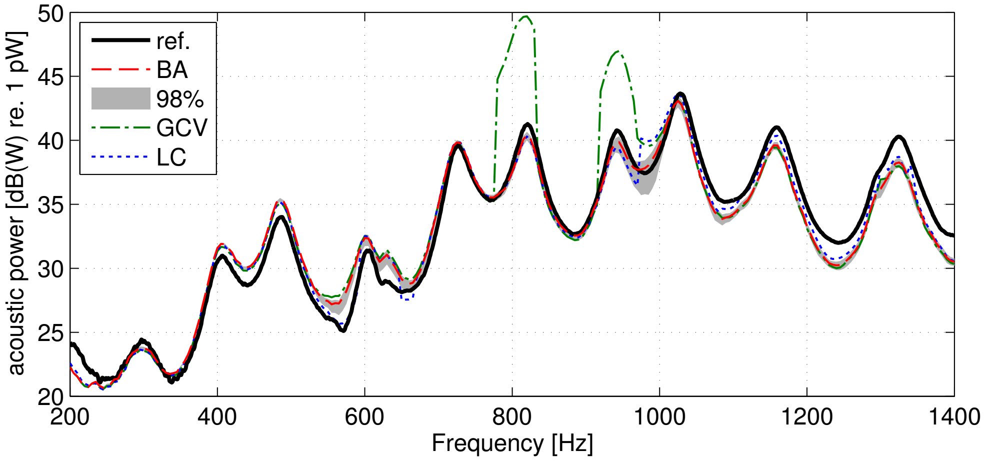

Figure 1: Estimation de la puissance acoustique obtenue par différents méthodes de sélection du paramètre de régularisation. BA: critère Bayésien; GCV: validation croisée généralisée; LC: courbe en L. La puissance de référence (ref.) a été obtenue par des mesures avec un capteur de pression et vitesse particulaire (p-u).

Nous avons consacré la dernière partie du Chapitre 3 à l'étude de la sensibilité du problème inverse en acoustique face à la régularisation. Ceci, est encore un des avantages que le cadre Bayésien nous offre. Etant donné que la solution du problème inverse est sous la forme d'une densité de probabilité (ddp) nous pouvons l'utiliser pour obtenir différents indicateurs. Un indicateur particulièrement intéressant est la variance de cette distribution, qui peut être facilement propagée vers les quantités acoustiques reconstruites, par exemple, le champ source, la puissance acoustique, l'intensité acoustique, entre autres. Cela nous permet, par exemple, de calculer des intervalles de confiance sur des quantités reconstruites. Nous analysons deux façons de faire, une par l'utilisation des méthodes dites MCMC (Markov chain Monte Carlo) et une deuxième par l'approximation de la distribution *a posteriori* par une Gaussienne. Ces deux approches sont ensuite testées sur des cas de simulations numériques.

Après les considérations sur la régularisation du problème inverse, nous nous sommes intéressés à l'application de la méthode au cas cible dans cette thèse, l'identification de sources de bruit à l'intérieur des espaces clos. Dans ce contexte, nous avons été initialement confrontés à deux difficultés majeures: la première liée au positionnement de l'antenne de capteurs à l'intérieur de l'habitacle et la seconde liée au caractère très sous-déterminé du problème. Afin de surmonter ces difficultés, une approche par pondération itérative a été proposée.

Selon le choix de la position de l'antenne à l'intérieur de l'habitacle, la distance entre chaque source équivalente et l'antenne de microphones peut varier considérablement. En conséquence, les sources équivalentes qui sont plus proches de l'antenne ont besoin de moins d'énergie pour générer un niveau de pression donné (à la position de l'antenne) que les sources plus lointaines. Autrement dit, plus de "poids" est donné aux sources équivalentes plus proches de l'antenne de capteurs. Ceci a été la motivation pour la première stratégie de pondération proposée. L'idée est de considérer un nouveau problème de minimisation, qui est pondéré par une matrice diagonale avec ces éléments diagonaux proportionnels à la distance entre chaque source équivalente et le centre de l'antenne.

La deuxième difficulté à laquelle nous nous sommes confrontés est due au caractère très sous-déterminé du problème qu'on cherche à résoudre. Nous avons vu que la solution du problème très sous-déterminé donne lieu à des sources reconstruites avec des caractéristiques non-physiques. Plus précisément, nous remarquons que les sources reconstruites présentent une directivité très prononcée en direction de l'antenne, engendrée par la phase relative entre les sources identifiées. En conséquence, l'estimation de la puissance acoustique est fortement sous-déterminée. Afin de surmonter cette difficulté, une deuxième stratégie de pondération a été proposée, qui, par conception, est implémentée de façon itérative. L'idée consiste en l'utilisation des résultats d'identification d'une étape précédente pour pondérer un nouveau système à résoudre.

Dans la première partie du Chapitre 4 nous discutons ces deux stratégies de pondération. Dans une deuxième partie, nous présentons des résultats de simulations numériques afin de valider l'approche proposée. Nous observons que, la première stratégie de pondération nous permet de corriger des effets indésirables relatifs au positionnement de l'antenne. Ensuite, nous montrons que la résolution spatiale est considérablement amélioré par la deuxième stratégie (pondération itérative). Nous constatons finalement que la pondération itérative permet de contrôler l'effet lié à la sous-détermination du problème et avec un certain nombre d'itérations la puissance acoustique identifiée converge vers la "vraie" puissance acoustique.

Par la suite, nous nous sommes intéressés à l'étude de la sensibilité de l'approche proposée face aux erreurs commis lors de la simplification du problème ainsi que face à l'hétérogénéité de la distribution des sources équivalentes. Pour cela, nous avons analysé l'impact des réverbérations qui peuvent exister dans les environnements réels. Nous constatons que la méthode est sensible aux conditions non-anéchoïques, dans le sens où les réflexions sont identifiées comme des "vraies" sources. L'amélioration de la résolution spatiale, n'est quant à elle, pas perturbée. En ce qui concerne l'aspect quantitatif de la méthode, nous avons vu que l'estimation de la puissance acoustique est affectée par les réflexions. Plus précisément, nous notons l'apparition des "creux" dans le spectre de puissance. L'intervalle de ces creux étant lié à la différence de la distance de propagation entre la source principale et ces réflexions. Cela nous indique que ce résultat est dû aux phénomènes d'interférence des ondes acoustiques au niveau de l'antenne de microphones.

En ce qui concerne la sensibilité de la méthode face à la distribution des sources équivalentes, nous avons montré l'importance d'analyser les résultats de localisation à partir des cartographies de puissance par unité de surface. Cela est nécessaire pour prendre en compte des possibles hétérogénéités sur la distribution des sources équivalentes. En plus, nous avons noté que l'approche classique tend à donner plus de poids aux régions ayant une densité de sources équivalentes plus importante. En revanche, l'approche par pondération itérative nous a permis de corriger cet effet.

Finalement, dans la dernière partie du Chapitre 4 nous présentons une application de l'approche par l'analyse de la causalité des sources identifiées. Nous constatons que cette approche peut être utile afin de distinguer entre des "vraies" sources et leurs réflexions.

Le dernier chapitre de cette thèse est consacré aux validations expérimentales et applications pratiques de la méthode. Pour ce faire, nous avons conçu une antenne sphérique de microphones. Le nombre de capteurs a été limité par le nombre de voies du système d'acquisition disponible, c'est-à-dire 32. Conséquemment nous avons réfléchi sur une distribution avantageuse pour 32 capteurs autour de la sphère. En particulier, la géométrie d'un icosaèdre tronqué s'est avérée intéressante pour ce nombre de microphones. Ce choix consiste à placer les microphones au centre de chacune des 32 faces de l'icosaèdre tronqué (voir Figure 2). Ce choix nous donne une distribution avec un espacement uniforme entre les microphones. Un avantage de cette configuration est la possibilité d'effectuer une rotation de $\pi/5$ afin de doubler la densité de capteurs, en arrivant à une configuration avec 61 microphones. Cette dernière demandera l'acquisition en deux passes et la synchronisation des mesures non-simultanées, donc ne pouvant être appliquée qu'à des conditions stationnaires. La mesure de la directivité de la sphère utilisée (rayon 14,5 cm) nous a permis de valider le modèle de diffraction utilisé.

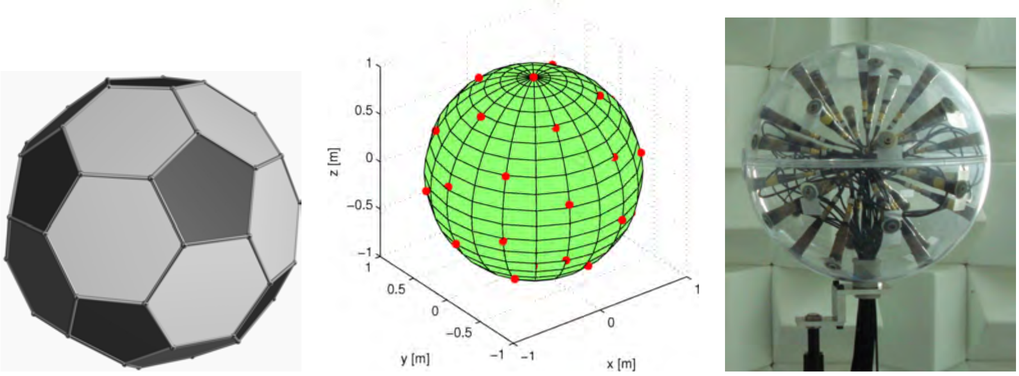

Figure 2: Gauche: géométrie d'un icosaèdre tronqué. Centre: distribution des points au centre de chaque face de l'icosaèdre tronqué. Droite: Antenne sphérique de rayon 14.5 cm avec 31 microphones conçue pour les validations expérimentales.

Ensuite, plusieurs validations académiques ont été réalisées. Nous présentons initialement une première validation, dont le but a été d'étudier l'effet de la pondération par la distance (première stratégie). Nous avons observé des effets similaires à ceux obtenus par les simulations numériques, et la pondération par la distance nous a permis de les corriger. Par la suite, nous présentons une validation de la deuxième stratégie de pondération. Le but a été d'estimer la puissance acoustique d'une source, supposée omnidirectionnelle pour la bande de fréquence étudiée, placée à l'intérieur d'une salle semi-anéchoïque. Cette validation nous a illustrée les difficultés liés à la sous-détermination du problème, notamment le caractère hyper-directif des sources reconstruites. Des résultats de quantification acceptables ont été obtenus par la méthode de pondération itérative, avec un certain nombre d'itérations (8 dans ce cas particulier), comme montré sur la Figure 3.

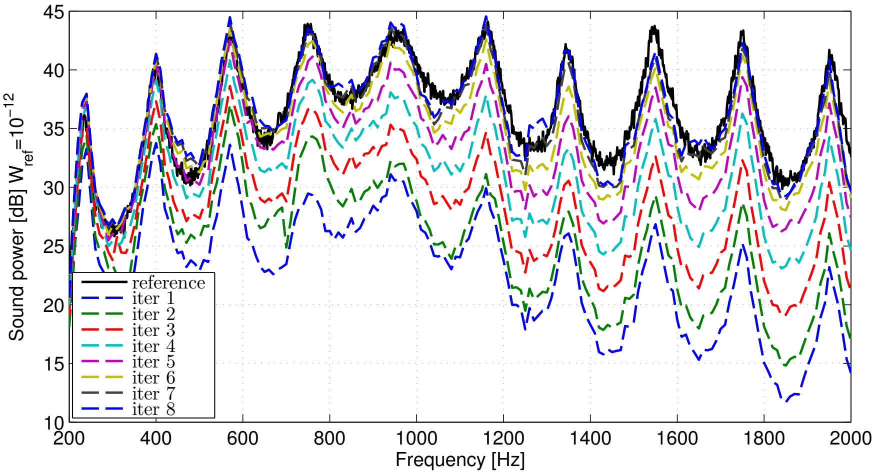

Figure 3: Puissance acoustique en fonction de la fréquence pour : (—) mesure référence et obtenue par l'approche de pondération itérative de la première à la huitième itération.

Nous montrons ensuite une troisième étude expérimentale, dont le but a été de localiser et quantifier deux sources corrélées et placées sur le sol d'une salle semi-anéchoïque (cf. Figure 4(a)). Les résultats de cette expérimentation nous ont illustré l'amélioration de la résolution spatiale, notamment, la contribution des deux sources a été séparée même en basses fréquences (cf. Figure 5). En revanche, nous avons pu noter une limite de la méthode en termes de quantification de la puissance acoustique, liée à la directivité des sources physiques. D'après la Figure 4(b) nous pouvons noter que les sources utilisées ne sont pas bafflées et la sortie de la chambre de compression est à une distance donnée du sol rigide. Cette configuration a généré (dans la bande de fréquence d'étude) une source avec des caractéristiques de directivité similaires à celles de deux monopoles en phase. Nous avons vu que, pour une bande de fréquence donnée, l'antenne acoustique a été placée dans une zone de directivité faible de la source. En conséquence, les capteurs de l'antenne ont perçu très peu d'énergie rayonnée par les sources, et donc, leurs puissances ont été sous-estimées.

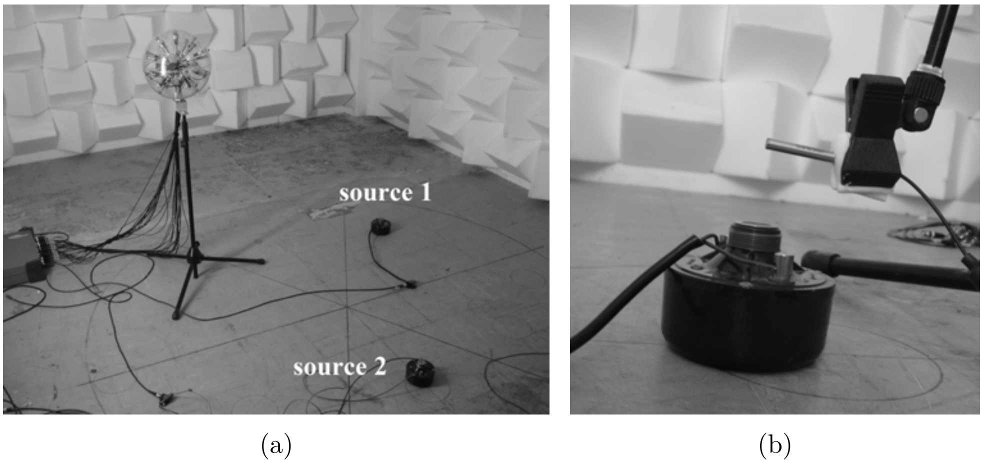

(a) (b)

Figure 4: (a) Protocole expérimental montrant l'antenne sphérique et deux sources placées sur le sol d'une salle semi-anéchoïque. (b) Détail de la source (chambre de compression).

Ensuite, nous presentons une quatrième étude afin de mettre en œuvre une technique expérimentale pour effectuer des mesures en deux passes avec une antenne sphérique. Pour ce faire, nous avons utilisé une technique permettant de synchroniser des mesures non-simultanées. Cette technique requiert un nombre de références fixes au moins égal au nombre de phénomènes physiques (sources) incohérentes. Nous avons vu que l'approche en deux passes nous donne des résultats relativement meilleurs en hautes fréquences.

Finalement, la dernière partie du Chapitre 5 est consacrée à une application pratique de la méthode pour localiser des faiblesses acoustiques à l'intérieur d'un bus. Pour cela, un système double sphère développé par l'entreprise MicrodB a été utilisé pour mesurer

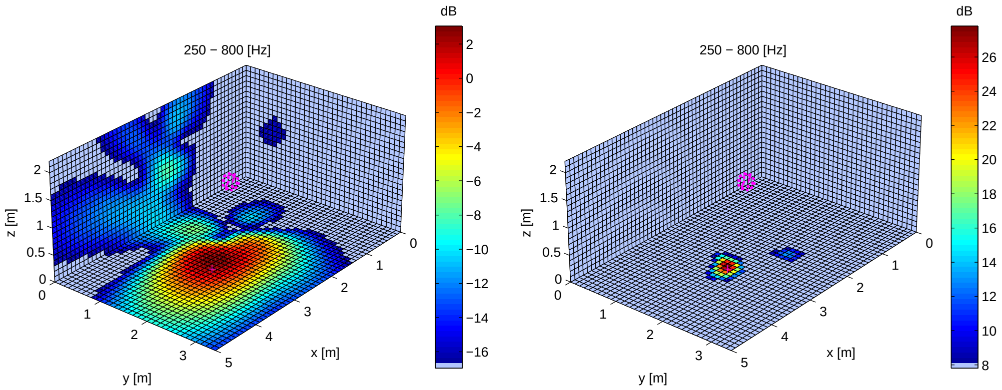

(a) approche classique (b) troisième itération

Figure 5: Cartographies de débit intégrées dans la bande de fréquence de 250-800 Hz avec une dynamique de 20 dB. (a) approche classique ; (b) troisième itération de la méthode par pondération itérative

le champ acoustique à l'arrière d'un bus hybride (diesel et électrique) conçu par IVECO France Irisbus (cf. Figure 6). Le système double-sphère est composé d'une sphère rigide de rayon 15 cm et 24 microphones et une sphère transparente de rayon 40 cm, avec 24 microphones. Nous avons vu que ce système apporte des avantages en basses fréquences, notamment une meilleure résolution spatiale. Ensuite, nous avons appliqué l'approche par pondération itérative présentée au Chapitre 4. Les résultats d'identification nous ont illustré l'importance de la première stratégie de pondération (pondération par la distance) afin de corriger le positionnement de l'antenne. D'après ces résultats nous avons pu identifier des faiblesses acoustiques au niveau des portes arrières (cf. Figure 7) ainsi qu'au plancher bas arrière.

Comme nous avons vu dans cette thèse, l'application des techniques d'imagerie acoustique pour l'identification de sources à l'intérieur des espaces clos pose plusieurs difficultés. Dans ce contexte, une approche par pondération itérative a été proposée afin de pallier à certaines de ces difficultés. Une quantification raisonnable de la puissance acoustique des sources identifiées a été seulement possible en utilisant l'approche itérative. En particulier, les sources identifiées ont fourni une bonne reconstruction de la pression acoustique au niveau de l'antenne mais une reconstruction erronée en dehors de cette région. En d'autres termes, les sources identifiées concentrent toute leur énergie rayonnée vers l'antenne de microphones. Compte tenu des considérations précédentes, nous proposons ici des voies de poursuite de ces travaux. Dans ce contexte, il serait intéressant en quelque sorte d'imposer *a priori* que la reconstruction soit acceptable non seulement sur la surface de mesure, mais aussi ailleurs dans l'habitacle.

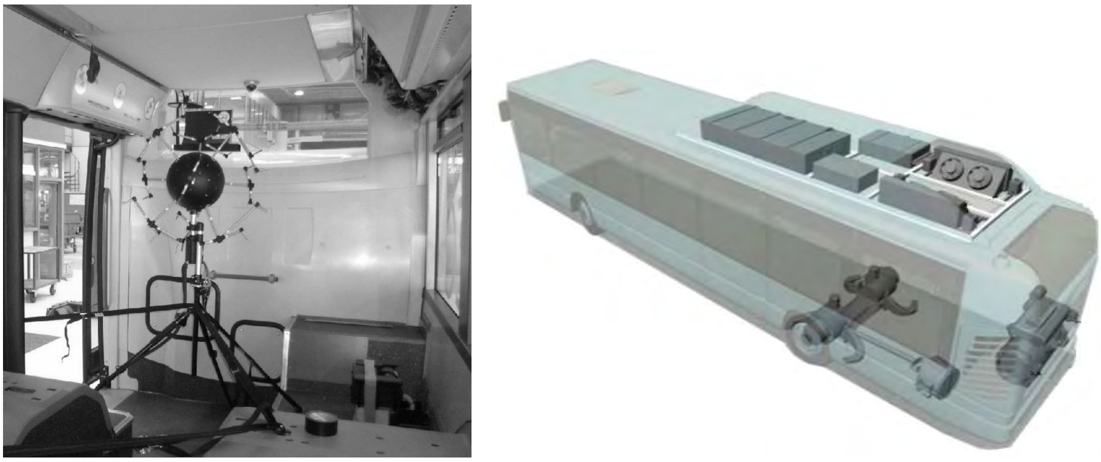

(a) (b)

Figure 6: (a) Configuration expérimentale pour les mesures acoustiques à l'intérieur du bus. La figure montre le système double-sphère (MicrodB) placé à l'arrière du bus. (b) Schéma d'un bus hybride (diesel et électrique) - IVECO France Irisbus.

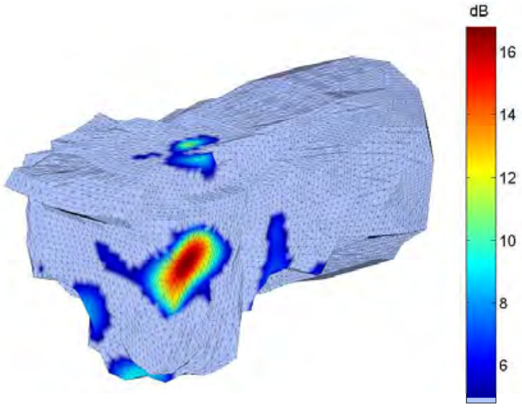

Figure 7: Cartographie de débit (dB ref. m^3/s) intégrée sur la bande de fréquence de 440 à 490 Hz avec une dynamique de 12 dB. Ce résultat correspond à la première itération de l'approche par pondération itérative.

Afin de surmonter les difficultés liées à l'aspect fortement sous-déterminé du problème, les techniques qui imposent un *a priori* de parcimonie afin de régulariser le problème pourraient être appropriées, comme par exemple dans les travaux de A. Peillot [Pei12] et N. Chu *et al.* [CPMD11, CMDP13]. Etant donné que dans la formulation utilisée tout au long de cette thèse le nombre de sources "réelles" est largement inférieur au nombre de sources équivalentes (ou candidates), nous pouvons supposer que le champ source est parcimonieux dans l'espace de reconstruction. En termes de la formulation mathématique, au lieu de minimiser la norme l_2 (i.e. l'énergie) du champ source, le nouveau problème consisterait à minimiser sa norme l_1. Contrairement à la minimisation de la norme l_2, il n'y a pas de solution analytique pour le problème de minimisation l_1, et donc nous devons recourir à des algorithmes plus sophistiqués et complexes. Dans le cas où la base de sources équivalentes ne peut pas être supposée parcimonieuse, il serait nécessaire de trouver une base qui représente le champ source de manière parcimonieuse.

D'autre part, la question liée à la directivité des sources réelles semble plus difficile à répondre. Une solution envisageable serait d'utiliser une approche similaire à celle présentée par Castellini [CS10], dans laquelle les mesures sont effectuées en plusieurs endroits à l'intérieur de l'habitacle. Une difficulté additionnelle, toutefois, serait la synchronisation des mesures non simultanées. En effet, la possibilité de synchroniser les mesures sans avoir besoin d'autant de références que de phénomènes incohérents est une autre perspective pour la suite de ces travaux.

Contents

Introduction

Noise and vibration are important parameters for the comfort of passengers and operators inside transportation vehicles, such as buses, trains, aircrafts, among others. Communities have been aware of noise pollution and are forcing authorities to impose new legislation in order to regulate noise emissions. In turn, this motivates manufacturers to produce machines and products having a quieter performance.

Let us take an example of the design of a machine or vehicle that emits noise at operating conditions. If acoustic and vibration performance is not considered since the early design stage, noise and vibration concerns may appear very late in the design cycle, when making changes on the product is normally expensive and of limited options. Generally speaking, noise and vibration issues can be separated in two categories:

1. The noise level radiated by the product is not in agreement with regulations or specifications;

2. The product presents a poor sound and vibration quality, for instance, as compared to a different manufacturer.

Whenever any of the above conditions is not met, one might need to perform modifications or design changes into the product. The first step to take is normally to characterize the noise emissions, in other words, to localize the main noise sources as well as their transfer paths. In order to identify and quantify the noise sources and transmission paths, testing of the product is necessary. Nowadays, the engineers have at their disposal several techniques, such as modal analysis, transfer path analysis (TPA) or acoustic imaging techniques [Plu05, CG11].

In the context of noise reduction from industrial vehicles, this thesis was carried out in the framework of the project ACOUBUS, with support provided by the ADEME. One of the global aims of the project is to consider the acoustics at the design stage of industrial vehicles. In view of the communities, the acoustical performance of transportation vehicles, is of importance for two main reasons: (1) contribute to a pleasant acoustic comfort for passengers and operators, which in turn can motivate the citizens to use public transportation; (2) ensure a quiet sound environment for inhabitants in general by reducing the noise radiated by those vehicles.

The study carried out in this thesis, is within the part of the project concerned with the acoustical performance in the interior of buses. The main objective is to propose acoustic imaging techniques which are capable of locate and quantify the noise sources contributing to the overall noise level inside these vehicles. In addition, it is of importance for the technique to be fast enough such as to reduce the time required for the acoustic adjustment.

Traditionally, the acoustic tuning of industrial vehicles is carried out by the so-called "masking" method. The basic idea is to mask all interior surfaces with acoustic absorbent material, such as lead plates, and to uncover each region one by one. Acoustic quantities such as acoustic intensity are measured at each step and a contribution of each zone to the overall noise level is estimated. Given the estimate of individual contribution, acoustic engineers discuss potential noise abatement options. Often, several iterations are necessary to attain a target sound level, which makes it a time consuming method.

In view of these considerations, the ideal approach based on acoustic imaging techniques should be able to produce similar results to the masking method, however, using a unique pass and without the need to cover the interior surfaces. More precisely, the idea is to use a set of field measurements, as returned by a microphone array, in order to identify those regions which contribute the most to the overall noise level.

Overview of the thesis

In this Section we provide the reader with a general view of the work carried out during this doctoral thesis. The remainder of this thesis is divided in five Chapters:

- In Chapter 1 we provide a literature survey of the various acoustic imaging techniques, with special attention to those techniques applied to interior spaces. This discussion involves techniques such as beamforming, near-field acoustic holography as well as inverse methods. In addition, we discuss practical implementation aspects, such as the configuration of microphone arrays.

- In Chapter 2 we present the theoretical background which is the base of following developments in this thesis. In particular, we describe the equivalent source formulation and its extension to interior problems. An introduction to the ill-posedness of the underlying problem and few regularization techniques are then discussed. Next, we discuss the acoustic propagation model which relates the measured acoustic pressure to the set of equivalent sources used to describe the problem. The last part is dedicated to a technique based on causality analysis which is then applied in later chapters.

- Chapter 3 is dedicated to the issue of regularization of the inverse acoustic problem. In the first part we discuss few preliminary aspects of regularization with emphasis on the so-called *regularization parameter*. A literature review of parameter choice techniques is then presented. Afterwards, we discuss the issue of regularization within a Bayesian framework, which inherently produces regularization mechanisms as well as new criteria to set-up the regularization parameter. The latter is subject of next developments, in which we discuss the implementation of the well-known L-curve method as well as an extension to its criterion. Finally, the last part is devoted to an extensive comparison of parameter choice techniques by means of both numerical and experimental validations.

- In Chapter 4, we describe an iterative weighted technique which is proposed to the equivalent source method. This technique is proposed to overcome the issues found in the practical application of the original equivalent source formulation to interior problems. In particular, we propose a first weighting scheme that aims to take into account the positioning of the array inside the enclosure. A second weighting strategy, which is iteratively implemented, is proposed to improve the capabilities of the method in terms of spatial resolution, dynamic range and especially, the ability to quantify the identified acoustic sources. Several numerical simulations are then reported in the second part of this Chapter. The aim of simulations is to study the capabilities of the proposed method, as well as its sensitivity with regard to modeling errors. The last part of the Chapter discuss the application of the causality technique presented in Chapter 2.

- In Chapter 5 we present several experimental validations and a practical application of the proposed method. In the first part, we describe the practical design of a spherical microphone array used for the experimental validations. Next, the two weighting strategies described in Chapter 4 are tested by means of experimental validations carried in a semi-anechoic chamber. In the second part, we discuss the implementation of an experimental technique to perform acoustic measurements in two-passes using a spherical array. The latter is an attempt to improve the high frequency limits of the method. Finally, a practical application of the proposed technique is reported. The application consists in identifying the noise sources or acoustic weakness inside a bus at driving conditions.

1

Literature Survey - Acoustic imaging in closed spaces

In the previous Chapter we have discussed few methods that are traditionally applied to acoustic adjustment or troubleshooting inside vehicle cabins. Although robust, these methods are usually time consuming and often require several passes to achieve the desired results. The advance of signal acquisition performance and the availability of acoustic arrays has certainly opened many interesting research directions in this field. Various methods have thus been proposed for noise source characterization based on array measurements. Originally, these methods were intended to applications in free-field conditions and more recently many research has been carried to extend these methods to arbitrary environments.

In a general framework, the various methods that have been proposed in this area may be divided into three main groups, namely: (1) beamforming methods; (2) near-field acoustical holography (NAH) methods; (3) inverse methods. This general classification is based on their underlying assumptions and processing to solve a given problem. Indeed, when applied to noise source characterization, all the above methods fall in the same category of inverse problems in the sense that, based on measured field data (*effect*) they wish to identify the source properties (*cause*).

Over the last three decades, acoustic imaging methods have been constantly developed and still are the subject of ongoing research. Our aim in this Chapter is thus to cover the state-of-the-art of acoustic imaging technologies, in particular those applied to closed spaces. In a second part we discuss the recent developments in acoustic arrays for interior noise source applications. In the last part, we briefly present the study that has been carried out throughout this doctoral thesis work.

1.1 Beamforming methods

Since the precursory work of Billingsley and Kinns [BK76] in 1976, the concept of beamforming has been extensively applied in various fields of acoustics. The basic principle of beamforming is to use an array of microphones whose signals are processed with the aim to focus onto a desired position in space. This processing is consecutively performed to a set of candidate positions, yielding the so-called *array output*. The noise sources are then identified by those directions corresponding to the maximum output. Following the advance of data acquisition systems and computer performance, several techniques to extend and improve beamforming capabilities have been proposed in the literature. The review of all beamforming algorithms and extensions is beyond the scope of this thesis and the reader can refer to [Mic06] for a historical overview of acoustics applications or to [JD93] for further insight concerning the algorithms. Our interest in this section is to provide a review of beamforming techniques for noise source localization, in particular, applied to confined environments.

For applications of noise source localization techniques in enclosed spaces, it is essential to distinguish between sound waves coming from the front and from the back of the array. Since the traditional use of planar arrays with pressure microphones distributed on a single layer does not allow one to achieve the above performance, different array configurations have been proposed. In this context, Pascal and Li [PL03, PL06] discussed the use of a microphone array consisted of two closely-spaced layers, in which finite difference approximation is employed to estimate the particle velocity. The combined information of acoustic pressure and particle velocity allows one to distinguish between sources on both sides of the array. Another branch of beamforming aimed at interior source localization is based on spherical arrays, such as the spherical harmonics beamforming (SHB) presented by Haddad and Hald [HH08]. The latter is based on a decomposition of the pressure field (sampled on the sphere) onto a spherical harmonics basis, which is then used to "focus" the array towards a given position in space. The array is then independently steered towards a set of candidate positions and an output is obtained for each look direction, the latter being defined by both azimuth and elevation angles.

The aforementioned methods rely on a free field propagation model between the focusing point and the microphones on the array. Other studies, such as the one presented by Castellini and Sassaroli [CS10], have been intended to reduce the effects of reverberation. In their work, the latter is achieved by measuring the acoustic field with the microphone array sequentially placed at different positions inside the enclosure. The method thus relies on the assumption that the source field is stationary and is based on the fact that the position in which reflection takes place on the boundaries is changed according to the position of the microphone array. Conversely, the original source is "seen" by the microphone array always at the same position, independently of the location of the array inside the enclosure. A statistical processing of the beamforming output for all different array positions yields a sort of "weight", which is then used to reduce the reverberation effects. An application of the above method inside a helicopter cabin was recently presented in reference [CSP+13].

Another approach to reduce the effects of reverberation was motivated by aeroacoustic testing in closed-section wind tunnels [Fen09]. In this context, Fenech [Fen09] used the concept of image sources to take into account the effect of the test section walls. A modified beamforming is then constructed by adding the contribution of image sources to the original steering vector.

The main advantages of beamforming are its simplicity, robustness and fast computation, which for instance, allows the engineer to test several configurations in a short period of time. On the other hand, the inconvenient is the resolution depending of the frequency, which leads to a poor resolution at low frequencies and the difficulty to obtain correct source quantification in terms of acoustic power. Although, the latter issue may be balanced by deconvolution techniques such as DAMAS [BH06] or CLEAN [Sij07].

1.2 Near-field acoustical holography methods

Another group of methods which can be applied to noise source identification is based on the concept of near-field acoustical holography (NAH), introduced by Maynard *et al.* [MWL85]. Originally, the NAH is based on a spatial Fourier transformation of the pressure field spatially sampled on a surface (i.e. *hologram*) to the wave number domain. The measured pressure field in the wave number domain is then projected to any surface conformal to the hologram surface by a particular propagator. Finally, an inverse spatial Fourier transform is taken to obtain the acoustic quantity of interest in the frequency domain. An important feature of NAH, indeed, is that the measurements are taken in the near field of the source, thus the so-called *evanescent waves* are captured, which ensures an enhanced spatial resolution.

The application of acoustical holography techniques in non-anechoic environments was firstly considered by Villot *et al.* [VCR92], who studied the radiation of plane structures inside an enclosure. The studied problem was modeled by a radiator placed at one end of a semi-infinite rectangular duct. The influence of the rigid boundaries is taken into account by considering the standing waves created by the multiple reflections on the side boundaries. One particularity of this approach, however, is the fact that it is only applicable to geometries expressed in separable coordinates and simple boundary conditions.

The use of double layer microphone arrays have also been proposed for NAH techniques. The concept was described by Tamura [Tam90] who used this technique to separate incident and reflected waves on the surface of a test material, in order to estimate its reflection coefficients at oblique incidence. This idea was then used to interior noise source identification purposes [HBD+94]. The idea of separating contributions from both sides of a planar array has also been proposed to other extensions of NAH, such as the statistically optimized near field acoustic holography (SONAH) [Hal06]. One of the main features of SONAH is that it avoids spatial Fourier transforms by directly operating in the spatial domain. The drawback of these techniques when applied to large cabins is the large measurement time required to cover all surfaces, which limits its application to non-stationary conditions.

Another acoustical holography technique aimed at interior source characterization has been proposed by Williams *et al.* [WVHK06]. The principle is to measure the acoustic pressure field on a spherical microphone array placed nearby an interior surface. The measured pressure field is transformed to the spherical harmonics domain and acoustic quantities, in particular, the acoustic intensity field is imaged on spherical surfaces concentric to the spherical array. Since this technique is based on the spherical NAH the reconstruction can only be computed in a spherical volume whose outer surface does not cross any boundaries. Applications of this technique inside an airplane during flight and inside an automobile are reported in references [WVHK06, WT10].

One of the main advantages of techniques based on near field acoustical holography is the enhanced spatial resolution, independent of the frequency. Indeed, the spatial resolution is related to the inter-microphone spacing on the hologram surface. Another advantage is the easy determination of the acoustic particle velocity from measured pressured and vice versa, by means of the Euler's equation [Wil99]. Therefore, any other acoustic quantity depending on these two (e.g. acoustic intensity, acoustic power) can be also determined. One practical drawback, however, is the requirement to carry measurements on the near field of the source, which for certain cases (i.e. large source surfaces or enclosures) can be time consuming.

1.3 Inverse methods

The third group of methods applied to source reconstruction are labeled here as inverse methods. The word "inverse" in this particular context is used to group those methods which are somehow based on a matrix inversion operation.

1.3.1 Inverse boundary element method (iBEM)

The first method discussed in this section is the inverse boundary element method (iBEM), which was originally proposed in acoustics to overcome the limits of NAH related to the application to arbitrarily shaped sources [GB88, VM89, Bai92]. This method is based on the Kirchhoff-Helmholtz integral equation, which relates the acoustic pressure within a bounded domain to the normal surface velocity and surface pressure on the bounding surfaces. This integral equation is then discretized according to the boundary element method (BEM).

In the context of interior source reconstruction, Kim and Ih [KI96] illustrated (by numerical simulations) an application of iBEM to reconstruct the source field on the surfaces of a scaled automotive cabin. They have shown that the position of measurement points is very important in order to obtain a correct reconstruction. In this context they propose the use of a technique so-called effective independence (EfI) [Kam92] method in order to optimize the position of field measurements inside the domain.

The possibility of application to complex shaped geometries and the flexibility of measurements positions are the main advantages of iBEM over NAH. On the other hand, a considerable number of boundary elements and nodes are required (normally 6 nodes per wavelength) to discretize the surfaces. This restriction, in turn, limits the application of iBEM to medium/high frequencies since the number of discretization elements become excessively large. A further difficulty of iBEM techniques, when applied to industrial cases, is the necessity to use model updating approaches in order to adjust the numerical model to the real physical behavior of the structure.

1.3.2 Equivalent source methods (ESM)

A simplified alternative to iBEM, suggested by Koopmann *et al.* [KSF89], is the so-called equivalent source method (ESM), whose idea originated from a calibration procedure used for boundary element problems [KSF89]. Note that this method is also referred to as the wave superposition method. Originally, the ESM was developed to acoustic radiation problems from arbitrarily shaped radiators. The basic principle is that the acoustic field generated by an arbitrary radiator can be replaced by the superposition of fields due to a set of elementary sources (placed within the radiator). The optimal parameters of equivalent sources (amplitude and phase) are determined such that they match the prescribed surface velocities of the radiator. The acoustic pressure field outside the radiator can be then easily evaluated.

Jeans and Mathews [JM92] studied the numerical stability and robustness of the equivalent source formulation. Particularly, they have shown that the original formulation presents a lack of uniqueness when the model of equivalent sources represent an imaginary cavity within the radiation. This effect happens at a set of critical wave numbers related to the eigenvalues of the interior equivalent source domain. In order to overcome this problem they propose a hybrid formulation which combines single and double layer potentials. Although the formulations above are aimed at forward propagation problems (acoustic radiation), a matrix inversion is required to obtain the parameters of the equivalent sources. The matrix to be inverted relates the source strength of equivalent sources to the normal surface velocity at the evaluation points.

The application of ESM to the reconstruction of interior pressure field was discussed by

Johnson *et al.* [JEBGB98]. They have used the principle of equivalent sources to compute the acoustic pressure field inside an enclosure containing scattering objects. Two main assumptions are made in this work: 1) the surface velocity at some evaluation positions on the boundaries is known; 2) the position and number of sources within the enclosure is also known. The problem is solved such that the equivalent sources, which are placed outside the enclosure, match the prescribed surface velocity at evaluation points in a least squares sense. Once the equivalent sources are determined the pressure field inside the enclosure is fully determined. In this work, the equivalent sources are carefully placed according to two strategies: 1) to coincide with the first order images of the source placed inside the enclosure; 2) on a spherical surface of large radius compared to the enclosure dimensions, to account for the far-field image sources.

Another method that may be viewed as a particular case of the ESM, is the so-called Helmholtz equation least-squares (HELS) which was introduced by Wang and Wu [WW97]. The idea is to express the pressure field as an expansion of particular solutions to the Helmholtz equation, which for interior problems may represent acoustic modes. The coefficients of the expansion are determined such that the assumed-form solution match the measured pressure field in a least-squares sense. The implementation of HELS for the reconstruction of interior pressure fields is described in reference [WY98]. It was suggested that the number of measurement positions should be at least equal or larger than the number of acoustic modes used to express the interior acoustic pressure field. Reference [MW02] reports an application of the above method using synthetic measurements generated by the boundary element method (BEM), which simulates a rigid-walled vehicle compartment. It is argued that one of the advantages of HELS is the fact that it is based on a direct formulation of the Helmholtz equation and thus it is not sensitive to the problem of instability of the solution with respect to measurement errors. On the other hand, it shows difficulty of convergence when the cavity deviates considerably from a sphere as well as for high frequencies.

Later on, Wu [Wu04] proposed a hybrid approach in order to overcome the limitations of NAH, namely, the reconstruction of arbitrary sources within non-anechoic environments. The method, which is a combination of HELS and iBEM, is named as hybrid near field acoustical holography (hNAH). Particularly, the near-field acoustic pressure measured on a surface conformal to the source is used as input to HELS which returns the coefficients of the corresponding expansion. The coefficients of the expansion are used to generate as much as necessary synthetic acoustic pressure on the measurement surface. Precisely, the number of synthetic measurement positions is equal or larger than the number of nodes used to discretize the source surface. In turn, these synthetic measurements are used as input to iBEM, which finally returns the normal surface velocities and pressures over the source surface. In the case where the source is not within an anechoic environment, the measurements need to be carried on two conformal surfaces and a modified version of HELS which includes incoming and outgoing waves on the expansion is used.

A common aspect of many of the inverse methods cited above is their ill-conditioned nature, in Hadamard's sense [Han98]. In particular, their solutions are very sensitive to errors in the measurement data. Therefore, in order to obtain reasonable solutions, one should introduce *a priori* assumptions in the underlying problem that often reveals itself in the form of the so-called regularization techniques. Many research effort has been dedicated to the field of regularization and consequently various techniques have been proposed in the literature. Due to its relevance to the problem studied in this thesis work, the Chapter 3 is dedicated to the issue of regularization of the inverse acoustic problem. A more detailed description and literature review are presented therein.

1.4 Field separation methods

More recently, researchers have been interested on the separation of acoustic fields based on combined information of particle velocity and acoustic pressure, measured either with two pressure microphones (p-p) or with a microphone and particle velocity probe (p-u). In this context, Langrenne *et al.* [LMG07] have presented a method of field separation based on the BEM formulation, aiming to recover the acoustic field that a source would radiate in free-field conditions. To that purpose, the pressure field on a surface surrounding a source within a non-anechoic environment is decomposed into "incoming" and "outgoing" fields. While the incoming field comprises the field reflected by walls and any secondary sources in the room, the outgoing field comprises the direct field as well as the field scattered by the source surfaces. The proposed method firstly separates incoming and outgoing fields, then, the outgoing field is decomposed in order to obtain the field that the source would radiate in free-field conditions. It is shown that, indeed, the field scattered by the source (which is assumed to be rigid) has a significant influence as long as the wavelength is of comparable size or smaller than the source dimensions. An experimental validation of the above approach is reported by Langrenne *et al.* in reference [LMG09].

The concept of separation of acoustic fields have also been proposed in conjunction with the equivalent source method [ZJBC09]. In this context Fernandez-Grande *et al.* [FGJL12] compared the reconstruction accuracy of ESM using the field separation for different array configurations, namely: 1) a double layer of particle velocity probes (u-u); 2) a single layer of combined pressure and particle velocity probes (p-u); 3) single layer of particle velocity probes. They have shown that reconstruction based on u-u approach is more robust to measurement noise and less disturbed by flanking sound due to reflections. Indeed, it has also been shown that when the perturbing sound is not critical, the single layer of particle velocity probes provides reasonably reconstruction and is thus a more convenient configuration. The above is true whenever the measurements are taken at very close range (near-field) of the source and the latter can be assumed to be rigid, since the particle velocity generated by disturbing sources vanishes on the source surface.

Recently, an application of field separation to source identification inside a car trunk was carried out by Garcia *et al.* and is reported in [GBL+12]. In this case, the separation is performed in the spherical harmonics domain and allows one to estimate the outgoing field radiated by the source. The measurements are carried out by a hemispherical array of radius 0.175 m consisting of a double layer of microphones, which lays on the source surface. The array is then consecutively moved in order to cover the whole interior source surface, with the latter assumed to be rigid.

Yet in the context of source reconstruction within non-anechoic environments, the method, so-called inverse patch transfer function (iPTF), was proposed by Vigoureux et al. [VTG10]. The method, which is based on the Helmholtz integral formulation, requires combined measurements of particle velocity and acoustic pressure over a fictitious surface surrounding the source. The principle is to discretize both the source and measurement surfaces into smaller surfaces so-called *patches* [Vig12]. The transfer matrix or impedance matrix between *patches* is then computed numerically by means of a finite element modeling of the fictitious volume delimited by both the source and measurement surfaces. The normal surface velocity of the source is finally obtained by computing the inverse of the impedance matrix, which in turn is ill-conditioned, thus requiring the use of regularization methods.

The inconvenient of field separation methods discussed above is the need to perform measurements on the near-field and on a conformal surface surrounding the source. This limitation, in turn, constrains these approaches to non-stationary cases and leads to time consuming measurements to cover a large surface.

1.5 Experimental approaches (measured FRF)

A rather different approach from those discussed in previous sections is based on experimental techniques. The basic idea is to obtain the propagation model between microphones and candidate source positions experimentally, instead of analytically or numerically. This approach was studied by Dumbacher *et al.* [DBHW95] for the identification of tire noise sources. The main advantages of this technique are a more realistic representation of the environment, by including any reverberant path between sources and microphones, as well as no restriction on the geometry of source surfaces. On the other hand, it raises several experimental implementation issues such as: a) the artificial source must radiate enough sound to be detected by the array microphones in the presence of background noise; b) the responses measured by the microphone array must be due only to the artificial source (this issue can be verified by inspection of coherence between input signal and measured signal); c) for a large source surface with a required resolution the number of measurement points can be excessive. A possible implementation is to combine this technique with one of the previous approaches and perform the measurements only at those regions previously indicated by other methods. In addition, care should be taken when inverting the experimental frequency response functions, in order to avoid the amplification of measurement errors.

This approach has also been tested by Holland and Nelson [HN03, HN12] in order to quantify the source strength of acoustic sources. Experimental results with 4 correlated sources within an anechoic room with added reflective surfaces have shown that accurate source quantification is possible using this approach.

1.6 Causality approaches

As we have seen in previous sections, the identification of noise sources within an enclosure is not an easy task. Several approaches to tackle this problem have been proposed in the literature, for instance by measuring in the near-field of the source, use of field separation techniques or by an approximate modeling of the environment. One of the difficulties that one faces in situations involving a multi-path propagation, is the identification of reflections along with the "real" sources. Results are of difficult interpretation in this cases and may mislead the user to consider reflections as real sources.

In this section we discuss some techniques that may be used to gain better understanding in this situations, for instance, to facilitate the interpretation of results. We anticipate that, a convenient alternative would be to determine the possible reverberant paths and thus find which is the original source.

In this context, the analysis carried out by Bae and Kim [BK98] shed us some light into this problem. Particularly, they proposed a technique to verify the causality between a pair of correlated inputs. The target application was to determine the priorities between correlated inputs to be used with Partial Coherence function approach. The causality checking technique is based on the Hilbert transform of the FRF between inputs and can detect a frequency dependent causality relationship. Similar idea may be used, for instance, to evaluate the causality relationship between reconstructed sources in order to determine possible source-reflection paths and, in addition, distinguish between real sources and reflections. This issue is further discussed in the next Chapter and finds its application in the numerical simulations and experimental validations respectively presented in Chapters 4 and 5.

1.7 Microphone array design

As we have noticed from some methods discussed above, the configuration of the acoustic array plays an important role when solving interior noise source identification problems. Our aim in this section is thus to provide a review of different microphone arrays proposed in the literature, as well as some guidelines that can be used for their design.

The design of a microphone array critically depends on the desired application. Parameters such as the frequency range, the size of the object to be characterized and the measurement environment (i.e. interior or exterior domain) are the major constraints which will guide the user towards a given array configuration. Hereafter, we focus the discussion in the configurations best suited for applications in closed spaces. In this particular case, it is crucial for the array the ability to distinguish between waves coming from any direction in the space. A planar array with a single layer of pressure probes, for instance, is usually applicable to reconstruct sound fields coming from only one side of the array. The extension of planar arrays for interior problems applications has become possible through the use of double-layer arrays. A first development in that direction was the use of sound pressure measurements in two closely spaced parallel surfaces [Tam90,PL03,PL06,Hal06,BCC08], where the particle velocity is obtained by a finite difference approximation of the pressure gradient. More recently, with the advent of particle velocity transducers [dB03], combined pressure and particle velocity transducers in a single layer [JJ07, ZJBC09] and two layers of particle velocity probes [FGJL12, FGJ11] have been proposed.

Due to its three-dimensional symmetry, a spherical geometry is well-adapted to interior problems since it easily allows one to take into account waves coming from any direction. In beamforming terms, a spherical configuration is able to “steer” an identical beam in any 3D direction. However, the choice of a spherical geometry raises several other questions such as: 1) How to define its diameter? 2) How to spatially distribute the microphones? 3) How to decide between an open or a rigid configuration? The discussion provided in the next section aims to help us to answer the above questions.

1.7.1 Spherical microphone arrays

In this section we discuss some practical aspects concerning the design and implementation of spherical microphone arrays for acoustic imaging purposes. First of all, the major constraints that will guide the user towards a given configuration are the frequency band of interest, the number of microphones available and the operational conditions (i.e. stationary or non-stationary acoustic field). The two first constraints are directly related to the size or diameter of the array. Indeed, the choice of the array diameter is usually a trade-off between low frequency robustness and sensitivity to spatial aliasing at higher frequencies. Particularly, for a given number of microphones, a larger radius would increase the robustness at low frequencies, on the other hand the average inter-microphone spacing would also increase, that in turn will limit the high frequency of application due to spatial aliasing.

Another parameter that must be adjusted is the sphere configuration. Both rigid [HH08, SLD10] and transparent sphere [MD06] configurations have been previously studied in the literature and are already commercially available. The main advantages and inconvenient of each are summarized in what follows.

In terms of practical construction the rigid configuration is somewhat more simple than an open sphere that would require a custom structure. The rigid sphere, however is limited in size, either due to a practical constraint of mobility or physically by the scattering effect due to the rigid body. Indeed, as we shall see in the next Chapter, the scattering effects can be carefully taken into account into the propagation model of incoming waves, however, at the expense of a higher computational cost. In addition, the scattering phenomenon yields a better numerical robustness in comparison to an open sphere configuration, which shows a numerical instability at some particular frequencies. This behavior for the open sphere is observed for analysis based on the spherical harmonics decomposition, more details on this issue can be found in references [Raf05, BR07]. Recent research studies have been carried to propose configurations to avoid this problem, for instance the use of cardioid microphones or a dual-sphere configuration [BR07]. A further advantage of the rigid configuration is the fact that the rigid spherical baffle provides an artificial directivity to the microphones, which in turn enhances the ability of the array to distinguish waves coming from the front or from the back of the array.

Another practical advantage of the rigid configuration is that the interior of the sphere can serve as housing for cables and other necessary equipment. The open sphere, in turn, offers the possibility for larger arrays, that could be beneficial at low frequencies for instance. A good compromise to enlarge the operating bandwidth is to combine a rigid sphere of small diameter with a open sphere of large diameter, at the expense of a larger number of microphones, as proposed in reference [CDPL12].

An additional parameter that also must be adjusted is the microphone distribution or sampling scheme on the sphere. Due to practical constraints such as the number of channels of an acquisition system or the cost of acoustic probes, the acoustic field must be sampled at discrete spatial positions over the sphere. Similarly to sampling in time domain, the spatial sampling of the acoustic field on a sphere is subject to a limited bandwidth to avoid aliasing. For analysis based on the spherical Fourier transform, the conversion from spatial domain to spherical harmonics domain requires an integration of a function (e.g. acoustic pressure) over a sphere. In practice this integration is approximated by a finite summation which is truncated up to a maximum order N. In order to have a negligible error in the integration up to a given order N, the number of microphones or spatial samples should be [AW02, WT10]:

$$L \geq (N+1)^2, \tag{1.1}$$

where L is the number of microphones. Equation (1.1) may be interpreted as a spatial and spherical version of Shannon-Nyquist theorem, such that this condition must be respected in order to have an aliasing free result. However, as shown by Rafaely *et al.* [RWB07], in practice this condition depends on the distribution of microphones over the sphere. In turn, the choice of the sampling scheme is usually a compromise between simplicity of the arrangement and the required number of microphones to perform an aliasing-free decomposition.

The design of spherical microphone arrays has been the subject of various researches, mainly in connection with spherical harmonics formulation [Raf05, AW02, LD07]. In this context, Rafaely [Raf05] provides an analysis of different types of errors that these microphone arrays are subjected, namely: a) measurement noise; b) inaccuracy on the positioning of microphones and c) spatial aliasing error. It was shown that at low frequencies measurement noise and positioning error have a similar contribution to the global noise and at higher frequencies the aliasing errors predominate. In addition, it was shown that the choice of sampling scheme has mainly influence on the spatial aliasing performance, other errors being independent of the microphone distribution.

The distribution or sampling of points on the sphere with the aim to minimize the number of required points for a given order N has been widely studied. The reader may refer to references [Raf05, RWB07, LD07, Zot09, AR12, HS96, FM99] for more detailed information.

In Section 5.1 we discuss the practical implementation of a microphone array for the applications studied in this thesis.

2

Study of the equivalent source method for interior domain problems

Based on the review given in the previous chapter, the equivalent source method is recognized as the one that best suits the target application and specifications in this work. Several advantages of the ESM motivated this choice, such as its flexibility to embrace irregular source geometries, relatively low computational cost, combined noise source localization and quantification and its model simplicity.

Particularly, one of the main interests in this thesis is towards the combination of the equivalent source method with spherical arrays, for interior noise identification. As we shall see, this is a highly underdetermined and ill-posed problem, thus a special attention is also given to the critical aspect of regularization of this acoustical inverse problem. The latter issue is specially covered in the next Chapter.

Our aim in this chapter is to give an outline of the equivalent source method which is the base for the subsequent developments in this thesis. A particular care will be addressed to the extension of ESM for interior domain problems. Afterwards, few preliminary aspects of inverse problems, such as their ill-posedness and the need for regularization will be discussed. Next, the combination of ESM with spherical array of microphones will be investigated with emphasis on the propagation models used for the source reconstruction. Given an estimate of the reconstructed source field (in terms of the source strength of equivalent sources), we explain how to assess other acoustic quantities, namely the acoustic pressure field and the radiated acoustic power. Finally, we discuss the implementation of a post-processing tool which aims to provide further insight into the reconstructed source field.

2.1 The equivalent source concept

In the late eighties, Koopmann [KSF89] introduced the equivalent source concept into the field of acoustics. In its original formulation the method was proposed for sound radiation problems from sources of arbitrary geometry. Assuming that the normal velocity on the surface of a radiator is known, the idea is to find a set of equivalent sources (placed on an arbitrary surface within the radiator) that matches the prescribed normal velocity. Once the ideal source strength of equivalent sources is obtained, the acoustic pressure field on the surface of the radiator can be easily predicted. Basically, the method reduces to the solution of an inverse problem for the equivalent source coefficients and a forward propagation model is then used to predict the exterior pressure field.

Later on, Jeans and Mathews [JM92] proposed an extension of the method by using a combination of single and double-layer potentials (monopoles and dipoles) to model the equivalent sources. The main motivation of the latter is to avoid the nonuniqueness problem at the eigenvalues of the interior source surface, used to model the actual source.

Johnson *et al.* [JEBGB98] then investigated the equivalent source method for interior and scattering problems. The formulation is based on the *a priori* knowledge of the surface velocity at the boundaries of an enclosure. In this case, a set of equivalent sources placed outside the enclosure can be driven to match the prescribed surface velocities at the boundaries. The identified equivalent sources are then used to evaluate the pressure field inside the enclosure. The location of equivalent sources are carefully chosen according to two criteria: firstly, to coincide with the first order images of the real source (which is inside the enclosure); and secondly on a large sphere surrounding the enclosure, to account for higher order images (far field). Therefore, the application of the method depends on: (a) the knowledge of the real sources position inside the enclosure; (b) prior knowledge of the normal velocity at several "control points" on the boundaries and (c) the characterization of the boundary behavior in terms of its admittance at the "control points".

Since in the cases studied in this thesis no information of acoustic quantities at the boundaries of the cabin is available, the above matching criterion can not be verified. On the other hand, we indeed have a set of field measurements delivered by a microphone array, which in turn can be used as a compatibility criterion. The idea is to find an equivalent source distribution that reproduces the information on the measured surface with minimum discrepancy. However, as we shall see in the next sections, this is not an easy task, specially due to the inherent ill-posedness of the underlying problem.

2.2 Extension to interior domain problems

The formulation for the interior problem is based on the Kirchhoff-Helmholtz equation, which defines that the pressure field inside an enclosure is fully determined by the normal particle velocity and acoustic pressure at the boundaries plus the acoustic sources within the enclosure. The geometry of the problem is depicted in Figure 2.1.

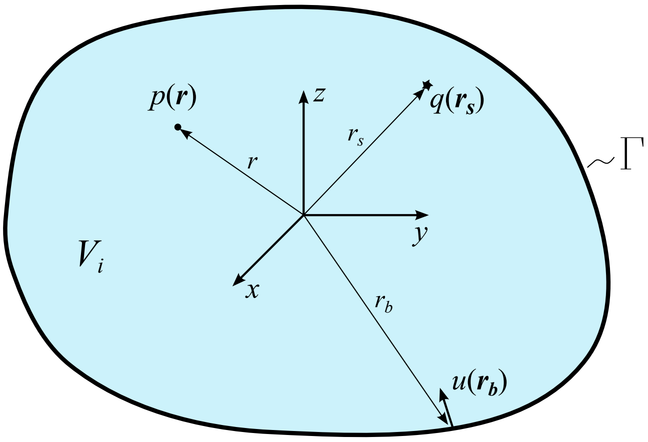

Figure 2.1: The figure shows a volume V_i which is enclosed by a boundary Γ with normal surface velocity $u(\mathbf{r}_b)$. Acoustic receivers are defined by $p(\mathbf{r})$ and internal sources by $q(\mathbf{r}_s)$.

According to the Kirchhoff-Helmholtz equation [Les88] and an implicit harmonic time dependence of the form $e^{\mathrm{j}wt}$, the pressure anywhere in the enclosure is given by:

$$p(\mathbf{r}) = \int_{\Gamma} \left[p(\mathbf{r}_b) \frac{\partial G(\mathbf{r}|\mathbf{r}_b)}{\partial n} + \mathrm{j}\omega\rho u(\mathbf{r}_b) G(\mathbf{r}|\mathbf{r}_b) \right] d\Gamma + \int_{V_i} \mathrm{j}\omega\rho q(\mathbf{r}_s) G(\mathbf{r}|\mathbf{r}_s) dV_i, \tag{2.1}$$

where the position vectors, $\mathbf{r}, \mathbf{r}_b$ and $\mathbf{r}_s$ respectively correspond to an evaluation position inside the enclosure, a point on the surface and the location of any source inside the volume. The angular frequency is ω, ρ is the density of the fluid and $G(\mathbf{r}|\mathbf{r}_b)$ is the (known) Green's function of the medium between positions $\mathbf{r}$ and $\mathbf{r}_b$. This integral equation gives us the direct formulation of the interior problem. In particular, the first integral has the contribution of two terms, namely: (a) a distribution of monopoles corresponding to a single layer potential; (b) a distribution of dipoles corresponding to a double layer potential. The last integral represents the contribution of sources within the volume.

Our interest in this work is on the inverse problem, that is, the identification of the (unknown) source distribution on the bounding surface Γ. Indeed, one way to proceed is to consider both single and double layer potentials. However, this would require the precise knowledge of the bounding geometry as well as a refined discretization scheme, such as typically given by boundary element methods. This is, in fact, the approach used by the inverse boundary element method, which seeks to numerically solve this integral equation (see, for example, [KI96]).

A simplified formulation of this interior problem is based on the equivalent source method. This approach consists in avoiding the direct use of the Kirchhoff-Helmholtz equation (2.1) by identifying a set of equivalent sources that matches the conditions (originally the normal particle velocity) at the boundaries. If this requirement is met, the equivalent sources are also able to reproduce the acoustic field within the domain. In this case, equation (2.1) is simplified and the acoustic pressure inside the enclosure is given by

$$p(\mathbf{r}) = \int_{V_o} \mathrm{j}\omega\rho q(\mathbf{r}_e) G(\mathbf{r}|\mathbf{r}_e) dV_o + \int_{V_i} \mathrm{j}\omega\rho q(\mathbf{r}_s) G(\mathbf{r}|\mathbf{r}_s) dV_i, \tag{2.2}$$

where V_o is the volume outside the boundary Γ and $\mathbf{r}_e$ is the vector which gives the position of the e-th equivalent source. This equation gives us the acoustic field inside the enclosure as a function of both internal sources $q(\mathbf{r}_s)$ and equivalent sources $q(\mathbf{r}_e)$.

Typically, for sound radiation problems (i.e. direct formulation), the normal velocity distribution on the actual source surface is frequently known *a priori*. In this case, the properties of equivalent sources are determined by minimization of the error between the prescribed normal velocity distribution and the one generated by the equivalent sources. Conversely, for back propagation or inverse problems the information on the boundaries is usually unknown, thus requiring a different *matching criterion*. What we do often have at our disposal in this cases, is a set of acoustic measurements (e.g. acoustic pressure) in the field. The alternative is then to force the equivalent source distribution to reconstruct an acoustic field such that it matches the one given by the set of field measurements.

From now on, we assume that there is no sources within the volume bounded by Γ, thus the second integral in equation (2.2) is set to zero. In addition, we define a set of measurement or control points within the enclosure, as shown in Figure 2.2. In turn, this information is used to identify the equivalent source distribution over a fictitious surface, as shown in Figure 2.2.

We remark at this point that, as long as in this case the "matching" surface (field measurements) is usually significantly far from the equivalent source surface, the position of the latter relative to the actual enclosure does not introduces the singularities[1] in the formulation as observed in [KSF89]. In addition, we remark that a major simplification of the problem is made by considering a single layer potential only. Indeed, by making this assumption we are neglecting the boundary effects such as reflections and, as we shall see in Chapter 4, this may introduce few inconvenient consequences.

Assuming that the acoustic pressure is measured at M discrete positions and N equiva-

---

[1] More precisely, these correspond to singularities in the Green's function as the equivalent source distribution approaches the matching surface, which in [KSF89] is the actual surface of the radiator.

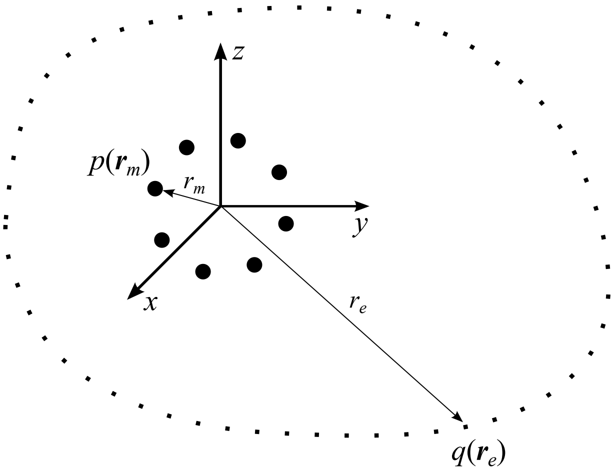

Figure 2.2: Geometry of the problem used for the equivalent sources formulation. The figure shows a set of discrete measurement positions $p(\mathbf{r}_m)$ and the equivalent source distribution.

lent sources are used in the model, we can write the following linear system, using a matrix notation:

$$\mathbf{p} = \mathbf{G}\mathbf{q} + \mathbf{n}, \tag{2.3}$$

where $\mathbf{p} \in \mathbb{C}^M$ is a vector of complex measured acoustic pressure, $\mathbf{q} \in \mathbb{C}^N$ the volume velocity of equivalent sources, $\mathbf{n} \in \mathbb{C}^M$ accounts for measurement noise and $\mathbf{G} \in \mathbb{C}^{M \times N}$ is a matrix of Green's functions. The solution of the linear system in Equation (2.3) depends on the problem size. In the case $M = N$, the matrix $\mathbf{G}$ is square and its inverse can be computed, thus leading to a unique solution. When the number of measurement positions is greater than the number of equivalent sources ($M > N$), the system is overdetermined and has no solution. In this case, the key is to find a solution that minimizes the residual $\mathbf{p} - \mathbf{G}\mathbf{q}$, in a least-squares sense. More precisely, the idea is to find $\mathbf{q}$ that minimizes $\|\mathbf{p} - \mathbf{G}\mathbf{q}\|^2$. The solution of this minimization problem is given by the left pseudo-inverse of $\mathbf{G}$

$$\hat{\mathbf{q}} = (\mathbf{G}^H\mathbf{G})^{-1}\mathbf{G}^H\mathbf{p}, \tag{2.4}$$

where ^{H} stands for the complex conjugate (Hermitian) transpose. However, when no *a priori* on the underlying problem is available and one seeks to find noise sources in a rather large space (e.g. in the interior of a bus) the number of equivalent sources used to map the surfaces is usually greater than the number of discrete measurements ($M \ll N$). The system is thus underdetermined and has an infinite number of solutions. The common approach in this case is to seek the solution of minimum squared norm which satisfies the equality $\mathbf{p} = \mathbf{G}\mathbf{q}$. More strictly, one must solve the following minimization problem:

$$\begin{aligned} &\text{minimize} && \|\mathbf{q}\|^2 \\ &\text{subject to} && \mathbf{p} = \mathbf{G}\mathbf{q}. \end{aligned}$$

A solution of the above problem can be obtained by using a Lagrange multiplier [Bra83] which yields the following cost function

$$J(\mathbf{q}, \mathbf{q}^*, \lambda) = \mathbf{q}^H\mathbf{q} + \lambda^H(\mathbf{G}\mathbf{q} - \mathbf{p}) + \lambda^T(\mathbf{G}^*\mathbf{q}^* - \mathbf{p}^*), \tag{2.5}$$

where J is the Lagrangian, λ a Lagrange multiplier and the last term in the right hand side, which is the complex conjugate of the constraint, is used to make the Lagrangian real valued. Setting the derivative of J with respect to $\mathbf{q}^*$ to zero and keeping $\mathbf{q}$ as a constant leads to

$$\mathbf{q} + \mathbf{G}^H\lambda = 0. \tag{2.6}$$

Premultiplying Equation (2.6) by $\mathbf{G}$ and using the constraint relation $\mathbf{p} = \mathbf{G}\mathbf{q}$ yields

$$\begin{aligned} \mathbf{G}\mathbf{q} + \mathbf{G}\mathbf{G}^H\lambda &= 0 \\ \mathbf{p} + \mathbf{G}\mathbf{G}^H\lambda &= 0 \\ \lambda &= -(\mathbf{G}\mathbf{G}^H)^{-1}\mathbf{p}. \end{aligned} \tag{2.7}$$

Substituting for the Lagrange multiplier λ into Equation (2.6) gives the *least norm solution*:

$$\hat{\mathbf{q}} = \mathbf{G}^H(\mathbf{G}\mathbf{G}^H)^{-1}\mathbf{p}, \tag{2.8}$$

from which we notice the appearance of the right pseudo-inverse of $\mathbf{G}$. Although this approach provides a unique solution for the underdetermined system, it is often a useless solution, specially because it is not stable with respect to errors in the measured data $\mathbf{p}$. This issue will be covered in the next section.

2.3 Ill-posedness of the problem

We start the discussion in this section by reconsidering the integral equation that models our problem, that is, Equation (2.2). Keeping the assumption that there is no sources inside the enclosure and limiting the equivalent sources to be located on a closed surface

(Γ_e), we can rewrite this equation as

$$p(\mathbf{r}) = \mathrm{j}\omega\rho \int_{\Gamma_e} G(\mathbf{r}|\mathbf{r}_e)q(\mathbf{r}_e)d\Gamma_e. \tag{2.9}$$

Since our aim is to reconstruct the source field $q(\mathbf{r}_e)$ based on the measurements in $p(\mathbf{r})$, this equation becomes an integral equation, particularly, a Fredholm equation of the first kind. This equation, which models a variety of problems in physics, is a classical example of ill-posed problems [Han98]. The term *ill-posed* goes back to Jacques Hadamard, who in the early 20th century defined that to be well-posed, a problem must satisfy the following three conditions:

1. The solution exists.
2. The solution is unique.
3. The solution depends continuously on the problem data.

If any of these conditions is not respected, the problem is said to be ill-posed. The first condition is related to the feasibility of the problem and is normally satisfied for the problems studied in this thesis. The second condition is rarely satisfied since the proposed model is highly under-determined. Finally, the last condition concerns the stability of the solution with regard to small variations on the measured data. The solutions based on the pseudo-inverse of $\mathbf{G}$ presented in the previous section, satisfy Hadamard's conditions 1 and 2, however the stability condition is not guaranteed. This means that small amount of noise in the measured pressure, for instance, might lead to large perturbations on the reconstructed source field. A remedy to ill-posed problems is often to reformulate them (normally by imposing additional requirements to the solution) such that the new problem is more stable to the perturbations. This is the central point of regularization techniques which will be discussed hereafter.

2.3.1 Tikhonov regularization

A classical technique to regularize ill-posed problems is the so-called Tikhonov regularization [AT76]. The idea is to include a term in the minimization that is the squared norm of the solution weighted by a regularization parameter η, the following minimization problem holds

$$\hat{\mathbf{q}}(\eta) = \mathrm{Argmin}\left\{\|\mathbf{p} - \mathbf{G}\mathbf{q}\|^2 + \eta^2\|\mathbf{q}\|^2\right\}, \tag{2.10}$$

where η^2 controls the weight between the residual and the solution norms. The key is to find a suitable regularization parameter η that produces a solution that is useful and fits the measurement data well enough. The solution of this minimization problem can also be obtained by setting the derivative with respect to $\mathbf{q}$ to zero. The following results holds

$$\hat{\mathbf{q}}(\eta) = \mathbf{G}^H(\mathbf{G}\mathbf{G}^H + \eta^2\mathbf{I})^{-1}\mathbf{p}, \tag{2.11}$$

where $\mathbf{I}$ is the identity matrix of dimension M.

A critical aspect, however, is how to automatically set the regularization parameter with few prior information on the underlying problem. Several approaches have been proposed in that context, such as the Morozov discrepancy principle [MNA84], the Generalized Cross-Validation (GCV) [GHW79], the L-curve method [HO93], and the Normalized Cumulative Periodgram (NCP) [HKK06, RO08], to cite only a few. Due to its crucial importance to the solution of the inverse problems in this thesis, the next chapter is dedicated to the issue of regularization of the inverse acoustic problem. We shall give a deeper insight into the selection of reasonable regularization parameters and an extensive comparison of different methods will be provided.

2.3.2 Singular Value Decomposition

The singular value decomposition is a powerful mathematical tool that allows us to gain more insight into the inverse problem. The singular value decomposition of the rectangular matrix $\mathbf{G}$ yields

$$\mathbf{G} = \mathbf{U}\lceil\mathbf{S}\rfloor\mathbf{V}^H, \tag{2.12}$$

where, for $M < N$, $\mathbf{U} \in \mathbb{C}^{M\times M}$ is a unitary matrix and $\mathbf{V} \in \mathbb{C}^{N\times M}$ such that $\mathbf{V}^H\mathbf{V} = \mathbf{I}_M$. The columns of $\mathbf{U}$ and $\mathbf{V}$ are respectively the left and right singular vectors. In turn, $\mathbf{S} \in \mathbb{R}^{M\times M}$ is a diagonal matrix with singular values stored in decreasing order $s_1 \geq s_2 \geq \dots s_M \geq 0$. If we insert the singular value decomposition of $\mathbf{G}$ into Equation (2.11) we obtain the result

$$\hat{\mathbf{q}}(\eta) = \mathbf{V}(\mathbf{S}^2 + \eta^2\mathbf{I})^{-1}\mathbf{S}\mathbf{U}^H\mathbf{p}. \tag{2.13}$$

From this particular solution we clearly notice the role of Tikhonov regularization as a filter of singular values. Indeed, the singular values that are on the order of magnitude of the regularization parameter will be amplified by η^2, while the singular values larger than η^2 remain nearly unaltered. The smallest singular values are more sensitive to noise in the data and their simple inversion often leads to a high amplification of errors.

2.4 Radiated acoustic pressure field

Once the reconstructed volume velocity of equivalent sources is obtained, their radiated acoustic pressure over the space can be computed. The Green's function between adjacent equivalent sources is used to obtain the acoustic pressure on the position of equivalent sources due to the neighbors sources. The acoustic pressure at the position of the e-th equivalent source is given by

$$p(\mathbf{r}_e) = \mathrm{j}\omega\rho \sum_{\substack{i=1 \\ i\neq e}}^{N} G(\mathbf{r}_e|\mathbf{r}_i)q(\mathbf{r}_i), \tag{2.14}$$

in which the requirement $i \neq e$ is simply to avoid the computation of the acoustic pressure due to the equivalent sources at their self-position and N is the number of equivalent sources. Figure 2.3 provides a geometric representation of the position vectors in Equation (2.14).

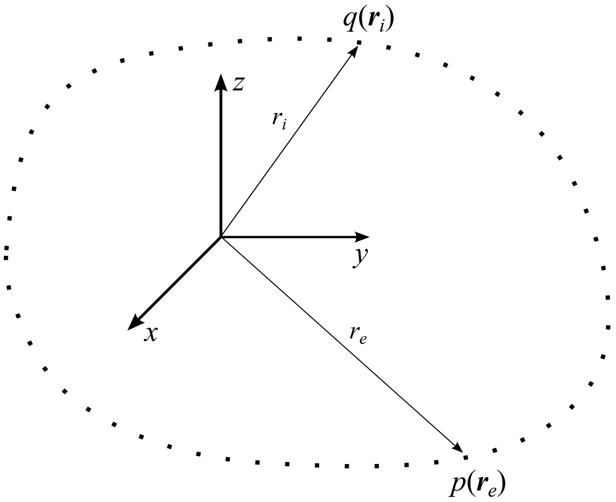

Figure 2.3: Geometry of the problem used for the computation of the radiated acoustic pressure by the reconstructed equivalent sources.

This information is useful to provide further insight into the properties of the reconstructed source field. It will be particularly handful to explain some limitations of the highly under-determined system of equations, as we shall see in Chapter 4. The radiated acoustic pressure by equivalent sources is also essential to the computation of the radiated acoustic power, as we shall see in the next section.

2.5 Radiated acoustic power

The acoustic power radiated by an elementary source is not only dependent on its strength (volume velocity), it also depends on the pressure field in which it is inserted. This means that, the presence of other correlated sources will modify the sound power radiated by the elemental source. Since the total radiated acoustic power is given by the integral of the normal active intensity over a surface Σ surrounding the source, we have

$$W_e = \int_{\Sigma} \vec{I}(\mathbf{r}_s) d\Sigma, \quad \text{with} \quad \vec{I}(\mathbf{r}_s) = \frac{1}{2}\Re\left\{p(\mathbf{r}_s)u^*(\mathbf{r}_s)\right\}, \tag{2.15}$$

where $\Re(a)$ is the real part of a and * the complex conjugate. The acoustic pressure and particle velocity on the surrounding surface are given by

$$p(\mathbf{r}_s) = p_i(\mathbf{r}_s) + p_o(\mathbf{r}_s) \tag{2.16a}$$

$$u(\mathbf{r}_s) = u_i(\mathbf{r}_s) + u_o(\mathbf{r}_s) \tag{2.16b}$$

where p_i and u_i are the acoustic pressure and particle velocity due to the monopole inside Σ and p_o and u_o are the acoustic quantities due to the sources outside the surface Σ. Thus, we can decompose total radiated acoustic power as follows

$$\begin{aligned} W_e = \frac{1}{2}\Re\Big\{ &\int_{\Sigma} p_i(\mathbf{r}_s)u_i^*(\mathbf{r}_s)d\Sigma + \int_{\Sigma} p_o(\mathbf{r}_s)u_o^*(\mathbf{r}_s)d\Sigma \\ &+ \int_{\Sigma} p_i(\mathbf{r}_s)u_o^*(\mathbf{r}_s)d\Sigma + \int_{\Sigma} p_o(\mathbf{r}_s)u_i^*(\mathbf{r}_s)d\Sigma \Big\}. \end{aligned} \tag{2.17}$$

Let us now define Σ as a spherical surface centered on the monopole and with a vanishingly small radius. Since all other sources are located outside the spherical surface, the net flux of u_o through Σ tends to zero, hence

$$\int_{\Sigma} u_o(\mathbf{r}_s) d\Sigma = 0. \tag{2.18}$$

Equation (2.17) then simplifies to

$$W_e = \frac{1}{2}\Re\left\{ \int_{\Sigma} p_i(\mathbf{r}_s)u_i^*(\mathbf{r}_s)d\Sigma + \int_{\Sigma} p_o(\mathbf{r}_s)u_i^*(\mathbf{r}_s)d\Sigma \right\}. \tag{2.19}$$

The acoustic pressure and particle velocity at the position $\mathbf{r}_s$ due to the monopole inside the surface Σ are given by

$$p_i(\mathbf{r}_s) = \mathrm{j}\rho c k q(\mathbf{r}_e)\frac{e^{-\mathrm{j}kr_s}}{4\pi r_s} \tag{2.20}$$

$$u_i(\mathbf{r}_s) = \mathrm{j}kq(\mathbf{r}_e)\frac{e^{-\mathrm{j}kr_s}}{4\pi r_s}\left(1-\frac{\mathrm{j}}{kr_s}\right)\vec{n}, \tag{2.21}$$

where $q(\mathbf{r}_e)$ is the identified volume velocity of the equivalent source at position $\mathbf{r}_e$, r_s is the length of the vector $\mathbf{r}_s$ and $\vec{n}$ is the normal to the surface Σ. These expressions can be further simplified when the radius r_s becomes small, and we have

$$p_i(\mathbf{r}_s) = \frac{\mathrm{j}\rho c k q(\mathbf{r}_e)}{4\pi r_s} \tag{2.22}$$

$$u_i(\mathbf{r}_s) = \frac{\mathrm{j}kq(\mathbf{r}_e)}{4\pi r_s}\left(1-\frac{\mathrm{j}}{kr_s}\right)\vec{n}. \tag{2.23}$$

Substituting Equations (2.22) and (2.23) into the right hand side of Equation (2.19) and remembering that $q(\mathbf{r}_e)q^*(\mathbf{r}_e) = |q(\mathbf{r}_e)|^2$ yields

$$W_e = \frac{1}{2}\Re\left\{\int_\Sigma \frac{\rho c k^2 |q(\mathbf{r}_e)|^2}{(4\pi r_s)^2}\left(1+\frac{\mathrm{j}}{kr_s}\right)\vec{n}d\Sigma + p_o\int_\Sigma \frac{-\mathrm{j}kq^*(\mathbf{r}_e)}{4\pi r_s}\left(1+\frac{\mathrm{j}}{kr_s}\right)\vec{n}d\Sigma\right\}. \tag{2.24}$$

Since the normal to the surface $\vec{n}$ is always on the same direction as the vector pointing from the center of the sphere to a position on its surface and the radius is constant over Σ, we have

$$W_e = \frac{1}{2}\left(\frac{\rho c k^2 |q(\mathbf{r}_e)|^2}{(4\pi r_s)^2}4\pi r_s^2 + \Re\left\{\frac{-\mathrm{j}kp_o q^*(\mathbf{r}_e)}{4\pi r_s}\left(1+\frac{\mathrm{j}}{kr_s}\right)4\pi r_s^2\right\}\right). \tag{2.25}$$

If we consider that $\mathrm{j}/kr_s \gg 1$ as r_s becomes vanishingly small we also have

$$W_e = \frac{1}{2}\left(\frac{\rho c k^2 |q(\mathbf{r}_e)|^2}{4\pi} + \Re\left\{\frac{p_o q^*(\mathbf{r}_e)}{4\pi r_s^2}4\pi r_s^2\right\}\right), \tag{2.26}$$

that finally simplifies to

$$W_e = \frac{\rho c k^2 |q(\mathbf{r}_e)|^2}{8\pi} + \frac{\Re\{p_o q^*(\mathbf{r}_e)\}}{2}, \tag{2.27}$$

with p_o the acoustic pressure at the position $\mathbf{r}_e$ due to the other correlated sources, as given by Equation (2.14). The first term on the right hand side of Equation (2.27) is the acoustic power produced by the monopole in isolation. The second term is the influence of other sources, which depends on the relative phase between p_o and $q(\mathbf{r}_e)$. This term is maximum when p_o and $q(\mathbf{r}_e)$ are in phase and minimum if they are out of phase.

Therefore, Equation (2.27) tells us that the acoustic power of an elementary source is not a strictly positive quantity. Indeed, if the volume velocity $q(\mathbf{r}_e)$ and the pressure generated by neighbor sources p_o are out of phase and the latter is sufficiently large, the total radiated acoustic power might be negative, which corresponds to a sink of energy.

2.6 Acoustics in spherical coordinates

Up to this point we did not entered into the details of the propagation operator G. As we have seen in Chapter 1, in order to accurately model the sound field in the interior of enclosures, numerical techniques such as BEM, FEM or the image source method (ISM) at some extent, are normally required. However, the effectiveness of these methods strongly depends on the frequency and on the knowledge of several other parameters, such as the impedance of surfaces and their precise geometry. On the other hand, the equivalent source method simplifies the problem by using a set of elementary sources (such as monopoles and dipoles) to model the original sources. Although the consideration of the interior surfaces of a vehicle as a combination of monopoles radiating into free-field is a strong assumption, it allows a significant simplification of the underlying problem.

An important factor that must be taken into account in the propagation model is the shape or type of the microphone array. According to the review in Chapter 1, several microphone arrays have been proposed for noise source identification issues. Spherical microphone arrays are advantageous due to their 3D symmetry and specially the rigid configuration, which enjoys certain advantages over the transparent sphere. However, a somewhat rigid surface will surely perturb the sound field around its body, due to the scattered sound waves. Thus, the consideration of the scattered waves is of importance to correctly model the sound field measured by a rigid spherical surface.

Since rigid spherical microphone arrays are adopted in the framework of this thesis, we provide in this section a careful analysis of the underlying theory. Our aim is to derive the analytical expressions of the wave propagation models used throughout this work. In the first part we review the solution of the wave equation in spherical coordinates, with emphasis on the solution to interior problems. In the second part, we establish the expressions which give the acoustic pressure on the surface of a sphere due to a monopole-like source and a plane wave. Finally, we present an analysis of the truncation errors closely related to the aforementioned expressions.

2.6.1 Solution of the Helmholtz equation

The solution of the wave equation is well detailed in many text books in the field of acoustics (see for example [Wil99, GD05]). We start by considering the time dependent wave equation for the sound pressure $p(\mathbf{r},t)$, which is written as:

$$\Delta p(\mathbf{r},t) - \frac{1}{c^2}\frac{\partial^2 p(\mathbf{r},t)}{\partial t^2} = 0, \tag{2.28}$$

where Δ is the Laplacian, $\mathbf{r}$ is a position vector in space, c is the speed of sound and $\partial^2/\partial t^2$ is the second derivative with respect to time. Assuming a harmonic time dependence of $e^{\mathrm{j}\omega t}$, the time dependent sound pressure can be written as:

$$p(\mathbf{r},t) = \frac{1}{2\pi}\int_{-\infty}^{\infty} p(\mathbf{r},\omega)e^{\mathrm{j}\omega t}d\omega, \tag{2.29}$$

where ω is the angular frequency.

Taking the Fourier transform of the wave equation and replacing the second derivative with respect to time of Equation (2.29) yields the Helmholtz equation

$$\Delta p(\mathbf{r},\omega) + k^2 p(\mathbf{r},\omega) = 0, \tag{2.30}$$

where $k = \omega/c$ is the wavenumber. For the sake of notational simplicity, we hereafter omit the ω sign on the frequency dependent sound pressure, that is $p(\mathbf{r},\omega) = p(\mathbf{r})$. Equation (2.30) is a partial differential equation that can be solved according to the definition of the Laplacian in the desired coordinate system. We are particularly interested on the spherical coordinate system and the wave equation then reads [Wil99, GD05]:

$$\frac{1}{r^2}\frac{\partial}{\partial r}\left(r^2\frac{\partial p(\mathbf{r})}{\partial r}\right) + \frac{1}{r^2\sin\theta}\frac{\partial}{\partial\theta}\left(\sin\theta\frac{\partial p(\mathbf{r})}{\partial\theta}\right) + \frac{1}{r^2\sin^2\theta}\frac{\partial^2 p(\mathbf{r})}{\partial\phi^2} + k^2 p(\mathbf{r}) = 0, \tag{2.31}$$

with the spherical coordinate system relative to the Cartesian coordinates shown in Figure 2.4. Separation of variables is the usual approach to solve this equation, and the acoustic pressure reads

$$p(\mathbf{r}) = R(kr)\Phi(\phi)\Theta(\theta) \tag{2.32}$$

This procedure leads to three known differential equations, namely: (a) a spherical Bessel differential equation for the radial dependency; (b) a linear differential equation for the angular part depending on ϕ; (c) an associated Legendre differential equation for the angular part depending on θ. In turn, their corresponding solutions are respectively given by [WA04]: (a) spherical Bessel and Neumann functions or spherical Hankel functions of first and second kind; (b) sinus and cosines or complex exponentials and (c) Legendre functions of first and second kind. The solutions of both angular parts are often conveniently combined into a single function, the spherical harmonic $Y_l^m(\theta,\phi)$.

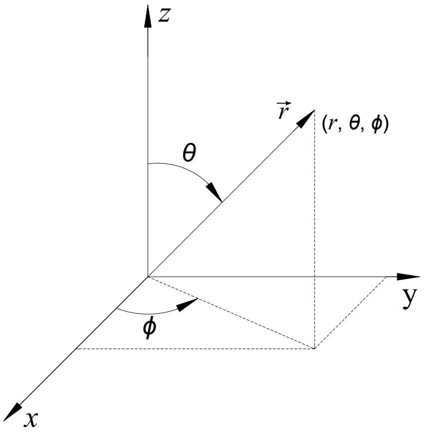

Figure 2.4: Cartesian and spherical coordinate systems employed throughout this thesis. The azimuth angle ϕ measured from the x-axis in the xy plane ranges from 0° to 360° and the elevation angle θ measured from the z-axis ranges from 0° to 180°.

The total solution of the Helmholtz equation in spherical coordinates is a combination of the aforementioned solutions. However, the selection of feasible solutions depends on the underlying problem (e.g. interior or exterior problems) as well as on the sign convention used for the harmonic dependence of the sound field. For instance, for interior problems (all souces outside a given boundary) the selected functions must be non-singular in a bounded domain $kr < kr_s$, r_s being the source boundary. In this case, the spherical Neumann functions are discarded since they exhibit a singularity at $kr = 0$ (see Figure B.1). Another constraint that must be respected is the Sommerfeld's radiation condition, which states that any finite extent source in free-field must provide a positive dissipation of energy into the far-field [GD05]. According to the analysis given in Appendix B and the selected time convention ($e^{j\omega t}$), the only appropriate function to describe a radiating field in this case is the spherical Hankel function of second kind $h_l^{(2)}$.

Finally, the general solution for both interior and exterior problems can be written as

$$p(\mathbf{r}) = \sum_{l=0}^{\infty} \sum_{m=-l}^{l} \left[b_{lm} j_l(kr) + c_{lm} h_l^{(2)}(kr) \right] Y_l^m(\theta, \phi), \tag{2.33}$$

where $\mathbf{r} = (r, \theta, \phi)$, b_{lm} and c_{lm} are coefficients depending on boundary conditions and the nature of sources, $j_l(kr)$ are the spherical Bessel functions, and $Y_l^m(\theta, \phi)$ are the spherical harmonics depending on the elevation θ and azimuth ϕ angles.

2.6.2 Solution for Interior Problems

The geometry of the problem studied throughout this thesis is depicted in Figure 2.5. It can be seen that all the sources to be reconstructed lie outside the boundary Γ_B. In addition, the underlying problem depends on the properties of the measurement boundary Γ_M. For instance, if the latter is transparent, we are dealing with a pure interior problem. On the other hand, if the measurement surface is assumed to be rigid, a scattered field will be produced, with waves propagating outwards the surface Γ_M. Thus, in this case, we have a "mixed" problem, since the rigid body may be viewed as an additional source.

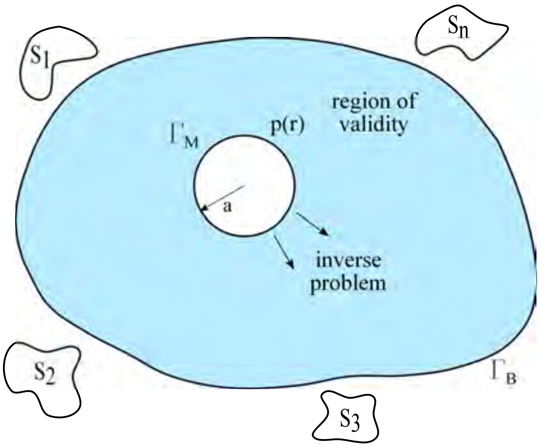

Figure 2.5: Geometry of the problem studied in this thesis. All the sources are located outside the region delimited by Γ_B. Depending on the properties of the measurement boundary Γ_M it is either an interior problem or a "mixed" problem. The reconstruction of the source field outwards the measurement surface is an inverse problem.

Let us first consider a purely incident sound field on the measurement surface. In this case, the acoustic pressure at any point on the sphere is completely given by the first set of solutions from Equation (2.33), which models an interior problem. It follows that

$$p_i(\mathbf{r}) = \sum_{l=0}^{\infty} \sum_{m=-l}^{l} b_{lm} j_l(kr) Y_l^m(\theta, \phi), \tag{2.34}$$

where the coefficients b_{lm} are obtained according to the source properties, as we shall see later.

In the case of a perfectly transparent sphere this expression describes the whole measured sound field. This is not the case, however, for a somewhat rigid sphere which "perturbs" the sound field by generating scattered waves. The latter are propagated outwards the rigid spherical surface and are thus described by outgoing spherical waves. The scattered acoustic pressure can thus be defined by traveling wave type solutions of the

Helmholtz equation as follows

$$p_s(\mathbf{r}) = \sum_{l=0}^{\infty} \sum_{m=-l}^{l} c_{lm} h_l^{(2)}(kr) Y_l^m(\theta, \phi). \tag{2.35}$$

The total acoustic pressure field is simply given by the sum of the incident and scattered sound fields:

$$p_t = p_i + p_s. \tag{2.36}$$

Assuming a perfectly rigid sphere of radius a, we have that the particle velocity must vanish on its surface, that is $r = a$. The following boundary condition holds:

$$u_n(r = a) = \left.\frac{\partial p_t}{\partial r}\right|_{r=a} = \left.\frac{\partial (p_i + p_s)}{\partial r}\right|_{r=a} = 0. \tag{2.37}$$

Inserting equations (2.34) and (2.35) into equation (2.37) allows us to obtain the following relationship between the coefficients b_{lm} and c_{lm}:

$$c_{lm} = -b_{lm} \frac{j_l'(ka)}{h_l'^{(2)}(ka)}, \tag{2.38}$$

where $j_l'(ka)$ stands for the first derivative of the spherical Bessel function and $h_l'^{(2)}(ka)$ for the first derivative of the spherical Hankel function of second kind. Inserting Equation (2.38) back into Equation (2.35) and evaluating the expression in equation (2.36) yields the total pressure field:

$$p_t(\mathbf{r}) = \sum_{l=0}^{\infty} \left(j_l(kr) - \frac{j_l'(ka)}{h_l'^{(2)}(ka)} h_l^{(2)}(kr) \right) \sum_{m=-l}^{l} b_{lm} Y_l^m(\theta, \phi). \tag{2.39}$$

This equation gives the total acoustic pressure (incident plus scattered) in any position in the space delimited by $r \geq a$. The coefficients b_{lm} depend on the assumed source properties and in the next sections they are obtained for a monopole-like source as well as for a plane wave.

2.6.3 Point source expansion

The key to obtain the coefficients b_{lm}, is to express incident waves (e.g. plane waves, spherical waves) in terms of a series expansion of spherical harmonics. Let us consider the case of a spherical wave generated by a point source, which in terms of Cartesian coordinates we have the following closed-form Green's function:

$$G(\mathbf{r}|\mathbf{r}_s) = \frac{e^{-\mathrm{j}k\|\mathbf{r}-\mathbf{r}_s\|}}{4\pi\|\mathbf{r}-\mathbf{r}_s\|}, \tag{2.40}$$

where $\mathbf{r}$ and $\mathbf{r}_s$ respectively corresponds to position vectors of the receiver and the source. An expansion of the above expression in spherical coordinates can be written as [WA04]

$$G(\mathbf{r}|\mathbf{r}_s) = -\mathrm{j}k\sum_{l=0}^{\infty}\begin{Bmatrix} j_l(kr)h_l^{(2)}(kr_s), & r_s > r \\ j_l(kr_s)h_l^{(2)}(kr), & r_s < r \end{Bmatrix}\sum_{m=-l}^{l} Y_l^m(\theta,\phi)Y_l^{m*}(\theta_s,\phi_s), \tag{2.41}$$

where we notice two cases depending on the position of the source relative to the observation point in the problem. Since in this work we are always concerned with source fields surrounding the measurement surface, we hereafter consider only the case $r_s > r$. Comparing the concerned expression to the solution of the Helmholtz equation for an incident wave (2.34) gives us the coefficients b_{lm} for an incident spherical wave:

$$b_{lm} = -\mathrm{j}kh_l^{(2)}(kr_s)Y_l^{m*}(\theta_s,\phi_s). \tag{2.42}$$

Inserting the coefficients above back into equation (2.39) yields the following expression for the total acoustic pressure field:

$$p_t(\mathbf{r}|\mathbf{r}_s) = -\mathrm{j}k\sum_{l=0}^{\infty}h_l^{(2)}(kr_s)\left(j_l(kr) - \frac{j_l'(ka)}{h_l'^{(2)}(ka)}h_l^{(2)}(kr)\right)\sum_{m=-l}^{l} Y_l^m(\theta,\phi)Y_l^{m*}(\theta_s,\phi_s), \tag{2.43}$$

where $\mathbf{r}_s = (r_s, \theta_s, \phi_s)$.

The above expression gives the total pressure field (incident plus scattered by a rigid sphere of radius $r = a$) at any position in the space delimited by $a \leq r \leq \Gamma_{\mathrm{B}}$. For the acoustic pressure directly on the surface of the sphere ($r = a$), equation (2.43) yields:

$$p_t(\mathbf{r}_a|\mathbf{r}_s) = -\mathrm{j}k\sum_{l=0}^{\infty}h_l^{(2)}(kr_s)\left(j_l(ka) - \frac{j_l'(ka)}{h_l'^{(2)}(ka)}h_l^{(2)}(ka)\right)\sum_{m=-l}^{l} Y_l^m(\theta,\phi)Y_l^{m*}(\theta_s,\phi_s), \tag{2.44}$$

where in this case $\mathbf{r}_a = (a, \theta, \phi)$. We may simplify this rather extensive expression by firstly putting the terms in parenthesis in a common denominator and recognizing that the numerator holds the Wronskian relation [WA04, Wil99]:

$$j_l(x)h_l'^{(2)}(x) - j_l'(x)h_l^{(2)}(x) = \frac{1}{\mathrm{j}x^2} \tag{2.45}$$

In addition, we may also use the addition theorem for spherical harmonics [WA04, GD05], that establishes:

$$P_l(cos\Theta) = \frac{4\pi}{2l+1}\sum_{m=-l}^{l} Y_l^m(\theta,\phi)Y_l^{m*}(\theta_s,\phi_s), \tag{2.46}$$

where P_l is the Legendre polynomial of order l and Θ is the angle between the directions defined by (θ,ϕ) and (θ_s,ϕ_s), respectively representing a vector pointing from the center of the sphere to a microphone on its surface and the direction of an incoming wave, as shown in Figure (2.6). Giving these two vectors $(\mathbf{r}_s,\ \mathbf{r}_m)$, they form an angle which is defined as

$$\Theta = \arctan\left(\frac{\|\mathbf{r}_s \times \mathbf{r}_m\|}{\mathbf{r}_s \cdot \mathbf{r}_m}\right). \tag{2.47}$$

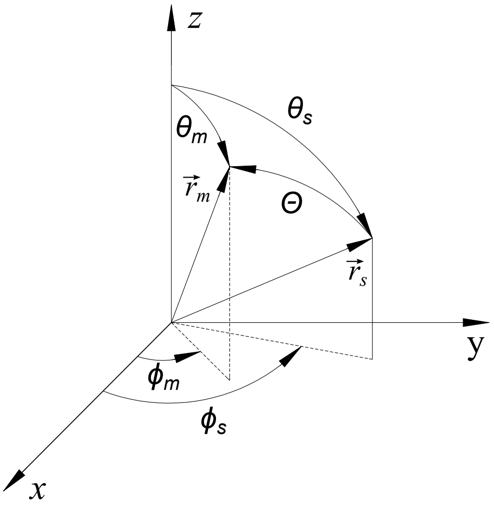

Figure 2.6: Angle Θ between the direction of an incoming wave $(\mathbf{r}_s)$ and the vector defining the position of a receiver $(\mathbf{r}_m)$.

Finally, by using the relations from equations (2.45) and (2.46), the expression yielding the total acoustic pressure on the surface of a rigid sphere simplifies to:

$$p_t(\mathbf{r}_a|\mathbf{r}_s) = -\frac{1}{4\pi k a^2}\sum_{l=0}^{\infty}\frac{h_l^{(2)}(kr_s)}{h_l'^{(2)}(ka)}(2l+1)P_l(cos\Theta) \tag{2.48}$$

Inserting the source term corresponding to a point source, that is $\mathrm{j}\omega\rho Q = \mathrm{j}ck\rho Q$, we finally have:

$$p_t(\mathbf{r}_a|\mathbf{r}_s) = -\frac{\mathrm{j}\rho c Q}{4\pi a^2}\sum_{l=0}^{\infty}\frac{h_l^{(2)}(kr_s)}{h_l'^{(2)}(ka)}(2l+1)P_l(cos\Theta) \tag{2.49}$$

The numerical evaluation of the spherical radial functions entering in equation (2.49) is facilitated by the following relationships

$$h_l^{(2)}(x) \equiv j_l(x) - \mathrm{j}y_l(x) = \sqrt{\frac{\pi}{2x}}\left[J_{l+1/2}(x) - \mathrm{j}Y_{l+1/2}(x)\right], \tag{2.50}$$

where $J_l(x)$ and $Y_l(x)$ are respectively the Bessel and Neumann functions, which are both implemented in MATLAB®. The derivative of the spherical Hankel function $h_l'^{(2)}(x)$ may be computed by using the important recurrence relation [WA04]:

$$f_l'(x) = f_{l-1}(x) - \frac{n+1}{x} f_l(x), \tag{2.51}$$

where f_l may be replaced by any of the spherical functions j_l, y_l, $h_l^{(1)}$ or $h_l^{(2)}$.

2.6.4 Plane wave expansion

We can derive similar expression for the case of an incident plane wave coming from the direction θ_s, ϕ_s. In order to compute the spherical wave expansion of the incident plane wave, we can take the limit of equations (2.40) and (2.41) as $r_s \to \infty$. Considering firstly the limit of the Green's function in equation (2.40), for the denominator we simply have $\|\mathbf{r} - \mathbf{r}_s\| \approx r_s$ [WA04], while for the numerator we need to be more precise because of the complex exponential, which leads to:

$$\|\mathbf{r} - \mathbf{r}_s\| \approx r_s - \mathbf{r}_{s_n} \cdot \mathbf{r}, \ \text{as} r_s \to \infty, \tag{2.52}$$

where $\mathbf{r}_{s_n}$ is a unit vector pointing in the direction of $\mathbf{r}_s$. To obtain the limit of equation (2.41) as $r_s \to \infty$, we may use the far field approximation of the spherical Hankel function of second kind [WA04]:

$$h_l^{(2)}(kr_s) \approx \mathrm{j}^{l+1} \frac{e^{-\mathrm{j}kr_s}}{kr_s} \tag{2.53}$$

Inserting these limits back into equations (2.40) and (2.41) yields

$$\frac{e^{-\mathrm{j}kr_s}}{4\pi r_s} e^{\mathrm{j}k\mathbf{r}_{s_n}\cdot\mathbf{r}} = -\mathrm{j}k \sum_{l=0}^{\infty} j_l(kr)\mathrm{j}^{l+1} \frac{e^{-\mathrm{j}kr_s}}{kr_s} \sum_{m=-l}^{l} Y_l^m(\theta,\phi) Y_l^{m*}(\theta_s,\phi_s). \tag{2.54}$$

Simplifying both sides yields the spherical expansion of a plane wave:

$$e^{\mathrm{j}k\mathbf{r}_{s_n}\cdot\mathbf{r}} = 4\pi \sum_{l=0}^{\infty} \mathrm{j}^l j_l(kr) \sum_{m=-l}^{l} Y_l^m(\theta,\phi) Y_l^{m*}(\theta_s,\phi_s). \tag{2.55}$$

Therefore we directly obtain the b_{lm} coefficients for an incident plane wave by comparing equation (2.55) to the expression which describes an incident field solution to the Helmholtz equation (2.34), yielding

$$b_{lm} = 4\pi \mathrm{j}^l Y_l^{m*}(\theta_s, \phi_s). \tag{2.56}$$

Inserting these coefficients into equation (2.39) which describes the total pressure field (incident plus scattered) on the surface of a rigid sphere and using the same simplifications as for the spherical wave case, yields the acoustic pressure on the surface of a rigid sphere due to a plane wave

$$p_t(\mathbf{r}_a|(\theta_s, \phi_s)) = \frac{-\mathrm{j}}{k^2 a^2} \sum_{l=0}^{\infty} \frac{\mathrm{j}^l}{h_l'^{(2)}(ka)} (2l+1) P_l(cos\Theta) \tag{2.57}$$

As we have seen, all the expressions describing the acoustic pressure field on the surface of a rigid sphere depend on a summation over an infinite number of orders l. However, in practice the summation must be truncated up to a finite order L. In the next section we investigate the errors due to the truncation and provide some guidelines for the selection of a reasonable truncation order.

2.6.5 Study of the truncation error

The computation of the total pressure field on the surface of a rigid sphere, either due to a point source (equation (2.49)) or to a plane wave (equation (2.57)), requires the evaluation of a sum over an infinite number of orders l. In practice, the sum must be approximated by a truncated version up to a given order L. The aim of this section is to provide some guidelines on how to choose a suitable order L which gives a good balance between approximation errors and computational cost. As a reference, we firstly compute the approximation errors for the case of an open sphere since in this case we have a closed-form expression (2.40) of the free-field Green's function. In the studied case (i.e. sources outside the evaluated domain), the expansion of equation (2.40) in the spherical harmonics domain is given by equation (2.41) for $r_s > r$. In order to estimate the approximation errors, we consider a sphere of radius $a = 0.145$ m with 31 microphones and 200 sources at varying distances from the center of the array. The source's azimuth and elevation angles are respectively drawn from $\mathcal{U}(0, 2\pi)$ and $\mathcal{U}(0, \pi)$, where $\mathcal{U}$ stands for the uniform distribution. The average magnitude errors are evaluated as

$$\varepsilon_{mag} = \frac{\sqrt{\sum_{i=1}^{M} \sum_{j=1}^{N} \left| G(\mathbf{r}_i|\mathbf{r}_j) - \hat{G}(\mathbf{r}_i|\mathbf{r}_j, L) \right|^2}}{\sqrt{\sum_{i=1}^{M} \sum_{j=1}^{N} \left| G(\mathbf{r}_i|\mathbf{r}_j) \right|^2}}, \tag{2.58}$$

where M is the number of microphones, N is the number of simulated sources and L the order used in the expansion. In turn, $G(\mathbf{r}_i|\mathbf{r}_j)$ is the exact expression of Green's function given in (2.40) and $\hat{G}(\mathbf{r}_i|\mathbf{r}_j, L)$ its approximation up to order L. The average phase error is defined as:

$$\varepsilon_{phase} = \left(\frac{1}{MN} \sum_{i=1}^{M} \sum_{j=1}^{N} (\angle G(\mathbf{r}_i|\mathbf{r}_j) - \angle \hat{G}(\mathbf{r}_i|\mathbf{r}_j, L))^2 \right)^{1/2}. \tag{2.59}$$

We evaluate the errors for orders L ranging from 0 up to 40 and for a wide frequency range. Figure 2.7 shows the magnitude errors in dB as a function of frequency and order L for different distances from the center of the array. We defined ρ in the figure as the adimensional distance ($\rho = r_s/a$). We only show the results for distances up to 1.5m since results for higher distances were essentially the same. Firstly, we notice a somewhat linear behavior of errors with frequency as ρ increases. In addition, we notice that above a given order depending on the frequency, the errors stop to decrease and reach the level of machine precision ($\approx 10^{-16}$). We remark that distances smaller than 0.3 m were not consider in the analysis since in practice the array is normally not placed that close to a surface. Similar results were obtained for the averaged phase error (see Figure 2.8). Comparing to the previous results, we notice that the phase errors tend to zero faster than the magnitude errors, indicating that a criterion to bound the order L for magnitude errors may suffice for the phase.

Given this reference, we now proceed to the analysis for the rigid sphere. Unfortunately, we have no closed-form solution for the total pressure on the rigid sphere since the scattering effects can only be evaluated in the spherical harmonics domain. Therefore, to use as a “true” reference we evaluate the expression in equation (2.48) up to an order $L = 50$ (note that this choice was based on the results for the open sphere). Indeed, we see in Figure 2.9 that the results are very similar to the open sphere case and the same observations follows.

The definition of a normalized frequency as in reference [DM98], may help us to provide some guidelines for a good choice of the order L

$$\mu = f\frac{2\pi a}{c} = \frac{2\pi a}{\lambda} = ka, \tag{2.60}$$

where $2\pi a/c$ is the time that it takes for a wave to travel once around the sphere. Notice that when $\mu = 1$ the wavelength equals the circumference of the sphere. As a rule of thumb, to achieve approximation errors in the order of 10^{-9} we may choose L as

$$L > 1.2ka + 8\frac{(\rho + 1)}{\rho}, \quad \rho > 1, \tag{2.61}$$

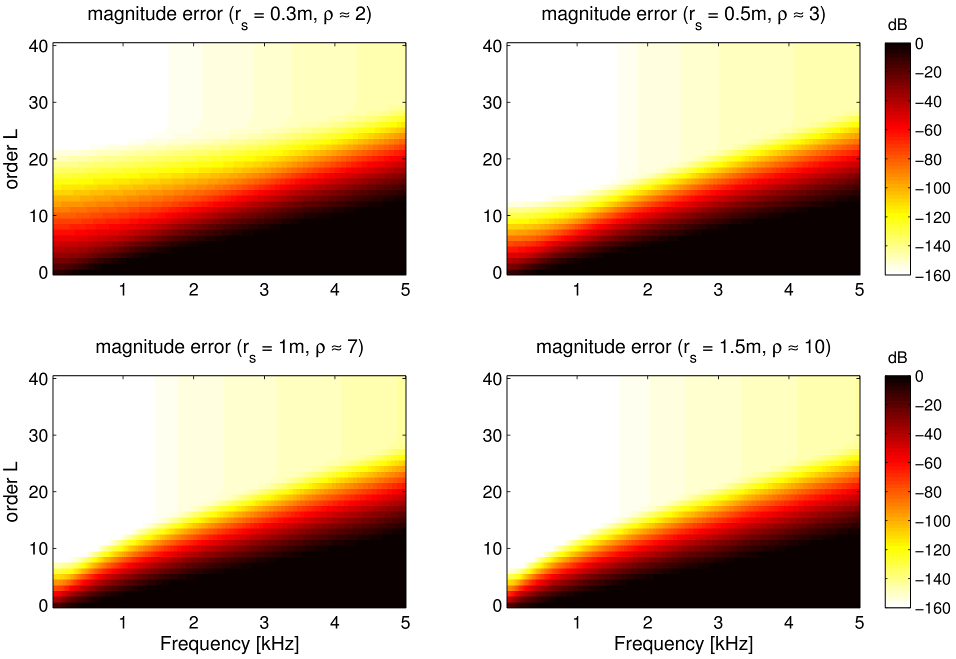

Figure 2.7: Averaged magnitude error as given in equation (2.58) for the open sphere configuration. The results are given for different distances (r_s) from the center of the array and a frequency range between 10 Hz to 5 kHz. Results for longer distances $r_s > 1.5\ m$ are not shown since they are essentially identical.

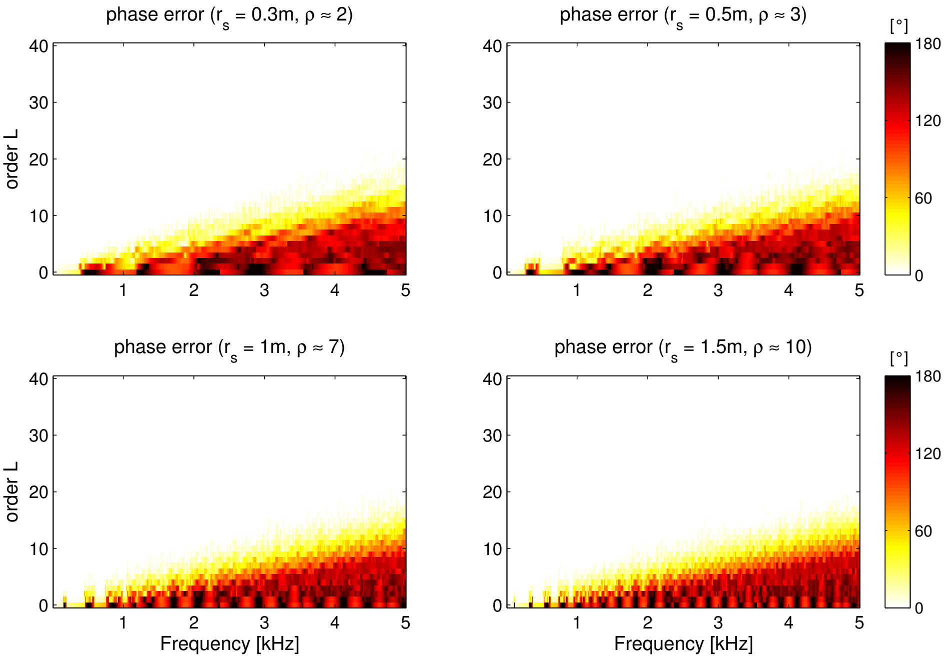

Figure 2.8: Averaged phase error in degrees [°] as given in equation (2.59) for the open sphere configuration. The results are given for different distances (r_s) from the center of the array.

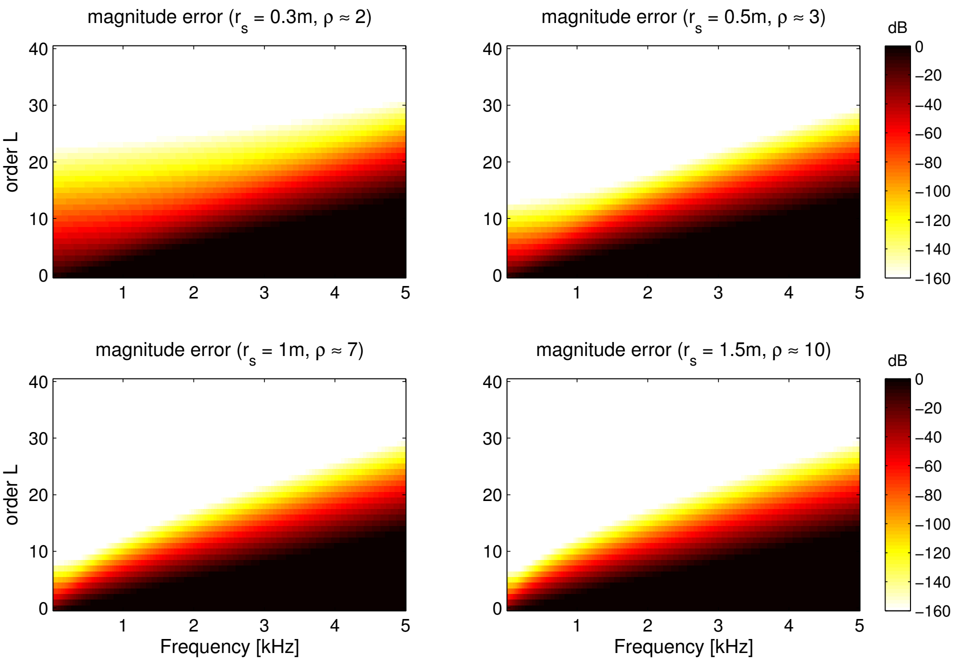

Figure 2.9: Averaged magnitude error as given in equation (2.58) for the rigid sphere configuration. The results are given for different distances (r_s) from the center of the array. Results for longer distances $r_s > 1.5\ m$ are not shown since they are essentially identical.

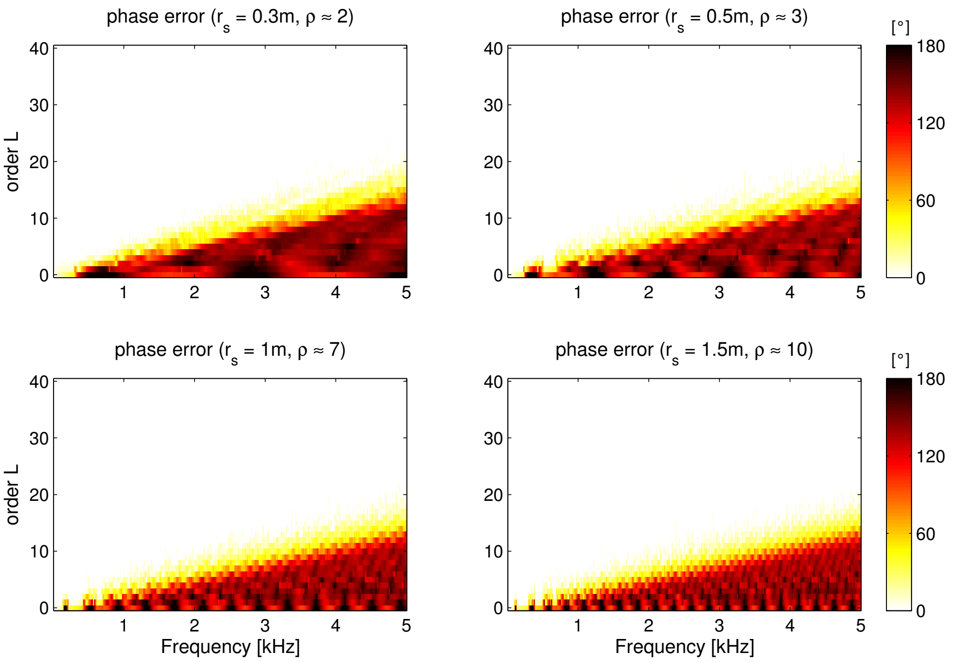

Figure 2.10: Averaged phase error in degrees [°] as given in equation (2.59) for the rigid sphere configuration. The results are given for different distances (r_s) from the center of the array.

with $\rho = r_s/a$ the adimensional distance from the center of the array. This choice is illustrated in Figure 2.11. It can be seen that this criterion allows one to keep the approximation errors small and avoids the computation of unnecessary orders specially at low frequencies, which leads to a saving in computational time.

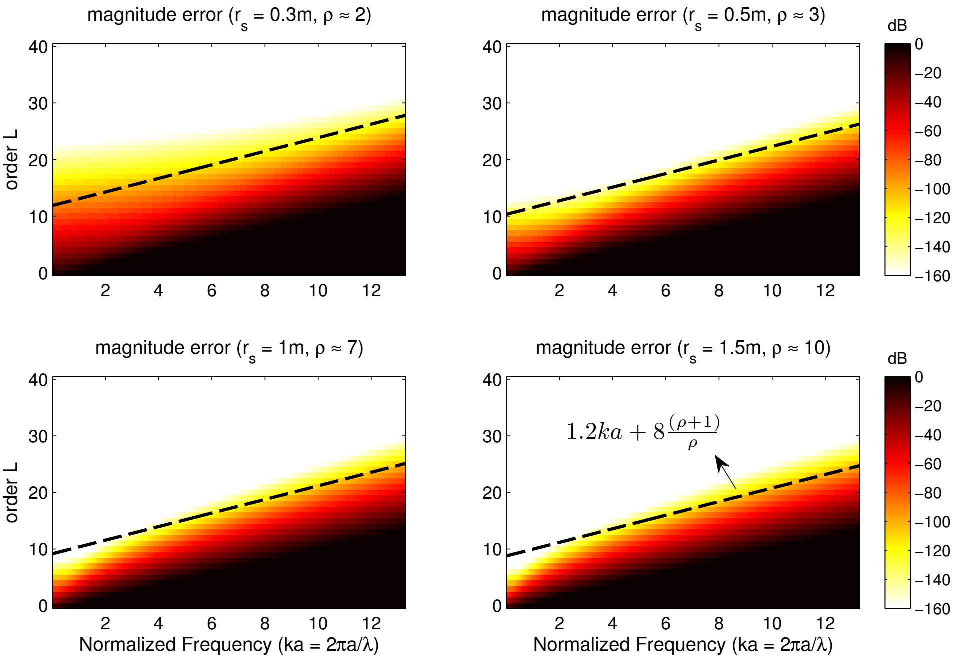

Figure 2.11: Averaged magnitude error as a function of normalized frequency (ka) for the rigid sphere configuration. The results are given for different distances (r_s) from the center of the array. The figure also shows the regression line from equation (2.61) used to bound the number of orders to be evaluated.

2.7 Causality analysis of identified sources

As we have noticed, the proposed method is based on a rather strong assumption of a free-field propagation of acoustic waves inside the enclosure. In practice, this is usually not the case in the interior of vehicles such as buses, due to the presence of acoustic reflecting materials. Therefore, depending on the strength of the reflected waves, they will have a significant contribution to the measured acoustic pressure. As a consequence, in addition to the original sources, their first order reflections may be reconstructed, what can be misleading if one essentially wishes to identify the original sources of noise. On the other hand, the knowledge of the regions where the reflection takes place may be advantageous in some situations. We can imagine, for instance a situation in which no design modifications can be performed around the original noise source, one alternative would be to eliminate its reflections by adding absorbing material on those regions where reflections take place.

In order to obtain further insight into the reconstructed source field, a technique based on a causality analysis of the identified sources is proposed. Let us first consider the simplified model represented in Figure 2.12. It basically models a sound source positioned at $\mathbf{r}_1$ and radiating inside an enclosure. Assuming that one boundary is a sound reflective surface, a first order reflection will take place at position $\mathbf{r}_2$. Thus, the microphone array will perceive the two incoming waves and since they are originated from the same source they are mutually correlated. In this case, the reconstructed source field will indicate the presence of two sources, one corresponding to the reflected wave and another to the original sound source. Assuming that the user has few *a priori* information on the position of real sources before making the experiment, it is not evident to decide whether the identified sources are actually two different sources or they share a source-reflection relationship.

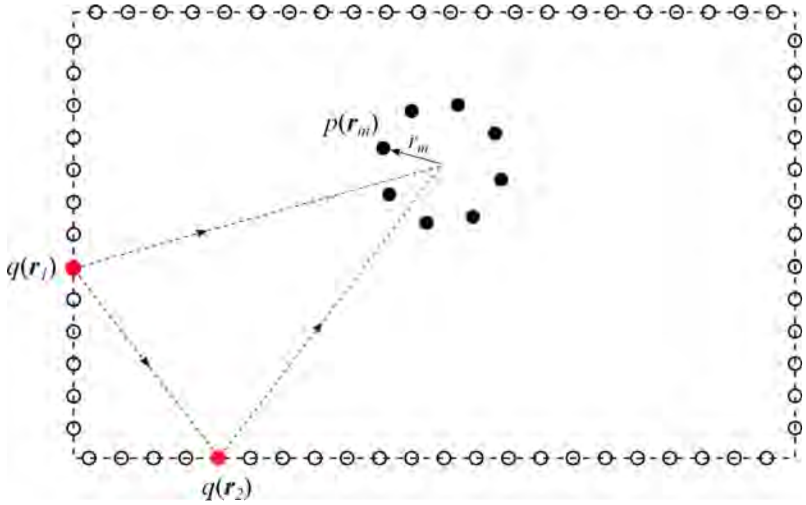

Figure 2.12: Simplified model of the underlying problem. The enclosure is modeled by a set of equivalent sources and the sound field is measured by an array of microphones. The figure shows a sound source located at the position $\mathbf{r}_1$ along with its first reflection which takes place at position $\mathbf{r}_2$.

The basic idea of the proposed approach is to analyze the causality relations between the reconstructed sources in order to identify those corresponding to reflected waves. Based on Cauchy's Integral Theorem, a linear system is causal if the real and imaginary parts of its corresponding frequency response function (FRF) are the Hilbert transform pair [BK98]. Assuming that $R(\omega)$ and $J(\omega)$ are respectively the real and imaginary parts of a frequency response function $H(\omega)$, they should satisfy the following Hilbert transform pair [BK98]:

$$R(\omega_0) = -\frac{1}{\pi}\int_{-\infty}^{\infty}\frac{J(\omega)}{\omega-\omega_0}d\omega \quad \text{and} \quad J(\omega_0) = \frac{1}{\pi}\int_{-\infty}^{\infty}\frac{R(\omega)}{\omega-\omega_0}d\omega, \tag{2.62}$$

Thus, the causality relation between a pair of identified sources can be checked by the Hilbert transform pair of the real and imaginary parts of their corresponding transfer functions, which is given by:

$$H_{12}(\omega) = \frac{q(\mathbf{r}_2,\omega)}{q(\mathbf{r}_1,\omega)} \quad \text{and} \quad H_{21}(\omega) = \frac{q(\mathbf{r}_1,\omega)}{q(\mathbf{r}_2,\omega)}, \tag{2.63}$$

If $H_{12}(\omega)$ satisfies equation (2.62), then $q(\mathbf{r}_1)$ must have caused $q(\mathbf{r}_2)$, conversely, if $H_{21}(\omega)$ satisfies equation (2.62) then $q(\mathbf{r}_2)$ must have caused $q(\mathbf{r}_1)$. In this particular case, it is clear that $q(\mathbf{r}_2)$ is a reflection of $q(\mathbf{r}_1)$ and thus $H_{12}(\omega)$ should satisfy the Hilbert transform pair. This approach may be used as a post-processing tool for the source reconstruction method, thus providing a better comprehension of identified sources. An application is demonstrated in Chapter 5 by means of a numerical simulation as well as an experimental validation.

3

Regularization of the inverse problem

As we have seen in Chapter 2, the achievement of useful source reconstruction results critically depends on the regularization of the problem. More precisely, it depends on the actual setting of a reasonable regularization parameter. Due to its relevance and importance to the proposed method, this chapter is dedicated to the matter of regularization of the inverse problem.

We start by introducing few preliminary aspects of regularization, with emphasis on the inherent instability of ill-posed problems with respect to measurement errors. A brief review of the most widely used regularization techniques is then provided. Next, we address the acoustic inverse problem within the Bayesian framework, which inherently yields to regularization mechanisms and particularly offers natural justification for the use of the well-known Tikhonov regularization.

In the second part of this Chapter we provide further insight into the issue of selecting the necessary amount of regularization, which is yet a critical aspect of most regularization techniques. In this context, we show how to pursue within the Bayesian formulation in order to adjust the regularization parameter. Furthermore, we also discuss the intuitive L-curve method, for which an extension of its criterion is proposed.

Finally, an important contribution of this work, the last part is devoted to an extensive comparison of parameter choice methods by means of numerical and experimental validations. The guidelines that shall be provided here serve not only for the purpose of this thesis but also for anyone who faces inverse problems in acoustics.

3.1 Preliminary aspects of regularization

In Section 2.3.1 we briefly introduced the concept of "regularization" of a discrete ill-posed problem. Basically, the idea behind regularization is to "modify" the original problem by imposing requirements to the solution, such that the new problem is more stable (less sensitive to measurement errors) and approximates the exact solution.

The immediate question that follows from the above definition is the practical meaning of the word "stable". To answer this question we propose to investigate the inherent instability of ill-posed problems by means of the so-called *discrete Picard Condition*. The latter follows from the *Picard Condition* for the continuous inverse problem and from the relationship between the SVD and the singular value expansion (SVE). A complete analysis of the mathematical background which leads to this condition is outside the scope of this thesis and the reader is referred to references [Han90, Han98, Han10] for a thorough description.

3.1.1 The discrete Picard condition

We start by rewriting the expression for the reconstructed source field in equation (2.8) in terms of the singular value decomposition (SVD) of the rectangular matrix $\mathbf{G}$. We thus have:

$$\hat{\mathbf{q}} = \mathbf{V}\lceil\mathbf{S}\rfloor^{-1}\mathbf{U}^H\mathbf{p} = \sum_{i=1}^{M}\frac{\mathbf{u}_i^H\mathbf{p}}{s_i}\mathbf{v}_i, \tag{3.1}$$

where s_i is the i-th singular value on the diagonal of matrix $\mathbf{S}$. We recall that this is the "naive" solution of the problem, that for underdetermined systems corresponds to the *least norm solution*. From the rightmost expression in equation (3.1) we emphasize the ratio between the coefficients $|\mathbf{u}_i^H\mathbf{p}|$ and the singular values s_i, which gives us an indication of how the measured data is coupled to the inverse model.

This discussion brings us to the following criterion for the satisfaction of the discrete Picard condition (DPC). The DPC is satisfied if for all numerically non-zero singular values s_i, the coefficients $|\mathbf{u}_i^H\mathbf{p}|$, on the average, decay to zero faster than s_i [Han90]. This is to avoid that the smaller singular values s_i over amplify the coefficients $|\mathbf{u}_i^H\mathbf{p}|$, yielding a useless solution for any practical purposes. We emphasize at this point that the decay do not need to be monotonic, as long as, on the average the coefficients $|\mathbf{u}_i^H\mathbf{p}|$ decay faster than s_i.

The checking for this condition can be done by visual inspection of a plot, as the example shown in Figure 3.1. However, for an acoustic problem which is generally solved for each frequency line, this approach is not feasible. In reference [Han90] Hansen proposed the *moving geometric mean* to numerically check for the satisfaction of the Picard condition:

$$\mu_i = s_i^{-1}\left(\prod_{j=i-k}^{i+k}\left|\mathbf{u}_j^H\mathbf{p}\right|\right)^{1/(2k+1)}, \quad i = k+1,\dots,M-k \tag{3.2}$$

where k is the size of the averaging window and M is the number of numerically non-zero singular values s_i. Typical values of k are 1, 2 or 3 and the Picard condition is satisfied up to the i-th term for which the coefficients μ_i decay monotonically to zero. In acoustics, the Picard condition was used by Gauthier *et al* [GCP+11] to compare different microphone array configurations for sound field reproduction.

An example of the Picard plot extracted from numerical simulations is shown in Figure 3.1, for: (a) an exact right hand side (i.e. no noise in the simulated acoustic pressure) and (b) acoustic pressure perturbed with additive complex Gaussian noise. As we can see, for the noise-free case the coefficients $|\mathbf{u}_i^H \mathbf{p}|$ and the singular values exhibit a similar decay and the DPC seems to be satisfied. On the other hand, when noise is added to the acoustic pressure, the coefficients $|\mathbf{u}_i^H \mathbf{p}|$ settle at some level depending on the amount of noise in $\mathbf{p}$. If, for the latter case, the "naive" solution in equation (3.1) is computed, it will be essentially dominated by those terms from which the DPC is not satisfied. For this particular case, it corresponds to $i > 19$ for a signal-to-noise ratio of 50 dB and $i > 5$ for a SNR of 20 dB.

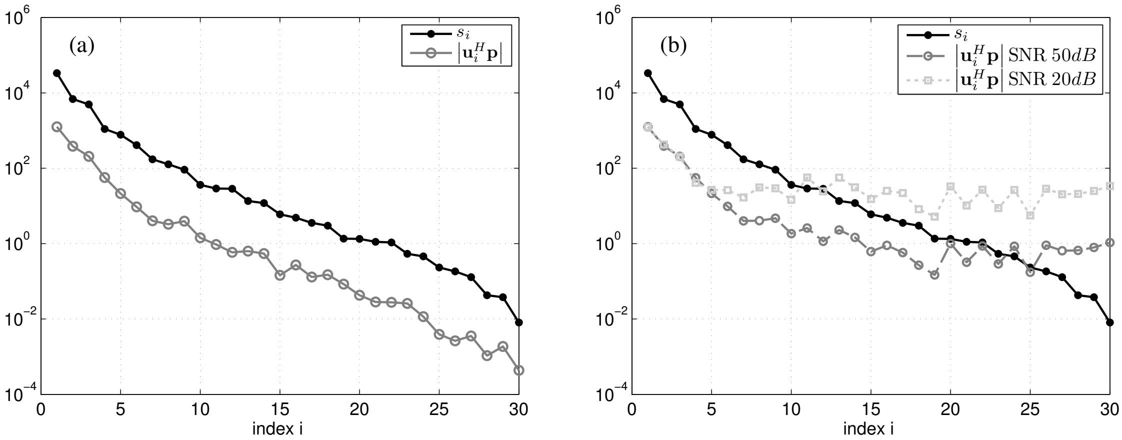

Figure 3.1: Singular values s_i and coefficients $|\mathbf{u}_i^H \mathbf{p}|$ for: (a) noise-free simulated acoustic pressure; (b) acoustic pressure perturbed with additive complex Gaussian noise of different signal-to-noise ratio (SNR).

The violation of the discrete Picard condition is a simple explanation for the instability of an ill-posed inverse problem with respect to measurement errors. Finally, the above discussion gives us a hint on how to handle this situation, particularly we want to filter those coefficients that violate the discrete Picard condition and over amplify the measurement noise. This is precisely the aim of the regularization techniques which will be discussed in the next section.

3.2 Regularization techniques

From the previous discussion it became clear that the noisy coefficients $|\mathbf{u}_i^H\mathbf{p}|$ associated to the smaller singular values are responsible for useless reconstructed source fields using the "naive" solution in Equation (3.1). An approach that immediatelly follows is to avoid those noisy coefficients by truncating the summation in equation (3.1) up to k components:

$$\hat{\mathbf{q}}_k = \sum_{i=1}^{k} \frac{\mathbf{u}_i^H\mathbf{p}}{s_i}\mathbf{v}_i, \tag{3.3}$$

where k must be chosen in order to keep only the significant components, thus avoiding the amplification of errors due to the inversion of the smaller singular values. This method is often called truncated SVD (TSVD) or *spectral cut-off*. The choice of a reasonable truncation parameter k may be done by inspection of the Picard plot or more commonly by parameter selection methods which will be investigated in the next section.

As previously introduced in Section 2.3.1, another regularization approach is the well-known Tikhonov regularization, which is certainly the prevailing approach in acoustics and vibration problems [NY00, YN00, Wil01, TT03, MT04, Lec09]. Similarly to the TSVD, Tikhonov regularization corresponds to a filtered version of the inverse operator. As we shall see later on in this chapter, Tikhonov regularization may also be naturally derived from a Bayesian perspective. The Tikhonov solution for the reconstructed source field may be written in terms of a explicit relation between singular values and the regularization parameter, as follows

$$\hat{\mathbf{q}}_\eta = \sum_{i=1}^{M} \frac{s_i^2}{s_i^2+\eta^2}\frac{\mathbf{u}_i^H\mathbf{p}}{s_i}\mathbf{v}_i, \tag{3.4}$$

where the terms $s_i^2/(s_i^2+\eta^2)$ are often referred to as *filter factors*, which are approximately 1 for $s_i \gg \eta$ and approach s_i^2/η^2 for $s_i \ll \eta$. From this analysis we observe that Tikhonov regularization imposes a smoother filtering of singular values in comparison to the cut-off filter of TSVD. However, a critical aspect of the above techniques is how to automatically determine a reasonable amount of "filtering", especially when no a priori information about the noise in the data is available. For TSVD it translates into the setting of the truncation parameter k and for Tikhonov regularization into the parameter η.

Recent publications in acoustics propose different regularization techniques, such as iterative methods (beneficial when dealing with large-scale problems) [VWHH12], Tikhonov regularization in its general form (i.e. by the use of discrete smoothing norms) [GCP+11], and regularization techniques by enforcing an a priori of sparsity [CDP+12, CMDP13], to cite only a few. Most of them still depend on either a regularization parameter that must be optimally tuned or on a stopping rule for the iterative methods.

The issue of selecting a good amount of regularization is still the subject of current research. Several strategies have been developed in this perspective, however, at the present time, there is still no absolutely universal method that is robust and always produces good results. Amongst the parameter choice methods traditionally used in the field of acoustics and vibration, we may cite the Generalized Cross Validation (GCV) [GHW79], the L-curve [HO93], the Normalized Cumulative Periodogram (NCP) [HKK06, RO08] and the Morozov discrepancy principle [MNA84]. The latter depends on a good estimate of the measurement noise level, that may not be available in practice. NCP is a relatively recent method whose idea is to track the aspect of the residual error as the regularization parameter changes and select the parameter for which the residual can be considered as close as possible to white noise. The L-curve, due to its intuitive character and ease of implementation, is probably one of the most widely used parameter choice method in acoustics [SHRH03, ZJBC09, LMG09].

Several papers in the literature provide comparisons of different parameter choice methods, either applied in acoustics [Wil01, KN04, GH08, Lec09, SHRH03, MT04] or in vibrations [CTT07]. In a more general context (i.e. outside the field of acoustics), reference [BL11] provides an extensive comparison of several parameter choice methods by means of a large simulation study. A general conclusion is that the behavior of each method is very problem-dependent and no consensus on which one is the best has been reached.

By introducing a Bayesian formulation of the acoustic inverse problem, the work carried by J. Antoni [Ant12] has afforded new perspectives into the automated selection of the regularization parameter.

Among the aforementioned parameter selection methods, we discuss in more detail the L-curve, for which we propose an extension to its criterion, as well as the criteria derived from a Bayesian approach. In the last part of this Chapter we present an extensive comparison of methods by means of numerical simulations and an experimental validation.

3.3 Regularization within the Bayesian framework

Before we discuss the issue of regularization into detail, we shall provide a brief introduction to the Bayesian formulation (which affords a statistical interpretation to the inverse problem) as well as point out its main differences from traditional deterministic approaches.

The first very practical difference between deterministic and statistical approaches is that, in the latter, one admits lack of information by modeling the problem unknowns as random variables and the nature of uncertainty is coded into probability density functions

[Rob01, CS08]. In addition, the Bayesian framework offers a natural way of taking into account pieces of qualitative information which are available prior to measurements. The application of the statistical point of view to inverse problems leads us to distinguish two major parts, the “likelihood” model and the “prior” model. The essence of both models and their direct interpretation into source reconstruction problems are:

- likelihood model: expresses the probability distribution of the measured data (acoustic pressure in this case) in terms of the problem unknowns, i.e. source coefficients. It is completely established by the knowledge of the direct model and the noise probability distribution.

- prior model: this part is responsible to incorporate any prior information on the problem unknowns (source parameters) into the *a priori* probability density function.

Bayes’ rule tells us how to assemble these two pieces of information in order to obtain the “posterior” probability density function (pdf), that is the “inverse probability” of the source field given the measurement data. Indeed, in the Bayesian framework, the “posterior” pdf is the solution of the inverse problem. Another difference from deterministic approaches follows from this discussion: the concept of “solution” is not reduced to a single value but to a probability distribution of possible values from which we can draw different estimates, the *maximum a posteriori* (MAP) estimator being a common choice. In the next sections, we shall see how particular choices for the likelihood and prior models naturally gives rise to the classical Tikhonov regularization and how we can pursue within the Bayesian formalism to intrinsically adjust the necessary amount of regularization.

Let us first rewrite the underlying problem given in equation (2.9) by explicitly expanding the unknown source field onto a known spatial basis $\phi_k(\mathbf{r})$:

$$q(\mathbf{r}) \approx \sum_{k=1}^{K} c_k \phi_k(\mathbf{r}), \quad K \geq M, \tag{3.5}$$

where c_k are source coefficients and the spatial basis is assumed to be normalized such that $\int_\Gamma |\phi_k(\mathbf{r})|^2 d\Gamma(\mathbf{r}) = 1$. Inserting the expansion into equation (2.9) yields the following direct model in matrix form:

$$\mathbf{p} = \mathbf{H}\mathbf{c} + \mathbf{n} \tag{3.6}$$

where $\mathbf{p} \in \mathbb{C}^M$ is a vector of measured acoustic pressure, $\mathbf{c} \in \mathbb{C}^K$ a vector of source coefficients, and $\mathbf{n} \in \mathbb{C}^M$ accounts for measurement noise. The matrix $\mathbf{H} \in \mathbb{C}^{M \times K}$ is the associated propagator with elements given by $[\mathbf{H}]_{ij} = \int_\Gamma G(\mathbf{r}_i|\mathbf{r})\phi_j(\mathbf{r}) d\Gamma(\mathbf{r})$, $i = 1, \dots, M$, $j = 1, \dots, K$. Notice that since the problem is formulated in the frequency domain, we are working with complex quantities. The corresponding inverse problem basically consists in identifying K unknown source coefficients c_k. In the next sections we shall see how the Bayesian formulation can be used to solve this problem by assigning probability density functions to the variables.

3.3.1 Likelihood function

The most natural variable in equation (3.6) to be represented by a pdf is the measurement noise in vector $\mathbf{n}$. In this context, we assign a complex Gaussian pdf to model $\mathbf{n}$. A plausible justification for this choice results from the fact the we are working in frequency domain and the acoustic pressure is measured in time domain. Thus, a Fourier transform is usually applied in order to obtain the acoustic pressure at a given angular frequency ω. Indeed, it is the passage from time to frequency domain that, owing to the Central Limit theorem applied to the Fourier Transform [Cra46], cause the variable to tend towards a Gaussian distribution.

In this work $\mathbf{n}$ is assumed with zero mean, i.e. $\mathbb{E}\{\mathbf{n}\} = \mathbf{0}$, where $\mathbb{E}$ stand for the expected value; this is because any residual bias should be captured by the direct model as is inherent to the definition of "measurement" noise. The noise covariance is defined as $\mathbb{E}\{\mathbf{n}\mathbf{n}^H\} = \beta^2\boldsymbol{\Omega}_n$ where ^{H} stands for the conjugate transpose operator, β^2 is the *unknown* expected noise energy, and $\boldsymbol{\Omega}_n$ is a *known* matrix which gives the correlation coefficients between the different components the noise field, normalized such that $\mathrm{Trace}\{\boldsymbol{\Omega}_n\} = \dim(\mathbf{n}) = M$. In the case in which no *a priori* information on the nature of the noise field is available, one may simple choose $\boldsymbol{\Omega}_n$ equal to the identity matrix, i.e. a spatially white noise. Thus, the probability density function of the noise, noted by $[\mathbf{n}|\beta^2]$ is given by the following complex Gaussian distribution

$$[\mathbf{n}|\beta^2] = \mathcal{N}_{\mathcal{C}}(\mathbf{0}, \beta^2\boldsymbol{\Omega}_n) = \frac{1}{\pi^M\beta^{2M}|\boldsymbol{\Omega}_n|}\exp\left(-\beta^{-2}\|\mathbf{n}\|^2_{\boldsymbol{\Omega}_n}\right), \tag{3.7}$$

where the notation $\mathcal{N}_{\mathcal{C}}$ stands for "complex Normal" and $|\boldsymbol{\Omega}_n|$ is the determinant of matrix $\boldsymbol{\Omega}_n$, which is $|\boldsymbol{\Omega}_n| = 1$ for $\boldsymbol{\Omega}_n = \mathbf{I}$. In addition, by notational convention $\|\mathbf{n}\|^2_{\boldsymbol{\Omega}_n} = \mathbf{n}^H\boldsymbol{\Omega}_n^{-1}\mathbf{n}$ represents the squared norm of vector $\mathbf{n}$ with metric $\boldsymbol{\Omega}_n$. Consequently, the pdf of the measured pressure $\mathbf{p}$ is also a complex Gaussian

$$[\mathbf{p}|\mathbf{c}, \beta^2] = \mathcal{N}_{\mathcal{C}}(\mathbf{H}\mathbf{c}, \beta^2\boldsymbol{\Omega}_n) = \frac{1}{\pi^M\beta^{2M}|\boldsymbol{\Omega}_n|}\exp\left(-\beta^{-2}\|\mathbf{p} - \mathbf{H}\mathbf{c}\|^2_{\boldsymbol{\Omega}_n}\right), \tag{3.8}$$

with the pdf $[\mathbf{p}|\mathbf{c}, \beta^2]$ defined as the "likelihood function", which gives us the direct probability of the measurement data allowed by the model in equation (3.6) given the random fluctuations of the measurement noise.

3.3.2 Prior probability density function

In this section we discuss the prior probability density function which is assigned to the unknown source parameters. Particularly, the prior pdf expresses what one knows or believes about the unknown variables of interest *before* making the experiments and shows much more flexibility than the likelihood model.

Our first assumption is that the complex-valued source field is *a priori* of zero mean (in the ensemble average) and with covariance matrix $\mathbb{E}\{\mathbf{c}\mathbf{c}^H\} = \alpha^2\mathbf{\Omega}_c$ where α^2 is the *unknown* source energy and $\mathbf{\Omega}_c$ a *known* matrix of correlation coefficients. In addition, the matrix $\mathbf{\Omega}_c$ is normalized such that $\mathrm{Trace}\{\mathbf{\Omega}_c\} = \dim(\mathbf{c}) = K$. The setting of $\mathbf{\Omega}_c$ depends on the actual problem and some a priori information on the source field that the user may possess. A typical choice is to assume that values at two different positions on the source are uncorrelated (i.e. a spatially white source field), which leads to $\mathbf{\Omega}_c = \mathbf{I}$. Indeed, the latter is an implicit assumption to most methods based on deterministic approaches. We finally remark that this is an *a priori* assumption and it does not impede the reconstruction of a sources presenting mutual correlation.

The last assumption concerns the prior probability density function of the unknown source parameters. Again, a complex Gaussian distribution is chosen, leading to:

$$[\mathbf{c}|\alpha^2] = \mathcal{N}_{\mathbb{C}}(\mathbf{0}, \alpha^2\mathbf{\Omega}_c) = \frac{1}{\pi^K \alpha^{2K}|\mathbf{\Omega}_c|} \exp\left(-\alpha^{-2}\|\mathbf{c}\|^2_{\mathbf{\Omega}_c}\right), \tag{3.9}$$

where conditioning on α^2 is explicitly reminded. The above choice is motivated by practical reasons, specifically, it will lead to tractable calculations and naturally give rise to well-known regularization mechanisms. In addition, we anticipate that the choice of the prior pdf will be directly related to the traditional regularization concept. In this context, the particular choice of a complex Gaussian will act such as to favor those solutions of low energy.

3.3.3 Posterior probability density function and MAP estimate

The solution to the inverse problem is finally returned by the posterior pdf $[\mathbf{c}|\mathbf{p}, \alpha^2, \beta^2]$ which assigns probabilities to possible values of coefficients c_k's once the measurements are taken. Bayes rule indicates how this pdf is obtained from updating the prior pdf $[\mathbf{c}|\alpha^2]$ with the likelihood function $[\mathbf{p}|\mathbf{c}, \beta^2]$. Namely,

$$[\mathbf{c}|\mathbf{p}, \alpha^2, \beta^2] = \frac{[\mathbf{p}|\mathbf{c}, \beta^2][\mathbf{c}|\alpha^2]}{[\mathbf{p}|\alpha^2, \beta^2]}, \tag{3.10}$$

where

$$[\mathbf{p}|\alpha^2,\beta^2] = \int [\mathbf{p}|\mathbf{c},\beta^2][\mathbf{c}|\alpha^2]d\mathbf{c} \tag{3.11}$$

is the "evidence" which will play a major role in deriving the Bayesian regularization criterion later on in section 3.4.1. As we can notice from equation (3.10), Bayes rule allows us to express an *inverse* probability in terms of *direct* probabilities. Once the full pdf $[\mathbf{c}|\mathbf{p},\alpha^2,\beta^2]$ is known, a relevant point estimate of the unknown vector $\mathbf{c}$ can be returned by the most probable value after observing the data, i.e. the maximum of the posterior pdf in equation (3.10) – the so-called "maximum a posteriori estimate" (MAP).

In what follows, we explain how to determine the MAP estimate for the unknown source field $\mathbf{c}$. Firstly, we substitute for the pdf's given in equations (3.8) and (3.9) into the right hand side of equation (3.10). Notice that the denominator (i.e. the "evidence") in equation (3.10) does not depend explicitly on the unknown source vector $\mathbf{c}$ and thus will not enter into the maximization. Next, taking the opposite of the logarithm we convert maximization into minimization and the MAP estimate of $\mathbf{c}$ is the vector which minimizes the following quadratic cost function:

$$\begin{aligned}\hat{\mathbf{c}} &= \text{Argmax}\left\{\mathcal{N}_{\mathcal{C}}(\mathbf{Hc},\beta^2\boldsymbol{\Omega}_n)\mathcal{N}_{\mathcal{C}}(\mathbf{0},\alpha^2\boldsymbol{\Omega}_c)\right\}\\ &= \text{Argmin}\left\{-\ln(\mathcal{N}_{\mathcal{C}}(\mathbf{Hc},\beta^2\boldsymbol{\Omega}_n)\mathcal{N}_{\mathcal{C}}(\mathbf{0},\alpha^2\boldsymbol{\Omega}_c))\right\}\\ &= \text{Argmin}\left\{M\ln(\beta^2)+K\ln(\alpha^2)+\beta^{-2}\|\mathbf{p}-\mathbf{Hc}\|^2_{\boldsymbol{\Omega}_n}+\alpha^{-2}\|\mathbf{c}\|^2_{\boldsymbol{\Omega}_c}\right\}.\end{aligned} \tag{3.12}$$

Expanding the terms in the third equality explicitly depending on $\mathbf{c}$ yield the following cost function:

$$J(\mathbf{c},\mathbf{c}^*) = (\mathbf{p}^H - \mathbf{c}^H\mathbf{H}^H)\boldsymbol{\Omega}_n^{-1}(\mathbf{p}-\mathbf{Hc}) + \eta^2\mathbf{c}^H\boldsymbol{\Omega}_c^{-1}\mathbf{c}, \tag{3.13}$$

in which the following relation was introduced

$$\eta^2 = \frac{\beta^2}{\alpha^2}. \tag{3.14}$$

Taking the derivative of equation (3.13) with respect to $\mathbf{c}$ and setting the result to zero yields

$$\begin{aligned}\frac{dJ(\mathbf{c},\mathbf{c}^*)}{d\mathbf{c}} &= \mathbf{c}^H\mathbf{H}^H\boldsymbol{\Omega}_n^{-1}\mathbf{H} + \eta^2\mathbf{c}^H\boldsymbol{\Omega}_c^{-1} - \mathbf{p}^H\boldsymbol{\Omega}_n^{-1}\mathbf{H} = 0\\ &= (\mathbf{H}^H\boldsymbol{\Omega}_n^{-1}\mathbf{H} + \eta^2\boldsymbol{\Omega}_c^{-1})\mathbf{c} = \mathbf{H}^H\boldsymbol{\Omega}_n^{-1}\mathbf{p},\end{aligned} \tag{3.15}$$

which finally yields the estimate:

$$\hat{\mathbf{c}} = (\mathbf{H}^H\boldsymbol{\Omega}_n^{-1}\mathbf{H} + \eta^2\boldsymbol{\Omega}_c^{-1})^{-1}\mathbf{H}^H\boldsymbol{\Omega}_n^{-1}\mathbf{p}. \tag{3.16}$$

Keeping in mind that the system is underdetermined, i.e. $K \geq M$, a more convenient equivalent expression for $\hat{\mathbf{c}}$ can be obtained by using the so-called matrix inversion lemma [Hjø11], which is given by:

$$(\mathbf{A} + \mathbf{BCD})^{-1} = \mathbf{A}^{-1} - \mathbf{A}^{-1}\mathbf{B}(\mathbf{C}^{-1} + \mathbf{DA}^{-1}\mathbf{B})^{-1}\mathbf{DA}^{-1}, \tag{3.17}$$

with $\mathbf{A}, \mathbf{B}, \mathbf{C}$ and $\mathbf{D}$ arbitrary matrices with the constraint that $\mathbf{A}$ and $\mathbf{C}$ are invertible. Applying the matrix inversion lemma to the matrix:

$$(\mathbf{H}^H\boldsymbol{\Omega}_n^{-1}\mathbf{H} + \eta^2\boldsymbol{\Omega}_c^{-1})^{-1}$$

in equation (3.16), with the following definitions

$$\mathbf{A} = \eta^2\boldsymbol{\Omega}_c^{-1}, \quad \mathbf{B} = \mathbf{H}^H, \quad \mathbf{C} = \boldsymbol{\Omega}_n^{-1}, \quad \mathbf{D} = \mathbf{H},$$

and after several algebraic manipulations (see Appendix C.1 for a detailed derivation), yields the following result, :

$$\hat{\mathbf{c}} = \boldsymbol{\Omega}_c\mathbf{H}^H\left(\mathbf{H}\boldsymbol{\Omega}_c\mathbf{H}^H + \eta^2\boldsymbol{\Omega}_n\right)^{-1}\mathbf{p}. \tag{3.18}$$

Indeed, the consideration of a complex Gaussian prior through the Bayesian framework has “mechanically” produced a regularized solution of the Tikhonov type – see e.g. Refs. [Han98, TA77]. The significance of the regularization parameter η^2 given in equation (3.14) is clearly that of a noise-to-signal ratio (NSR) (ratio of expected noise energy β^2 to expected source energy α^2). A similar interpretation is found in early references on classical NAH [Wil01], outside the Bayesian framework, and in statistical approaches such as SONAH [Hal09].

Further insight into the regularized solution (3.18) can be obtained by considering the following singular value decomposition:

$$\boldsymbol{\Omega}_n^{-1/2}\mathbf{H}\boldsymbol{\Omega}_c^{1/2} = \sum_{k=1}^{M} s_k\mathbf{u}_k\mathbf{v}_k^H \tag{3.19}$$

with right hand side parameters as previously discussed (see Section 2.3.2). Substituting for into equation (3.18), one has the simple result

$$\hat{\mathbf{c}} = \mathbf{\Omega}_c^{1/2}\mathbf{V}\left\lceil \frac{s_k}{s_k^2 + \eta^2} \right\rfloor \mathbf{U}^H \mathbf{\Omega}_n^{-1/2}\mathbf{p} \tag{3.20}$$

where $\lceil a_k \rfloor$ symbolizes a diagonal matrix with generic diagonal element a_k. As we have previously seen in Section 3.2, this is the structure of a generalized pseudo-inverse of $\mathbf{H}$ where the smallest singular values s_k are progressively filtered out from the inversion, i.e. $s_k/(s_k^2+\eta^2) \simeq 1/s_k$ if $s_k \gg \eta^2$ and $s_k/(s_k^2+\eta^2) \simeq 0$ if $s_k \ll \eta^2$ so as to prevent instability due to over-amplification of measurement noise or simply numerical overflow when $\mathbf{H}$ is ill-conditioned. However, as common to all regularization techniques, the difficulty remains in how to optimally adjust the value of the parameter η^2 when no information on the noise level is available. The aim of the next section is to explain how this is obtained within the Bayesian formalism.

3.4 Choosing the regularization parameter

3.4.1 Bayesian regularization criteria

In this section we discuss how to pursue within the Bayesian formalism in order to estimate η^2 directly from the measured data and the model which relates the latter to the problem's unknowns. Indeed, this is a great advantage of the Bayesian approach which naturally answers this question, conversely to other methods cited in Section 3.2, which are rather imposed *ad hoc*. From now on, we distinguish two possible strategies: (1) the estimation of η^2 indirectly as the ratio of the most probable values of β^2 and α^2 and (2) the estimation of η^2 directly from the marginal pdf of η^2 by selecting its value of maximum probability.

More precisely, the first strategy leads to the following problem:

$$\hat{\eta}^2_{\text{Joint}} = \frac{\hat{\beta}^2}{\hat{\alpha}^2}, \quad \text{where } (\hat{\alpha}^2, \hat{\beta}^2) = \text{Argmax}[\alpha^2, \beta^2|\mathbf{p}], \tag{3.21}$$

with $[\alpha^2, \beta^2|\mathbf{p}]$ the pdf of α^2 and β^2 given the measurements $\mathbf{p}$. In turn, the second strategy formally writes:

$$\hat{\eta}^2_{\text{MAP}} = \text{Argmax}[\eta^2|\mathbf{p}] \text{ where } [\eta^2|\mathbf{p}] = \int [\alpha^2, \beta^2 = \alpha^2, \eta^2|\mathbf{p}] \left| \frac{\partial\beta^2}{\partial\eta^2} \right| d\alpha^2, \tag{3.22}$$

with $|\partial\beta^2/\partial\eta^2| = \alpha^2$ standing for the Jacobian of the change of variables $(\alpha^2, \beta^2) \mapsto (\alpha^2, \eta^2)$.

In what follows, the two strategies are discussed into a unified treatment since they share the same elements, namely: (1) the evaluation of the likelihood function $[\mathbf{p}|\alpha^2, \beta^2]$; (2) the definition of the prior $[\alpha^2, \beta^2]$ and (3) the evaluation of the posterior pdf $[\alpha^2, \beta^2|\mathbf{p}]$.

In addition, for the subsequent developments we consider the reconstructed source field expressed in terms of the singular value decomposition, i.e. equation (3.20).

3.4.1.1 Likelihood function for regularization

The likelihood function $[\mathbf{p}|\alpha^2,\beta^2]$ is obtained from marginalizing the likelihood function $[\mathbf{p}|\mathbf{c},\beta^2]$ of section 3.3.1 over $\mathbf{c}$, which is nothing else than the "evidence" defined in equation (3.11). Based on equations (3.8) and (3.9), the exact expression of the likelihood is given as follows:

Proposition 1.

$$
\begin{aligned}
[\mathbf{p}|\alpha^2,\beta^2] &= \mathcal{N}_{\mathcal{C}}\left(\mathbf{0},\alpha^2\mathbf{H}\boldsymbol{\Omega}_c\mathbf{H}^H+\beta^2\boldsymbol{\Omega}_n\right) && \text{(3.23a)}\\
&= \frac{\exp\left(-\alpha^{-2}\sum_{k=1}^{M}\frac{|y_k|^2}{s_k^2+\eta^2}\right)}{\pi^M\alpha^{2M}|\boldsymbol{\Omega}_n|\prod_{k=1}^{M}(s_k^2+\eta^2)} && \text{(3.23b)}
\end{aligned}
$$

where y_k is the k-th element of vector

$$\mathbf{y}=\mathbf{U}^H\boldsymbol{\Omega}_n^{-1/2}\mathbf{p}, \tag{3.24}$$

the projection of the measurements on the array subspace.

Proof. : see Appendix D.1 □

3.4.1.2 Prior pdf for regularization

The Bayesian framework offers the possibility to take any *a priori* information that the user might have on either the noise β^2 or source energies α^2. This is known as a hierarchical Bayes approach [Rob01]. In this work, we assume that no knowledge on these parameters is available *a priori*, and thus we simply set the prior pdf $[\alpha^2,\beta^2]\propto 1$ (with $\propto$ the "proportional" sign). This choice may be viewed as the "worst case", in the sense that all outcomes of those parameters have the same probability *a priori*.

3.4.1.3 Joint pdf of noise and source energies

Given all the above preliminaries, one can now evaluate the joint pdf of the parameters (α^2,β^2) given the measurements in $\mathbf{p}$, that is

$$
\begin{aligned}
[\alpha^2,\beta^2|\mathbf{p}] &\propto [\mathbf{p}|\alpha^2,\beta^2][\alpha^2,\beta^2]\\
&= \mathcal{N}_{\mathcal{C}}\left(\mathbf{0},\alpha^2\mathbf{H}\boldsymbol{\Omega}_c\mathbf{H}^H+\beta^2\boldsymbol{\Omega}_n\right), && \text{(3.25)}
\end{aligned}
$$

with the prior $[\alpha^2, \beta^2] \propto 1$ as discussed in the previous Section. In addition, Bayes' rule has been used and all quantities not explicitly depending on α^2 and β^2 have been factored out. Again, we turn maximization into minimization by taking the opposite of the logarithm of equation (3.25) and we insert the expression of the complex Gaussian given in equation (3.23b). Finally, the MAP estimates of (α^2, β^2) are given as follows:

$$\begin{aligned}(\hat{\alpha}^2, \hat{\beta}^2) &= \text{Argmax}\left\{\ln\left(\mathcal{N}_{\mathbb{C}}\left(\mathbf{0}, \alpha^2 \mathbf{H}\boldsymbol{\Omega}_c\mathbf{H}^H + \beta^2\boldsymbol{\Omega}_n\right)\right)\right\} \\ &= \text{Argmin}\left\{M \ln \alpha^2 + \ln|\boldsymbol{\Omega}_p| + \|\mathbf{p}\|^2_{\boldsymbol{\Omega}_p}\right\} \qquad (3.26)\end{aligned}$$

where $\boldsymbol{\Omega}_p = \alpha^2 \mathbf{H}\boldsymbol{\Omega}_c\mathbf{H}^H + \beta^2\boldsymbol{\Omega}_n$. The cost function to be minimized with respect to α^2 and β^2 then reads:

$$\mathbf{J}_{\text{Joint}}(\alpha^2, \beta^2) = \sum_{k=1}^{M} \ln\left(\alpha^2 s_k^2 + \beta^2\right) + \sum_{k=1}^{M} \frac{|y_k|^2}{\alpha^2 s_k^2 + \beta^2}, \qquad (3.27)$$

as expressed in terms of the singular value decomposition (3.19) and the elements of vector $\mathbf{y}$ defined in equation (3.24).

The minimization of the cost function $\mathbf{J}_{\text{Joint}}(\alpha^2, \beta^2)$ is detailed hereafter. Let us first introduce the change of variables $(\alpha^2, \beta^2) \mapsto (\alpha^2, \eta^2)$. Then, setting the derivative of

$$\mathbf{J}_{\text{Joint}}(\alpha^2, \eta^2) = \sum_{k=1}^{M} \ln\left(s_k^2 + \eta^2\right) + \frac{1}{\alpha^2}\left(\sum_{k=1}^{M} \frac{|y_k|^2}{s_k^2 + \eta^2}\right) + M \ln \alpha^2 \qquad (3.28)$$

with respect to α^2 to zero, one immediately gets the following MAP estimate of α^2

$$\hat{\alpha}^2 = \frac{1}{M}\left(\sum_{k=1}^{M} \frac{|y_k|^2}{s_k^2 + \eta^2}\right). \qquad (3.29)$$

Unlike the source energy, there is no closed-form solution for the regularization parameter η^2. Substituting for $\hat{\alpha}^2$ in expression (3.28), we finally have

$$\hat{\eta}^2_{\text{Joint}} = \text{Argmin}\ \mathbf{J}_{\text{Joint}}(\eta^2) \qquad (3.30)$$

with

$$\begin{aligned}&\mathbf{J}_{\text{Joint}}(\eta^2) \triangleq \mathbf{J}_{\text{Joint}}(\hat{\alpha}^2, \eta^2) - M \\ &\mathbf{J}_{\text{Joint}}(\eta^2) = \sum_{k=1}^{M} \ln\left(s_k^2 + \eta^2\right) + M \ln \hat{\alpha}^2. \qquad (3.31)\end{aligned}$$

Thus, the estimate of the regularization parameter $\hat{\eta}^2_{\text{Joint}}$ is obtained by minimization of the above cost function with respect to η^2. In practice, this minimization can be carried out by firstly defining a grid of candidate values for η^2. A convenient choice for latter should span the range of singular values given by the decomposition in (3.19). For instance, the lower and higher values of η^2 respectively at the order of the minimum and maximum singular value. Next, a refined search can be carried out by techniques such as the dichotomy method. In turn, the MAP estimate of the noise energy, if needed, is given by $\hat{\beta}^2 = \hat{\alpha}^2 \times \hat{\eta}^2_{\text{Joint}}$.

3.4.1.4 Marginal pdf of the regularization parameter

As anticipated in Section 3.4.1, the second strategy to estimate the regularization parameter from the data is to directly find its posterior pdf, $[\eta^2|\mathbf{p}]$, without requiring the intermediate estimates of the noise and source energies, $\hat{\alpha}^2$ and $\hat{\beta}^2$. The exact expression of $[\eta^2|\mathbf{p}]$ is carried out by marginalization of the joint pdf $[\alpha^2, \beta^2|\mathbf{p}]$ in equation (3.25). Particularly, we obtain the following result:

Proposition 2.

$$[\eta^2|\mathbf{p}] \propto \left(\eta^2 \left(\sum_{k=1}^{M} \frac{|y_k|^2}{s_k^2+\eta^2}\right)^{M-2} \prod_{k=1}^{M} (s_k^2+\eta^2)\right)^{-1}. \tag{3.32}$$

Proof. : see Appendix D.2 □

The value of maximum probability of the above pdf can be obtained using the same strategy as before. More specifically, we take the opposite of the logarithm of (3.32) thus turning maximization into minimization. After few algebraic manipulations we obtain the following MAP estimate of the regularization parameter:

$$\hat{\eta}^2_{\text{MAP}} = \text{Argmin } \mathbf{J}_{\text{MAP}}(\eta^2) \tag{3.33}$$

with

$$\begin{aligned} \mathbf{J}_{\text{MAP}}(\eta^2) &\triangleq \sum_{k=1}^{M} \ln\left(s_k^2+\eta^2\right) + (M-2)\ln\hat{\alpha}^2 \\ &= \mathbf{J}_{\text{Joint}}(\eta^2) - 2\ln\hat{\alpha}^2, \end{aligned} \tag{3.34}$$

and $\hat{\alpha}^2$ as previously given in equation (3.29).

3.4.1.5 Comparison of strategies

It is anticipated that the two estimates $\hat{\eta}^2_{\text{Joint}}$ and $\hat{\eta}^2_{\text{MAP}}$ found in Sections 3.4.1.3 and 3.4.1.4 must be closely related – since $\mathbf{J}_{\text{MAP}} = \mathbf{J}_{\text{Joint}} - 2\ln\hat{\alpha}^2$ according to equation (3.34) – although they have no reason to be *identical* since the MAP estimate of a ratio is generally

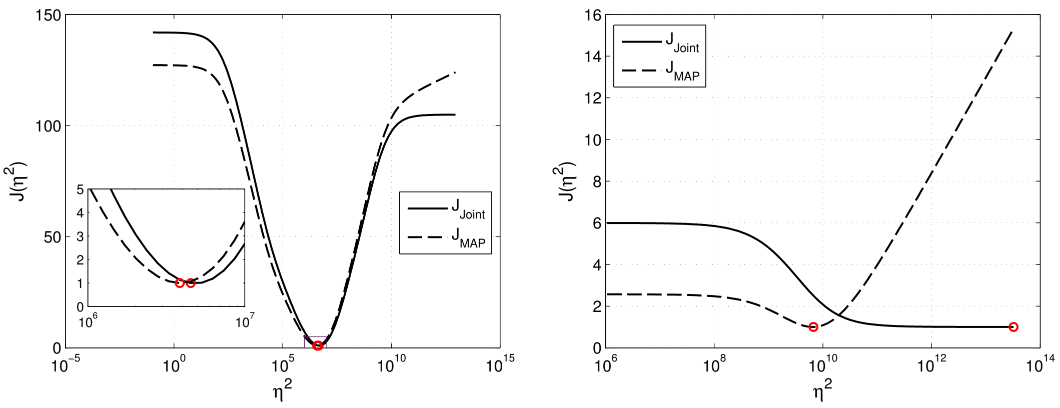

Figure 3.2: In most practical situations $\hat{\eta}^2_{\text{Joint}}$ and $\hat{\eta}^2_{\text{MAP}}$ are found nearly equal (see left panel). One exception is when the SNR is so poor that $\mathbf{J}_{\text{Joint}}$ tends to see only noise, thus rejecting its minimum to infinity and returning an unbounded value of the regularization parameter. Such a situation is forbidden by $\mathbf{J}_{\text{MAP}}$ which, by construction, advantageously forces a finite value of η^2 (see right panel).

not equal to the ratio of the MAP estimates. Indeed, since $-2\ln\hat{\alpha}^2$ is a monotonically increasing function of η^2, it comes that

$$\hat{\eta}^2_{\text{MAP}} \leq \hat{\eta}^2_{\text{Joint}}, \tag{3.35}$$

meaning that $\hat{\eta}^2_{\text{MAP}}$ in general yields a "less regularized" solution than $\hat{\eta}^2_{\text{Joint}}$. In addition, the term $-2\ln\hat{\alpha}^2$ acts as a penalty that forbids solutions (i.e. source fields) with zero energy α^2. This is confirmed by the asymptotic behavior of $\mathbf{J}_{\text{Joint}}$ and $\mathbf{J}_{\text{MAP}}$ as $\eta^2 \to \infty$, given as follows:

$$\mathbf{J}_{\text{Joint}}(\eta^2) \sim CM, \quad \text{as } \eta^2 \to \infty \tag{3.36a}$$

$$\mathbf{J}_{\text{MAP}}(\eta^2) \sim 2\ln\eta^2, \quad \text{as } \eta^2 \to \infty, \tag{3.36b}$$

with C a constant. Notice that $\mathbf{J}_{\text{Joint}}$ tends to a constant while $\mathbf{J}_{\text{MAP}}$ still grows to infinity. This property might be advantageous in some low SNR configurations where $\mathbf{J}_{\text{Joint}}$ tends to "see" only noise and thus returns an infinite value for $\hat{\eta}^2_{\text{Joint}}$. Figure 3.2 illustrates the above remarks by means of an example selected from the simulations to be presented in Section 3.5.1.

3.4.2 L-curve

The L-curve basically consists in a plot (on a logarithm scale) of the norm of the regularized solution $\|\hat{\mathbf{q}}_\eta\|$ against the corresponding residual norm $\|\mathbf{p} - \mathbf{G}\hat{\mathbf{q}}_\eta\|$ for all potential values of the regularization parameter η. The principle is based on the existence of a distinct corner which separates the horizontal part of the curve, where the regularization errors dominate, from the vertical part, where the perturbation errors dominate. The vertical part is characterized by a sharp decrease of the norm $\|\hat{\mathbf{q}}_\eta\|$ for small regularization parameters η, whereas the horizontal part represents a significantly increase of the residual norm with η while the norm of the regularization solution only slightly decreases. A simulation example is used to clarify this behavior. The simulation parameters are the same as those to be presented in Section 4.2. The exact (known) source field $\mathbf{q}_0$ is used to simulate the acoustic pressure at some field points, represented by the vector $\mathbf{p}_0$. A complex Gaussian noise stacked in the vector $\mathbf{n}$ is added to simulated pressure with the condition $\|\mathbf{n}\| \leq \|\mathbf{p}_0\|$. The simulated acoustic pressure is then given as

$$\mathbf{p} = \mathbf{G}\mathbf{q}_0 + \mathbf{n}. \tag{3.37}$$

Hereafter, we consider two cases for the right hand side of equation (3.37): (a) a noise-free right hand side (i.e. $\mathbf{n} = 0$); (b) a right hand side consisting of only noise. The L-curve corresponding to both cases is shown in Figure 3.3. As can be seen, for small regularization parameters η, the curve is dominated by perturbation errors (red dashed curve) and from a certain value of η the regularization errors start to dominate (black solid curve). The L-curve corresponding to a perturbed right hand side will be a combination of these two curves.

From this analysis we observe that the idea of the method is to find a regularization parameter corresponding to the corner of the L-curve, which is a trade-off between the minimization of the regularized solution and its residual norm. Since the regularization parameter is continuous for Tikhonov regularization, the L-curve is also continuous and, consequently, twice differentiable. Therefore, it is straightforward to compute its curvature by means of the formula [HO93]:

$$\kappa(\eta) = \frac{\rho' \upsilon'' - \rho'' \upsilon'}{((\rho')^2 + (\upsilon')^2)^{3/2}}, \tag{3.38}$$

where $\rho = \log\left(\|\mathbf{p} - \mathbf{G}\hat{\mathbf{q}}_\eta\|\right)$, $\upsilon = \log\left(\|\hat{\mathbf{q}}_\eta\|\right)$, and the superscripts $'$ and $''$ denote the first and second derivatives with respect to the regularization parameter η. Therefore, the L-curve validation is equivalent to find the regularization parameter which maximizes the curvature in equation (3.38). Nevertheless, in practical applications one may deal with cases in which the corner of the L-curve is not clearly identified, as we shall see in the next sections.

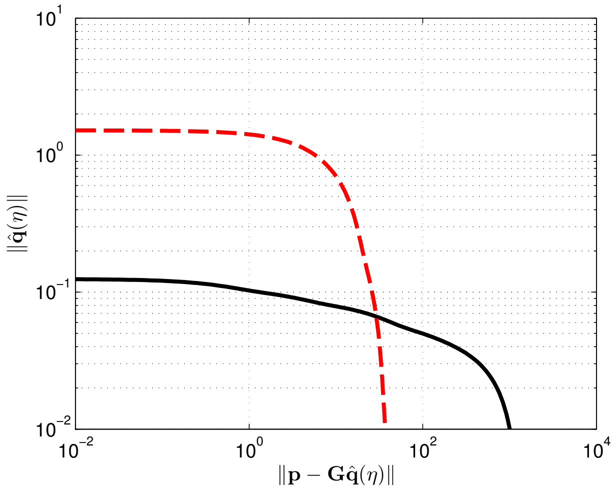

Figure 3.3: Example of L-curve for a noise-free right hand side $\mathbf{n} = 0$ (black solid line) and for a right hand side with only noise (red dashed line). The behavior of the curve for a perturbed right hand side $\mathbf{p} + \mathbf{n}$ is merely a combination of the above curves.

3.4.3 Extending the L-curve criterion

The idea proposed in this section was based on the behavior of the L-curve's curvature (as a function of the frequency) for source reconstruction problems. More specifically, we noticed that discontinuities on the reconstructed acoustic power of sources are related to some particular behaviors of the L-curve. Two different cases have been distinguished based on numerical and experimental observations: (1) the L-curve's curvature exhibits multiple local maxima and (2) the curvature presents negative local maxima. Indeed, an analysis carried out in reference [BF09] has shown that the L-curve may have several local convex corners. In addition, the presence of more than one "corner" has been observed by authors in other applications such as, near-field acoustical holography [Gom08] or damage detection problems [LL10].

The approach proposed in this work consists of an extension of the classic L-curve criterion by considering the several local maxima as candidate solutions and computing a final solution as a weighted combination of them. In reference [HR12], an approach based on the linear combination of several candidate solutions is also proposed, however, in this case the candidate solutions are computed from different regularization methods and different parameter choice criteria. It was shown by numerical examples that in many cases the linear combination approach provides a better estimate of the desired solution than any of the candidate solutions [HR12].

3.4.3.1 Multiple local maxima

The classic L-curve criterion for Tikhonov regularization consists in selecting the solution which maximizes the curvature function in equation (3.38). Assuming that local maxima can also carry potential information to the solution, the above criterion may not yield the best regularized solution. For instance, let us consider a case in which the L-curve's curvature function in equation (3.38) has two closely spaced local maxima with similar magnitude. As long as the use of Tikhonov regularization leads to the choice of a solution between several quasi-solutions, there is no obvious reason why favor one solution over the other. A different perspective to deal with this case may be to combine the two potential solutions in order to consider the information that each can afford to the problem. Following these considerations, a weighting procedure is proposed to account for possible local maxima.

The proposed procedure for this case consists on three steps: (1) check for the existence of local maxima; (2) discard the negligible maxima by taking into account only those maxima which are greater than an attenuated version the global maximum, for instance, $\kappa(\eta_i) \geq 0.25\kappa_{max}$ (see Figure 3.4); (3) filter out the maxima corresponding to highly energetic solutions by considering only those with solution norm $\|\mathbf{q}_\eta\|$ smaller than the norm of the minimum potential solution amplified by a factor, for instance, $\|\mathbf{q}_{\eta_i}\| \leq 2\|\mathbf{q}_\eta\|_{min}$ (see Figure 3.5).

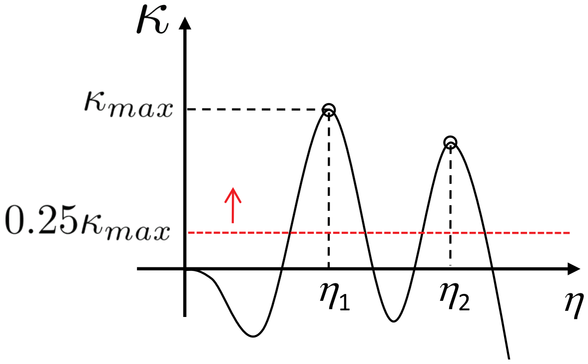

Figure 3.4: Schematic representation of the L-curve's curvature as a function of the regularization parameter showing multiple local maxima.

After the selection of potential regularized solutions, the weight attributed to each of them is given by:

$$P_{\eta_i} = \frac{\kappa(\eta_i)}{\sum_{i=1}^{s} \kappa(\eta_i)}, \tag{3.39}$$

where s is the number of potential solutions and η_i is the regularization parameter corresponding to the ith solution. Therefore, the final solution for this particular case is

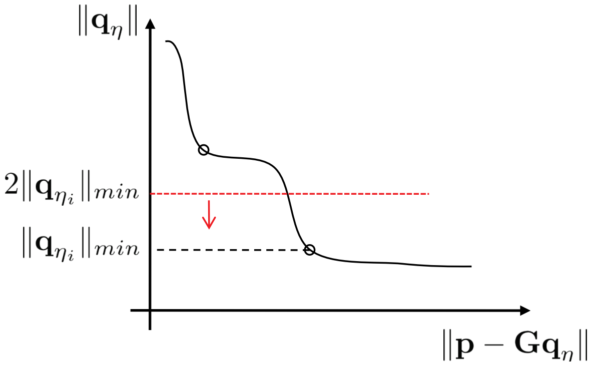

Figure 3.5: Schematic L-curve for the case with multiple local maxima.

obtained as follows:

$$\hat{\mathbf{q}}_\eta = \sum_{i=1}^{s} \hat{\mathbf{q}}_{\eta_i} P_{\eta_i}. \tag{3.40}$$

3.4.3.2 Negative local maxima

In this part we direct the analysis to circumstances in which the log-log L-curve is concave. Looking at the evolution of the L-curve's curvature as a function of frequency, we notice that as the system becomes less ill-conditioned, the maximum of curvature decreases until it reaches a negative value. Using the classic curvature maximization approach, when the local maximum becomes just slightly smaller than zero, no regularization will be used, which in turn, generates a discontinuity on the reconstructed source spectrum (see Figure 3.7). Based on this observation, the method presented here consists in weighting the regularized and non-regularized solutions. One can note that the existence of a negative local maximum is directly connected to the presence of a negative local minimum. According to this condition, the weights are computed as the ratio between the curvature extrema, given by:

$$P_r = \frac{\kappa_{max}(\eta) - \kappa_{min}(\eta)}{|\kappa_{min}(\eta)|} \quad \text{and} \quad P_{nr} = 1 - P_r, \tag{3.41}$$

where $\kappa_{max}(\eta)$ and $\kappa_{min}(\eta)$ respectively corresponds to the negative local maximum and minimum (see Figure 3.6). In addition, P_r and P_{nr} are the weights given to the regularized and non-regularized solutions. The final solution for the reconstructed source strength is then:

$$\hat{\mathbf{q}} = \hat{\mathbf{q}}_{nr} P_{nr} + \hat{\mathbf{q}}_r P_r \tag{3.42}$$

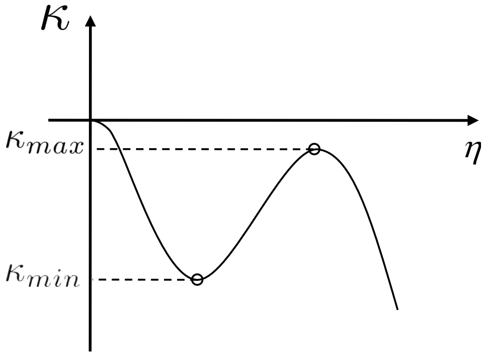

Figure 3.6: Schematic representation of the L-curve's curvature as a function of the regularization parameter showing a negative local maxima.

In this manner, the weight given to each solution, viz. regularized and non-regularized, will depend on the difference between the local extrema. For instance, when the negative local maximum is just slightly greater than the negative local minimum, the weight applied to the regularized solution will be significantly smaller than the one given to the non-regularized one.

3.4.3.3 Experimental illustration

An experimental academic validation has been carried out to illustrate improvements generated by the proposed method. The studied source is a compression driver coupled to a tube system (22 mm diameter) with three openings, constituting three correlated acoustic monopoles in the frequency range of interest ($f < 2kHz$). The source is placed in a semi-anechoic room at 20 cm in front of a rectangular 6×5 microphone array, sampling the acoustic field with a constant step of 10 cm. The virtual monopoles to be identified are distributed on the source plane, over a rectangular surface of 80×70 cm (the microphone array aperture extended by 10cm on edges), with a resolution of 4 cm. The equivalent source distribution is placed on the plane coinciding with the physical tube openings and the total number of source DOFs is 483. The idea of the equivalent source method is used to estimate the acoustic source strength (volume velocity) of the equivalent sources at the source plane. The sound power is then directly obtained from the source strength distribution assuming a monopole source radiation and taking into account the pressure field in which the equivalent sources are inserted. In this case, real sources are omnidirectional in the frequency range of interest, the acoustic power of the equivalent sources can thus be assumed to be representative of the acoustic power of the real sources.

The sound radiated from an open-ended tube can be approximated by the radiation of a point source for wavelengths much larger than the tube radius [dBB08]. Hence, by measuring the acoustic intensity at a distance r of the source and multiplying by a spherical surface of radius r one can obtain the sound power radiated by the monopole.

Here, the acoustic intensity generated by each opening is measured using a Microflown p-u probe at 5 cm from the exit, not closer to avoid the high sensitivity to phase mismatch errors between the pressure and particle velocity probes in the very near field. Another reason is to limit the uncertainties on the distance r. These measurements will constitute the reference to assess the reliability of quantification results.

The identification is processed according to different regularization strategies:

- without regularization
- with classic L-curve's curvature maximization (no regularization in the concave case)
- with L-curve's curvature local maximization and consideration of negative maxima

The acoustic power corresponding to each equivalent source is assessed according to equation (2.27). The estimate of the total acoustic power for each frequency line is obtained by an integration over the source plane.

First of all, the acoustic power integrated over the identified source distribution is compared to the acoustic power estimated from measurements using the P-U probe. The result is given in Figure 3.7, without regularization and with the classic L-curve principle (maximization of the curvature).

The effect of regularization is clearly seen up to 1200 Hz. Below this frequency, the power identified without regularization is overestimated, of about 5dB from 750 to 1000 Hz and 10dB below 750 Hz. Upon 1200 Hz, the L-curve is concave, the regularization parameter is zero, and the regularized result is thus equal to the non regularized one. The identified power using regularization is matching the measured one between 200 Hz and 1700 Hz, with an error not exceeding $\pm 2dB$ at each frequency. Upon 1700 Hz, the identified power is generally underestimated. It can be explained by the spatial sampling of the array, that becomes lower than half the acoustic wavelength.

The L-curve and its curvature are drawn in Figure 3.8 at 800 Hz and 1400 Hz, illustrating simple cases requiring regularization at 800 Hz, or no regularization, at 1400 Hz, where the L-curve is concave. These results are generally satisfying, the global acoustic power is correctly identified on a wide frequency range. However, some discontinuities are observed on the identified power spectrum (see Figure 3.7) , because of the regularization that is processed at each frequency. These discontinuities remain acceptable from a quantitative point of view, but can be interpreted as non-physical results if the source is known to exhibit a continuous spectral density. Moreover, the identified power is continuous over several frequency bands, and discontinuities are observed on few frequencies only, as if the regularization process was jumping from one solution to the other at these particular frequencies. This observation is confirmed in Figure 3.9, where the L-curve's curvature

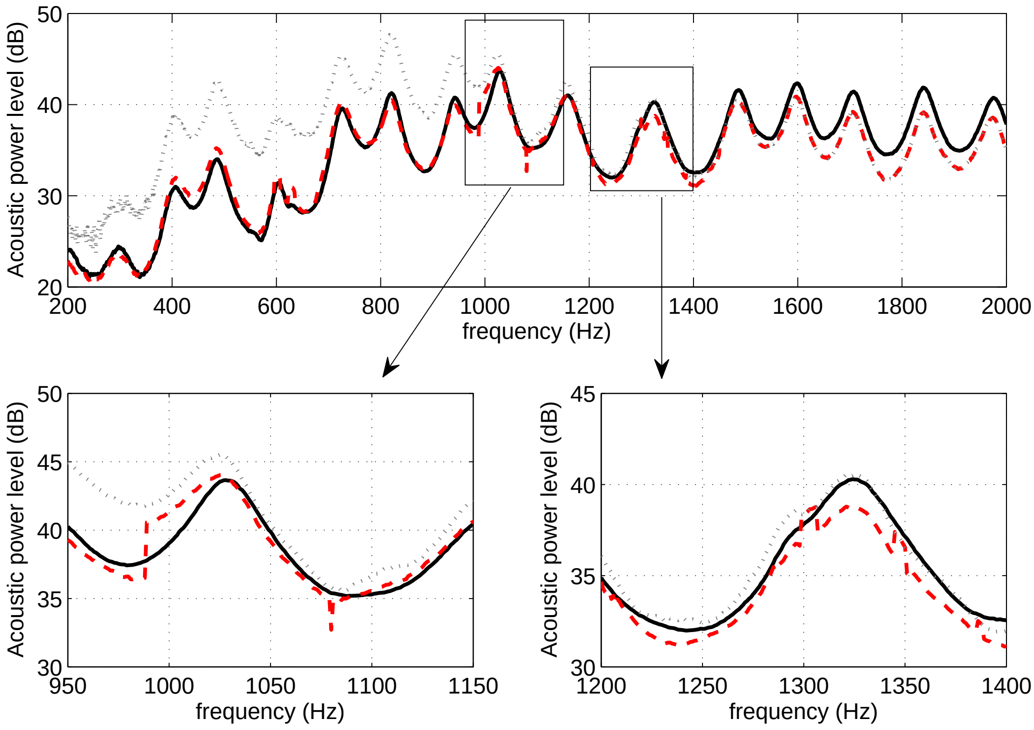

Figure 3.7: Acoustic power of the source, measurements (black solid line) and identification (dotted gray: non regularized, dashed red: regularized)

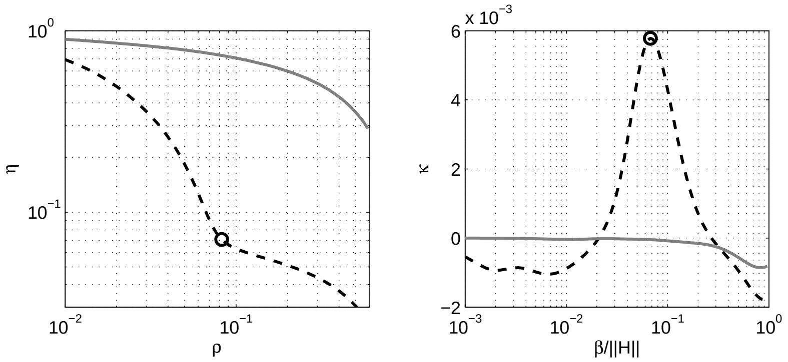

Figure 3.8: L-curve (left) and its curvature (right) at 800 Hz (dashed black) and 1400 Hz (solid gray).

(equation 3.38) is drawn as a function of the frequency, normalized by its maximum absolute value at each frequency for clarity purpose. It is clear on this 2D representation — that has to be maximized at each frequency — that the curvature exhibits sometimes several local maxima corresponding to different potential solutions, that are valuable on overlapping frequency bands. For example, one local maximum is varying continuously between 750 and 1000 Hz, and another one is found to vary between 950 and 1050 Hz. In

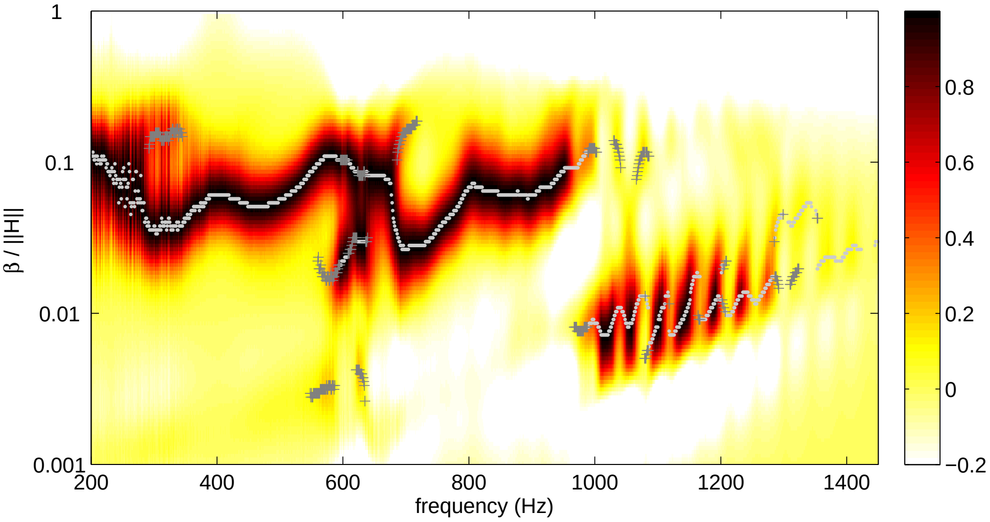

Figure 3.9: L-curve's curvature as a function of frequency and regularization (color scale). The figure also shows the value of η maximizing the curvature (gray dots: global maximum, gray +: local maxima).

such a case, the classic strategy consisting in maximizing the curvature leads to choose between two potential solutions in the frequency band 950-1000 Hz. This approach leads to a suddenly jump from one solution to the other at the frequency where the rank of the local maxima is inverted, generating a discontinuity of about 4dB on the power spectrum at 985 Hz. The same phenomenon (coexistence of at least 2 potential solutions in a frequency band) is also the reason of the discontinuities observed at 1080, 600 and 250 Hz. The L-curve and its curvature at 980 and 990 Hz are drawn in Figure 3.10.

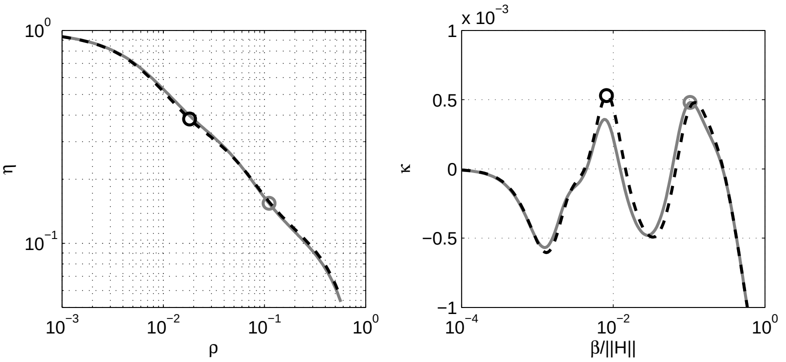

Figure 3.10: L-curve(left) and its curvature (right) at 980 Hz (dashed black) and 990 Hz (solid gray).

The two potential solutions have comparable curvatures, but the basic curvature's maximization leads to choose one or the other for the two frequencies. The reconstructed source field at 980 Hz is shown in Figure 3.11, illustrating the two potential solutions obtained at this frequency. As can be seen, the reconstructed source strength corresponding to the local maximum (right) has a slightly lower resolution since a higher regularization parameter is chosen, however, it is less disturbed by “ghost sources”.

Other discontinuities are observed at higher frequencies, where the regularization algorithm “hesitates” between a regularized and a non regularized solution. The classic L-curve analysis is to consider that if the curvature is always negative, the identification do not need regularization. The L-curve and its curvature at 1295 and 1300 Hz (on both sides of a discontinuity) are drawn in Figure 3.12.

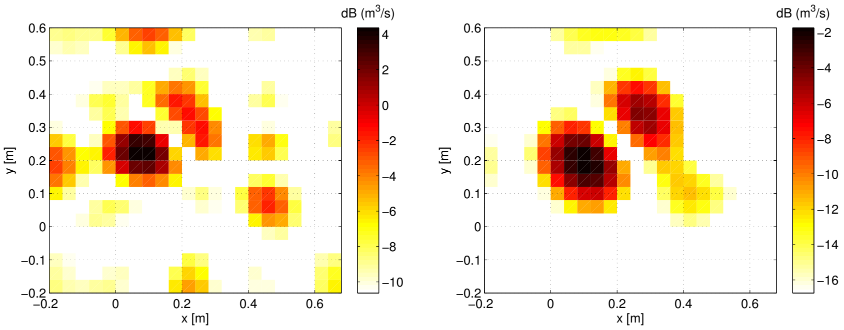

Figure 3.11: Reconstructed source strength at 980 Hz corresponding to the solution obtained from the global maximum of curvature (left) and from the local maximum of curvature (right).

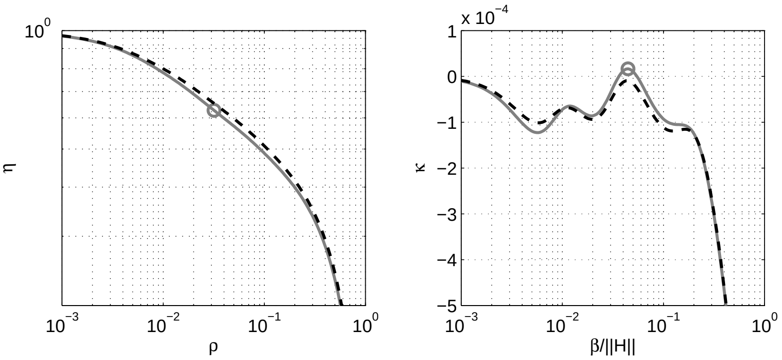

Figure 3.12: L-curve (left) and its curvature (right) at 1295Hz (solid gray) and 1300Hz (dashed black).

In this frequency range, the curvature is quite always negative, but still exhibits a maximum, just greater than zero before the discontinuity and just lower than zero after the discontinuity, where the regularization strategy leads to choose no regularization. It generates a discontinuity of about 2dB on the identified power spectrum. In order to illustrate the solutions obtained at 1300 Hz, we present in Figure 3.13 the reconstructed source field when no regularization is used (left) and a solution corresponding to a negative local maximum (right). We can observe from this results that a small amount of regularization is still beneficial at this frequency, since the regularized solution is much less disturbed by "ghost sources".

Some pragmatic considerations have been presented in earlier sections, allowing to refine the regularization strategy in such cases. The total acoustic power estimated by this approach is compared to results using the classic method in Figure 3.14. The refined strategy gives satisfying results for two reasons. First of all, the identified spectral density is continuous, showing that the combination between all potential quasi-solutions at each frequency naturally leads to a kind of continuity of the regularization process. The second satisfying point is that the results using the proposed refinements match measurements better than the classic approach. This is particularly true between 900 and 1000 Hz, but it is generally the case for each frequency band in which the classic approach was generating discontinuities.

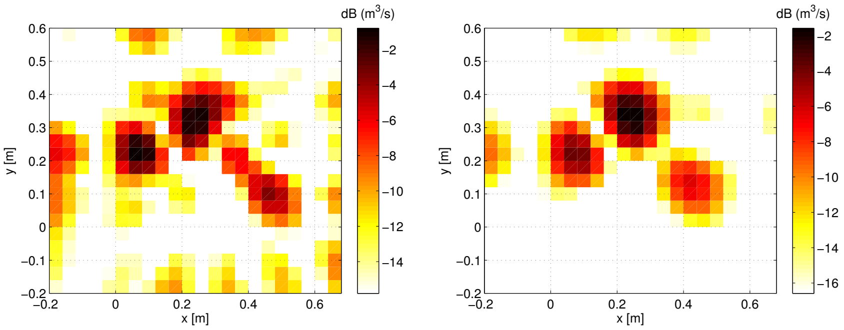

Figure 3.13: Reconstructed source strength at 1300 Hz without regularization (left) and with regularization determined by a negative local maximum (right).

3.5 Comparison of parameter choice methods

3.5.1 Numerical comparison

In order to examine the performance of the different parameter choice methods, numerical experiments of acoustic inverse problems are presented in this section. Two reference papers on this field are selected as benchmarks [KN04, Lec09], illustrating a wide range of source reconstruction configurations. In both papers, the performance of GCV and the L-curve was compared in the framework of numerical acoustic simulations. It was shown that the behavior of both methods varies significantly with the simulation parameters (i.e. level of measurement noise, frequency or distance between microphone array and

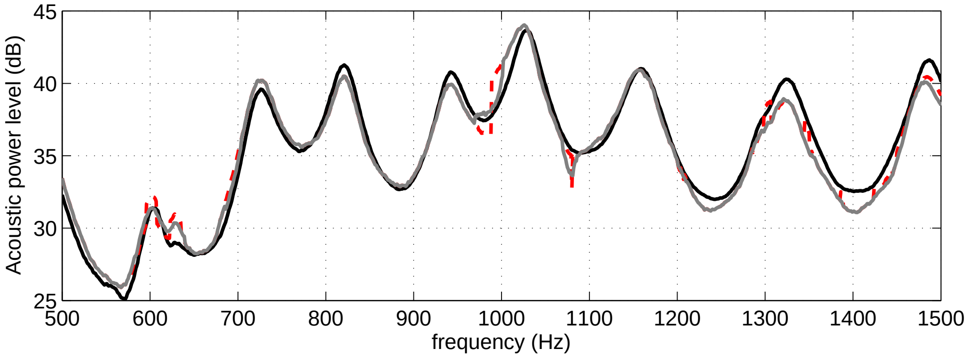

Figure 3.14: Acoustic power of the source, measurements (black solid line) and identification (dashed red : classic, solid gray : refined)

source surface) and no prevailing method could be indicated. Our aim here is to check the effectiveness of the Bayesian regularization criterion applied to the cases investigated in the aforementioned references. For that purpose, the geometry of the acoustic problem treated in each reference is reproduced and is briefly recalled in the next subsections.

The direct problem employed in the simulations is given by equation (2.3) and a free-field propagation is assumed, with Green's function given by:

$$G(\mathbf{r}_i|\mathbf{r}) = \frac{e^{-\mathrm{j}k\|\mathbf{r}_i-\mathbf{r}\|}}{4\pi\|\mathbf{r}_i-\mathbf{r}\|}, \tag{3.43}$$

where $k = \omega/c$ is the acoustic wavenumber, ω is the angular frequency and c is the speed of sound. The solution of the inverse problem for the source coefficients ($\hat{\mathbf{c}}$) is given by equation (3.20) and the different parameter selection methods will be used to adjust the regularization parameter η^2 therein. The implemented cost functions for the GCV and L-curve methods are exactly the same as those described in references [KN04, Lec09], and a detailed analysis of each can be found in references [GHW79, Han92].

An indicator based on the knowledge of the exact solution of the inverse problem ($\mathbf{c}$) is obtained by computation of the mean squared error (MSE) [KN04] between $\mathbf{c}$ and solutions for all potential regularization parameters. A cost function can be written as:

$$\mathbf{J}_{MSE} = \|\hat{\mathbf{c}}(\eta^2) - \mathbf{c}\|. \tag{3.44}$$

The optimal regularization parameter is thus returned by the minimum of the cost function:

$$\eta^2_{MSE} = \text{argmin}\ \mathbf{J}_{MSE}(\eta^2). \tag{3.45}$$

This indicator illustrates the "best we can do" scenario and the effectiveness of each method is evaluated as the relative error to the optimal solution, as follows:

$$\varepsilon_{BA} = \frac{\|\hat{\mathbf{c}}_{BA} - \hat{\mathbf{c}}_{MSE}\|}{\|\hat{\mathbf{c}}_{MSE}\|}, \ \varepsilon_{LC} = \frac{\|\hat{\mathbf{c}}_{LC} - \hat{\mathbf{c}}_{MSE}\|}{\|\hat{\mathbf{c}}_{MSE}\|}, \ \varepsilon_{GCV} = \frac{\|\hat{\mathbf{c}}_{GCV} - \hat{\mathbf{c}}_{MSE}\|}{\|\hat{\mathbf{c}}_{MSE}\|}, \tag{3.46}$$

where, from now on, we use the notation BA for the proposed Bayesian criterion and LC for the L-curve. The noise term entering on the right hand side of equation (2.3), used to simulate the acoustic pressure, consists of multiplicative and additive perturbations, with signal-to-noise ratio (SNR) ranging from 40 dB (1% noise) to 6 dB (50% noise). The noise term corresponding to the i-th microphone is given by:

$$\nu_i = 10^{-\mathrm{SNR}/20}\left(\gamma e^{\mathrm{j}\theta} p_0(\mathbf{r}_i) + \delta e^{\mathrm{j}\phi}\sqrt{\frac{\|\mathbf{p}_0\|^2}{M}}\right), \tag{3.47}$$

where γ and δ are zero mean Gaussian random variables with $Var(\gamma) = Var(\delta) = 1$, θ and ϕ are random variables uniformly distributed between 0 and 2π, $\mathbf{p}_0$ is the vector of noise-free pressure and $p_0(\mathbf{r}_i)$ its i-th component. The employed frequency band ranges from 100 Hz to 2500 Hz and the simulations are carried over 500 random trials of measurement noise for each frequency and SNR. In addition to the relative error to the optimal solution, a second indicator is used to evaluate the performance of different methods. It consists in estimating the signal-to-noise ratio (SNR) a posteriori, which is given by the following expression

$$\hat{\mathrm{SNR}} = \frac{1}{M}\frac{\sum_{k=1}^{M} s_k^2}{\hat{\eta}^2}, \tag{3.48}$$

with $\hat{\eta}^2$ the regularization parameter estimated by each method. Hence, an average of this indicator over the number of trials can be directly compared to the SNR injected into the simulated pressure.

A MATLAB® implementation of the codes used for the simulations is available online [dat].

3.5.1.1 Case 1: Square system ($M = K$)

The geometry of this problem is reproduced from reference [KN04] and is sketched on the left panel of Figure 3.15. A planar array of 9×9 microphones is placed at z_h from a vibrating surface modeled as a distribution of 9×9 monopole sources. The inter-source spacing is set to be identical to the inter-microphone spacing ($r_s = r_m$). Simply one point source is placed at the center of the source surface with volume velocity equal to unity. The condition number of the transfer matrix for this scenario is shown on the right panel of Figure 3.15 for three different distances to the source plane. We observe that as the distance is increased, the conditioning of the matrix is increased (specially at low frequencies) and that the problem is mainly ill-conditioned at low frequencies.

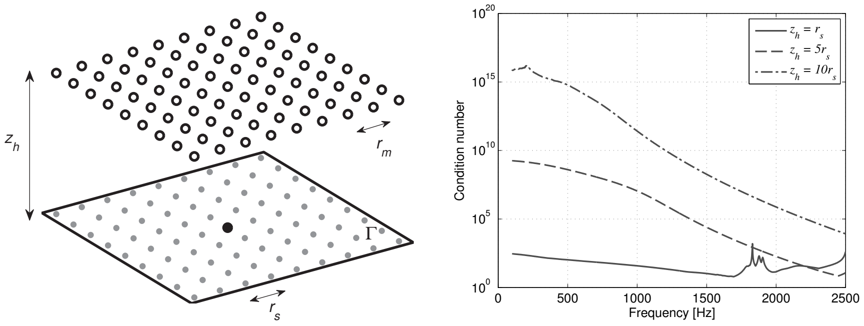

Figure 3.15: Left: Geometry of the problem for the first scenario, showing the discretized source surface, the microphone array and the simulated point source placed at the center of the surface. Right: Condition number for three different distances from the source plane (z_h).

The results of the simulations are given by the average of the indicator (3.46) over all random trials. Figure 3.16 shows the results for three distances from the array to the source surface respectively equal to $z_h = r_s$ (first row), $z_h = 5r_s$ (second row) and $z_h = 10r_s$ (third row), with $r_s = r_m = 12$ cm. Note that the results for the non-regularized case (NR) are added on the last column. We observe that GCV gives satisfactory results when the array is placed close to the source, however, when the microphone array is moved farther away (increasing on the condition number) it provides very poor results for a wide frequency range and all levels of noise, showing that GCV is very sensitive to the conditioning of the problem. In fact, although GCV returned reasonable regularization for some noise ensembles at those range, it occasionally fails to do so and this failure leads to completely anomalous solutions, because the regularization parameter η^2_{GCV} is too small. This is confirmed by the histogram plot shown in Figure 3.17, which corresponds to the 500 trials for a SNR of 30 dB, frequency of 1000 Hz and distant $z_h = 5r_s$ from the source surface. It shows the ratio between the regularization parameter estimated by each method and the optimal one. The closer the ratio is to 1, the better is the estimate. We note that the GCV's histogram presents a tail towards very small values, which means a severe underestimation of the regularization parameter. This behavior was observed for all range of SNR and frequencies which GCV gives high relative errors ε_{GCV}.

The results of the L-curve do not present a common trend for the three studied cases, however it is clearly not effective for high levels of measurement noise (low SNR) and at very low frequencies. On the other hand, the results returned by the Bayesian regularization criterion are satisfactory for the whole set of tested acoustical configurations, with errors rarely exceeding 20% of the optimal MSE solution. We remark that the results returned by the cost functions $\mathbf{J}_{\text{Joint}}$ and $\mathbf{J}_{\text{MAP}}$ were very similar, therefore just the case of $\mathbf{J}_{\text{Joint}}$ is presented here.

Figure 3.18 finally presents the SNR estimated *a posteriori* as given by equation (3.48). These results may indicate us the tendency to over- or under- regularize the solution, although they are relatively trickier to interpret. First of all, we remark that the ensembles in which the criteria returned $\hat{\eta} = 0$ and thus $\widehat{\text{SNR}} = \infty$ were not taken into account in the average. Looking first at the results for the L-curve (second column) we notice that the regions in black correspond to cases in which the L-curve criterion yields $\hat{\eta} = 0$ (no regularization), whereas in other regions the SNR is generally underestimated which leads to over-regularized solutions. The results for the GCV (third column) show that for $z_h = 5r_s$ and $z_h = 10r_s$ the SNR is often overestimated and thus the solutions are highly under-regularized. This explains the higher error levels in Figure 3.16. The Bayesian regularization criterion is the only to yield reasonable estimates of SNR for the whole range of configurations.

Finally, by observing the results for the optimal MSE criterion (last column), it is interesting to notice the appearance of some patterns for $z_h = 5r_s$ and $z_h = 10r_s$, which indicate that in fact the estimated SNR is frequency dependent. Indeed, comparing this behavior to the results of relative error for the Bayesian criterion (see first column of Figure 3.16) we realize that the "white stripes" therein exactly correspond to the aforementioned patterns.

3.5.1.2 Case 2: Under-determined system ($M \ll K$)

The geometry of the second case is reproduced from reference [Lec09] and is depicted in Figure 3.19. A planar array of 6×5 microphones is placed at a distance z_h from a source surface which is modeled by a grid of 28×23 monopole-like sources. The inter-microphone and inter-source spacings are respectively set to 10 cm and 2 cm in both x and y directions. This configuration models an under-determined scenario, with the number of measurement positions much lesser than the number of unknown source coefficients. In this case, the simulation is done by randomly placing 3 monopoles on the source distribution and assigning random complex strength to each of them. The simulated acoustic pressure is then perturbed with the noise model given by equation (3.47).

The same indicator (relative error to the MSE solution) is used and the results are presented in Figure 3.20. We note that the GCV presents similar behavior to the first scenario, producing satisfactory results when the array is placed relatively close to the source (except at low frequencies and low SNR) and poor results when it is moved farther away (higher condition number). The L-curve seems to treat this case better than the previous one except at very low frequencies and a frequency band depending on the

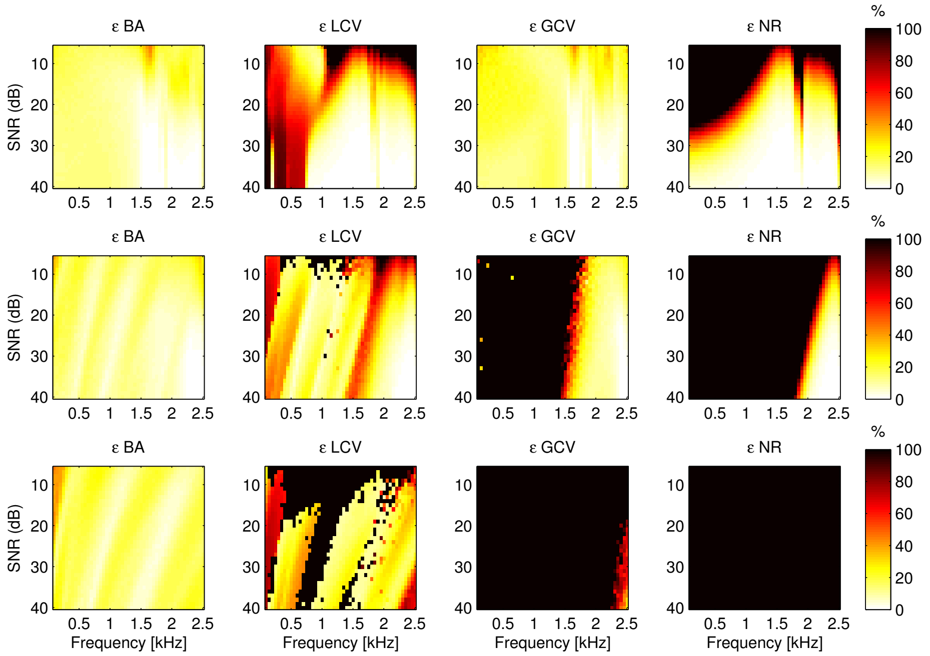

Figure 3.16: Average value of the relative error to the optimal (MSE) solution over 500 realizations of measurement noise. Each row corresponds to a given distance from the array to the source surface. First row: $z_h = r_s$, second row: $z_h = 5r_s$ and third row: $z_h = 10r_s$.

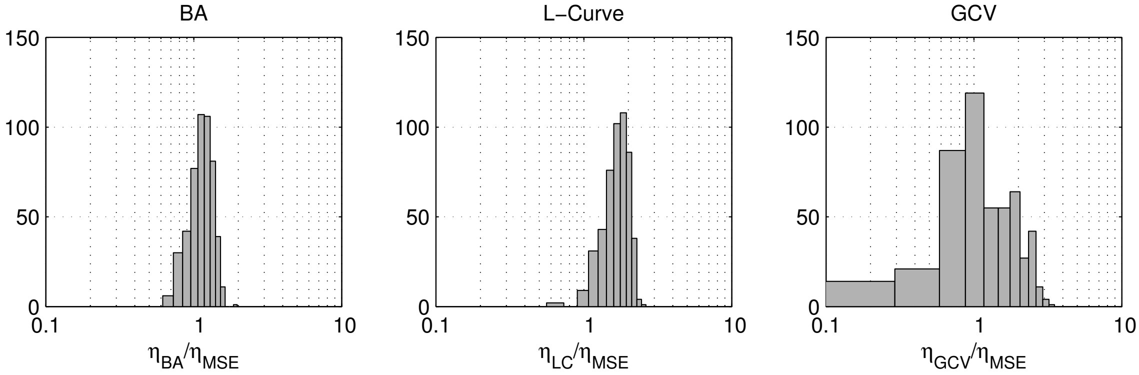

Figure 3.17: Histogram plot of the ratio between estimated and optimal regularization parameters for Bayesian regularization (BA), L-curve and GCV. They correspond to 500 realizations of measurement noise with a SNR of 30 dB, frequency 1000 Hz and distance source-array $z_h = 5r_{ss}$.

array-source distance. Again, the Bayesian regularization criterion is able to produce satisfactory results for all source-array distances and over the full range of SNR levels and frequencies. We can notice, however, that the relative error ε_{BA} at high frequencies and high SNR are slightly greater than the errors for the non-regularized (NR) and L-curve (LC) cases. It is apparent that no regularization is the best option at those ranges, indeed, the L-curve had no corner for those cases and the employed algorithm applies no

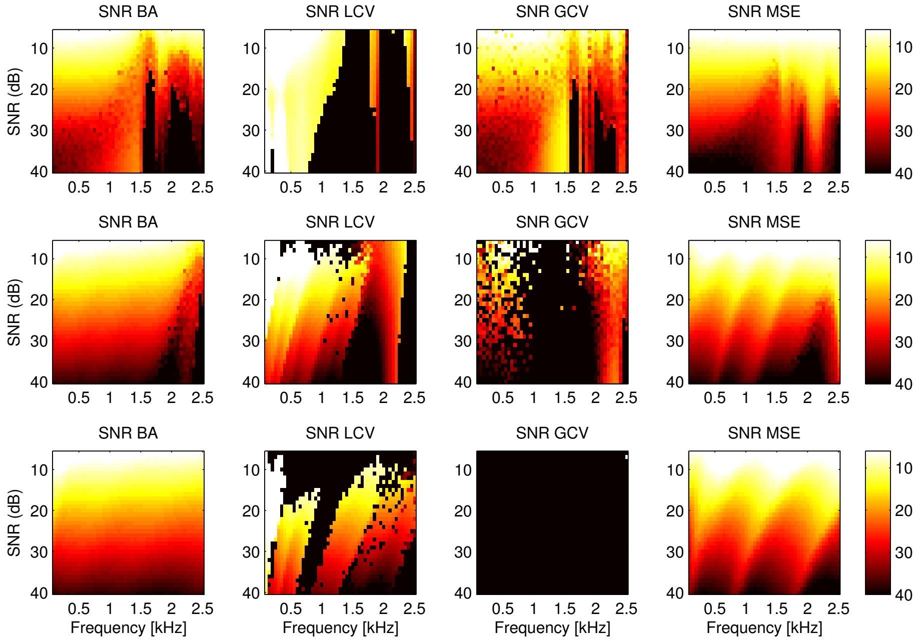

Figure 3.18: Average value of the estimated SNR over 500 realizations of measurement noise. The colorbar ranges from 6 to 40 dB. Each row corresponds to a given distance from the array to the source surface. First row: $z_h = r_s$, second row: $z_h = 5r_s$ and third row: $z_h = 10r_s$.

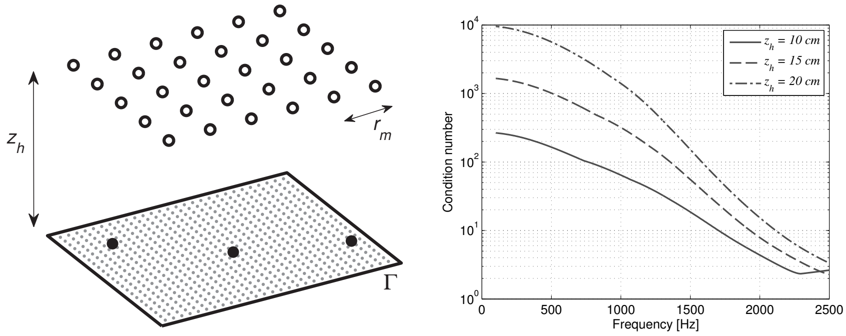

Figure 3.19: Left: Geometry of the problem for the second scenario. It shows the microphone array, the discretized source surface and 3 point sources randomly placed at the source surface.; Right: Condition number of the transfer matrix for distance z_h equals to 10, 15 and 20 cm.

regularization. On the other hand, the Bayesian cost function still exhibits a minimum and the solution is slightly oversmoothed. Although, as it will be shown in the next section, introducing a small amount of regularization when the problem is not very ill-conditioned (high frequencies on the simulations) has a small impact on the reconstructed acoustic quantities.

We finally show in Figure 3.21 the average estimate of the SNR for different approaches. Similarly to the first scenario, the Bayesian regularization criterion leads to fairly good

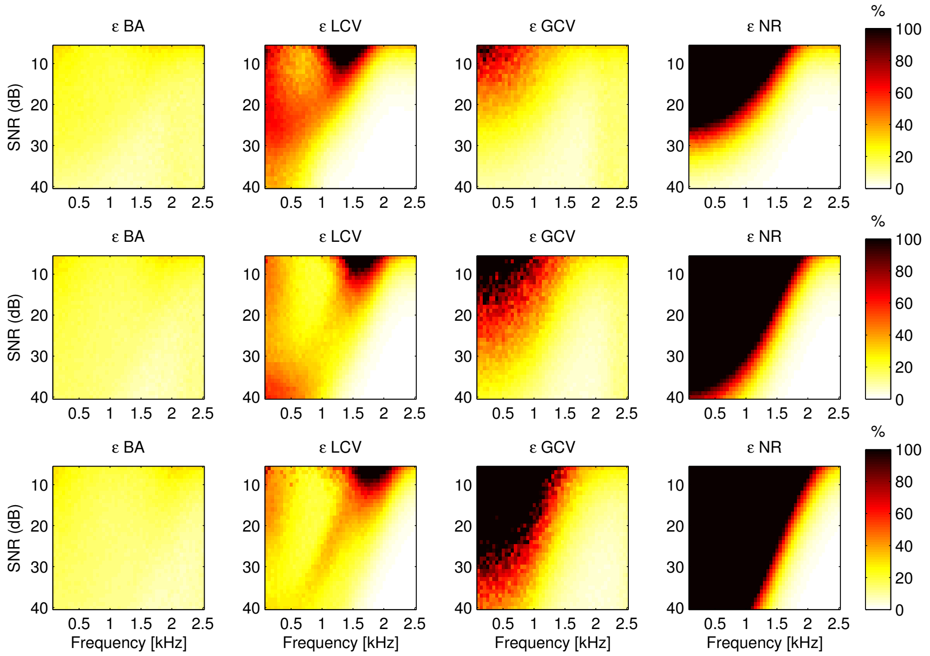

Figure 3.20: Average value of the relative error to the optimal (MSE) solution over 500 realizations of measurement noise. Each row corresponds to a given distance from the array to the source surface. First row: z_h = 10 cm, second row: z_h = 15 cm and third row: z_h = 20 cm.

estimates of SNR for all different configurations. In addition, we observe the appearance of a transition region depending on the distance from the array to the source surface. In fact, the transition occurs because in this range the criterion alternates between regularizing or not the solution.

Looking now at the results for the L-curve (second column) we clearly identify the region where the L-curve yields no regularization at all (black area). It can also be seen that for z_h = 10 and z_h = 15 cm the L-curve in general underestimates the SNR level, which in turn leads to a slightly over-regularized solution. The results for the GCV method indicate that in general the SNR is overestimated and thus the solutions are underestimated.

3.5.2 Experimental comparison

This section illustrates an application of the studied regularization criteria in an experimental set-up. The source of interest is a driver unit connected to a piping system with three outlets (diameter 2.2 cm), as shown in Figure 3.22. This source is a good approximation of three correlated monopoles in the frequency range of interest (200-2000 Hz). A planar array of 6×5 microphones (inter-microphone spacing of 10 cm) is placed at 20 cm from the plane comprising the three outlets. A fictitious source surface (on the plane of

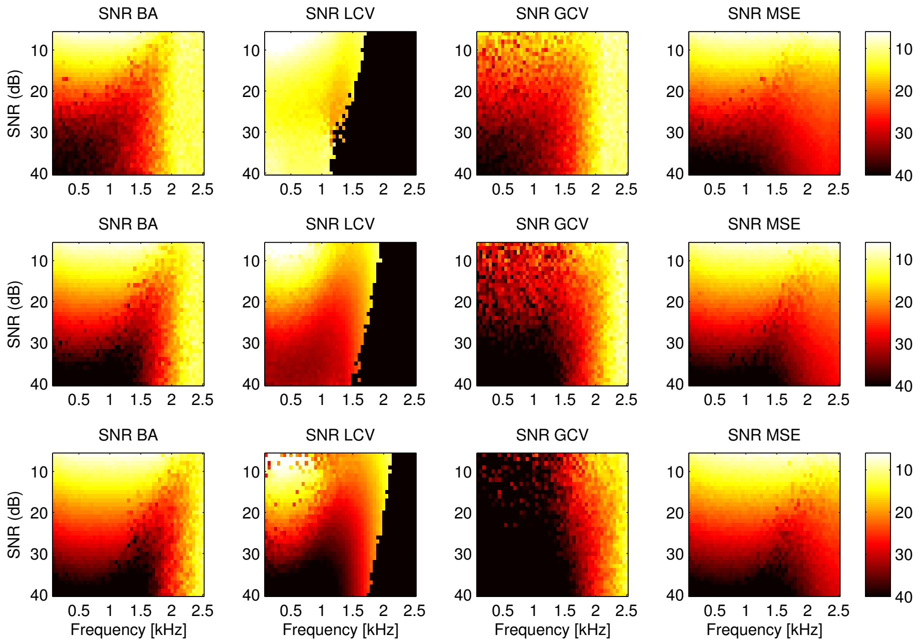

Figure 3.21: Average value of the estimated SNR over 500 realizations of measurement noise. The colorbar ranges from 6 to 40 dB. Each row corresponds to a given distance from the array to the source surface. First row: $z_h = 10$ cm, second row: $z_h = 15$ cm and third row: $z_h = 20$ cm.

outlets) with dimensions 80×70 cm^2 is discretized with a constant spacing of 4 cm. The virtual sources are modeled as point sources and the Green's function given in equation (3.43) is used for the inversion. Equation (3.20) is again used to solve for the source coefficients that in this case correspond to the volume velocity (source strength) of each virtual source. The experiment was carried out in a semi-anechoic room of dimensions 5×3.40×2 m^3 and the source was driven with white random noise. The particle velocity and the sound pressure were measured at 5 cm from each opening using a Microflown p-u intensity probe, allowing an estimation of their acoustic power. The radiated acoustic power is estimated by integrating the measured acoustic intensity over a spherical surface of radius 5 cm and centered at each opening.

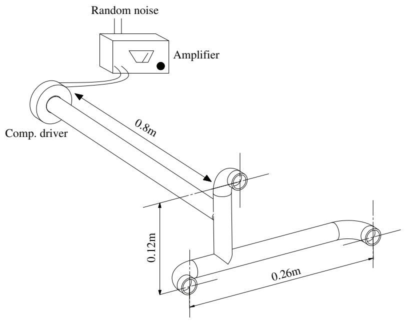

Figure 3.22: Acoustic source of interest.

Figure 3.23 shows the reconstructed source field (volume velocity) at 945 Hz using the regularization parameter returned by the Bayesian criterion (BA), the L-curve and GCV. It can be seen that GCV fails to compute a reasonable solution, on the other hand, the reconstruction obtained by the L-curve and the proposed Bayesian criterion is fairly good. The cost function at this frequency for each method is shown in Figure 3.24. We notice that the L-curve and the Bayesian criterion yield similar regularization parameter, yet in a more convincing way for the latter (note the presence of a local maxima on the L-curve's curvature). We can also observe that the minimum of the GCV function (not visible with the employed scale) is located towards smaller values of η^2, which led to the undersmoothed solution shown in Figure 3.23 (right hand side). The reconstructed source field at 650 Hz is shown in Figure 3.25. In this case, the GCV and the Bayesian criterion yield similar results, on the contrary, the L-curve criterion led to a rather over-smoothed solution. We remark that at this discrete frequency only two of the three sources radiate significant energy, as shall be confirmed by the measurements to be presented next (see Figure 3.28). The cost functions corresponding to this case are represented in Figure 3.26. We note that GCV and the proposed Bayesian criterion returned similar regularization parameters. On the other hand, the L-curve's curvature exhibits two local maxima very close to each other in level. A better alternative in this particular case, would rather be to select the local maximum slightly on the left of the global maximum.

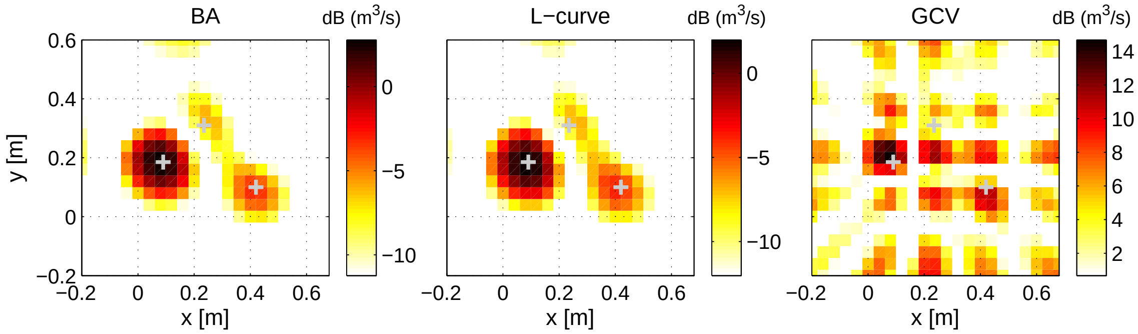

Figure 3.23: Reconstructed source field (volume velocity) at 945 Hz corresponding to each regularization criterion. A dynamic range of 15 dB is used for all.

The acoustic power radiated by the reconstructed source field was computed in a similar manner as in reference [CLG10]. It essentially consists of summing the power radiated by each virtual point source in isolation and a term that is the power generated by each source in working against the induced pressure generated by neighbor sources (see, for example, [Fah00]). Figure 3.27 compares the reconstructed global acoustic power (as integrated over the source surface) to the reference p-u measurements. As can be seen, the GCV results diverge at some frequencies, which are related to a severe underestimation of the regularization parameter. For the L-curve, although the results are globally satisfactory, we notice few discontinuities for instance around 650 and 970 Hz. Further

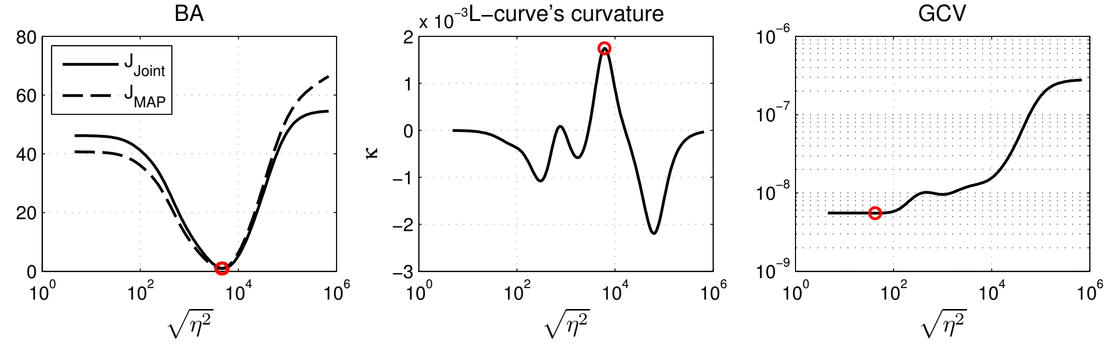

Figure 3.24: Cost functions associated to each regularization criterion at the frequency of 945 Hz. Left: the proposed Bayesian regularization criteria. Middle: curvature of the L-curve (whose corner is the point with maximum curvature). Right: the GCV cost function.

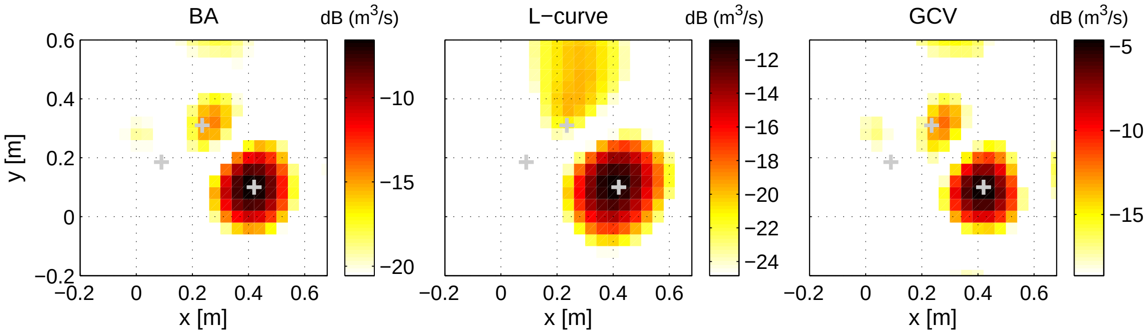

Figure 3.25: Reconstructed source field (volume velocity) at 650 Hz corresponding to each regularization criterion. A dynamic range of 15 dB is used for all.

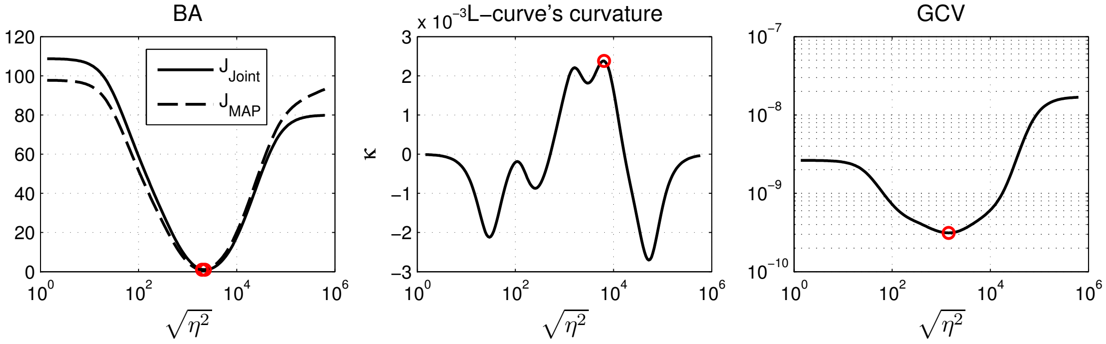

Figure 3.26: Cost functions associated to each regularization criterion at the frequency of 650 Hz. Left: the proposed Bayesian regularization criteria. Middle: curvature of the L-curve (whose corner is the point with maximum curvature). Right: the GCV cost function.

investigation has shown that they are due to alternations among competing local maxima of curvature evolving with frequency. In turn, the estimate given by the Bayesian criterion is found more stable in the whole frequency range, illustrating its robustness. The acoustic power radiated by each opening has also been predicted and compared to the measurements (see Figure 3.27). The predictions were obtained by carefully choosing an integration area around each identified source, as shown on the top left panel of Figure 3.28. One can notice that a confidence interval around the point estimate returned by the Bayesian regularization is shown in Figures 3.27 and 3.28, illustrating another advantage of the Bayesian approach. In the next Section we discuss in detail how to obtain these interval estimates. Finally, we can notice from Figure 3.28 that the three sources are well located around their real positions and their individual contributions in terms of acoustic power are fairly well predicted.

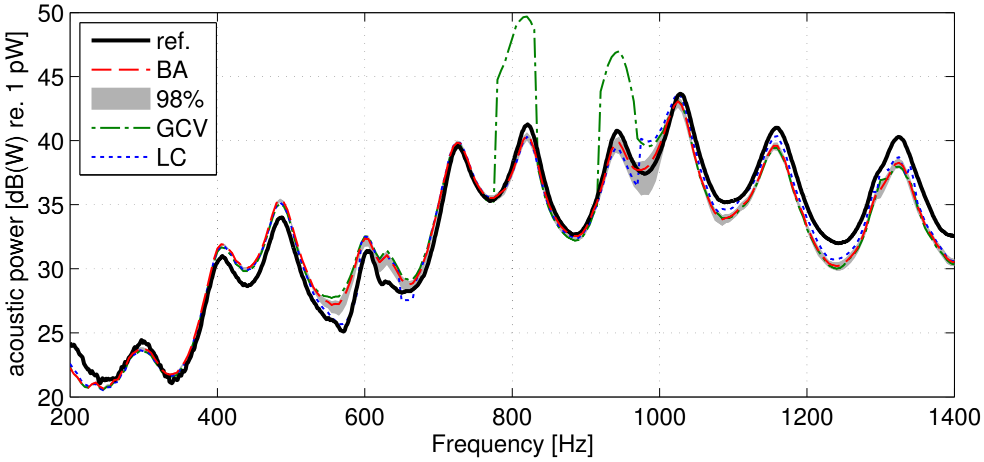

Figure 3.27: Estimate of the total acoustic power for different regularization strategies. The reference (ref.) was obtained from p-u measurements. The figure also shows a 98% Bayesian confidence interval around the point estimate returned by the proposed Bayesian criterion (BA).

3.6 Sensitivity of the acoustic inverse problem to regularization

As mentioned before, the art of regularization is as risky as essential for successfully solving the acoustic inverse problem. Therefore, it is crucial to assess which effect small modifications in the regularization parameter will have on the reconstructed source field. In short, the question to be addressed is how sensitive the reconstruction is to the actual setting of the regularization parameter? One particular difficulty is the fact that η^2 intervenes in a non-linear way into the estimation of the source field $\hat{\mathbf{c}}$. Since the Bayesian frameworks treats η^2 as a random variable with a given pdf, it offers a rather unique answer to the above question.

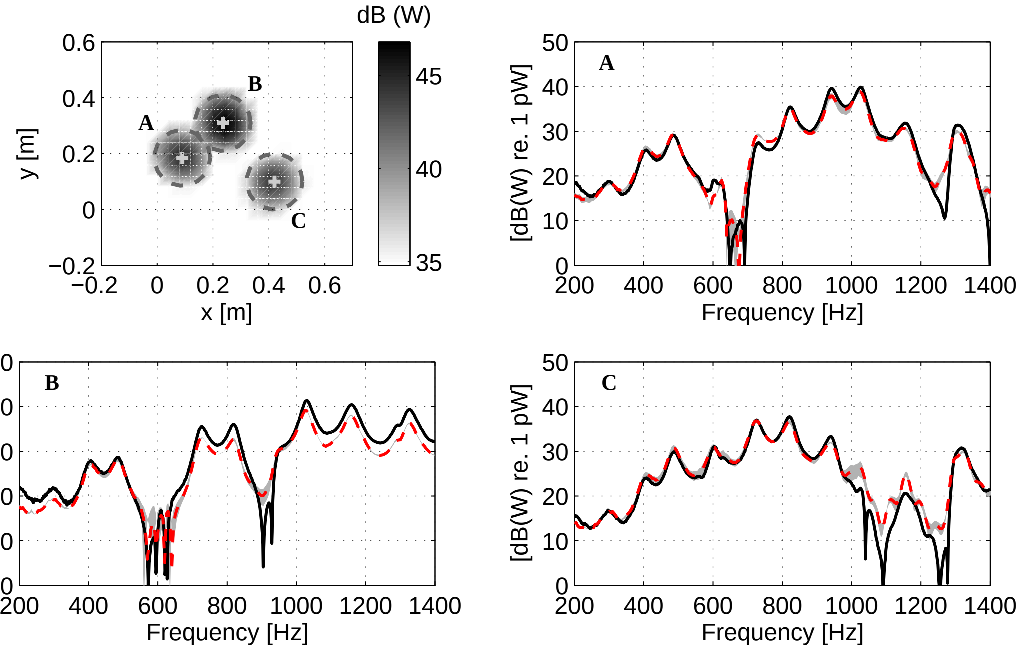

Figure 3.28: Top left: reconstructed acoustic power map integrated over the frequency band 200-1400 Hz. The + symbols are the real source positions and the dashed circles are the integration area used to compute the partial PSD of each source. The other panels show the PSD of each source identified by the proposed method (red) and obtained from p-u measurements (black).

3.6.1 Markov Chain Monte Carlo sampling

The posterior pdf $[\eta^2|\mathbf{p}]$ found in Proposition 2 fully answers the goal of quantifying the uncertainty arising from regularization. In particular, by allowing to sample values of η^2, it makes possible to propagate the variability due to regularization to any acoustical quantity of interest functionally depending on the regularization parameter, such as the source field, the acoustical intensity, or the acoustical power. Since such a pdf does not seem to pertain to a standard family, one has to resort to MCMC methods, such as the popular Metropolis-Hasting algorithm [Rob01], to sample it.

3.6.2 Gaussian approximation

Should one not require the full posterior pdf $[\eta^2|\mathbf{p}]$ but simply characterize it by its variance, then the following simple Gaussian approximation may be useful:

Proposition 3.

$$[\eta^2|\mathbf{p}] \approx \mathcal{N}\left(\hat{\eta}^2;\sigma^2\right) \quad \textit{with} \quad \sigma^2 = \left(\frac{d^2\mathbf{J}_{MAP}(\eta^2)}{(d\eta^2)^2}\right)^{-1}_{\eta^2=\hat{\eta}^2}, \tag{3.49}$$

$\hat{\eta}^2$, *and* $\mathbf{J}_{MAP}(\eta^2)$ *given in equations* (3.33) *and* (3.34), *respectively.*

Proof. : see Appendix D.3 ☐

The second derivative of $\mathbf{J}_{\text{MAP}}(\eta^2)$ arising in equation (3.49) may be evaluated analytically or, more simply, numerically. Such an approximation has the benefit of ease of implementation, since it requires little more than a random generator of Gaussian variables to propagate errors related to regularization to any reconstructed acoustical quantity.

3.6.3 Simulation example

As previously stated, the Bayesian framework being a probabilistic approach, it allows one to compute parameters of the pdf's assigned to the problem unknowns. One particularly attractive is the posterior pdf of the regularization parameter $[\eta^2|\mathbf{p}]$, whose variability can be propagated to any acoustic quantity of interest in order to provide confidence intervals, for instance.

Two possible ways of performing this task were discussed in Sections 3.6.1 and 3.6.2, one by a simple Gaussian approximation of the posterior $[\eta^2|\mathbf{p}]$ and a second by its exact evaluation using MCMC methods. Both procedures are applied here by means of an example selected from the scenario described in Sec. 3.5.1.1. It corresponds to the configuration with the array placed at a distance $z_h = r_s$ from the source surface and with a SNR of 30 dB. A point estimate of the regularization parameter delivered by the Bayesian criterion is shown in Figure 3.29(a) along with its variability (filled gray area) estimated by a MCMC procedure. Figure 3.29(a) also shows, in dashed black lines, the confidence interval obtained by approximating the posterior pdf $[\eta^2|\mathbf{p}]$ to a complex Gaussian distribution. The latter is obtained by numerical evaluation of the second derivative in equation (3.49), which is related to the variance σ^2 of the distribution. We can note that the intervals given by the Gaussian approximation agree well with those computed by MCMC up to approximately 800 Hz. Above those frequencies the approximation of the posterior $[\eta^2|\mathbf{p}]$ by a Gaussian distribution does not hold anymore, illustrating the limits of this approximation. The discontinuities above 1500 Hz are related to oscillations on the condition number of the transfer matrix used in this example (see right panel of Figure 3.15 for $z_h = r_s$), since the regularization criterion alternates between a regularized and non regularized solution.

The reconstructed source field (volume velocity) is computed by equation (3.20), with the Green's function given in equation (3.43). An integration over the source surface at each frequency gives the source spectrum (see Figure 3.29(b)) for the Bayesian regularization criterion (red) and the optimal one (black). The variability of the regularization parameter is then propagated to the reconstructed source field as shown by the filled gray region in Figure 3.29(b). It is interesting to note that the reconstructed volume velocity is much more sensitive to the setting of the regularization parameter at low frequencies. Indeed, a small variation on the regularization parameter at low frequencies leads to higher uncertainties on the reconstructed source spectrum. On the other hand, a large variation on η^2 at higher frequencies had little effect on the reconstructed quantity. This analysis can be further extended to the acoustic power integrated over the source surface, as shown in Figure 3.29(c). We can see that the estimated acoustic power using the Bayesian regularization criterion is fairly close to the optimal (MSE) solution. Moreover, we note narrow confidence intervals on the acoustic power (± 0.5 dB), meaning that small variations on the regularization parameter generates small uncertainties on this quantity. We remark that this result is not to be interpreted as if the regularization was not important to the reconstruction, it actually shows how sensitive is the reconstruction of these acoustic quantities to small variations around the point estimate of the regularization parameter.

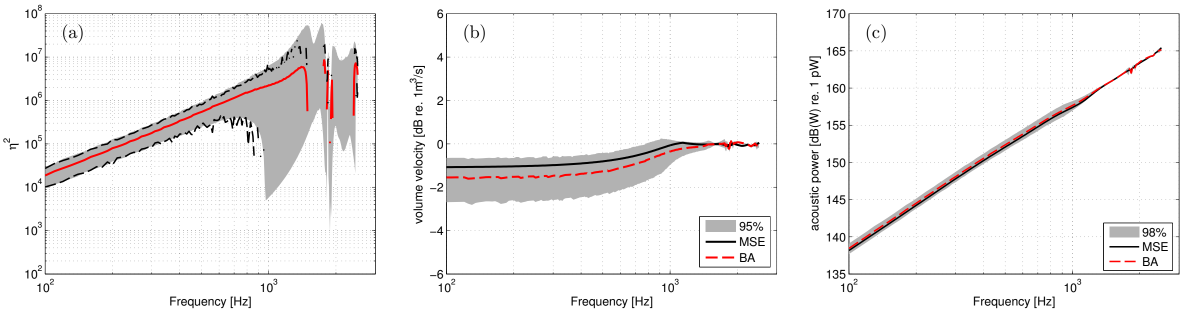

Figure 3.29: (a) Point estimate of the regularization parameter η^2 (red) with confidence intervals estimated by a MCMC procedure (gray region) and by a Gaussian approximation (dashed black lines). (b) The reconstructed source spectrum using the Bayesian regularization criterion (red) with a 95% confidence interval (gray region) and the optimal MSE solution (black). (c) Global acoustic power as integrated over the source surface for the Bayesian regularization criterion (BA) with a 98% confidence interval (gray region) and the optimal (MSE) one.

4

Iterative weighted equivalent source method

A description of interior noise source identification by means of an equivalent source formulation was given in Chapter 2. We have seen how this lead to the minimization of a underdetermined problem and we have also discussed acoustic propagation models which relate the measurements to the unknowns of the problem. Then, in Chapter 3 we provided several mathematical considerations to solve the underlying problem, with emphasis on how to adjust the amount of regularization to be imposed. In this Chapter, we combine these two parts in order to solve for the target application in this thesis (i.e. interior noise source identification). In this context, we were initially faced to two major difficulties: the first one is related to the positioning of the array inside the enclosure and the second one related to the high degree of underdetermination of the problem. In order to overcome these difficulties, an iterative weighted approach is proposed here.

This Chapter is organized as follows. In the first part we describe the formulation of the proposed approach for which two different weighting strategies are discussed. The technique is then applied to a simulation case to demonstrate its improvements as compared to traditional approaches. Later on, we discuss the sensitivity of the approach with regard to the presence of reverberation and the distribution of equivalent sources. Finally, the last part is devoted to the application of a technique that helps us to better comprehend the reconstructed source field.

4.1 General weighting concept

We start this section by recalling that our main goal is to locate and quantify noise sources on the boundaries of an enclosure based on acoustical field measurements within the enclosure. In Chapter 2 we discussed the idea to tackle this problem by the simplified modeling of the interior surfaces by a distribution of monopoles, in such a way that they match the acoustic field measured by a microphone array. A considerable difficulty arises when we must cover a large area (e.g. interior of a bus) with few *a priori* assumptions on the main radiating regions. As discussed in Chapter 1, a well adapted geometry of microphone array to perform this task in a single step[1] is the spherical one, placed somewhere inside the enclosure. The advantages of using a single step are the fast measurement time which allows to test several configurations in a short period of time and, for the case of vehicle noise, the possibility to apply for run-up tests or driving conditions.

The very first question that arises from the above considerations is where should one place the microphone array when few *a priori* information on the position of sources is available. In the case of transportation vehicles, a convenient choice is, for instance, at the driver's or passenger's head position. Depending on this choice, the relative distance between each equivalent source and the microphone array may differ considerably since we are searching potential sources over the whole surrounding surfaces. As a consequence, those equivalent sources which are closer to the microphone array will need less energy to generate the same pressure level (at the array position) as compared to equivalent sources placed farther away. In other words, more "weight" will be given to equivalent sources closer to the microphone array. Indeed, this questioning was the initial motivation for the approach presented hereafter.

In order to take into account the large range of relative distance from equivalent sources to the center of the array we introduce an a priori assumption into the underlying problem. It essentially consists in enforcing that each equivalent source needs equal amount of energy to generate the same pressure field on the microphone array. In terms of the considered problem formulation, it translates into the solution of a modified minimization problem. To that end, let us define a diagonal matrix $\mathbf{W}$ with its i-th diagonal element given by w_i, which is the distance between equivalent source i and the center of the spherical array. Instead of minimizing the norm of the reconstructed source field $\|\mathbf{q}\|^2$, we seek to minimize its weighted version $\|\mathbf{W}\mathbf{q}\|^2$ such that the following minimization problem is written

$$\text{minimize} \quad \left\{\|\mathbf{p}-\mathbf{G}\mathbf{q}\|_2^2+\eta^2\|\mathbf{W}\mathbf{q}\|_2^2\right\}, \tag{4.1}$$

with the square diagonal matrix $\mathbf{W} \in \mathbb{R}^{N\times N}$. The above problem is recognized as the general form of Tikhonov regularization in the literature [Han98,Han10]. If $\mathbf{W}$ is invertible such that $\mathbf{W}\mathbf{W}^{-1}=\mathbf{I}$, which is the case for any diagonal matrix with non-zero diagonal entries, we can modify the above minimization problem by introducing the transformation $\mathbf{q}=\mathbf{W}^{-1}\tilde{\mathbf{q}}$ and thus arrive at the following minimization problem:

$$\text{minimize} \quad \left\{\|\mathbf{p}-\mathbf{G}\mathbf{W}^{-1}\tilde{\mathbf{q}}\|_2^2+\eta^2\|\tilde{\mathbf{q}}\|_2^2\right\}, \tag{4.2}$$

---

[1] For "single step" we refer that the field quantities are measured with the microphone array placed at a single position within the enclosure.

which is promptly recognized as the standard-form of Tikhonov regularization, whose solution can be written as

$$\tilde{\mathbf{q}} = \tilde{\mathbf{G}}^H(\tilde{\mathbf{G}}\tilde{\mathbf{G}}^H + \eta^2\mathbf{I})^{-1}\mathbf{p}, \tag{4.3}$$

where $\tilde{\mathbf{G}}$ is defined as $\tilde{\mathbf{G}} = \mathbf{G}\mathbf{W}^{-1}$. The above solution is also conveniently expressed in terms of the singular value decomposition $\tilde{\mathbf{G}} = \mathbf{U}\lceil\mathbf{S}\rfloor\mathbf{V}^H$, which yields:

$$\tilde{\mathbf{q}} = \mathbf{V}(\mathbf{S}^2 + \eta^2\mathbf{I})^{-1}\mathbf{S}\mathbf{U}^H\mathbf{p}, \tag{4.4}$$

with η estimated by one of the techniques discussed in the previous chapter. The reconstructed source field is then simply given by the back transformation:

$$\hat{\mathbf{q}} = \mathbf{W}^{-1}\tilde{\mathbf{q}}. \tag{4.5}$$

Many choices are possible for the matrix $\mathbf{W}$ depending on our requirements or assumptions regarding the solution $\hat{\mathbf{q}}$. In references [Han98, Han10], Hansen shows how to introduce additional smoothness to the solution by solving the general form of Tikhonov regularization, in which the term $\|\mathbf{W}\mathbf{q}\|_2^2$ is coined as the discrete smoothing norm. In this context, the matrix $\mathbf{W}$ is given by a discrete approximation of a derivative operator. In addition, reference [CS08] discusses how to determine $\mathbf{W}$ from a statistical perspective, in which the term *preconditioner* is used to define the role of $\mathbf{W}$. Furthermore, within the field of acoustics and for sound field reproduction purposes, the general form of Tikhonov regularization has also been applied with the weighting matrix defined by prior beamforming results [GCP+11]. In the following sections we discuss how to implement the weighting matrix in order to take into account for the positioning of the microphone array within the enclosure as well as how to improve the properties of the solution using the same approach implemented in an iterative manner.

4.2 First weighting strategy

The first weighting strategy that we discuss is related to the microphone array positioning inside the enclosure. As we have introduced in the previous section, the choice for the array position may lead to a large range of distances between equivalent sources and the array. This, in turn can induce undesirable features on the solution as we shall see by means of numerical simulations and experiments presented in the next Chapter.

It has been anticipated in the previous section that in order to correct for this effect, one can enforce a priori that equivalent sources need equal energy to generate a given pressure field on the array. This lead to the choice of a matrix $\mathbf{W}$ with diagonal elements given by:

$$\mathbf{W} = \begin{bmatrix} 1/r_1 & 0 & 0 & 0 \\ 0 & 1/r_2 & 0 & 0 \\ 0 & 0 & \ddots & 0 \\ 0 & 0 & 0 & 1/r_N \end{bmatrix}, \tag{4.6}$$

where r_N is the distance between the N-th equivalent source and the center of the array. We remark that since this is a frequency independent matrix, the same weighting is applied to solve for each frequency line. The application of the above weighting is hereafter illustrated by means of a numerical simulation example.

The simulated environment is defined by a rectangular enclosure with dimensions $Lx = 4$ m, $Ly = 2.4$ m and $Lz = 2$ m, chosen in order to match the dimensions of a real room used for the experimental validation. The image source method (ISM) [AB79] is used to simulate the acoustic pressure field on the surface of a rigid sphere due to a point source, the latter being placed at one of the room surfaces. The monopole source with unitary volume velocity is positioned at coordinates $x = 1.2$ m, $y = 0$ m and $z = 0.5$ m and the spherical array at two different positions: (a) one relatively far from all surfaces at $x = 0.7$ m, $y = 1.2$ m and $z = 1.1$ m and (b) relatively close to one surface at $x = 0.3$ m, $y = 1.2$ m and $z = 1.1$ m. Only the floor of the enclosure is considered as a reflective surface (reflection coefficient $\beta_c = 0.9$), other surfaces are assumed to be fully absorbents with $\beta_c = 0$. In addition, only the reflections up to order 2 are taken into account in the image source model. We remark that the image source method is merely used to simulate the acoustic pressure on the spherical array, the acoustic propagation used for the reconstruction being of free-field type. The equivalent sources are regularly distributed along the enclosure's surfaces with inter-source spacing of 0.1 m and a rigid spherical microphone array with 31 microphones and radius $a = 0.145$ m is used to sample the acoustic field. Finally, white Gaussian noise is added to the simulated acoustic pressure with a signal-to-noise ratio (SNR) of 25 dB.

The inverse method is firstly solved for the case without weighting and the reconstructed volume velocity of equivalent sources is shown in Figure 4.1, for the microphone array distant 0.65 m (left panel) and 0.35 m (right panel) from the nearest wall. It can be seen that in both cases the method identifies "ghost sources" on the surface close to the array (plane $x = 0$ in the figure). Although they are not quantitatively significant for the first position of the array, for the second case they have similar level in comparison to the main source. One can also see that besides the identification of the original source, the method yet identifies the first reflection which takes place on the reflective ground. This effect is discussed with more detail in the next sections.

The positioning of a somewhat rigid sphere at the vicinity of a reflective surface could

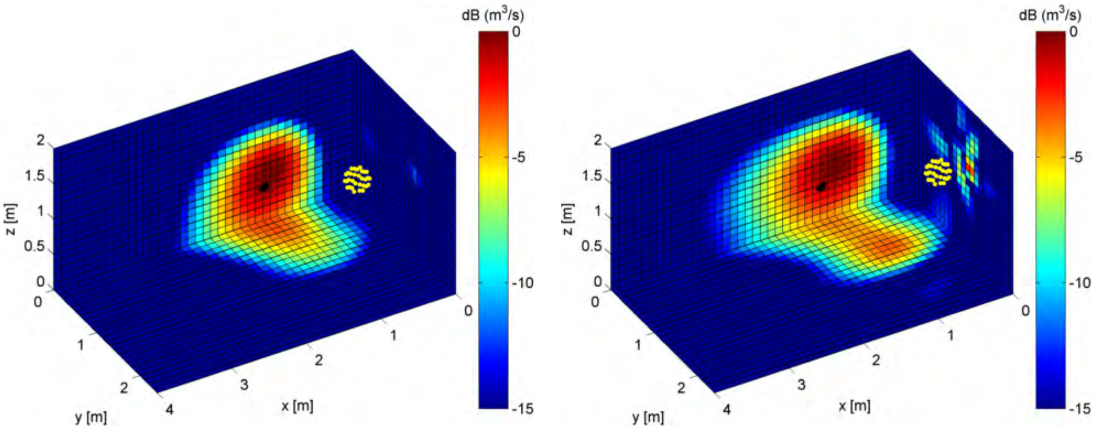

Figure 4.1: Volume velocity maps for the 1000 Hz one-third octave band. The images show 3 surfaces of the enclosure along with the spherical microphone array. Left: spherical array placed at 0.65 m from the closest boundary (plane $x = 0$). Right: spherical array at 0.35 m from the closest boundary.

certainly produce an additional effect. The acoustical waves scattered by the rigid sphere may be reflected by the neighbor boundary and, in turn, be considered as additional incoming waves on the sphere. This is not the case for this simulation example as the neighbor boundary is assumed to be non reflective. The effect of a nearby boundary on the acoustic field is in fact discussed in reference [GD01], in which the concept of an image sphere is used to model the reflection of waves scattered by the sphere. It was shown that the this is a secondary effect as compared to the influence of the reflected waves related to the original acoustic source. In addition, it was shown that the above effect is negligible when the sphere is several radii distant from the nearest boundary.

The same problem is now solved by the approach presented in the previous section and the weighting matrix given by Equation (4.6). The volume velocity maps for this case are shown in Figure 4.2. It can be seen that the undesirable effects on the nearby boundary are eliminated at the expense of a slightly reduction in resolution. For the case in which the array is at 0.65 m from the closest boundary (left hand side), there is almost no difference between the two approaches. Indeed, we can expect that when the distances between equivalent sources and the array are not significantly different, the proposed approach will have a minor effect.

Finally, we also analyze the behavior of the proposed approach when there is actually a real source on the closest boundary. We proceed with the same simulation set-up as above but with an extra source with unitary volume velocity placed at $x = 0$ m, $y = 1.7$ m and $z = 1.3$ m. Figure 4.3 shows the results for the two considered approaches. It can be seen that for the classic approach more importance is given to the source on the closest surface, whereas the weighted approach identifies both sources with more weight assigned to the source which is more distant to the array, yet at the expense of a reduction in

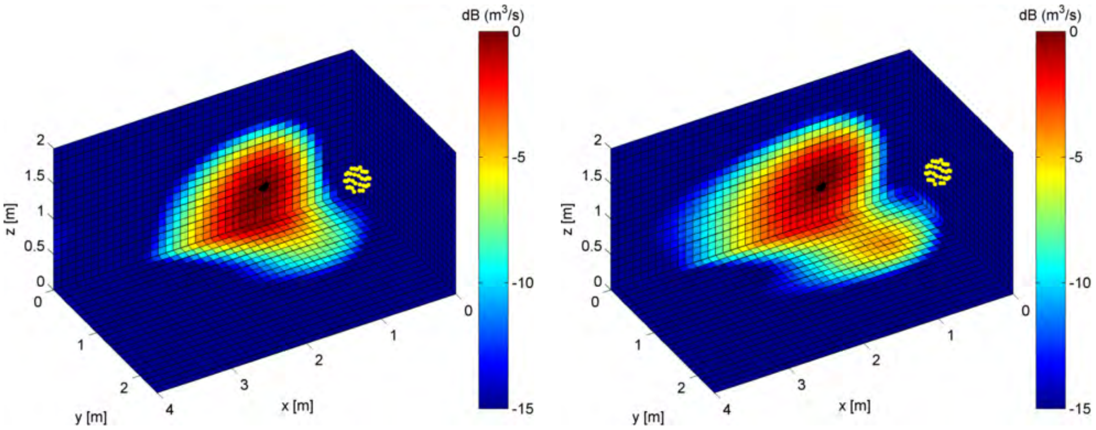

Figure 4.2: Volume velocity maps for the 1000 Hz one-third octave band using the weighted equivalent source method. Left: spherical array placed at 0.65 m from the closest boundary (plane $x = 0$). Right: spherical array at 0.35 m from the closest boundary.

resolution.

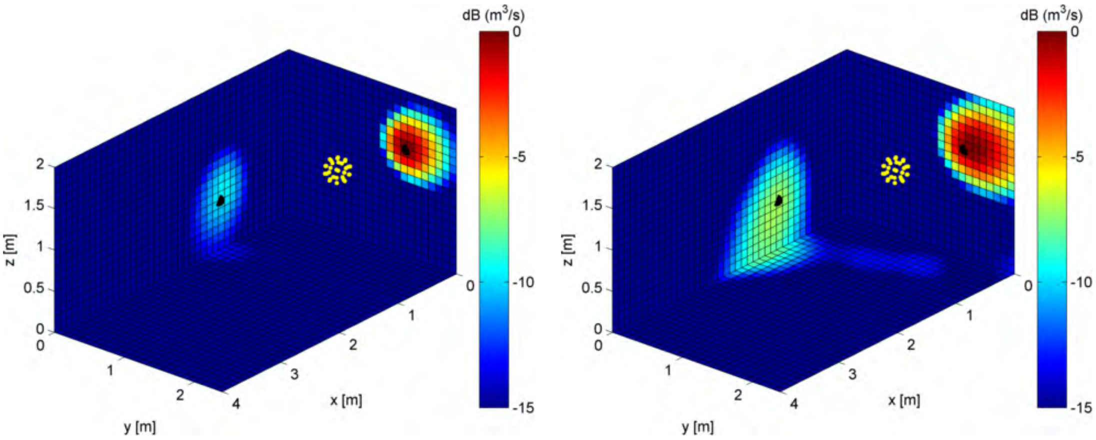

Figure 4.3: Volume velocity maps for the 1000 Hz one-third octave band for the case with two simulated sources. Left: classical approach. Right: weighted approach.

4.3 Second weighting strategy - iterative solution

In this section we discuss a second weighting strategy which by conception needs to be implemented in an iterative manner. The idea is to use the reconstructed source field, as given in Equation (4.5), as *a priori* information to solve for a new minimization problem in the form of Equation (4.1). The weighting matrix for this case reads

$$\mathbf{W}(f) = \begin{bmatrix} 1/\hat{q}_1(f) & 0 & 0 & 0 \\ 0 & 1/\hat{q}_2(f) & 0 & 0 \\ 0 & 0 & \ddots & 0 \\ 0 & 0 & 0 & 1/\hat{q}_N(f) \end{bmatrix}, \tag{4.7}$$

where $\hat{q}_N(f)$ (the N-th element of the vector $|\hat{\mathbf{q}}|$, where $|\mathbf{a}|$ stands for the absolute value of vector $\mathbf{a}$) is the volume velocity corresponding to the N-th equivalent source at the discrete frequency f. Notice that we have dropped the dependence on the regularization parameter η by assuming that the vector $\hat{\mathbf{q}}$ is given by the optimal choice of η, as returned by the techniques discussed in Chapter 3. At this point we emphasize the critical dependence on a robust setting of η, in the sense that, by no means the proposed approach will return a reasonable result if the parameter selection method fails in a previous step. In addition, we notice that contrary to the first weighting strategy, this one depends on the frequency, thus a different weighting matrix is computed at each frequency line.

The idea is thus to apply this weighting iteratively up to a given number of iterations or until some convergence criterion is met. As we shall see, the number of required iterations depends on the degree of under determination of the problem as well as on the frequency of analysis. Furthermore, if only the localization of sources is needed, few iterations may suffice to obtain reasonable spatial resolution. On the other hand, if precise quantification results are also required, the number of necessary iterations is usually higher. As we shall see, a conceivable way to adjust the number of iterations is to evaluate the energy of the reconstructed source field at each iteration and stop the process when the difference between consecutive iterations is less than a specified threshold. The proposed algorithm summarizes to:

Algorithm 1:

```
1. define the initial weighting matrix $\mathbf{W}_0$ as given in equation (4.6).
2. solve the weighted system in equations (4.4) and (4.5), with
   $\eta$ estimated by one of the techniques discussed in Section 3.4,
   output → $\hat{\mathbf{q}}_0$.
3. for $i = 1, 2, ..., l$
4. redefine the weighting matrix as: $\mathbf{W}_i = \mathrm{diag}\left\{|\hat{\mathbf{q}}_{i-1}|^{-1}\right\}$ then $\mathbf{W} = \mathbf{W}_0\mathbf{W}_i$
5. solve for equations (4.4) and (4.5),
   output → $\hat{\mathbf{q}}_i$
6. evaluate $T = \|\hat{\mathbf{q}}_{i-1}\| - \|\hat{\mathbf{q}}_i\|$
7. if $T \leq \tau$, stop the iteration process.
8. end
```

The maximum number of iterations is defined by the parameter l and τ is a threshold adjusted by the user. In most experimental and numerical situations it has been observed that the initial iterations are marked by a significant difference on the energy of the reconstructed source field for consecutive iteration steps. Conversely, as the iterative method approaches convergence the difference is considerably smaller. Based on the numerical simulations, a reasonable choice of τ could be approximately 1 or 0.5 dB. Finally, we shall see in the next sections, that this approach considerably improves the localization and quantification abilities of the reconstructed source field, however, at the expense of a higher computational cost.

4.4 Application to a simple numerical case

Given the theoretical explanation of the proposed approach we provide in this section an application to a simple numerical case. The main goal is to evaluate the localization and quantification aspect of the method. The localization is defined here as the ability to spatially locate the noise sources radiating acoustic power over the environment. The quantification aspect is defined as the ability to quantify, normally in terms of acoustic power, the noise sources located beforehand. The quantification is mainly useful for source ranking purposes, in which the identified sources are ranked in terms of their contribution to the observed acoustic field. In turn, this is useful for design purposes, where the knowledge of source characteristics is important to provide to the engineer the possibility of appropriate design changes.

4.4.1 Simulation parameters

The simulated environment is a rectangular enclosure with dimensions $5\times3.4\times2.2$ m^3. The acoustic field is sampled by a rigid spherical array with 31 microphones at a fixed position within the enclosure. The equivalent sources are distributed along the room boundaries with a constant inter-source spacing of 0.2 m. In a first configuration, reflections on the boundaries are not considered for the simulation of the "measured" acoustic pressure. The acoustic propagation model is thus given by Equation (2.49), which relates the source strength of a monopole to the acoustic pressure on the surface of a rigid sphere. The simulated acoustic pressure is then perturbed with multiplicative and additive Gaussian noise with SNR of 40 dB. In the next sections we evaluate the performance of the iterative weighted approach in terms of source localization and quantification.

4.4.2 Localization ability

In a first configuration two point sources with volume velocity equal to 0.01 m^3/s are placed at the room boundaries with coordinates defined by $\mathbf{r}_1 = [1.8, 3.4, 1.6]$ m and $\mathbf{r}_2 = [3.2, 3.4, 1.3]$ m, as shown by black dots in Figure 4.4. The spherical array is placed within the enclosure at coordinates $\mathbf{r}_a = [2.3, 1.4, 1]$ m. Thus the corresponding distances from the center of the array are respectively $\|\mathbf{r}_1 - \mathbf{r}_a\| = 2.1$ m and $\|\mathbf{r}_2 - \mathbf{r}_a\| = 2.2$ m. The distance between the sources is $\|\mathbf{r}_1 - \mathbf{r}_a\| = 1.4$ m. The equivalent sources are uniformly distributed over the enclosure's boundaries with an inter-source spacing of 0.2 m, leading to a total number of degrees of freedom (DOF) of 1745 in this case.

A common measure of the localization ability of noise source identification techniques is the spatial resolution. It is defined as the minimum distance between two sources from which they can be still separated (i.e. without merging into a single source). A deep analysis of the spatial resolution is not straightforward, especially because it normally depends on several parameters, namely: (a) frequency of interest; (b) array configuration (e.g. array size, number and inter-microphone spacing); (c) distance between the array and the reconstruction surface; (d) level of measurement noise. Our main interest in this section is to show how the spatial resolution of the reconstructed source field may be considerably improved using the iterative weighted approach. The acoustic pressure on the spherical array is simulated by the forward propagation model described in Equation (2.3) with propagation matrix given by Equation (2.49). The measurement noise is given by multiplicative and additive perturbations expressed in Equation (3.47) with a SNR of 40 dB. The inverse problem is then solved by Equation (4.5) and using the discussed weighting strategies.

The results for the frequency of 800 Hz are shown in Figure 4.4. The images represent the volume velocity of equivalent sources mapped onto the enclosure's boundaries along with the real source coordinates and the spherical microphone array. It can be seen that for the classical solution, Figure 4.4(a), the spatial resolution is not good enough to separate the contribution of the two sources. The results given by the proposed approach with weighting matrix defined in Equation (4.7) are shown in Figures 4.4(b) and 4.4(c) for the first and second iterations. As can be seen, the spatial resolution is successively improved and with the second iteration both sources are spatially separated. Indeed, the weighting procedure acts as a focusing on those regions more likely to radiate noise which leads to an enhanced resolution. Similar results (not shown here) were obtained for other discrete frequencies.

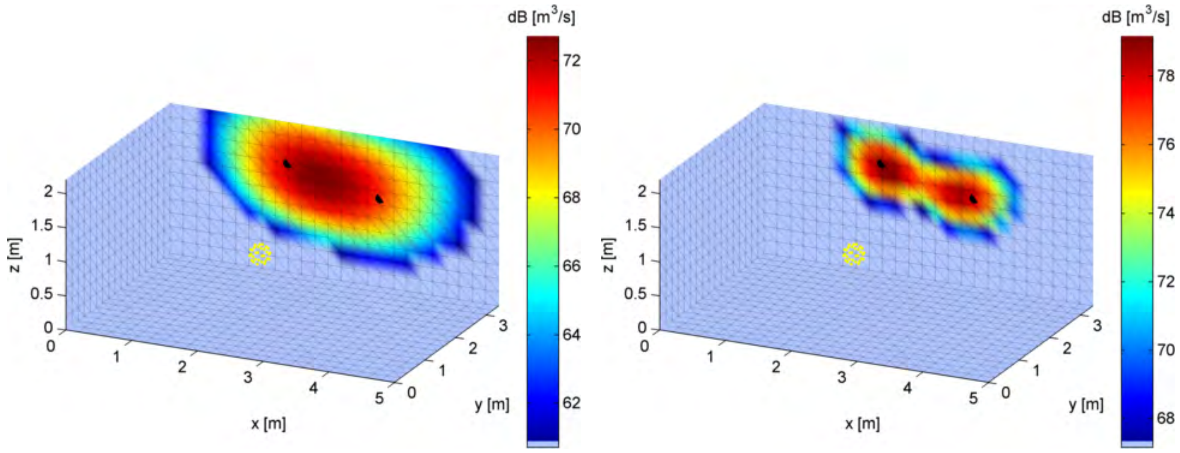

(a) Basic solution (b) 1st iteration

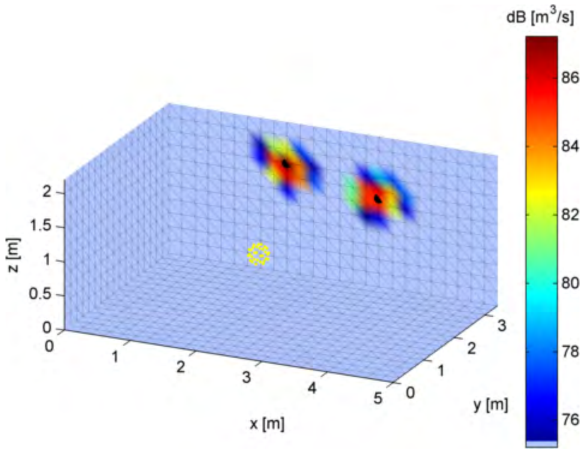

(c) 2nd iteration

Figure 4.4: Volume velocity maps in dB (m^3/s) for the frequency of 800 Hz using the proposed iterative weighted approach. The dynamic range is set to 12 dB.

4.4.3 Quantification ability

In this section we study the ability of the method to properly quantify the acoustic power of sources located beforehand. For the sake of simplicity, a case with only one source is considered first. The simulated point source with volume velocity equal to 0.01 m^3/s is placed at coordinates $\mathbf{r}_s = [3.5, 3.4, 1.3]$ m as shown in Figure 4.5. The inverse problem is solved as in the previous section and the volume velocity maps for the frequency band of 200-800 Hz are shown in Figure 4.5. It can be seen that the source is correctly located on its original position. The acoustic power of each equivalent source is then computed by using Equation (2.27). Given the acoustic power of equivalent sources, the power corresponding to the "original" source is obtained by integration of acoustic power maps over the position of the real source. The identified acoustic power is shown in Figure 4.6. First of all, we can notice a severe underestimation of the acoustic power for the classic solution (represented by “iter 1” in the figure). In the next section we discuss the reasons for this severe underestimaton, which as we shall see, has to do with the properties of the identified sources (namely their directivity). We can also observe that only after several iterations (6 in this case) the identified acoustic power converges to the simulated one, with a good agreement over the considered frequency band.

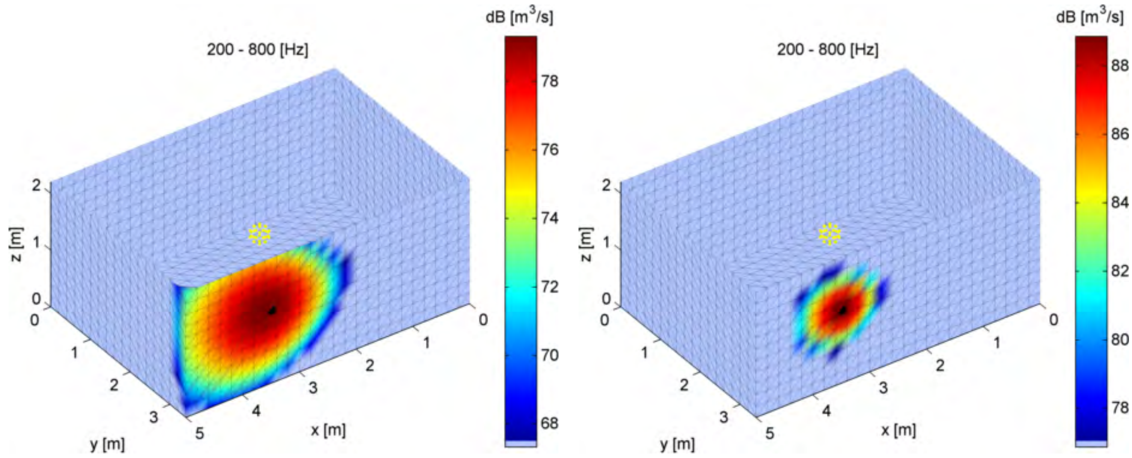

(a) Basic solution (b) 1^{st} iteration

Figure 4.5: Volume velocity maps in dB (m^3/s) for the 200-800 Hz frequency band using the proposed method for: (a) basic solution; (b) first iteration. The dynamic range is set to 12 dB.

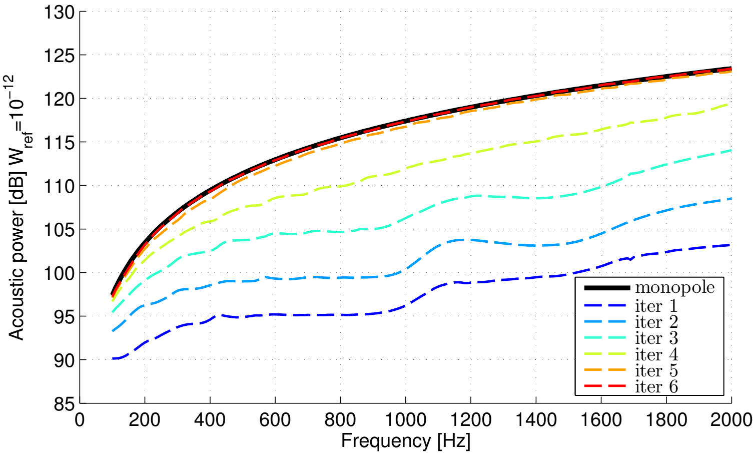

Figure 4.6: Identified acoustic power as a function of the frequency for consecutively iteration steps. The true acoustic power of simulated source is shown by the continuous black line.

4.4.4 Radiated acoustic pressure

The computation of the acoustic pressure radiated by the identified equivalent source distribution is a useful tool which allows one to gain more insight into their radiation properties. In the studied case, it allows us to explain the strong underestimation of acoustic power observed in the previous section. By way of an example, the acoustic pressure radiated by the source distribution identified in the previous section is shown in Figure 4.7 for the 200-800 Hz frequency band. The result for the initial solution, Figure 4.7(a), readily indicates that identified sources are highly directive on the direction of the microphone array, as if they concentrate all the radiated energy on this specific direction. This conclusion has been reached by observing the high levels of acoustic pressure on the boundary (y=0) which is facing the wall on which the "real" source is placed. Indeed, it is the relative phase of equivalent sources that enforces the radiation on a specific direction (in this case, vector pointing from the source to the microphone array) acting similarly to a piston. This effect is more pronounced as the frequency increases, which can be noticed in Figure 4.6 by the greater underestimation at higher frequencies. The explanation for the underestimation results from the fact that a highly directive source needs less acoustic power to generate the same pressure level (on the direction of its radiation axis) as compared to a omni-directional source.

The effect of the iterative weighted approach is such that it gradually attenuates this directive-like behavior until finally obtain a equivalent source distribution that better represents the physical source. This is illustrated in Figure 4.7(b) which shows the radiated acoustic pressure for the fifth iteration. We notice that in this case the radiation is more uniform. One can expect similar behavior in practice as long as real physical sources may be approximated as radiating like a point source.

The conclusions drawn from this analysis are: (1) The highly underdetermined aspect of the problem leads to (when minimized using the l_2-norm criterion) acceptable solution in a qualitative aspect but non-physical on a quantitative point of view. (2) The proposed iterative weighted approach allows to correct for this problem at the expense of a slightly higher computational cost; (3) The proposed approach provides not only better quantitative results but also better spatial resolution.

4.5 Sensitivity analysis

4.5.1 Influence of enclosure's boundaries

In practical applications, the conditions of pure free-field propagation are rarely respected, mainly due to the reflection of waves on the enclosure's boundaries. It is thus important to analyze the sensitivity of the method to modeling mismatches. In the proposed formu-

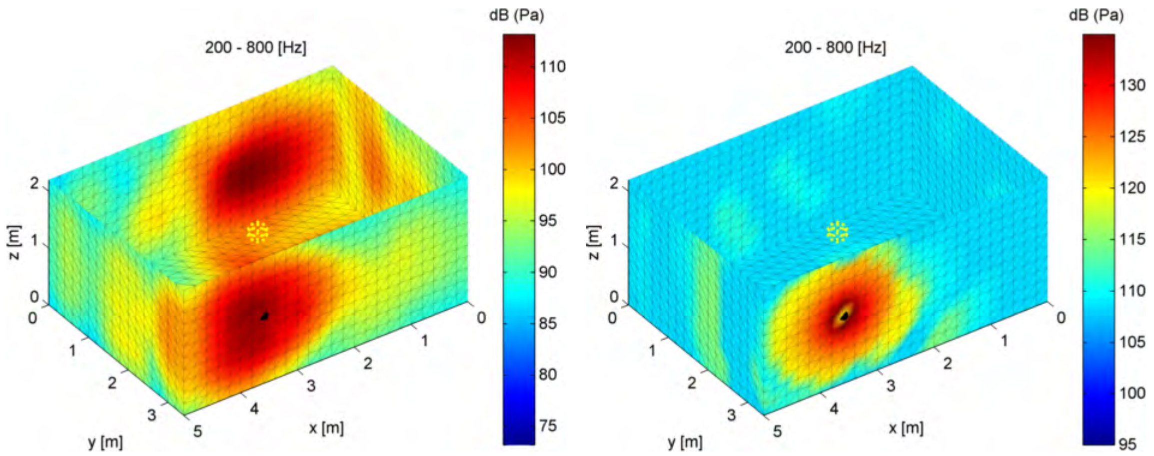

(a) Basic solution (b) 5th iteration

Figure 4.7: Acoustic pressure radiated by the identified source distribution over the frequency band 200-800 Hz. The figures show all the enclosure's boundaries except the roof, along with the real source position (black dot) and microphone coordinates (yellow dots). The dynamic range in both cases is 40 dB.

lation, the radiation of equivalent sources is assumed to be in free-field conditions or in the case of a rigid sphere the scattered waves are also taken into account.

A simulation example is used to analyze the sensibility of the method to the reflection of waves on the enclosure's boundaries. The image source method described by Allen and Berkley [AB79] is used to simulate the acoustic pressure on the microphone array by modeling the reflections on the enclosure's boundaries as image sources. An adaptation in the model is done in order to take into account the effect of the rigid sphere. The behavior of each boundary is represented by a reflection coefficient β_c, which is related to the absorption coefficient α_c by the relation:

$$\alpha_c = 1 - \beta_c^2. \tag{4.8}$$

The same enclosure's dimensions used in Section 4.4.1 are considered here, however with the following reflection coefficients associated to the enclosure's walls: (a) $\beta = 0.9$ for the surfaces $x = 0$ and $x = Lx$; (b) $\beta = 0$ for other surfaces. Only the reflections up to order 2 are taken into account into the simulation. The spacing between equivalent sources is set to 0.10 m, which leads to a number of DOF approximately equal to 7000. The position of real sources and microphone array are also kept unchanged from those in Section 4.4.2.

The free-field model in Equation (2.49) is used for the backpropagation problem and the results for the frequency of 800 Hz are shown in Figure 4.8. The figure shows the volume velocity maps in dB's for the first 3 iterations. We can see that the method localizes the original sources as well as their reflections on the side boundaries. Similarly to the case with no reflections, the iterative approach allows to separate the two sources by increasing the spatial resolution. In the case in which few a priori information on the position of real sources is available, it might be difficult to interpret these results in the sense that reflections could be viewed as additional sources. As we shall see in the next section, the causality analysis of identified sources can help the user to reach more precise conclusions. By means of this example, we have seen that in the presence of reverberation the method yet identifies the original sources (at the expense of identifying the reflections) and the iterative approach still increases the spatial resolution.

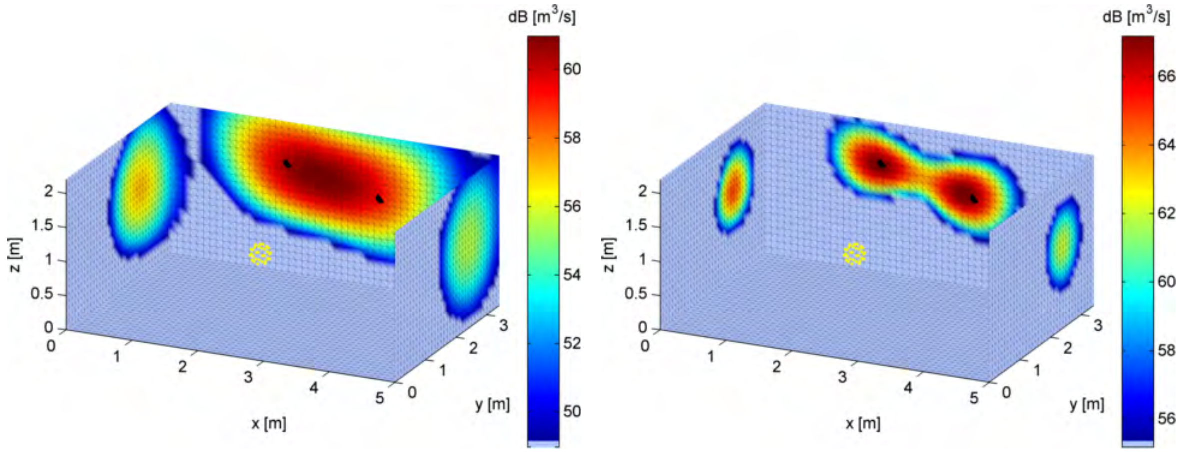

(a) Basic solution (b) 1st iteration

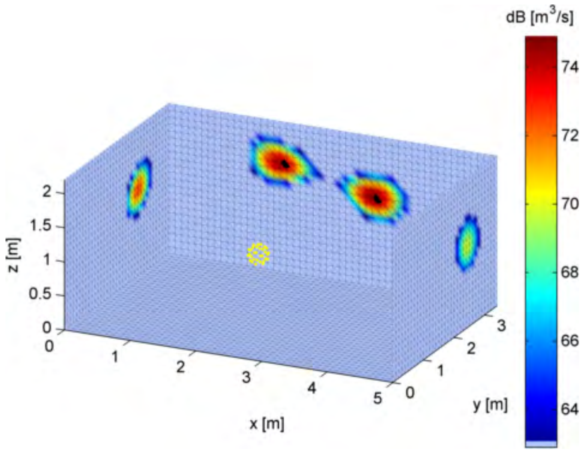

(c) 2nd iteration

Figure 4.8: Volume velocity maps in dB (m^3/s) for the frequency of 800 Hz. The dynamic range is set to 12 dB. These results are for the model considering reverberation.

In the following, we analyze the influence of the reverberation on the ability to quantify the identified sources. The same geometrical parameters and source position from section 4.4.3 are used, however with a reflection coefficient of $\beta = 0.9$ associated to the surfaces $x = 0$ and $x = Lx$. Only the first order reflections are taken into account. The identified acoustic power is shown in Figure 4.9 for the first 8 iterations. This results may be compared to those presented in Figure 4.6. It can be seen that the estimate of the acoustic power for the 8th iteration are in relatively good agreement with the simulated acoustic power. We also notice, however, the presence of dips at some discrete frequencies. Furthermore, it has been checked that the frequency interval between consecutive dips matches very well the frequency in which the wavelength is equal to the difference of distances $\|\mathbf{r}_s - \mathbf{r}_a\| - \|\mathbf{r}_i - \mathbf{r}_a\|$, where $\mathbf{r}_s$ are the Cartesian coordinates of the source, $\mathbf{r}_i$ the coordinates of the image source and $\mathbf{r}_a$ the coordinates of the array center. The presence of the dips can thus be explained by wave interferences between the original source and its reflections on the array position.

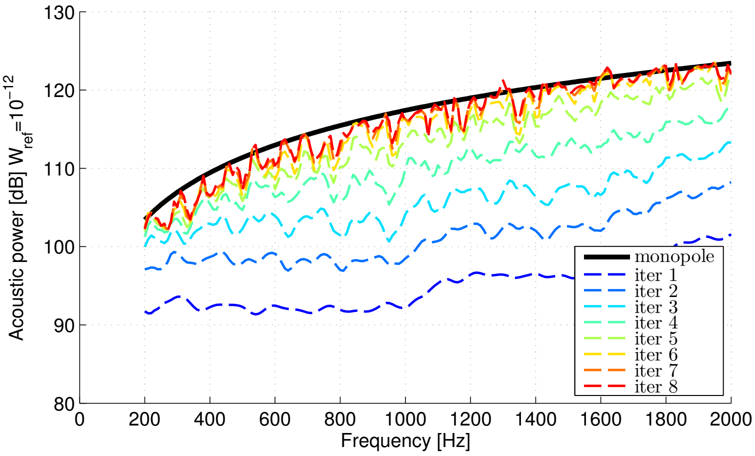

Figure 4.9: Identified acoustic power as a function of the frequency for consecutively iteration steps. The true acoustic power of simulated source is shown in black. These results correspond to the model including reflections on the enclosure's boundaries.

As a conclusion from this analysis, we have seen that both the localization and quantification aspects of the method are affected by the presence of reverberation in the enclosure. The main difficulty generated by the reflections of acoustic waves is that the reflections are also considered as incoming waves on the measurement array, and consequently the method "sees" these waves as additional sources. Indeed, it is this difficult that limits the application of separation methods (discussed in Chapter 1) which are based on the separation of incoming and outgoing waves. In section 4.6 we discuss a technique to analyze the relationship between identified sources in order to distinguish between sources and reflections. Finally, for a mildly reverberant scenario, one can expect that the proposed approach is yet able to provide fairly acceptable results.

4.5.2 Influence of equivalent sources distribution

In this section we study the sensitivity of the iterative weighted ESM with respect to the heterogeneity of the equivalent sources distribution. For that purpose the same rectangular enclosure with dimensions 5 × 3.4 × 2.2 m^3 is used for the numerical simulations. Two point sources with unitary volume velocity are placed on the boundaries as shown in Figure 4.10. A rigid spherical microphone array is used to sample the acoustic field with 31 microphones. The equivalent sources are distributed according to: (a) a uniform distribution with a regular inter-source spacing of 0.2 m and (b) similar distribution but with a local refinement (inter-source spacing 0.05 m) around one of the sources.

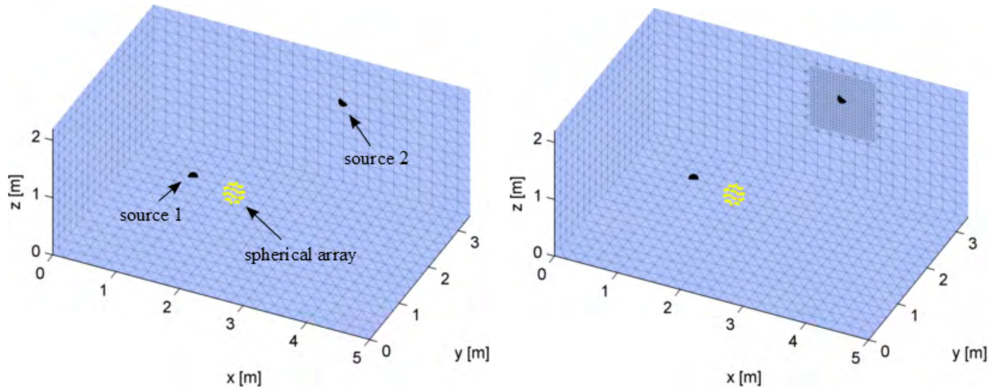

(a) Uniform inter-source spacing (b) Locally refined

Figure 4.10: Models used to study the influence of the homogeneity of equivalent sources distribution. (a) model with a uniform inter-source spacing of 0.2 m; (b) Model with a local refinement (inter-source spacing 0.05 m) around source 2.

Additive white Gaussian noise is added to the simulated acoustic pressure with SNR of 60 dB. The inverse problem is solved by the iterative weighted approach and the regularization parameter adjusted by the Bayesian criterion in equation (3.33). The reconstructed volume velocity is shown in Figure 4.11 for: (a) the model with regular distribution; (b) the model with a local refinement. As can be seen, the presence of the two sources is only detected for the model with a regular spacing of equivalent sources. In fact, as we shall see, volume velocity maps for irregularly spaced equivalent sources are not appropriated for localization purposes. This is because the dynamic range in volume velocity (m^3/s) is strongly dependent on the inter-spacing between equivalent sources. As an example, we show in Figure 4.12 the volume velocity map for the non-uniform model in which the dynamic range was adjusted to 30 dB. In this case we can notice the presence of the second source.

A more relevant representation, however, should consider the different range of inter-source spacing, for instance, by mapping the acoustic power of equivalent sources per unit of surface, as shown in Figure 4.13. Nevertheless, these results show that in fact, the classic approach identifies the source on the refined region as the most energetic one. On the other hand, the iterative approach is able to correct this effect from the first iteration, as can be seen in Figure 4.13(b). This results illustrate another advantage of the iterative

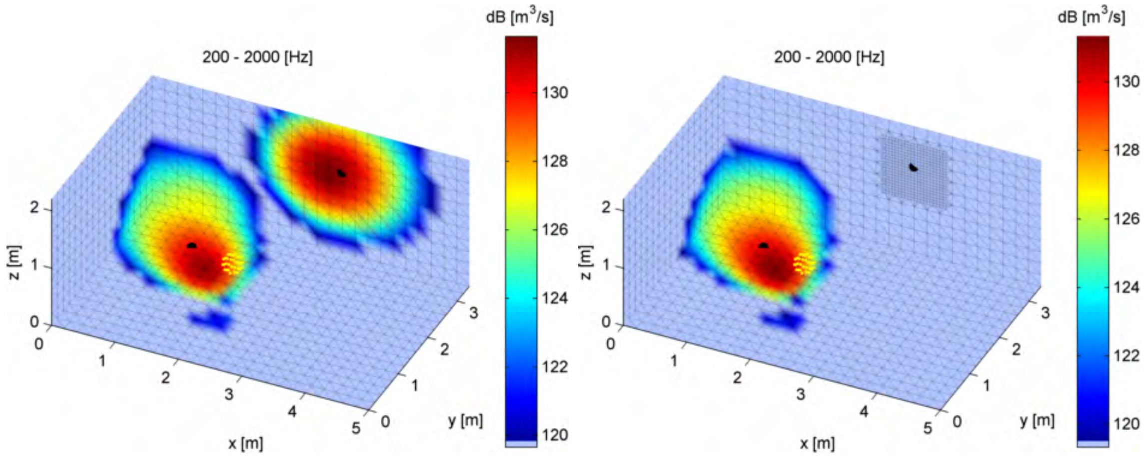

(a) (b)

Figure 4.11: Volume velocity maps integrated over the 200-2000 Hz frequency band without iteration. (a) uniform grid spacing; (b) local refinement around source 2. The dynamic range is set to 12 dB.

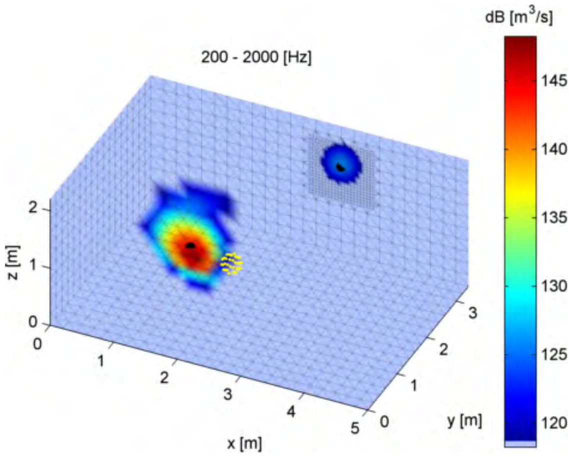

Figure 4.12: Volume velocity map integrated over the 200-2000 Hz frequency band using the iterative weighted approach. The results are for the model with local refinement and the second iteration. Notice that the dynamic range is set to 30 dB.

approach, that is the ability to correct for a non uniform equivalent sources distribution.

Given the analysis of the localization aspect, we hereafter study the influence on the quantification ability. The acoustic power of each source is obtained by carefully choosing an integration area around each source. The integration is carried out for each frequency and the results are shown in Figure 4.14, for the model with a uniform distribution. It can be seen that after 6 iterations the identified acoustic power converges to the simulated one for both sources. The results for the model with local refinement are shown in Figure 4.15. Notice that only the results for the second source (which is located on the refined region) are shown, since there is no significant difference for the first source as compared

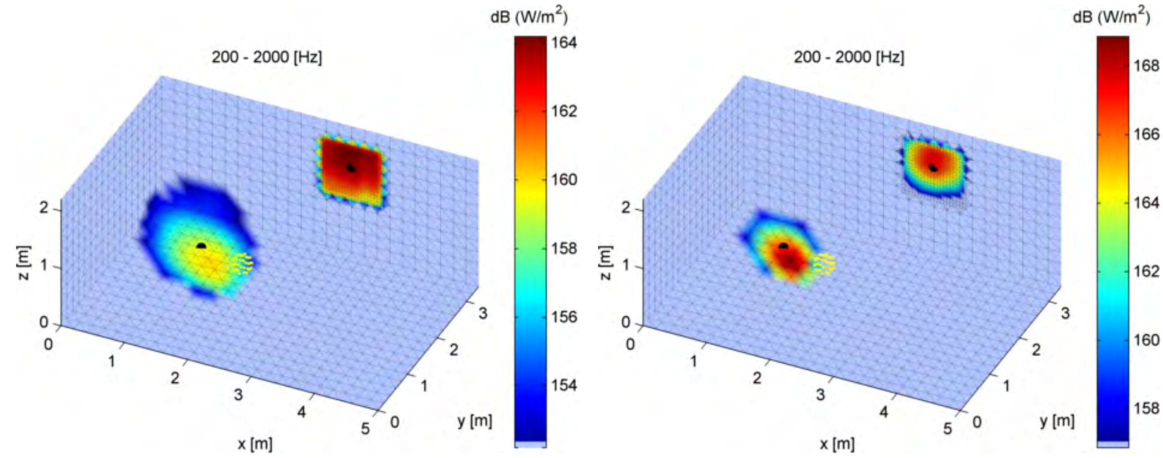

(a) classic solution (b) 1$^{\text{st}}$ iteration

Figure 4.13: Acoustic power maps per unit of surface for: (a) classic approach; (b) first iteration. The dynamic range is set to 12 dB.

to the uniform case. One can observe that the results also converge to the simulated acoustic power, however with the requirement of a higher number of iterations (8 in this particular case).

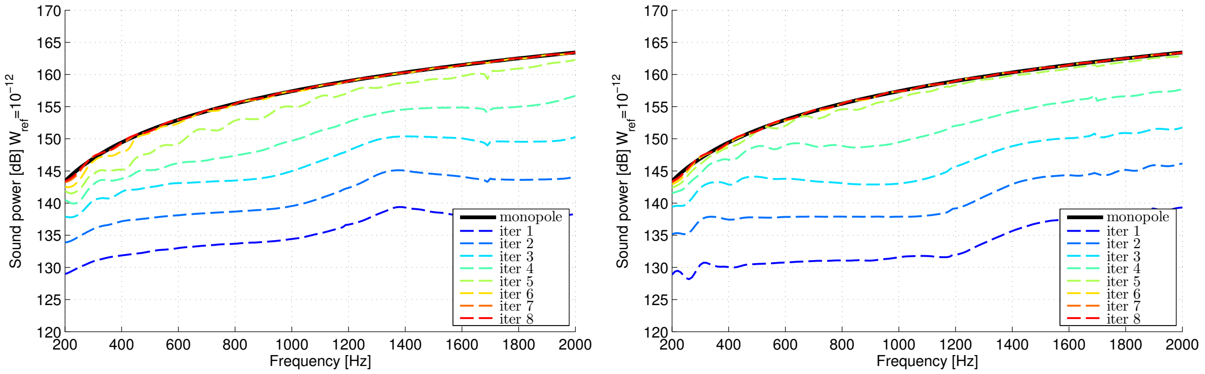

(a) source 1 (b) source 2

Figure 4.14: Identified acoustic power as a function of the frequency for the first 8 iterations (model with uniform grid spacing). The curve in black is the simulated acoustic power.

Finally, in order to emphasize the importance of the term of induced acoustic power due to neighbor equivalent sources (see equation (2.27)) we plot in Figure 4.16 the acoustic power due only to the individual equivalent sources (first term on the right hand side of equation (2.27)). This result is to be compared to the "total" identified acoustic power in Figure 4.15. It can be seen that, if the term of acoustic power induced by neighbors sources is not taken into account, the simulated acoustic power is strongly underestimated. One can expect that this term is progressively more important as more dense is the equivalent

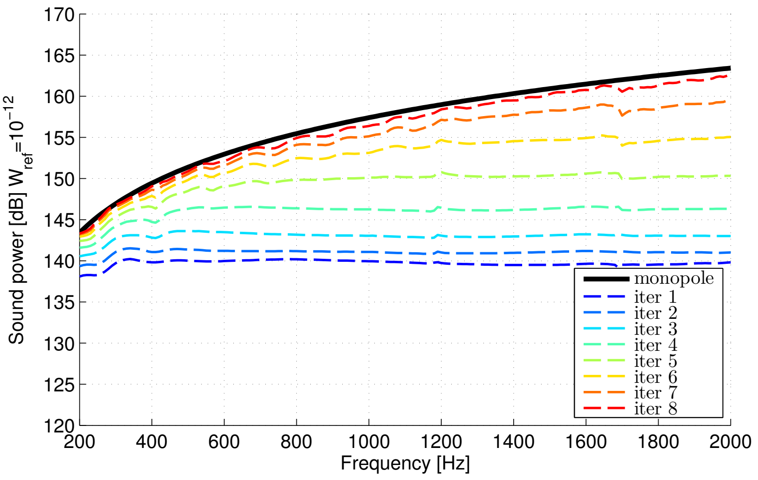

Figure 4.15: Identified acoustic power as a function of the frequency for the model with a local refinement area. The results are for the source 2, which is located on the refined region.

source distribution.

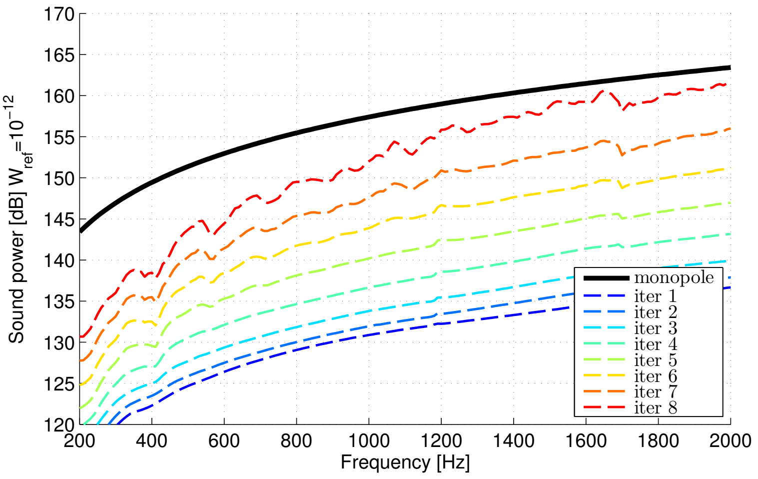

Figure 4.16: Acoustic power due only to the individual power of equivalent sources (i.e. first term on the right hand side of equation (2.27)) for the model with a local refinement. The results are for the source 2.

As a conclusion of this analysis, we have seen that whenever the distribution of equivalent sources is not uniform (i.e. not evenly spaced grid) one should resort to acoustic power maps per unit of surface, for noise source localization purposes. This is required in order to avoid misinterpretation related to the different dynamic range of identified sources. We have also seen that the classic approach tends to favor those regions where the inter-source spacing is more dense and that the iterative weighted approach allows to correct this effect. In addition, the use of more compact equivalent sources distribution, normally require a greater number of iterations to converge to the "true" acoustic power.

4.6 Application of the causality analysis

As we have seen in previous sections, the presence of reverberation leads to the identification of reflections along with the original sources. This in turn makes it difficult to interpret the results and draw up consistent conclusions. The major difficult in dealing with wave reflections is that they are usually correlated to the original sources and thus their contributions cannot be separated by signal processing techniques such as the Principal Spectral Analysis (PSA). Thus, it is of great relevance for troubleshooting purposes, to identify which is the original source of noise. A practical way to answer this question would be to mask each identified “hot spot” region at a time and evaluate the impact on other hot spots. If a reflection is masked one can expect no influence on the original sources. On the other hand, if a real source is masked, we should notice differences in both original source and reflections energy.

Another possible way to perform this task was discussed in section 2.7. The main idea is to evaluate the causality relationship between the identified hot spots in order to find those which correspond to reflections. A simulation example using the same enclosure of previous sections is used. Two correlated sources are placed on different walls of the enclosure (as shown in Figure 4.17). The floor of the room is considered fully rigid ($\beta_c = 1$) and other surfaces are assumed to be absorbent. The acoustic pressure is measured with a spherical array consisting of 31 microphones and radius $a = 0.145$m. The reconstructed volume velocity of equivalent sources is shown in Figure 4.17 for the 1$^{\text{st}}$ iteration and frequency band 100 to 3000 Hz. As we can see, the method locates the real sources (marked as black dots) as well as their reflections on the floor.

The frequency response function (FRF) between the identified hot spots are computed as given by equation (2.63) and the causality relationship of each are evaluated by means of the Hilbert transform. We firstly analyze the causality relation between hot spots labeled 1 and 3 (see Figure 4.17). The results are shown in Figure 4.18 for $H_{13}(f)$ and $H_{31}(f)$. It can be seen that the frequency response $H_{13}(f)$ satisfies the causality relationship for the whole considered frequency band leading to the conclusion that the hot spot 1 is indeed a source and 3 its reflection. The same is also observed for the relation between hot spots 2 and 4, as shown in Figure 4.19. Finally, we also verify the causality relation between hot spots 1 and 2, and the results are shown in Figure 4.20. In this case, no conclusion can be made from this analysis since 1 and 2 are actually two correlated sources.

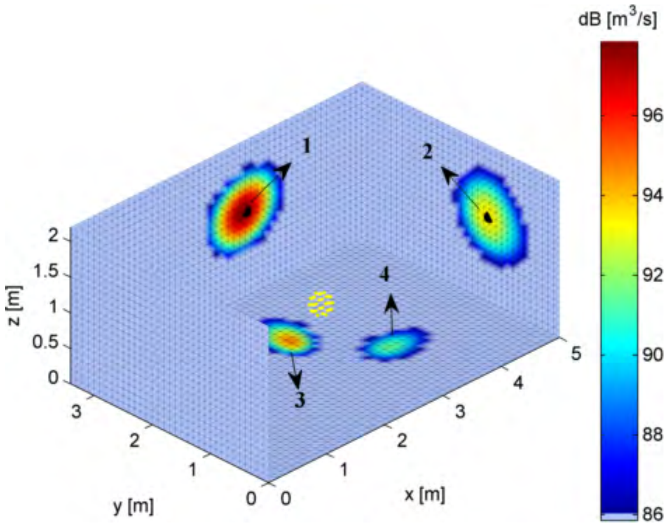

Figure 4.17: Volume velocity map integrated over the 100-3000 Hz frequency band for the first iteration. The position of real sources are marked as black dots. Notice that each hot spot is labeled by a number which is used for subsequent analysis. The dynamic range is 12 dB.

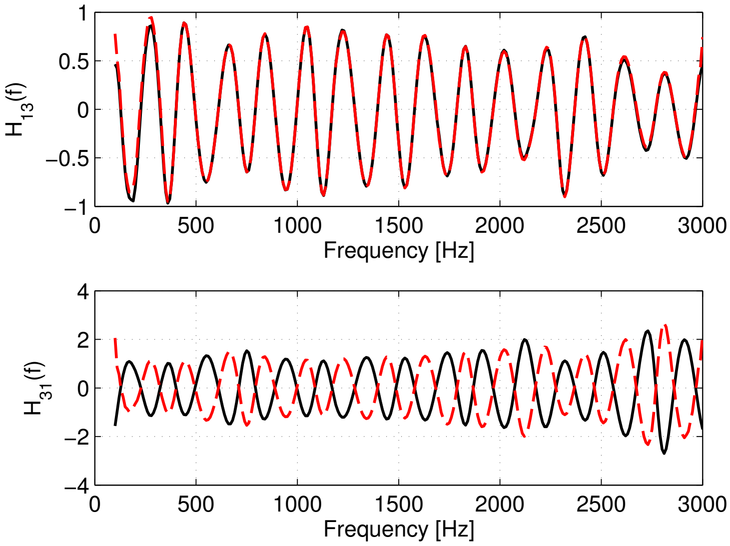

Figure 4.18: Verification of causality relations. (—) imaginary part of the frequency response function, (−−) Hilbert transform of the real part of the FRF. Top: $H_{13}(f)$; Bottom: $H_{31}(f)$.

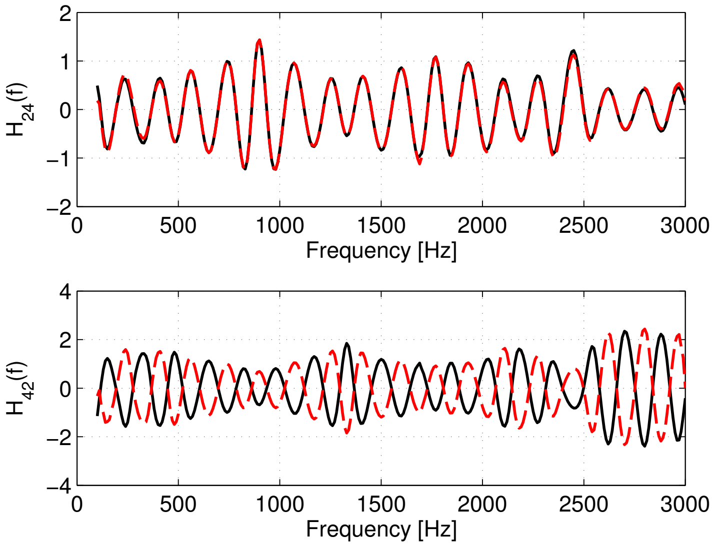

Figure 4.19: Verification of causality relations. (—) imaginary part of the frequency response function, (−−) Hilbert transform of the real part of the FRF. Top: $H_{24}(f)$; Bottom: $H_{42}(f)$.

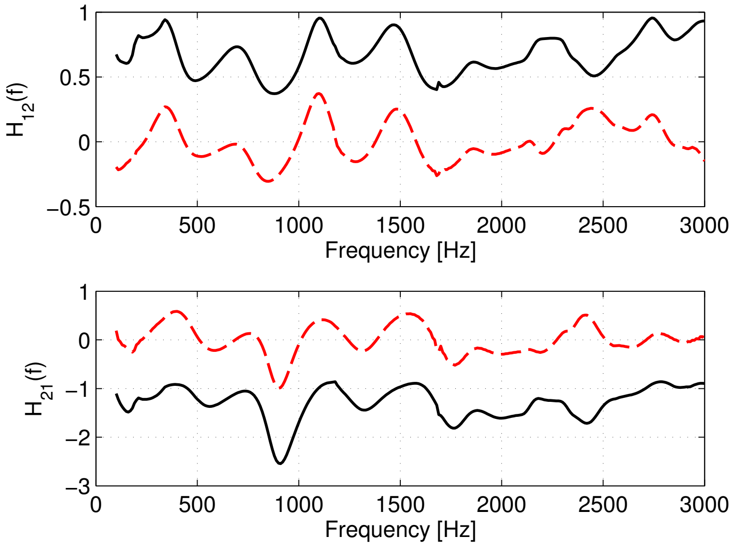

Figure 4.20: Verification of causality relations. (—) imaginary part of the frequency response function, (−−) Hilbert transform of the real part of the FRF. Top: $H_{12}(f)$; Bottom: $H_{21}(f)$.

5

Experimental validation and applications

5.1 Practical microphone array design

Following the guidelines presented in the previous sections a configuration which is well adapted to the target applications in this work has been chosen. The frequency range of interest is from 100 Hz to 3000 Hz and the number of microphones is limited to 32. Particularly, the truncated icosahedron geometry (see Figure 5.1) offers a convenient option for the distribution of 32 microphones on the surface of a sphere. It is an Archimedean solid [tru] with 12 regular pentagonal faces and 20 regular hexagonal faces and the choice consists in placing the microphones at the center of each face. This layout distributes microphones with a nearly uniform distance between neighbors. One of the advantages of this solution is that due to its nearly regular angular spacing, it is flexible enough to consider a single rotation of 36° over the z-axis in order to obtain a configuration with 61 microphones. This option is beneficial in cases where neither real time nor simultaneous measurements are required. In Section 5.5 , we will further investigate this flexibility by some validation experiments carried out in two passes.

In the practical construction, the microphone positioned at the south pole was removed to provide access for the cables outlet and mounting base. The microphones were finally flush-mounted on a Plexiglas sphere of radius 0.145 m and thickness of 4 mm. The constructed array is shown in Figure 5.2.

As far as we know, there is no definition in the literature on how to determine the Shannon-Nyquist limit for spherical arrays, besides its spherical and spatial version (1.1) for processing in the spherical harmonics domain. Normally, for planar arrays it is defined by the inter-microphone spacing, which should not be greater than half the wavelength of interest. In order to estimate the Shannon-Nyquist limit for the two configurations discussed above (31 and 61 microphones) we proceed as follows. First we compute the delaunay triangulation [BDH96, del] of microphones coordinates on the sphere. Next,

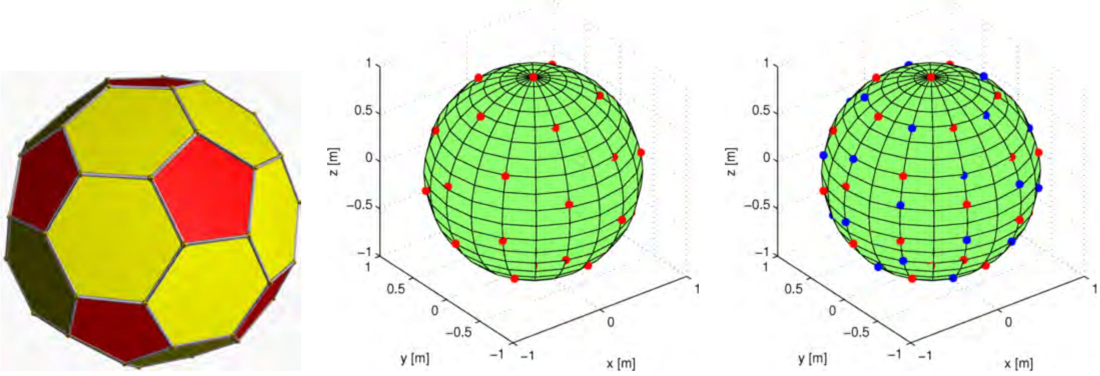

Figure 5.1: Left: Truncated icosahedron geometry, which has 20 regular hexagonal faces and 12 regular pentagonal faces. Middle: distribution of microphones corresponding to the center of faces of a truncated icosahedron. Right: configuration obtained after a 36°($\pi/5$) rotation around the z-axis.

we compute the average of the edge lengths returned by the triangulation. The average length gives us an estimate of the inter-microphone spacing for both configurations. For the configurations with 31 and 61 microphones we respectively have $0.65a$ and $0.50a$, where a is the radius of the sphere in meters. For a sphere of radius $a = 0.145$ m, this gives the following high frequency limits: $f_{31} = 1900$ Hz and $f_{61} = 2500$ Hz.

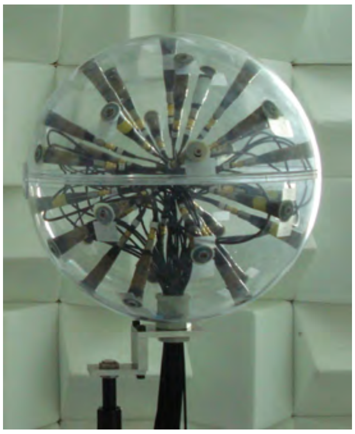

Figure 5.2: Spherical array of radius 14.5 cm with 31 microphones constructed for the validation experiments.

5.1.1 Array directivity

In order to validate the plexiglass sphere, its directivity was measured and compared to the theoretical one. The experiments were carried out in a semi-anechoic room with the sphere mounted on a vertical support which was manually rotated with an angular step of 15°. The center of the sphere was 1 m from the room floor and a single microphone was flush-mounted on the equator ($\theta = 90°$). A tube with exit diameter 15 mm and connected to a driver unit [dBB08] is used as a source, which is a good approximation of a monopole in the frequency range of interest (200 - 2000 Hz). The source was placed on the chamber floor at a distance of 2 m from the array center. The pressure measured on the surface of the sphere was then normalized by the free-field pressure measured at the center of the sphere, in order to obtain the sphere-related transfer function (SRTF). Directivity diagrams evaluated for different third octave frequency bands are shown in Figures 5.3 and 5.4. We notice that as the frequency increases and the wavelength becomes small in comparison to the circumference of the sphere, the response at the front approaches twice the free-field one. On the other hand, the response at the back becomes gradually smaller, revealing the sphere's shadowing effect. Finally, we observe that the experimental results are in general agreement with the theoretical values, thus validating the array as a rigid sphere model.

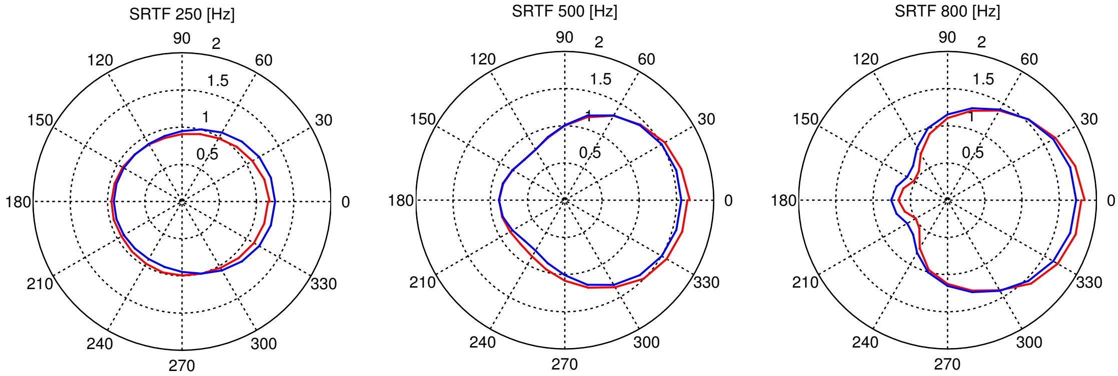

Figure 5.3: Theoretical directivity diagrams (—) and obtained from measurements (—) for different frequencies. The SRTF is the ratio between the pressure on the surface of the sphere and the free-field pressure (i.e. without the sphere) at the center of the sphere.

5.1.2 Array calibration

A custom calibration procedure for the microphone array was performed. A practical constraint is that the calibration has to be done with the microphones on the array since they are permanently fixed. The improvised calibration device consists of a small driver-unit in which a flexible tube is screwed. The idea is to drive the source with white noise signal and excite the microphones with the same signal. The device is placed against each microphone and the transfer function between the latter and the input signal is recorded. A reference is computed by the average of transfer functions over the array and a set of calibration curves are obtained by taking the ratio of each microphone transfer function and the reference. The magnitude and phase of the calibration curves for all microphones are shown in Figure 5.5. It can be seen that the fluctuations in magnitude are within the range of ±2 dB up to approximately 3 kHz. It is believed that the increase in errors for high

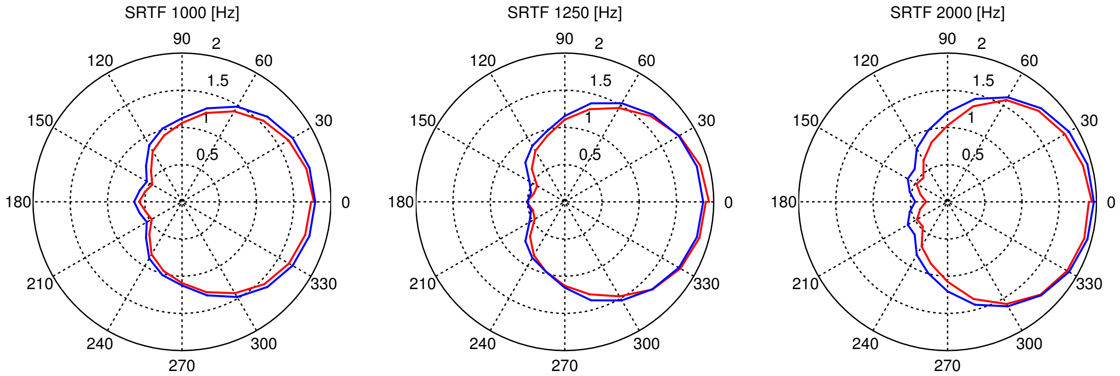

Figure 5.4: Theoretical directivity diagrams (—) and obtained from measurements (—) for different frequencies. Note that SRTF is the ratio between the pressure on the surface of the sphere and the free-field pressure (i.e. without the sphere) at the center of the sphere.

frequencies is due to limitations of the calibration device. A possible alternative for the calibration would be to place a previously calibrated microphone diaphragm-to-diaphragm with each microphone on the array and record their respective transfer functions. A set of calibration curves is then obtained by multiplying the ratio of transfer functions by the sensitivity of the reference microphone.

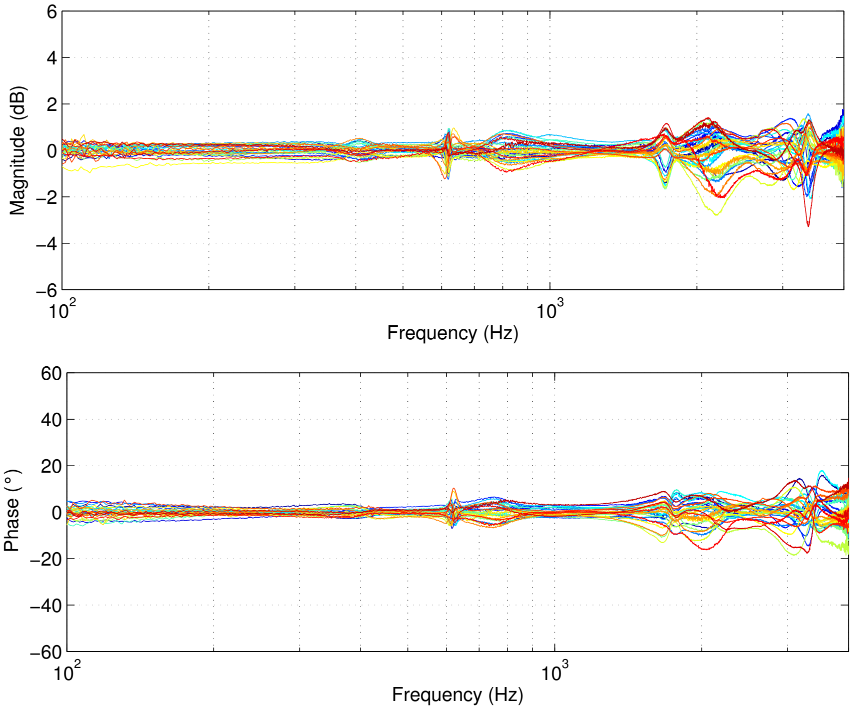

Figure 5.5: Calibration curves for each of the 31 microphones of the array, in magnitude (top) and phase (bottom).

5.2 Validation of the first weighting strategy

As we have seen in Chapter 4 an a priori information was introduced into the problem in order to correct for the positioning of the microphone array inside an enclosure. In this Section we present an experimental validation of the proposed weighting. The rigid spherical array described in the previous Section is used to measure the acoustic field inside a semi-anechoic cabin. A Microflown® acoustic source [dBB08] which consists of a tube of small diameter (d = 15 mm) connected to a compressor driver is used. This source is a good approximation of a monopole in the frequency range of 200 Hz to 4000 Hz. In addition, the source is implemented with a particle velocity probe at the end of the tube, which is used as a reference signal. The experimental set-up is shown in Figure 5.6. The monopole source is placed facing the door at a distance of 0.46 m from the ground and two different array positions are considered: (1) the first one relatively far from the closest boundary; (2) near to the enclosure surface.

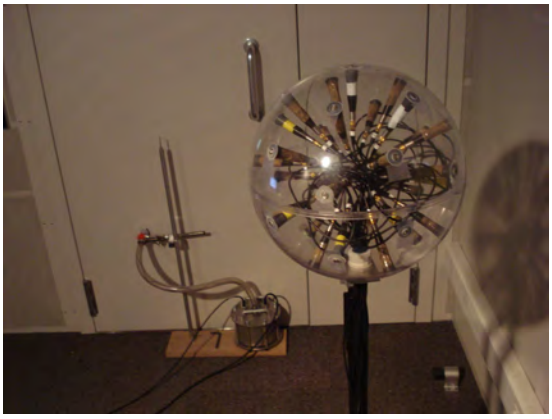

Figure 5.6: Measurement set-up.

The acoustic source is excited with white noise, the sampling frequency is set to 16 kHz and the recording length is 15s. The propagation model which relates the equivalent sources to the acoustic pressure on the spherical array is given in Equation (2.49). The complex acoustic pressure measured by each microphone is estimated by using the particle velocity probe at the exit of the tube as a reference signal. The inverse problem is then solved according to different strategies: (1) the classical ESM approach; (2) the first weighting strategy and (3) the iterative weighted approach. Firstly, we present in Figure 5.7 the results when the array is placed at the vicinity of a boundary for: (a) the classical approach; (b) the weighted approach. It can be seen that, similarly to the simulated example, the solution without weighting produces undesirable features, i.e. "ghost sources", on the nearby boundary (x = 0). On the other hand, the results using the proposed weighted approach allows to correct this effect at the expense of a worsened spatial resolution.

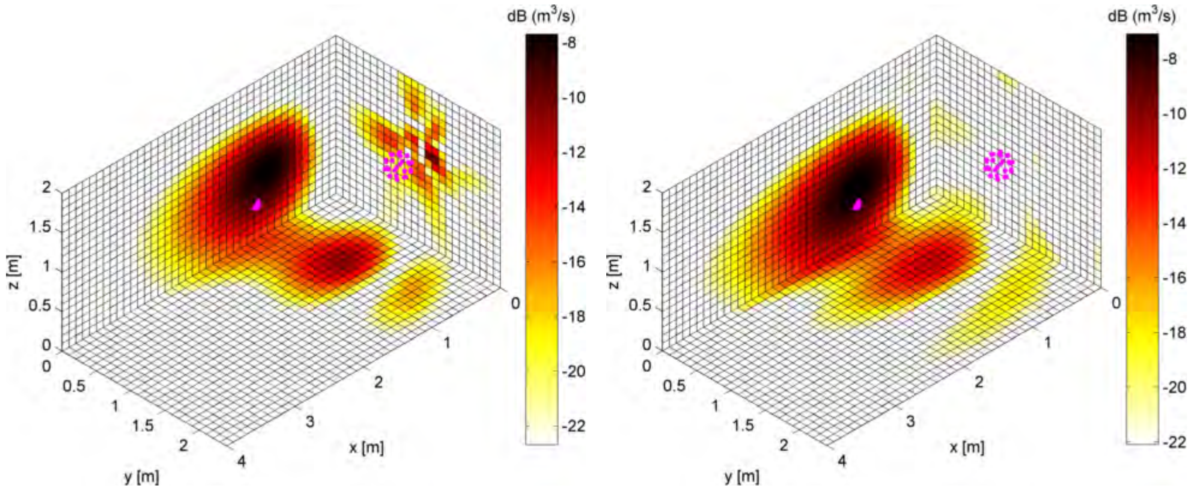

(a) classic approach (b) weighted approach

Figure 5.7: Volume velocity maps in dB (ref. 50 nm^3/s) integrated over the 1000 Hz third octave band. The figures show the floor and two boundaries of the enclosure, along with the microphones' coordinates and the real source position. The spherical array is at 35 cm from the nearby boundary and the results are given for: (a) classic ESM approach; (b) weighted approach. The dynamic range is set to 15 dB.

In addition, the iterative weighted strategy is applied for both cases (with and without the previous weighting by distance) and the results are shown in Figure 5.8. We can notice in Figure 5.8(a) that the iterative approach itself is able to reduce, at some extent, the effect of "ghost sources". For the case in which the initial weighting by distance is used, Figure 5.8(b), the unwanted effects are completely suppressed and we can notice the improvement in spatial resolution.

In addition, we present the results for the case in which the spherical array is placed at 66 cm away from the closest boundary (see Figure 5.9). We can notice that the above effects are less pronounced in this case. Indeed, the results for the classic approach, Figure 5.9(a), reveal the appearance of "ghost sources" however with energy 10 dB smaller than the original source.

As we have noticed from the above results, the method identifies the real source but also its first order reflection on the ground (which is not equipped with absorbent material). This behavior may pose an extra difficulty in practical cases in which the position of source is not known. For instance, it may mislead the user to assert that two sources are present. A possible way to gain better understanding was discussed in the previous Chapter. The idea is to analyze the causality relations between identified sources. This technique is applied here with the frequency response function (FRF) between the complex volume velocity corresponding to the real source and its image. The causality relation is then computed and the results are shown in Figure 5.10, where the label 1 is

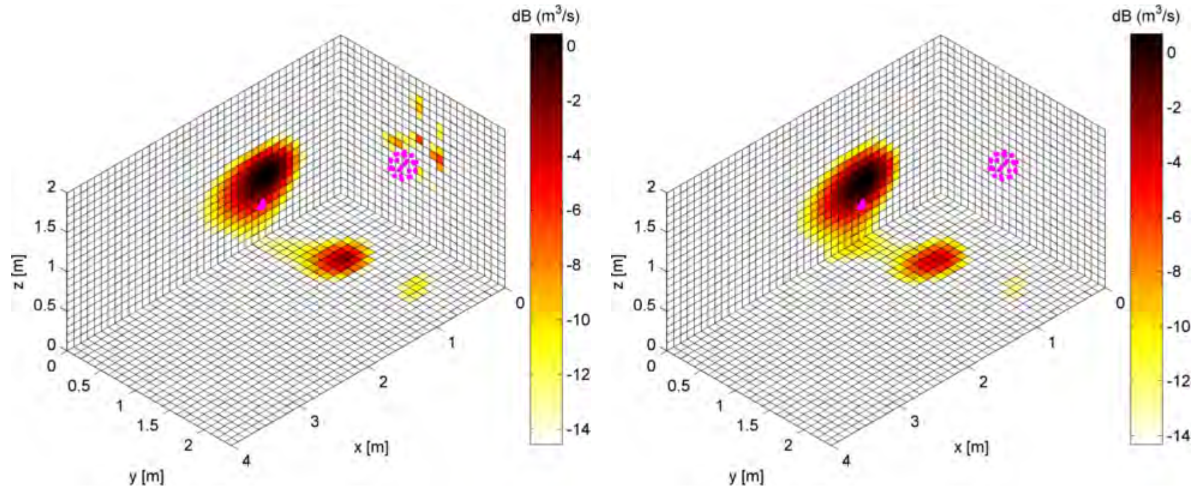

(a)

(b)

Figure 5.8: Volume velocity maps in dB (ref. 50 nm^3/s) integrated over the 1000 Hz third octave band. The results correspond to the 1st iteration returned by the iterative approach for: (a) without the initial weighting by distance; (b) with the initial weighting by distance. The dynamic range is set to 15 dB.

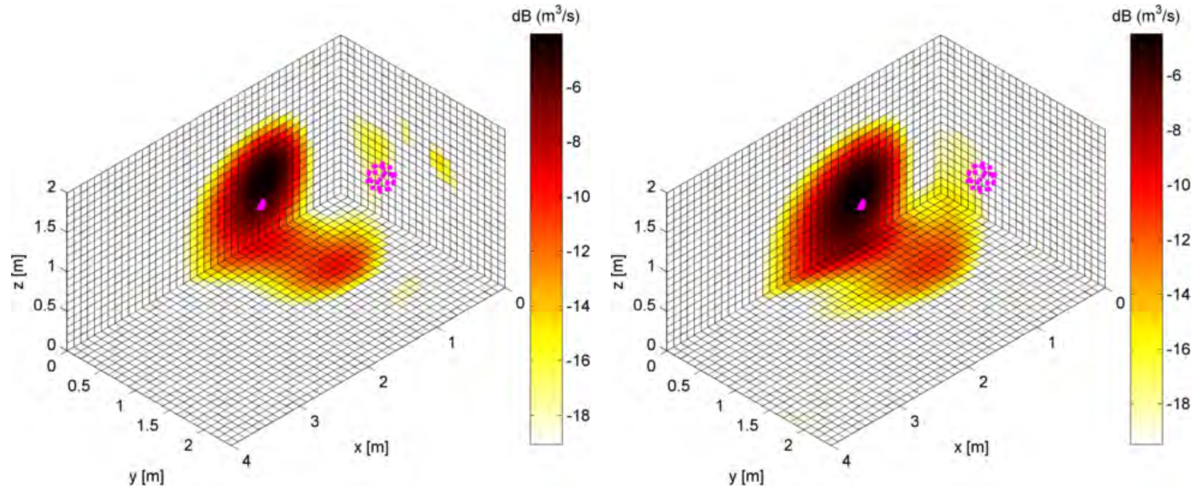

(a) classic approach

(b) weighted approach

Figure 5.9: Volume velocity maps in dB (ref. 50 nm^3/s) integrated over the 1000 Hz third octave band. The spherical array is at 66 cm away from the nearby boundary and the results are given for: (a) classic ESM approach; (b) weighted approach. The dynamic range is set to 15 dB.

assigned to the real source and the label 2 to its corresponding first order reflection. It can be seen that the frequency response $H_{12}(f)$ satisfies the causality relationship for the whole considered frequency band, which helps us to state that the "source 2" is indeed a reflection.

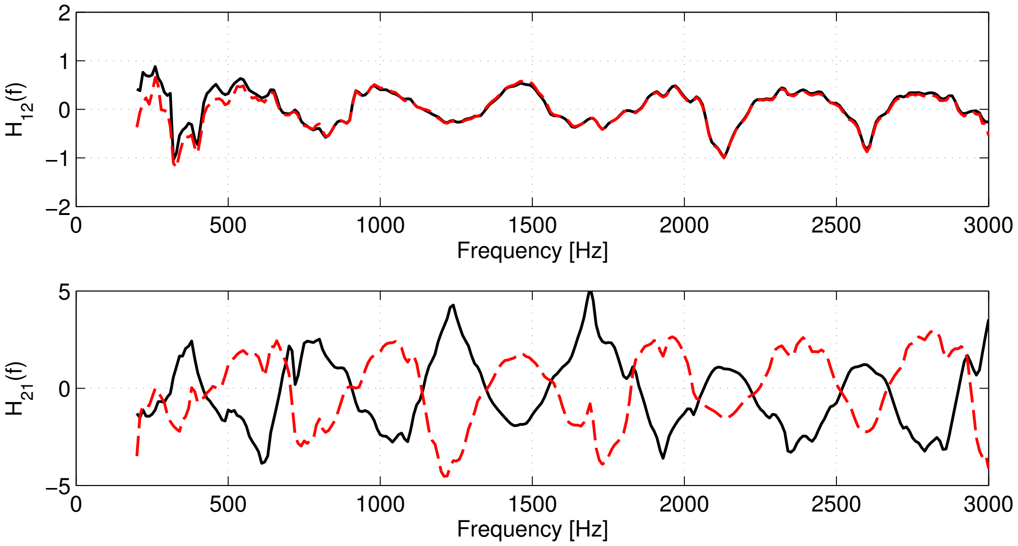

Figure 5.10: Verification of causality relations. (—) imaginary part of the frequency response function, (−−) Hilbert transform of the real part of the FRF. Top: $H_{12}(f)$; Bottom: $H_{21}(f)$.

5.3 Validation of the iterative weighted strategy

In this section, a different experimental configuration is used to validate the iterative approach, particularly in terms of the ability to quantify the acoustic power of identified sources. The experiment is carried out in a semi-anechoic room with dimensions 5×3.4×2.2 m^3. The same acoustic source and spherical array described in the previous section are used here. Figure 5.11 shows the experimental set-up. The acoustic source is placed at the floor of the chamber and is driven with white noise. The spherical array is located at 1 m from the floor and the distance from its center to the acoustic source is 1.2 m. The particle velocity probe placed at the exit of the tube is used as a reference signal and is used to estimate the acoustic power radiated by the source.

The inverse problem is then solved using the iterative weighting strategy discussed in Section 4.3. The reconstructed volume velocity corresponding to the first iteration is shown in Figure 5.12. It can be seen that the method locates the source in its correct position. In what follows, the measured reference acoustic power is compared with the reconstructed acoustic power. First of all, we show in Figure 5.13, the estimate of the acoustic power returned by the classic ESM. It can be readily seen a severe underestimation of the reference acoustic power, especially at higher frequencies. The same observation has been found in the numerical simulation from Section 4.4.3.

As noticed before, this underestimation is related to the directivity properties of the identified source distribution, which in turn, is due to the high degree of underdetermination of the problem. These remarks are illustrated in Figure 5.14, which shows the

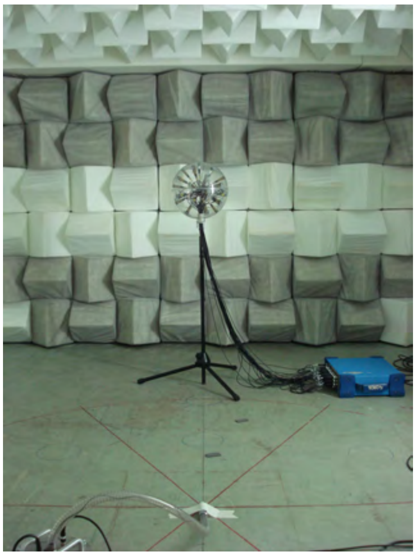

Figure 5.11: Measurement set-up.

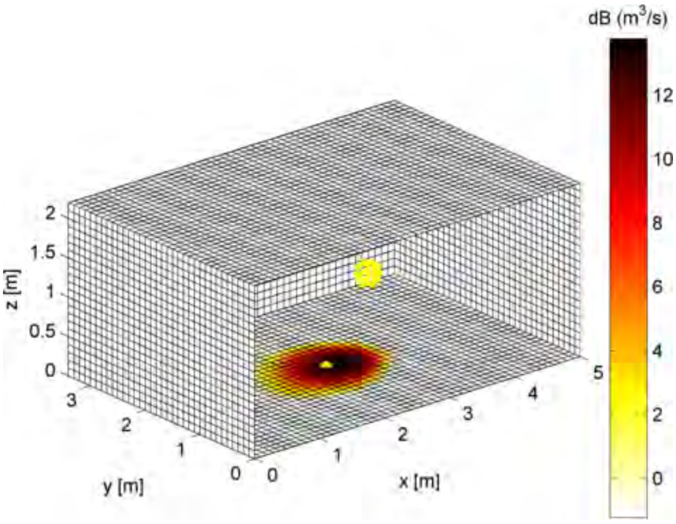

Figure 5.12: Volume velocity map integrated over the 200-2000 Hz frequency band for the first iteration. The position of real the source is marked by an yellow dot. The dynamic range is 15 dB.

acoustic pressure radiated by the identified source distribution. Figure 5.14(a) gives the results for the classic approach. As can be seen, the identified source distribution is hyper directive in the direction of the array (notice the high pressure levels on the ceiling of the chamber). The acoustic pressure radiated by the reconstructed source field (using the classical approach) is shown in Figure 5.15 for different frequencies. The figure shows the acoustic pressure evaluated at a hemi-spherical surface of radius 1 m and centered on the source position. As can be seen, the reconstructed source field becomes more directive as the frequency is increased. This results explain why the acoustic power is more underestimated at higher frequencies than at lower frequencies, as can be seen in Figure

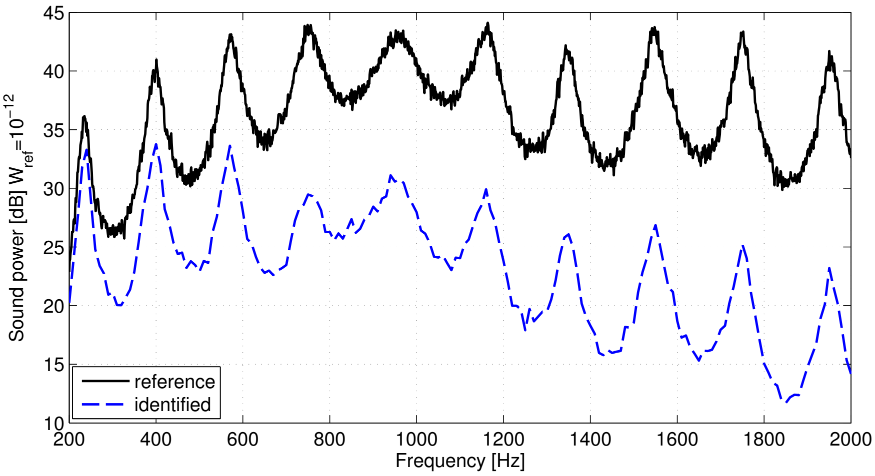

Figure 5.13: Acoustic power as a function of the frequency for: (—) measured reference acoustic power, (−−) reconstructed by the classic approach.

5.13. In addition, we show in Figure 5.14(b) the results returned by the iterative weighted approach after the 6th iteration. We can see that the above effect is corrected and the radiation of identified sources agrees better with the radiation of the real source.

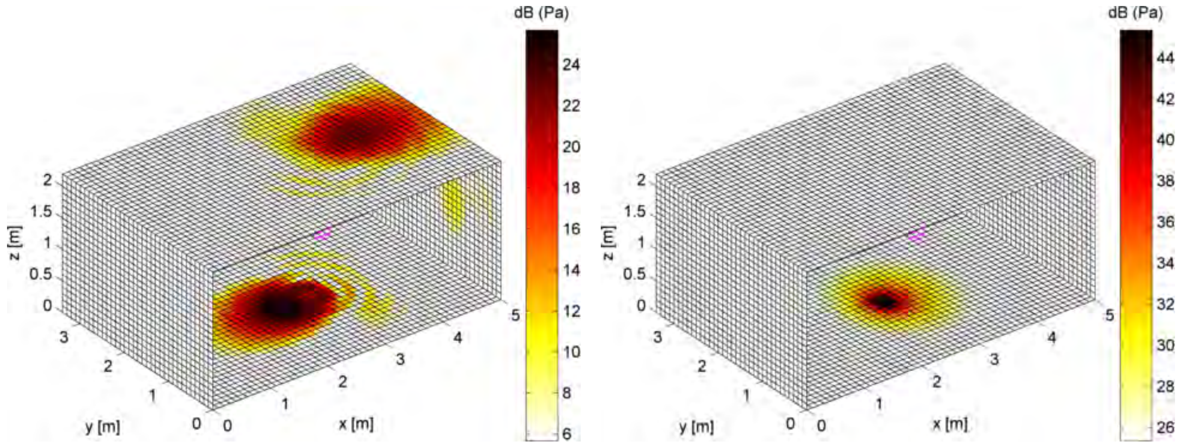

(a) classic approach (b) 6th iteration

Figure 5.14: Radiated acoustic pressure by the identified source distribution mapped on the enclosure's boundaries. The results correspond to the frequency of 700 Hz for: (a) the classic approach; (b) the iterative weighted approach at the 6th iteration. The dynamic range is 20 dB.

The iterative weighted approach was then applied to this case and an estimate of the acoustic power is computed at each iteration step. The results up to the 8th iteration are shown in Figure 5.16. It can be seen that the reconstructed acoustic power is progressively increased until convergence to the reference acoustic power. In this particular case, 8 iterations are required to obtain a good quantification. Finally, we present in Figure 5.17

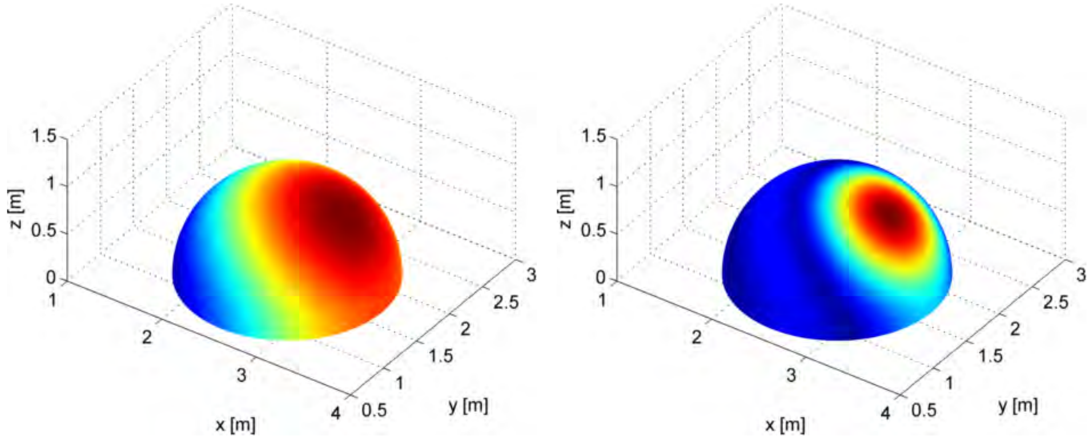

(a) 250 Hz (b) 500 Hz

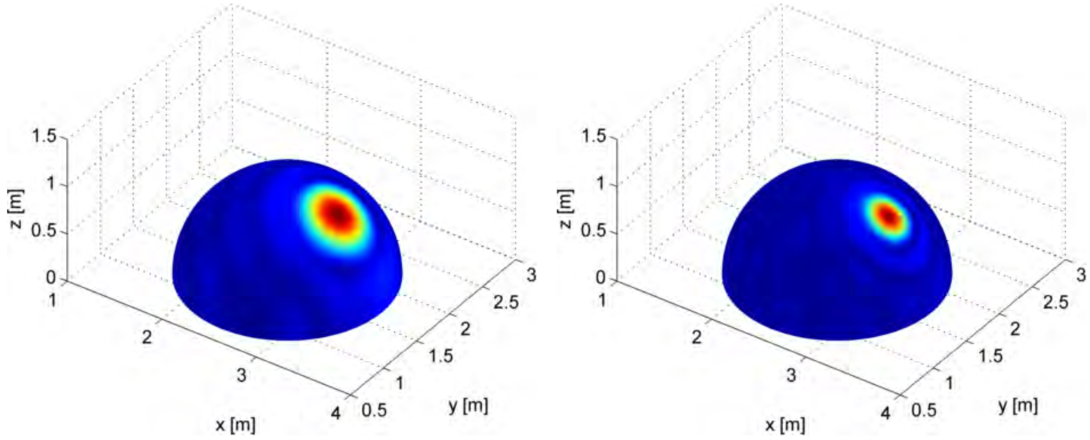

(c) 1000 Hz (d) 1600 Hz

Figure 5.15: Acoustic pressure generated by the reconstructed source field at a hemispherical surface of radius 1 m and centered on the source position. The results are given for the classic approach for (a) 250 Hz; (b) 500 Hz; (c) 1000 Hz; (d) 1600 Hz.

the estimate of the acoustic power given by the last iteration step. It can be seen that the estimate of the acoustic power agrees well with the reference acoustic power for the considered frequency band.

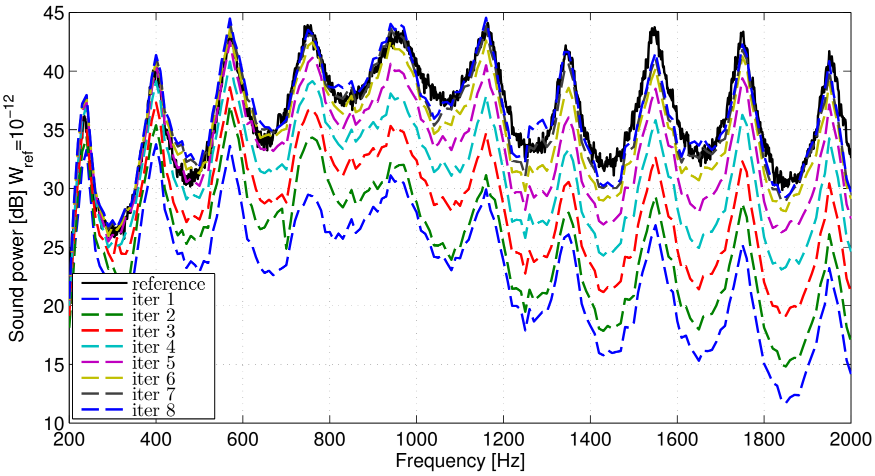

Figure 5.16: Acoustic power as a function of the frequency for: (—) measured reference acosutic power and returned by each iteration step from the 1st to the 8th iteration.

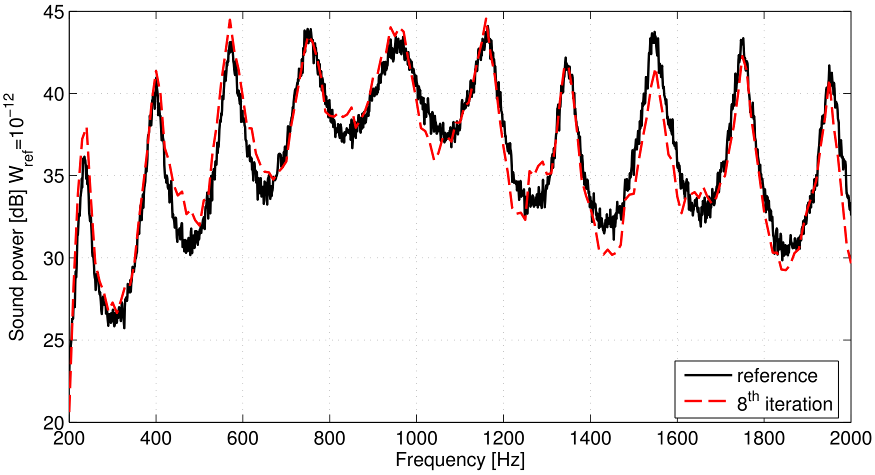

Figure 5.17: Acoustic power as a function of the frequency for: (—) measured reference acosutic power, (−−) reconstructed by the iterative weighted approach at the 8th iteration.

5.4 Localization and quantification of two noise sources

In this section we describe an application of the proposed iterative weighted method to locate and quantify two correlated noise sources. The experimental set-up is illustrated in Figure 5.18. The physical sources are two small drive units which are placed on the floor of the chamber (see Figure 5.18(a)). The distance between the two sources is approximately 1.2 m. In order to assess the acoustic power radiated by each source, the acoustic pressure at 5 cm from each source is measured as shown in Figure 5.18(b). The estimate of the acoustic power is obtained by assuming that the sources have a monopole-like behavior at the given distance. These measurements will serve as a reference to check the accuracy of the quantification results.

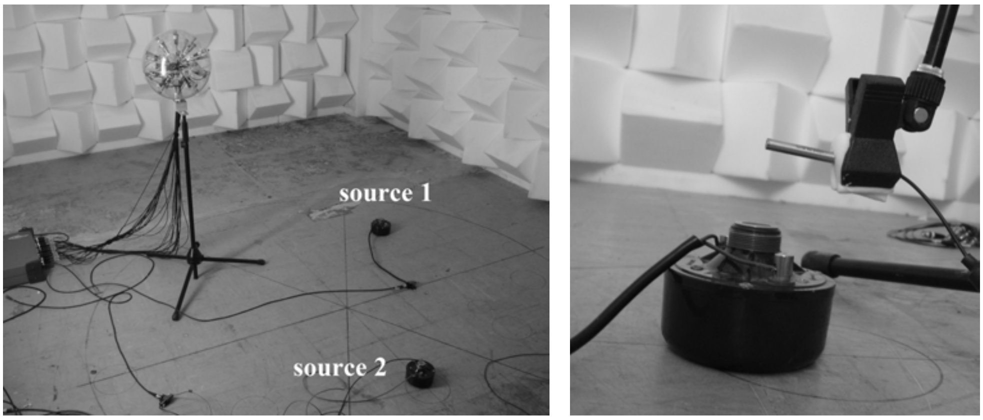

(a) (b)

Figure 5.18: (a) Measurement set-up showing the spherical array and two small sources placed on the ground of a semi-anechoic chamber. (b) Acoustic pressure measurement at 5 cm from the source, which is used to estimate its the acoustic power.

The equivalent source distribution is given by an equally spaced lattice of points representing the room surfaces, with a spacing of 0.1 m, which leads to a total number of 7000 degrees of freedom (DOF). The inverse problem is solved according to the proposed approach and the regularization is controlled by the Bayesian criterion in Equation (3.33). The results for the classic ESM approach are also computed for the sake of comparison. Figure 5.19 shows the volume velocity of equivalent sources obtained by the classic approach, as well as, by the iterative weighted approach. It can be seen that for the classic approach (Figure 5.19(a)) the two sources cannot be clearly separated, due to a poor spatial resolution at the considered frequency band. Conversely, after few iterations of the proposed approach (2 in this case) the two sources are already spatially separated. As we shall see, although few iterations are sufficient in order to acquire a reasonable spatial localization of sources, their correct quantification in terms of acoustic power requires a higher number of iterations.

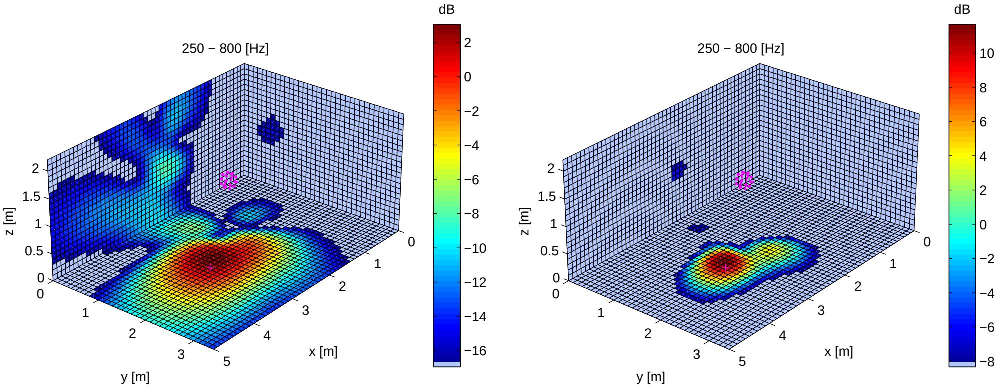

(a) classic approach (b) 1st iteration

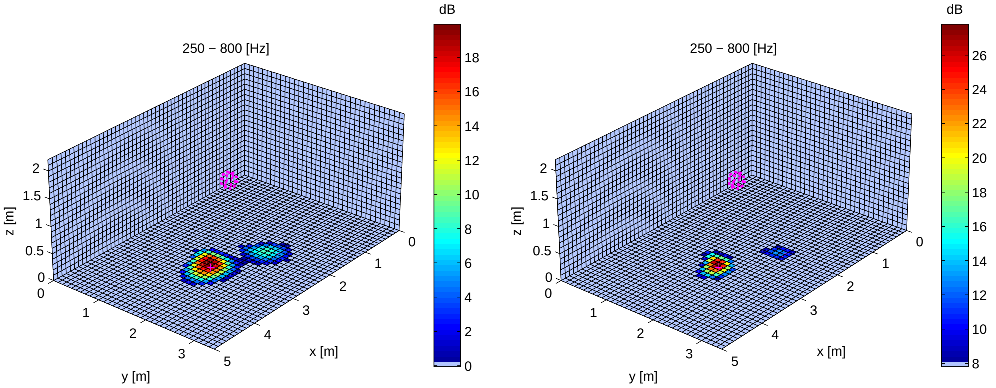

(c) 2nd iteration (d) 3rd iteration

Figure 5.19: Volume velocity maps integrated over the frequency band of 250-800 Hz with a dynamic range of 20 dB for all cases. (a) classic approach; (b) first iteration; (c) second iteration; (d) third iteration.

In what follows, we analyze the ability of the method to quantify the acoustic power of two correlated sources. The acoustic power of the above equivalent source distribution is computed by means of Equation 2.27. An estimate of the acoustic power corresponding to each physical source is obtained by the integration of the acoustic power map over a circular surface of radius 0.3 m centered at the position of each source. Not surprisingly, the estimated acoustic power is strongly underestimated for both sources, as shown in Figure 5.20. The acoustic power is also estimated by the iterative approach and the results up to the 8th iteration are reported in Figure 5.21. It can be seen that, in general, the agreement is acceptable, except at a frequency band ranging from 900 to 1700 Hz for the source 1 and from 1400 to 1800 Hz for the source 2, for which the acoustic power is underestimated. Indeed, it has been verified that this is related to the radiation pattern of the physical sources. As can be seen in Figure 5.18, the driver units are not baffled and their outlets are at approximately 8.2 cm from the ground, thus introducing a first order reflection.

In order to compute the radiation pattern of a source near a rigid boundary we use the concept of image sources. The acoustic pressure at a half circle of radius 1 m, as shown in Figure 5.22(a), is given by the sum of acoustic pressures generated by the source and its image. The acoustic pressure normalized by its maximum value at each frequency is reported in Figure 5.22(b). In the experimental set-up the spherical array is at an approximate angle of 40° relative to the sources. By inspection of Figure 5.22(b) we can notice that the radiation pattern exhibits a dip at this angle for those frequencies for which the underestimation is observed. This behavior may certainly explain the underestimation of the acoustic power. The above remarks show a limitation of the method in terms of quantification when the radiation of real sources differs considerably from an omni-directional radiation.

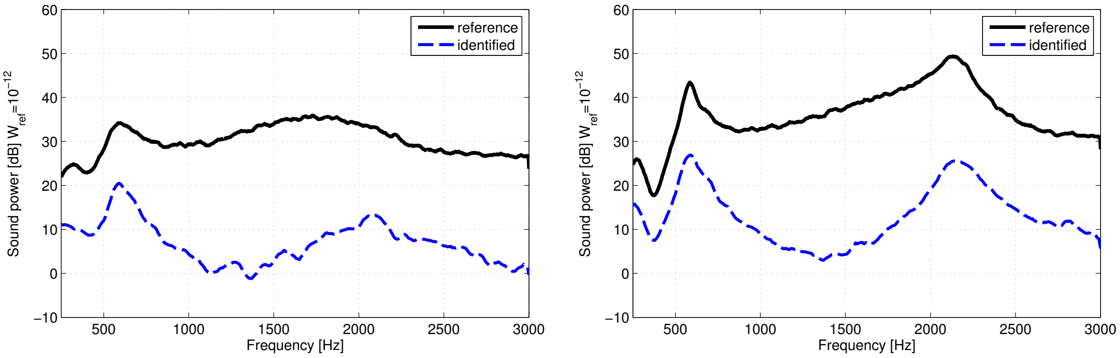

(a) source 1 (b) source 2

Figure 5.20: Acoustic power as a function of the frequency for: (—) measured reference acoustic power, (−−) reconstructed by the classic approach.

The acoustic pressure radiated by the identified source distribution is also reported in Figure 5.23. The same remarks as in the previous section are made here, the classic approach leads to reconstructed sources which are hyper directive towards the microphone array. In fact, this is a consequence of the highly underdetermined aspect of the system, in the sense that, the solution obtained by the method (among the infinite number of solutions), has no physical meaning in this case.

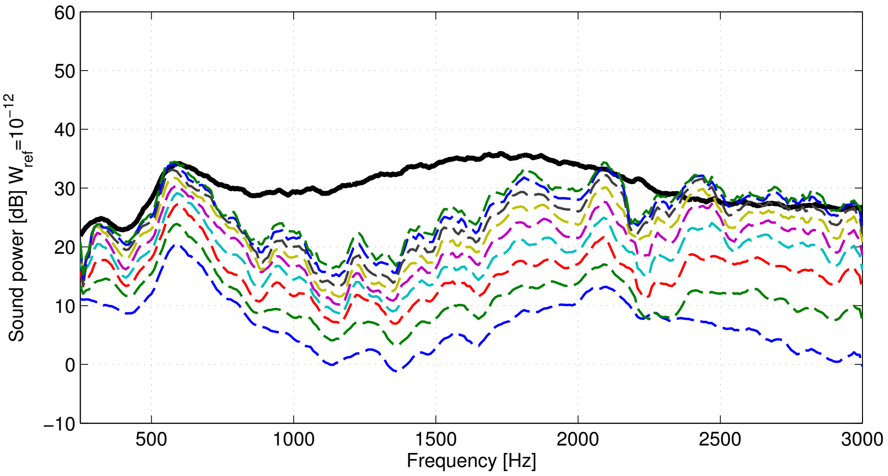

(a) source 1

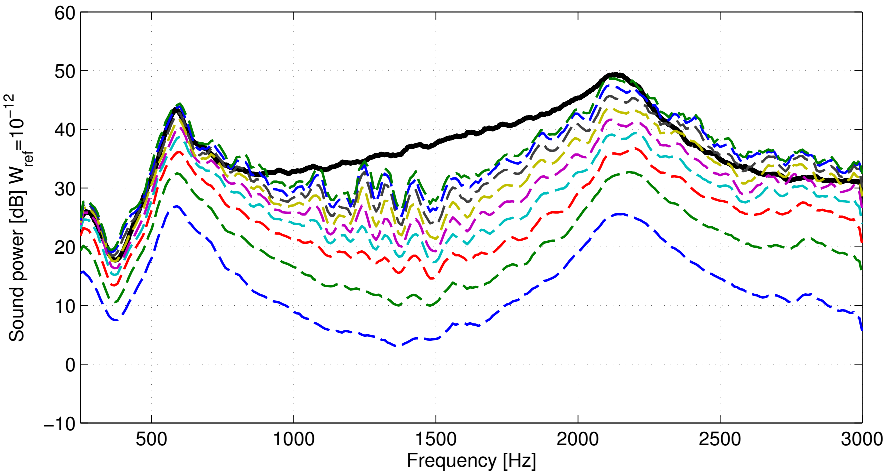

(b) source 2

Figure 5.21: Acoustic power as a function of the frequency for: (—) measured reference acoustic power and returned by each iteration step from the 1st to the 8th iteration.

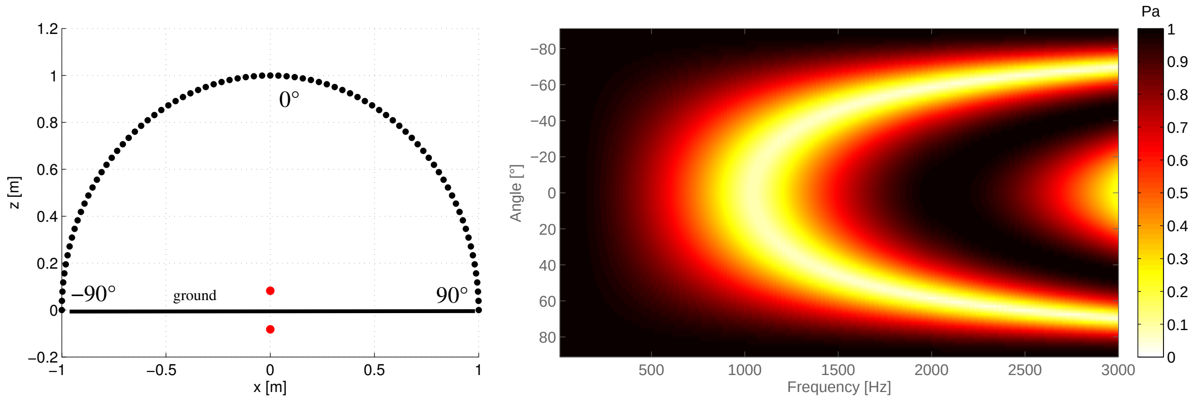

(a) (b)

Figure 5.22: (a) Model used to estimated the radiation pattern of a source near a reflective surface. A monopole source is placed at 0.08 m from the ground. The figure also shows a set of field points placed at a half circle of radius 1 m around the source. (b) Acoustic pressure at field points as a function of frequency. The acoustic pressure was normalized by its maximum value at each frequency.

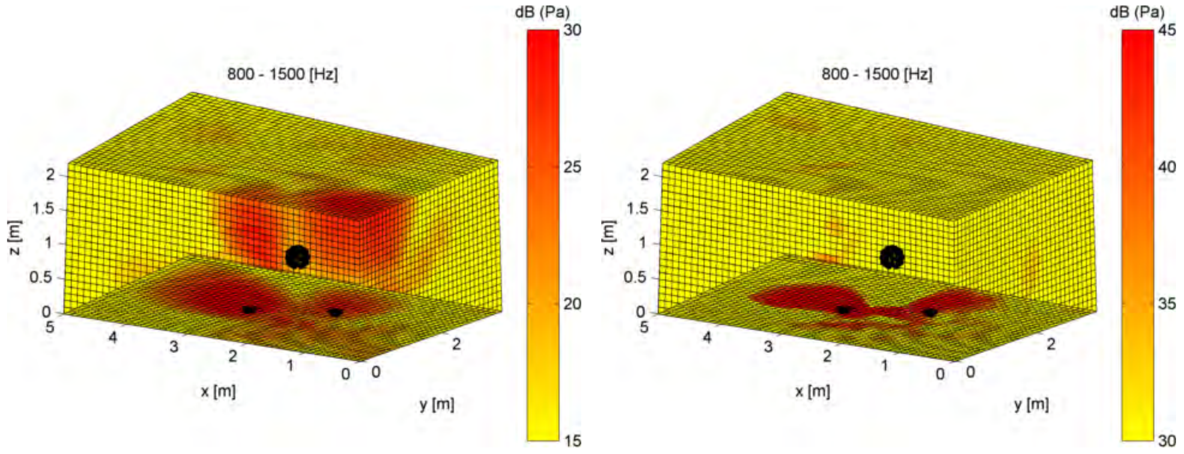

(a) classic approach (b) 9th iteration

Figure 5.23: Radiated acoustic pressure by the identified source distribution mapped on the enclosure’s boundaries. The results correspond to the frequency band from 800 Hz to 1500 Hz for: (a) the classic approach; (b) the iterative weighted approach at the 9^{th} iteration. The dynamic range is 15 dB.

5.5 Multi-pass measurements using a spherical array

In Section 5.1, we have mentioned that one of the advantages of the chosen distribution of microphones on the sphere was the possibility to perform a single rotation of $\pi/5$ radians to obtain a configuration with 61 microphones. This condition implies that the measurements have to be applied in two passes and thus restricts the application to stationary cases only. An additional difficulty of measurements performed in more than one step is the requirement to synchronize non-simultaneous measurements. Our aim in this section is to present experimental results that validate the proposed measurement set-up. The same acoustic sources from the previous Section are used here, and the experimental set-up is shown in Figure 5.24. The distance between the two sources is approximately 1 m.

In what follows, we summarize how the non-simultaneous measurements (in two steps) are synchronized. Since the cross-spectrum between moving microphones is not estimated, the full cross-spectral matrix comprising the two measurement positions is not available. An shown in reference [Lec09], virtual source analysis (VSA) may also be applied with a partial cross-spectral matrix. In the context of multiple pass acquisitions, whenever the signals measured by moving sensors are not fully coherent to each other (which is the case in the presence of multiple incoherent physical phenomena), several static reference probes are often required. Normally the number of reference static sensors must be at least equal to the number of observed incoherent phenomena. In the present experimental study we consider two uncorrelated acoustic sources, thus requiring a number of at least two fixed reference sensors. In this case we used a fixed reference microphone placed arbitrarily in the room (see Figure 5.25) and the second reference taken as the microphone located at the north pole of the sphere (which remains fixed after the rotation). The partial cross-spectral matrix $\mathbf{S}_{PR}$ between moving microphones and fixed references is then computed. $\mathbf{S}_{PR}$ being a rectangular matrix with rows corresponding to outputs and columns to references only.

The output holograms, hereafter stored in the columns of the matrix $\mathbf{X}$, are then obtained by means of the eigendecomposition of the cross-spectral matrix between fixed references ($\mathbf{S}_{RR}$) as follows

$$\mathbf{S}_{RR} = \mathbf{\Phi}\lceil\mathbf{\Sigma}\rfloor\mathbf{\Phi}^{H} = \overline{\mathbf{X}}_{R}\mathbf{X}_{R}^{T}, \tag{5.1}$$

with the columns of $\mathbf{\Phi}$ being the eigenvectors of the decomposition and the diagonal elements of $\mathbf{\Sigma}$ the eigenvalues. In addition, $\overline{\mathbf{A}}$ stands for the conjugate of matrix $\mathbf{A}$ and $\mathbf{A}^{T}$ the transpose of $\mathbf{A}$. The reference output vectors, stored in the columns of matrix

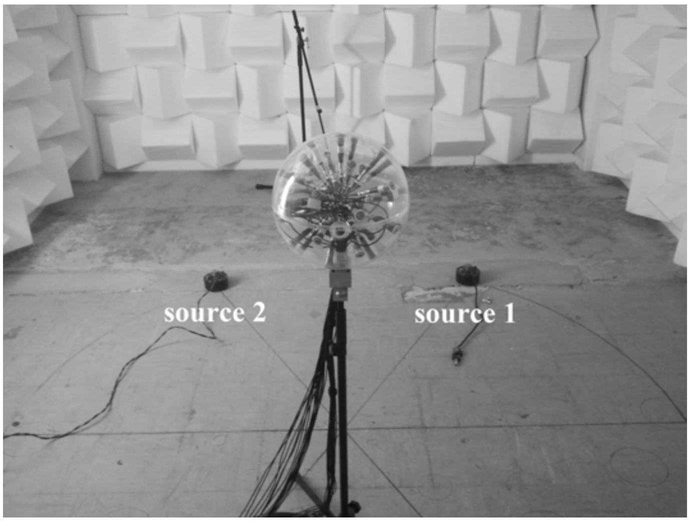

Figure 5.24: Experimental set-up.

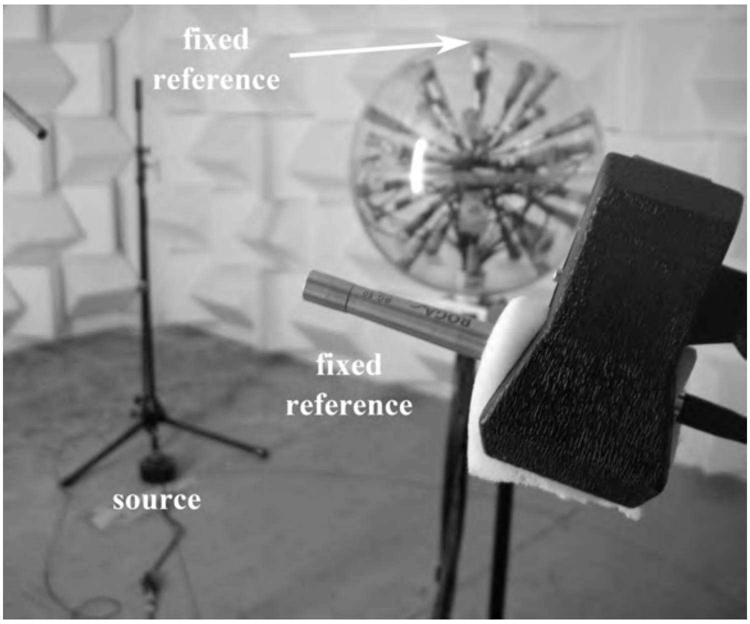

Figure 5.25: Experimental set-up showing the set of fixed references used to synchronize the non-simultaneous measurements.

$\mathbf{X}_R$, can thus be obtained by

$$\mathbf{X}_R = \overline{\mathbf{\Phi}}\lceil\sqrt{\mathbf{\Sigma}}\rfloor. \tag{5.2}$$

The partial cross-spectral matrix $\mathbf{S}_{PR}$ between moving microphones and fixed references may be given by the following relationship

$$\mathbf{S}_{PR} = \overline{\mathbf{X}}\mathbf{X}_R^T, \tag{5.3}$$

with $\mathbf{X}$ the unknown rectangular matrix with columns defined as the output holograms referenced to virtual sources and $\mathbf{X}_R$ a square matrix with dimension equal to the number of fixed references. Inserting Equation (5.2) into Equation (5.3) yields:

$$\mathbf{S}_{PR} = \overline{\mathbf{X}} \lceil \sqrt{\mathbf{\Sigma}} \rfloor \mathbf{\Phi}^H, \tag{5.4}$$

from which we finally obtain the output holograms based on the partial cross-spectral matrix and on the eigendecomposition of the references cross-spectral matrix, as follows

$$\mathbf{X} = \overline{\mathbf{S}_{PR} \mathbf{\Phi}} \lceil \sqrt{\mathbf{\Sigma}} \rfloor^{-1}. \tag{5.5}$$

We finally remark that the above computations are realized for each frequency line, the frequency dependency notation being neglected for notational simplicity. In practice, in order to reduce the uncertainties on the spectral estimators, the elements of the references cross-spectral matrix are averaged over the number of passes. Similarly, the elements of the partial cross-spectral matrix are computed by means of the H_1 estimator between moving sensors and references, with reference auto-spectra estimated over the number of passes. In order to ensure that all incoherent phenomena (sources) contributing to a given output i are captured by the available fixed references, one can make use of the multiple coherence function. The latter is defined as the ratio of the energy taken into account by a given number of virtual sources over the energy of a given output, as follows [Lec09]

$$\gamma_{i:1,\cdots,n}(f) = \frac{\sum_{k=1}^{n} |X_{ik}(f)|^2}{S_{ii}(f)}, \tag{5.6}$$

with n the number of virtual sources taken into account, X_{ik} the element of $\mathbf{X}$ corresponding to the i-th row and k-th column and S_{ii} the auto-spectrum of output i. This quantity is computed for the considered case taking into account the first two virtual sources and the result is shown in Figure 5.26. As can be seen, the multiple coherence is generally close to 1 except at the frequency of 1000 Hz for some outputs.

From now on, we compare the source reconstruction results obtained by the original array and the configuration with an additional rotated position. The distribution of microphones on the sphere for the combined configuration is shown in Figure 5.1. As can be seen, this configuration leads to a smaller the inter-microphone spacing. This property is advantageous in order to increase its upper frequency of application. As an example, Figure 5.27 shows the reconstructed volume velocity integrated over 2500-3000 Hz for: (a) one pass only; (b) combined array. By comparing both results, it can be seen that the configuration with two passes improves the sensibility to side lobes, since the energy of the latter is reduced in this case.

On the other hand, the above improvements are less pronounced at lower frequencies,

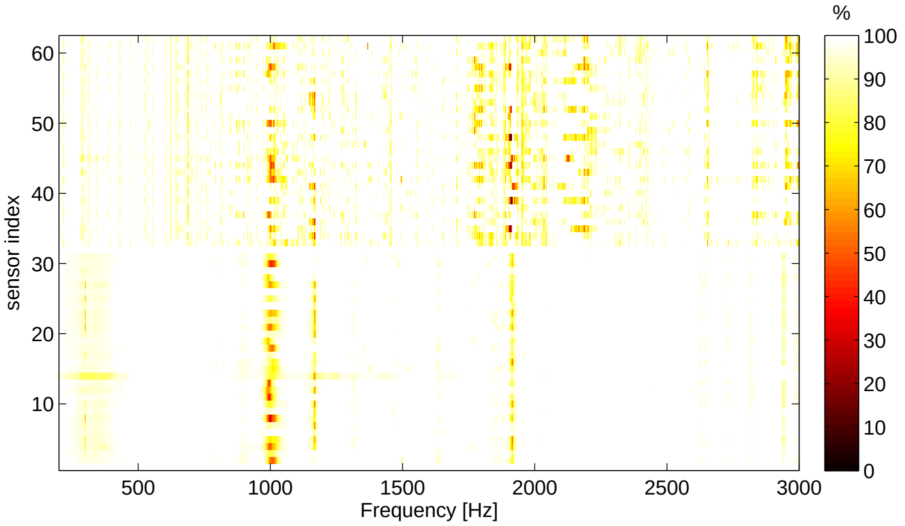

Figure 5.26: Multiple coherence function as a function of the frequency for all sensors. The multiple coherence is computed between moving microphones and the first two virtual sources.

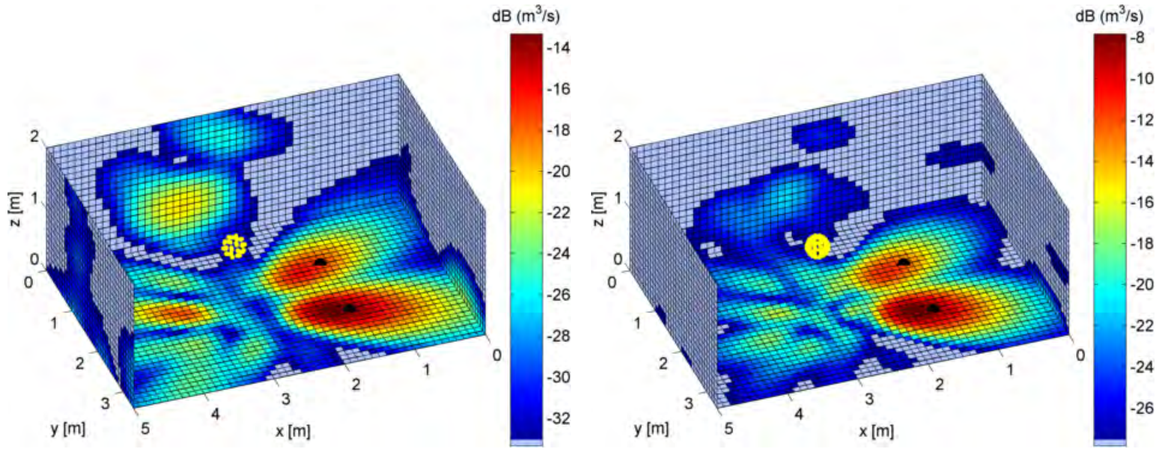

(a) single pass
(b) two passes

Figure 5.27: Volume velocity maps integrated over the 2500-3000 Hz frequency band. (a) results obtained by the original array with 31 microphones; (b) results for the configuration with an extra rotation leading to 61 measurement positions. The dynamic range is 20 dB.

as shown in Figure 5.28 for the 200-600 Hz frequency band. This result is not surprising since a denser microphone array provides little additional information at lower frequencies, a larger array would be a better configuration at this frequency range. Nevertheless, in combination with the iterative weighted approach, the denser array yet provides better results in terms of spatial resolution (see Figure 5.29).

The performance of both array configurations is also compared in terms of the quantification of the acoustic power. An estimate of the individual acoustic power of sources is given by the integration over an area surrounding each source. The results for the last

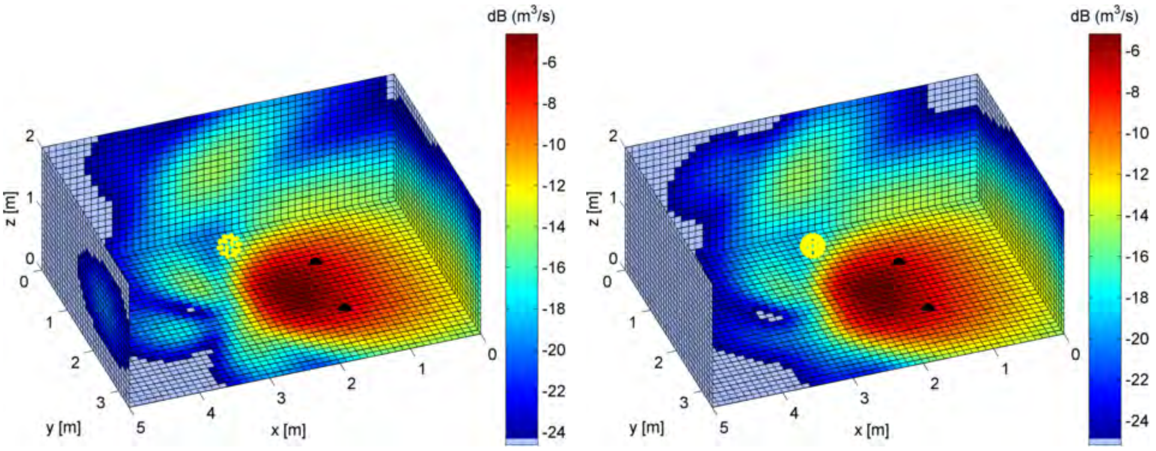

(a) single pass (b) two passes

Figure 5.28: Volume velocity maps integrated over the 200-600 Hz frequency band, for: (a) original array; (b) two passes configuration. The dynamic range is 20 dB.

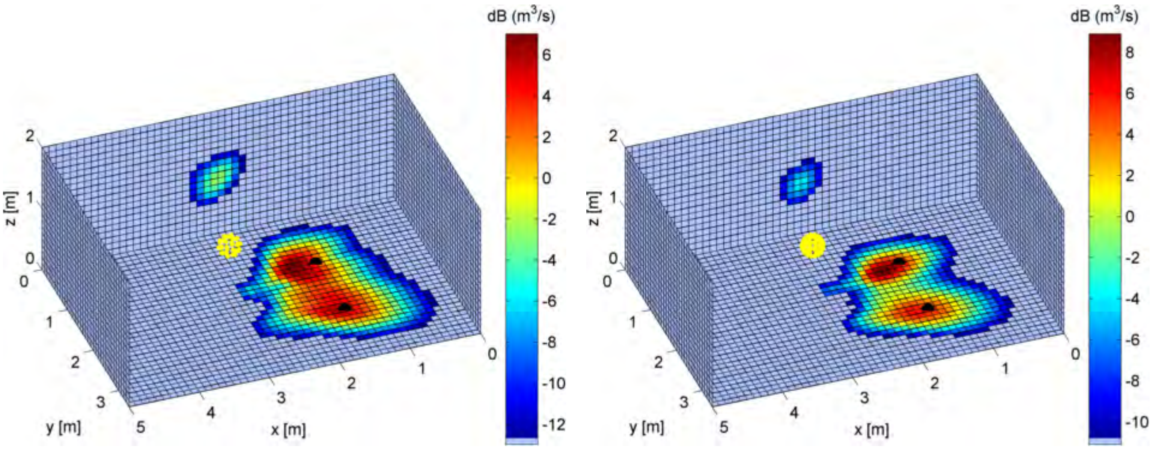

(a) single pass (b) two passes

Figure 5.29: Volume velocity maps integrated over the 200-600 Hz frequency band, using the iterative weighted approach. (a) original array; (b) denser array. These results corresponds to the 2$^{\text{nd}}$ iteration and the dynamic range is 20 dB.

iteration given by the iterative weighted approach are reported in Figure 5.30. The same underestimation as previously at the mid frequency range is observed. In general, the results for both configurations are similar, except at some particular frequencies in which the estimate returned by the configuration with two passes is slightly better, namely: low frequencies for the source 2 and mid frequency range for the source 1.

It has been shown in this section that it is possible to increase the number of measurement positions using a spherical array by means of a single rotation around its axis. One of the advantages of this experimental procedure is to improve the quality of reconstruction results at higher frequencies by decreasing the inter-microphone spacing. However, an

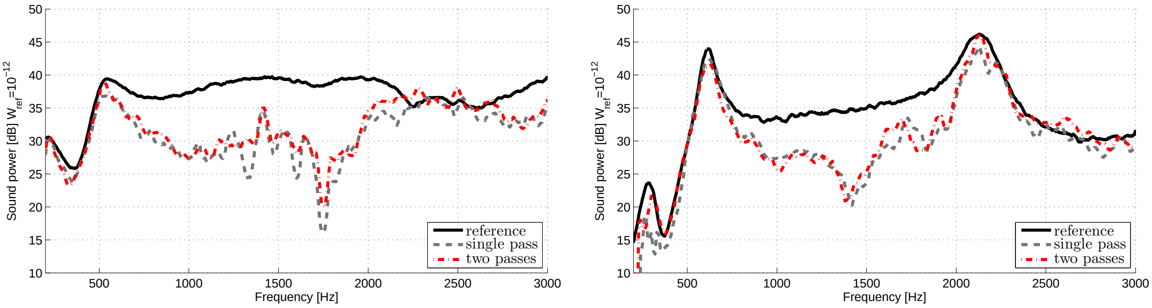

(a) source 1

(b) source 2

Figure 5.30: Acoustic power as a function of the frequency given by the measured reference and estimated for two different array configurations. (a) source 1; (b) source 2. These results correspond to the last iteration given by the iterative weighted approach.

additional difficulty is the requirement to synchronize non-simultaneous measurements, which by the approach used here, requires a number of fixed references at least equal to the number of incoherent phenomena. Further research is suggested in order to obtain a technique to synchronize non-simultaneous measurements without the need of fixed references.

5.6 Noise source localization inside a bus cabin

One of the practical applications of the described approaches concerns interior noise diagnostics in vehicles. Very often, acoustical performance receives little attention at early design stages of a vehicle and acoustic problems appears very late, when design changes are limited. Noise mapping techniques, such as the one discussed in this thesis, may help the engineer to understand the source of the acoustic problems, for instance a region of acoustic weakness or improper sealing.

Our interest in this section is the identification of noise sources inside a bus cabin using a commercially available dual-sphere microphone array, which was placed at the rear of the vehicle, near the engine compartment (see Figure 5.31(a)). Several configurations have been tested and, in what follows, we present the results for the condition in which the bus is stopped and the engine running at idle. A sketch of the bus illustrating its main components is shown in Figure 5.31(b). We can observe the diesel engine at the rear right compartment, an electric motor at the bottom and cooling systems and batteries at the top. The microphone array consists of a rigid sphere of radius 0.15 m with 24 microphones and an open sphere of radius 0.4 m with 24 microphones. An interior mesh of the bus is obtained by a meshing system which consists of a laser that points towards the interior surfaces with a predefined spatial step. The coordinates of the mesh nodes relative to the center of the array are then obtained. In this particular case, the total number of equivalent sources that represent the interior surfaces is approximately 14600.

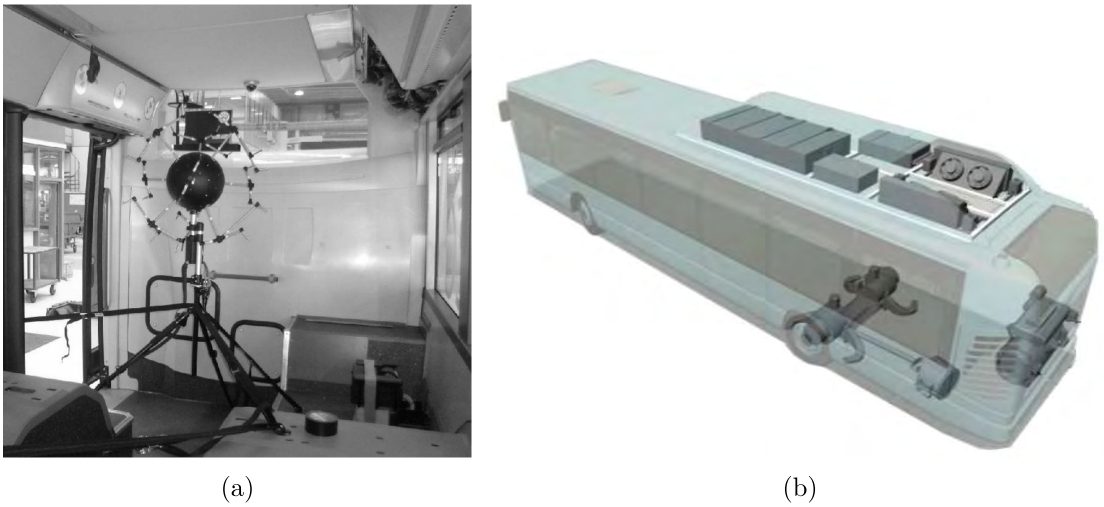
(a) (b)

Figure 5.31: (a) Measurement set-up showing the dual-sphere microphone array (courtesy of MicrodB). (b) Sketch of the bus (courtesy of IVECO France Irisbus).

The complex acoustic pressure holograms are obtained by means of principal spectral analysis (PSA) or virtual source analysis (VSA) [LPLP05]. Pressure holograms at each frequency are obtained for each principal component and used to solve for the inverse problem. The results (e.g. reconstructed source field) are then summed in energy. The acoustic pressure averaged over the ensemble of microphones is shown in Figure 5.32. In what follows, we focus on the frequency band from 250 to 550 Hz, in which most of the spectral energy is concentrated. The proposed iterative weighted approach is then applied in order to identify those regions which contribute the most to the interior sound field.

Figure 5.33 shows the volume velocity map of identified sources integrated over the frequency band of 440-490 Hz. The images show a 3D view of the interior surfaces of the bus. In Figure 5.33(a) we show the result obtained for the rigid sphere only, and Figure 5.33(b) shows the result for the dual-sphere array. One can see that the main contribution for this frequency band comes from the rear right side, around the rear exit door. It can also be noted the improvement in resolution when using the dual-sphere array configuration. Indeed, at low frequencies (large wavelengths) a larger array is advantageous.

The weighting by the distance from each equivalent source to the array center position, as described in Section 4.2, was used in both cases in order to correct for the positioning of the microphone array. As can be seen in Figure 5.31(a) the array is much closer to the ceiling than other surfaces, which implies that more weight will be given to equivalent sources on that region when no correction is applied. To illustrate this behavior, we present in Figure 5.34(a) the results when no correction is applied. It has been verified

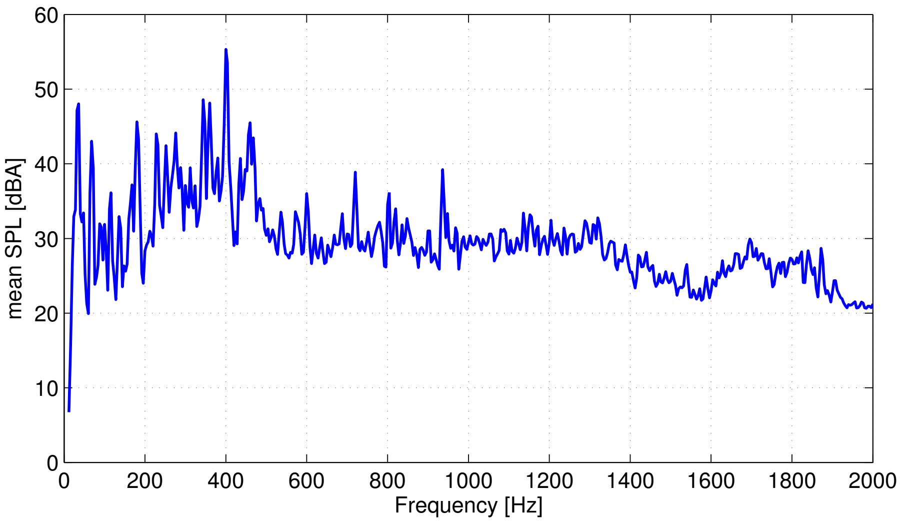

Figure 5.32: Measured acoustic pressure averaged over the ensemble of microphones in dBA.

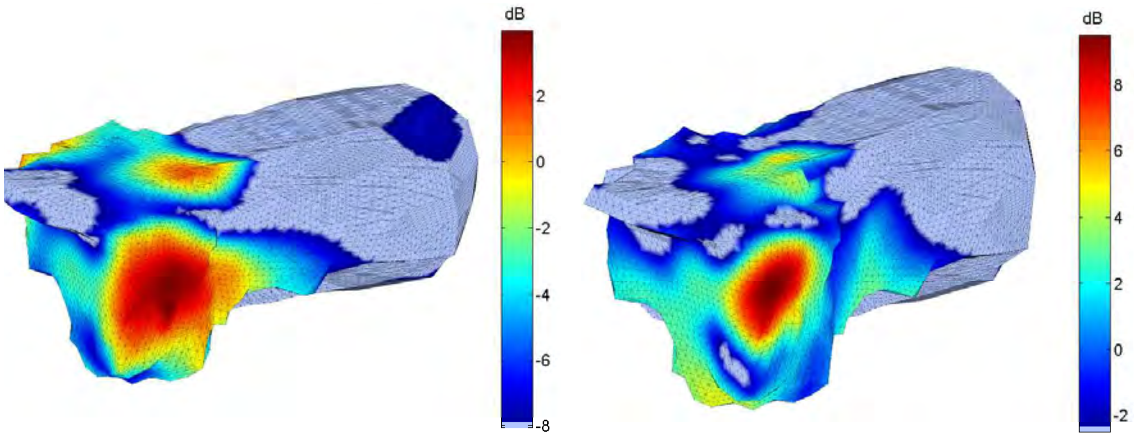

(a) rigid sphere only

(b) dual-sphere array

Figure 5.33: Volume velocity map integrated over 440-490 Hz corresponding to the bus interior surfaces with a dynamic range of 12 dB. (a) results using the rigid sphere only. (b) results using the dual-sphere array (rigid and open sphere). The weighting by the distance from the equivalent sources to the array center was used for both cases.

that, without correction, the method systematically identifies the main contributing region on the ceiling, near the microphone array. Hence, this results evidences the importance of the first weighting strategy in order to correct for the array positioning. The iterative weighted approach is finally applied to this configuration and the results are reported in Figure 5.34(b) for the first iteration. It can be noticed an improvement in spatial resolution as compared to the results in Figure 5.33(b). The results for the frequency band 390-410 Hz are shown in Figure 5.35. Figure 5.35(a) shows a 3D view of the ceiling and right-hand side and Figure 5.35(b) shows the rear and the floor parts. It can be seen that the main contribution in this frequency band comes from the rear part of the floor.

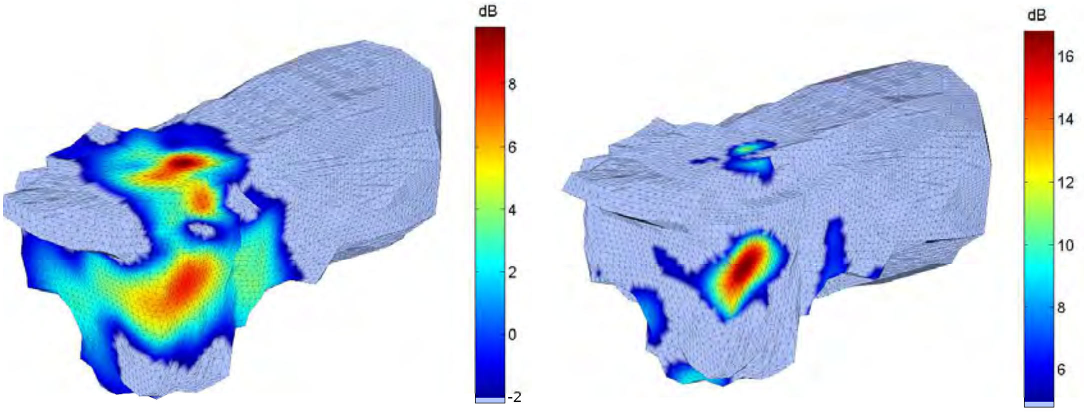

(a) classic approach

(b) 1st iteration

Figure 5.34: Volume velocity map integrated over the 440-490 Hz frequency band with a dynamic range of 12 dB. (a) results for the classic approach, in which no weighting by distance is applied. (b) results obtained for the first iteration returned by the iterative weighted approach.

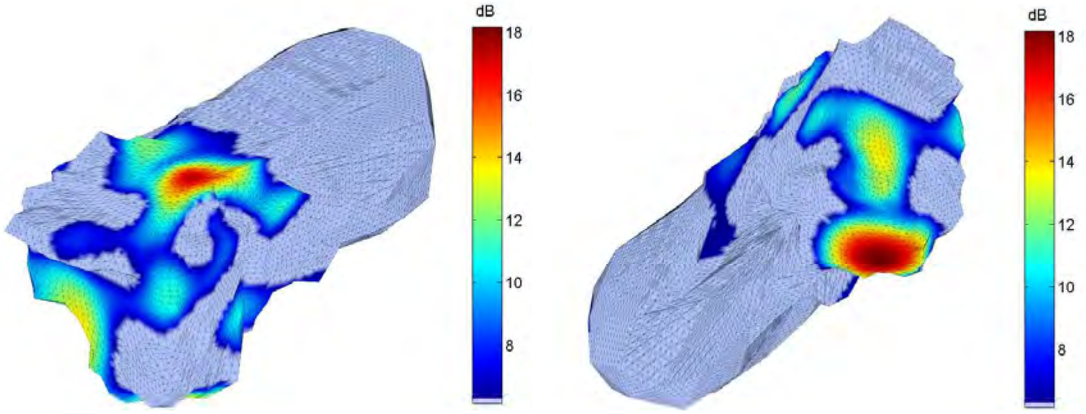

(a) top view

(b) bottom view

Figure 5.35: Volume velocity map integrated over the 390-410 Hz frequency band with a dynamic range of 12 dB. (a) results for the classic approach, in which no weighting by distance is applied. (b) results obtained for the first iteration returned by the iterative weighted approach.

Conclusions and Further Research

Conclusions

This work has been carried within the framework of inverse acoustic problems for interior spaces. In this context, the study has been built on the equivalent source method. Its simplicity, ease of implementation, relatively low computational cost and possibility to combine noise source localization and quantification are some of its advantages.

Initially, the application of the classic ESM approach to interior problems have been described and we have shown how to obtain the acoustic quantities that characterize the reconstructed source field, namely: the radiated acoustic pressure and acoustic power. In addition, the propagation models relating the equivalent sources to the microphone array have been discussed, with emphasis on the application with rigid spherical arrays.

Due to the ill-conditioning aspect of the proposed approach, a major part of this thesis has been dedicated to the aspect of regularization of the acoustic inverse problem. In this context, we have studied the well-known L-curve method, for which we proposed an extension to its criterion. The main motivation was to ensure the continuity of the frequency response which characterizes the reconstructed source field. Yet in the context of regularization, we have studied in detail an approach based on a Bayesian framework. The latter has provided us natural justification for the use of the well-known technique of Tikhonov regularization. Furthermore, the Bayesian formalism offers new perspectives on the selection of a reasonable amount of regularization. Finally, an important contribution of this work was dedicated to an extensive comparison of parameter choice methods, by means of both numerical and experimental validations. It has been shown that, the Bayesian regularization criterion provides a very robust tuning of the regularization parameter for varied acoustical conditions.

Given the analysis of the various regularization aspects, we have studied the application to noise source identification in closed spaces. At an early stage we were faced to two main difficulties, the first one related to the positioning of the microphone array inside the enclosure and the second related to the highly underdetermined aspect of the problem. An iterative weighted equivalent source method has then been proposed to overcome these difficulties. The method is basically dependent on two weighting schemes: (1) a first weighting strategy to take into account the positioning of the microphone array inside the enclosure; (2) a second weighting strategy which is data dependent and implemented iteratively.

The proposed method was then tested by extensive numerical simulations and it was shown that undesirable effects related to the array positioning were eliminated by the first weighting strategy. In addition, it was shown that only the iterative weighted ESM was able to provide reasonable quantification results for the underlying problem. In particular, we have shown that the solution obtained by classical ESM, when applied to highly underdetermined systems, was not realistic. The identified sources presented a hyper directivity towards the direction in which the array was placed. Consequently, the estimates of the radiated acoustic power largely underestimated the reference acoustic power.

Afterwards, we have studied the sensitivity of the approach with respect to non-anechoic conditions and to the distribution of equivalent sources. The first study has shown us that the method is disturbed by reverberation paths, in the sense that reflections are identified as “real” sources. Indeed, this is the price to pay for the simplifications in the model, namely the consideration of free-field propagation between equivalent sources and receivers. However, we have shown that for a mildly reverberant scenario, the proposed approach is still able to provide relatively good results in terms of source localization. In terms of source quantification, it was shown that the estimates of the acoustic power were disturbed by interferences between direct and reverberant paths. These interferences particularly appeared at frequencies multiple of the propagation distance between direct and reverberant path. Finally, we have illustrated the application of an approach based on the causality analysis of identified sources. It was shown that this approach can be used as a post-processing tool in order to identify those “hot spots” corresponding to direct or reverberant paths.

The last part of this thesis was dedicated to experimental validations and a practical application of the method. A rigid spherical array with 31 microphones has been built for the experimental tests. Both weighting strategies have been validated by means of academic experiments. In particular, we have noticed a limit of the proposed approach in terms of acoustic power quantification when the radiation pattern of real sources differs considerably from an omni-directional behavior. The limitation is not directly related to the radiation pattern itself, but it rather depends on the position of the array relative to the radiation pattern. This is because the recording of acoustic pressure is made with the array at a single position within the room. Consequently, if the array is placed on the direction of a directivity null of the real source, little energy will be perceived by the microphones and thus the global acoustic power is underestimated.

An experimental technique based on multi-pass measurements with a spherical array has also been reported. The approach is based on sequential acquisition by rotating the spherical array a given angle around its axis. Intended to stationary conditions, this approach allows to decrease the inter-microphone spacing used to sample the acoustic pressure and thus increase the high frequency limit of the array.

Finally, as a practical application, the approach was tested for noise source identification inside a bus at driving conditions. The aim was to locate the potential acoustical weakness which contributes to the overall noise level inside the bus. This application allowed us to show the advantages of the proposed approach, namely the correction for the array positioning and the improvement of spatial resolution and dynamic range.

Suggestions for further research

As we have seen, the application of acoustic imaging techniques to source identification inside closed spaces poses several difficulties. In this context, an iterative weighted approach has been proposed to overcome some of these difficulties. Reasonable quantification of the acoustic power was only possible using the iterative solution. It was shown that this is related to the highly underdetermined aspect of the problem that we seek to solve. In particular, the identified sources provided a good reconstruction of the acoustic pressure measured on the sphere but an incorrect reconstruction outside this region. In other words, the identified sources concentrated all their radiated energy towards the microphone array. In view of the above considerations, it would be of relevance to somehow impose an *a priori* requirement for the reconstruction to be acceptable not only on the measurement surface but elsewhere within the enclosure.

In order to overcome the difficulties related to the highly underdetermined aspect of the problem, techniques which impose an *a priori* of sparsity to regularize the problem might be appropriate, such as the work carried out by A. Peillot [Pei12] and N. Chu *et al.* [CPMD11, CMDP13]. Since in the formulation used throughout this thesis the number of real sources is largely inferior than the number of equivalent or candidate sources, we can assume that the source field is sparse on the reconstruction space. In terms of the mathematical formulation, instead of minimizing the l_2 norm (i.e. the energy) of the source field, the new problem would consist in minimizing its l_1 norm. Unlike the l_2 norm minimization, there is no closed form solution for the l_1 minimization problem, and thus one has to resort to more sophisticated and complex algorithms. In case the equivalent source basis cannot be assumed as a sparse, it would be necessary to find a basis which sparsely represents the source field.

On the other hand, the issue related to the frequency dependent directivity pattern of real sources seems more difficult to answer. A possible solution would be to use a similar approach such as the one presented by Castellini [CS10], in which measurements are carried out at several positions within the room. This would ensure that the array perceives enough energy radiated by the source. A refraining difficulty, however, would be the synchronization of non-simultaneous measurements. Indeed, the possibility to synchronize measurements without the need of as many references as incoherent phenomena is another perspective for further research.

A

Glossary

A.1 List of Acronyms

BEM	Boundary Element Method
DOF	Degrees of Freedom
DPC	Discrete Picard Condition
ESM	Equivalent Source Method
FEM	Finite Element Method
GCV	Generalized Cross-Validation
HELS	Helmholtz equation least-squares
hNAH	Hybrid Near-field Acoustical Holography
iBEM	inverse Boundary Element Method
iPTF	inverse Patch Transfer Function
ISM	Image Source Method
MAP	maximum a posteriori
NAH	Near-field Acoustical Holography
NCP	Normalized Cumulative Periodgram
NSR	Noise-to-Signal Ratio
pdf	probability density function
SHB	Spherical Harmonics Beamforming
SNR	Signal-to-Noise Ratio
SONAH	Statistically optimized near-field acoustic holography
SVD	Singular Value Decomposition
TSVD	Truncated Singular Value Decomposition

A.2 Notations

x	scalar quantity
$\mathbf{x}$	vector quantity
$\mathbf{X}$	matrix quantity

A.3 Operators

$\lvert x \rvert$	absolute value of x
$\lVert \cdot \rVert$	l_2 norm of a vector
$\mathbf{x} \cdot \mathbf{y}$	dot product between two vectors
$\mathbf{x} \times \mathbf{y}$	cross product between two vectors
$\mathbf{x}^*$	conjugate of vector $\mathbf{x}$
$\mathbf{x}^T$	transpose of vector $\mathbf{x}$
$\mathbf{x}^H$	conjugate transpose of vector $\mathbf{x}$
$\overline{\mathbf{X}}$	conjugate of matrix $\mathbf{X}$
$\mathbb{E}\{\cdot\}$	expected value
$\Re\{\cdot\}$	real part of a complex number

A.4 Symbols and Variables

j	imaginary unit ($\mathrm{j} = \sqrt{-1}$)
c	speed of sound
λ	wavelength
ω	angular frequency in rad/s
k	wave number
ρ	density of the fluid
$\mathcal{N}_\mathcal{C}$	complex Normal distribution

A.5 Special functions

$j_l(\cdot)$	spherical Bessel function of order l
$h_l^{(2)}(\cdot)$	spherical Hankel function of second kind and order l
$j_l'(\cdot)$	first derivative of the spherical Bessel function
$h_l'^{(2)}(\cdot)$	first derivative of the spherical Hankel function of second kind
$Y_l^m(\cdot)$	spherical harmonics of order l and degree m
$P_l(\cdot)$	Legendre polynomial of order l

B

Spherical radial functions

In this appendix we present the spherical radial functions employed throughout this thesis. As we have seen, any spherical radial function is the solution to the spherical Bessel equation. However, the choice of appropriate solutions for a given problem is made in order to satisfy certain conditions as $r \to 0$ or $r \to \infty$. The spherical Bessel function $j_l(kr)$ is the only solution which is regular at $kr = 0$, therefore it is appropriate to describe interior boundary value problems. The solution for pure exterior problems must be selected in order to satisfy the Sommerfeld radiation condition, which for a time-harmonic dependence of $e^{\mathrm{j}wt}$, is given by [GD05]:

$$\lim_{r\to\infty} r\left(\frac{\partial p(\mathbf{r})}{\partial r} + \mathrm{j}p(\mathbf{r})\right) = 0. \tag{B.1}$$

The only solution which satisfies this condition is the spherical Hankel function of the second kind $h_l^{(2)}(kr)$, thus justifying the set of solutions used in equation (2.33).

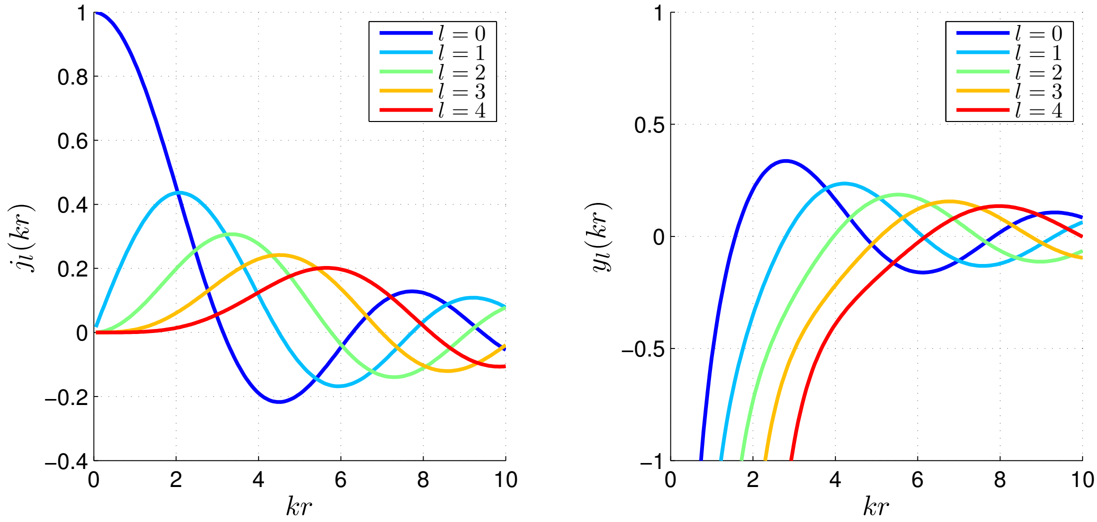

Figure B.1: Spherical radial functions: (left) spherical Bessel function $j_l(kr)$; (right) spherical Bessel function of the second kind or spherical Neumann function $y_l(kr)$. Notice that these are real-valued functions and they represent standing wave type solutions of the Helmholtz equation. Notice also the singularity of the spherical Neumann function when kr approaches 0.

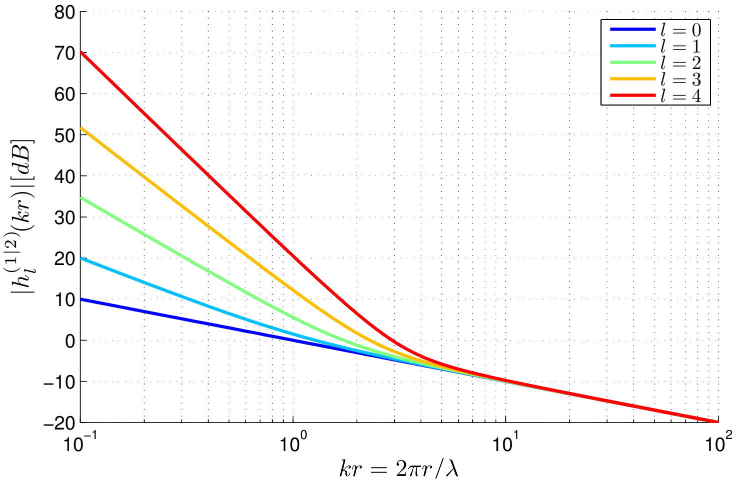

Figure B.2: Magnitude of the spherical Hankel functions $|h_l^{(1|2)}(kr)|$. Notice that higher-order components decay quickly with increasing kr. These functions represent traveling wave type solutions of the Helmholtz equation.

C

Derivation of source field estimate

C.1 Derivation of ĉ estimate

The aim of this Section is to detail the algebraic manipulations necessary to obtain the estimate of the source field $\hat{\mathbf{c}}$. Our goal is to provide an equivalent expression for the following estimate:

$$\hat{\mathbf{c}} = (\mathbf{H}^H \mathbf{\Omega}_n^{-1} \mathbf{H} + \eta^2 \mathbf{\Omega}_c^{-1})^{-1} \mathbf{H}^H \mathbf{\Omega}_n^{-1} \mathbf{p}. \tag{C.1}$$

As previously stated we will make use of the following matrix inversion lemma:

$$(\mathbf{A} + \mathbf{BCD})^{-1} = \mathbf{A}^{-1} - \mathbf{A}^{-1}\mathbf{B}(\mathbf{C}^{-1} + \mathbf{D}\mathbf{A}^{-1}\mathbf{B})^{-1}\mathbf{D}\mathbf{A}^{-1}. \tag{C.2}$$

Applying equation (C.2) to the term in brackets from equation (C.1) and with the following corresponding matrices

$$\mathbf{A} = \eta^2 \mathbf{\Omega}_c^{-1}, \quad \mathbf{B} = \mathbf{H}^H, \quad \mathbf{C} = \mathbf{\Omega}_n^{-1}, \quad \mathbf{D} = \mathbf{H},$$

yields

$$\begin{aligned}
\hat{\mathbf{c}} &= \left\{\eta^{-2}\mathbf{\Omega}_c - \eta^{-2}\mathbf{\Omega}_c\mathbf{H}^H(\mathbf{\Omega}_n + \eta^{-2}\mathbf{H}\mathbf{\Omega}_c\mathbf{H}^H)^{-1}\eta^{-2}\mathbf{H}\mathbf{\Omega}_c\right\}\mathbf{H}^H\mathbf{\Omega}_n^{-1}\mathbf{p} \\
&= \eta^{-2}\mathbf{\Omega}_c\mathbf{H}^H(\mathbf{\Omega}_n + \eta^{-2}\mathbf{H}\mathbf{\Omega}_c\mathbf{H}^H)^{-1}\left\{(\mathbf{\Omega}_n + \eta^{-2}\mathbf{H}\mathbf{\Omega}_c\mathbf{H}^H)\mathbf{\Omega}_n^{-1} - \eta^{-2}\mathbf{H}\mathbf{\Omega}_c\mathbf{H}^H\mathbf{\Omega}_n^{-1}\right\}\mathbf{p} \\
&= \eta^{-2}\mathbf{\Omega}_c\mathbf{H}^H(\mathbf{\Omega}_n + \eta^{-2}\mathbf{H}\mathbf{\Omega}_c\mathbf{H}^H)^{-1}\mathbf{p},
\end{aligned}$$

where in the second equality the term in curly brackets simplified to identity. Introducing the constant η^{-2} into the term in brackets in the last equality, gives us

$$\hat{\mathbf{c}} = \mathbf{\Omega}_c\mathbf{H}^H\left(\mathbf{H}\mathbf{\Omega}_c\mathbf{H}^H + \eta^2\mathbf{\Omega}_n\right)^{-1}\mathbf{p}, \tag{C.3}$$

which is the same expression as given in equation (3.18).

D

Proofs of some propositions

D.1 Proof of Proposition 1

The goal is to compute integral

$$[\mathbf{p}|\alpha^2, \beta^2] = \int [\mathbf{p}|\mathbf{c}, \beta^2][\mathbf{c}|\alpha^2] d\mathbf{c} = \int \mathcal{N}_{\mathcal{C}}(\mathbf{Hc}, \beta^2 \mathbf{\Omega}_n) \mathcal{N}_{\mathcal{C}}(\mathbf{0}, \alpha^2 \mathbf{\Omega}_c) d\mathbf{c}. \tag{D.1}$$

A direct calculation based on expanding the product of the Gaussians and "completing the square" is fastidious, although not difficult. A more direct proof proceeds as follows. Let us first suppose that $(K - M)$ extra measurements are taken (while keeping the number of coefficients c_k's constant), thus producing the extended vectors $\mathbf{p}_a \in \mathbb{C}^K$, $\mathbf{n}_a \in \mathbb{C}^K$, and matrices $\mathbf{\Omega}_{n,a} \in \mathbb{C}^{K \times K}$ and $\mathbf{H}_a \in \mathbb{C}^{K \times K}$, where $\mathbf{H}_a$ is supposed of full-rank. Solving for this new problem requires computing the integral

$$\begin{aligned} \int [\mathbf{p}_a|\mathbf{c}, \beta^2][\mathbf{c}|\alpha^2] d\mathbf{c} &= \int [\mathbf{n}_a = \mathbf{p}_a - \mathbf{H}_a \mathbf{c}|\beta^2][\mathbf{H}_a \mathbf{c}|\alpha^2] d(\mathbf{H}_a \mathbf{c}) \\ &= \int [\mathbf{p}_a|\mathbf{H}_a \mathbf{c}, \beta^2][\mathbf{H}_a \mathbf{c}|\alpha^2] d(\mathbf{H}_a \mathbf{c}) \end{aligned} \tag{D.2}$$

wherein $[\mathbf{n}_a = \mathbf{p}_a - \mathbf{H}_a \mathbf{c}|\beta^2]$ stands for the pdf of $\mathbf{n}_a$ evaluated at $\mathbf{p}_a - \mathbf{H}_a \mathbf{c}$ and the change of variable $\mathbf{c} \mapsto \mathbf{H}_a \mathbf{c}$ was used. From first principles of probability calculus, integral (D.2) is recognized as the pdf of the sum of two random variables, i.e. $\mathbf{p}_a = \mathbf{H}_a \mathbf{c} + \mathbf{n}_a$, with pdf's $[\mathbf{H}_a \mathbf{c}|\alpha^2] = \mathcal{N}_{\mathcal{C}}(\mathbf{0}, \alpha^2 \mathbf{H}_a \mathbf{\Omega}_c \mathbf{H}_a^H)$ and $[\mathbf{n}_a|\beta^2] = \mathcal{N}_{\mathcal{C}}(\mathbf{0}, \beta^2 \mathbf{\Omega}_{n,a})$, respectively. The sum of two independent Gaussian random variables is again a Gaussian [Pre05], with mean equal to the sum of their individual means and similarly for its covariance. Therefore,

$$[\mathbf{p}_a|\alpha^2, \beta^2] = \mathcal{N}_{\mathcal{C}}(\mathbf{0}, \alpha^2 \mathbf{H}_a \mathbf{\Omega}_c \mathbf{H}_a^H + \beta^2 \mathbf{\Omega}_{n,a}). \tag{D.3}$$

The last point is to marginalize the above pdf over the $(K - M)$ extra measurements. As well-known for Gaussian distributions, this is simply $\mathcal{N}_{\mathcal{C}}(\mathbf{0}, \alpha^2 \mathbf{H} \mathbf{\Omega}_c \mathbf{H}^H + \beta^2 \mathbf{\Omega}_n)$ [Pre05].

Next, expression (3.23b) is easily obtained using the singular value decomposition given in equation (3.19).

D.2 Proof of Proposition 2

The integral to be evaluated is

$$\begin{aligned}
[\eta^2|\mathbf{p}] &= \int [\eta^2,\alpha^2|\mathbf{p}]d\alpha^2 = \int [\alpha^2,\beta^2|\mathbf{p}] \underbrace{\left|\frac{d\beta^2}{d\eta^2}\right|}_{\alpha^2} d\alpha^2 \\
&\propto \int [\mathbf{p}|\alpha^2,\beta^2][\alpha^2,\beta^2]\alpha^2 d\alpha^2 \\
&\propto \int \mathcal{N}_{\mathcal{C}}(\mathbf{0},\alpha^2(\mathbf{H}\boldsymbol{\Omega}_c\mathbf{H}^H + \eta^2\boldsymbol{\Omega}_n))\alpha^2 d\alpha^2 \qquad \text{(D.4)}
\end{aligned}$$

where it was assumed that $[\alpha^2,\beta^2] \propto 1$ as discussed in section 3.4.1.2. Now, using equation (3.23b) we have,

$$[\eta^2|\mathbf{p}] \propto \frac{1}{\eta^2 \prod_{k=1}^{M}(s_k^2+\eta^2)} \int_0^\infty \frac{\exp\left(-M\hat{\alpha}^2/\alpha^2\right)}{\alpha^{2(M-1)}} d\alpha^2 \qquad \text{(D.5)}$$

with $\hat{\alpha}^2$ as given in equation (3.29). The integral in the above equation is

$$\Gamma(M-2)(M\hat{\alpha}^2)^{-(M-2)}, \quad M > 1,$$

thus proving equation (3.32). Notice that quantities not depending explicitly on η^2 have been factored out in (3.32).

D.3 Proof of Proposition 3

Let us expand $\mathbf{J}_{\text{MAP}}(\eta^2)$ in Eq. (3.34) into a second order Taylor series about $\hat{\eta}^2_{\text{MAP}}$:

$$\mathbf{J}_{\text{MAP}}(\eta^2) = \mathbf{J}_{\text{MAP}}(\hat{\eta}^2_{\text{MAP}}) + \frac{|\eta^2-\hat{\eta}^2_{\text{MAP}}|^2}{2}\left(\frac{d^2\mathbf{J}_{\text{MAP}}(\hat{\eta}^2_{\text{MAP}})}{(d\eta^2)^2}\right)_{\eta^2=\hat{\eta}^2_{\text{MAP}}} + \mathcal{O}\left(|\eta^2-\hat{\eta}^2_{\text{MAP}}|^3\right) \qquad \text{(D.6)}$$

where $d\mathbf{J}_{\text{MAP}}(\eta^2)/d\eta^2|_{\eta^2=\hat{\eta}^2_{\text{MAP}}} = 0$ (by definition of $\hat{\eta}^2_{\text{MAP}}$) has been used and $\mathcal{O}$ means "on the order of". Therefore,

$$[\eta^2|\mathbf{p}] \propto \exp\left(-\mathbf{J}_{\text{MAP}}(\eta^2)\right) \approx \exp\left(-\frac{|\eta^2-\hat{\eta}^2_{\text{MAP}}|^2}{2}\frac{d^2\mathbf{J}_{\text{MAP}}(\hat{\eta}^2_{\text{MAP}})}{(d\eta^2)^2}\right), \qquad \text{(D.7)}$$

which proves Proposition 3.

Bibliography

[AB79] J. B. Allen and D. A. Berkley, "Image method for efficiently simulating small-room acoustics," *The Journal of the Acoustical Society of America*, vol. 65, no. 4, pp. 943–950, 1979.

[Ant12] J. Antoni, "A bayesian approach to sound source reconstruction: Optimal basis, regularization, and focusing," *The Journal of the Acoustical Society of America*, vol. 131, no. 4, pp. 2873–2890, 2012.

[AR12] D. L. Alon and B. Rafaely, "Spindle-torus sampling for an efficient-scanning spherical microphone array," *Acta Acustica united with Acustica*, vol. 98, no. 1, pp. 83–90, 2012.

[AT76] V. Arsénine and A. Tikhonov, *Méthodes de résolution de problèmes mal posés.* Editions Mir, Moscou, 1976.

[AW02] T. Abhayapala and D. B. Ward, "Theory and design of high order sound field microphones using spherical microphone array," in *Acoustics, Speech, and Signal Processing (ICASSP), 2002 IEEE International Conference on*, vol. 2, 2002, pp. II–1949–II–1952.

[Bai92] M. R. Bai, "Application of bem (boundary element method)-based acoustic holography to radiation analysis of sound sources with arbitrarily shaped geometries," *The Journal of the Acoustical Society of America*, vol. 92, no. 1, pp. 533–549, 1992.

[BCC08] C.-X. Bi, X.-Z. Chen, and J. Chen, "Sound field separation technique based on equivalent source method and its application in nearfield acoustic holography," *The Journal of the Acoustical Society of America*, vol. 123, no. 3, pp. 1472–1478, 2008.

[BDH96] C. B. Barber, D. P. Dobkin, and H. Huhdanpaa, “The quickhull algorithm for convex hulls,” *ACM TRANSACTIONS ON MATHEMATICAL SOFTWARE*, vol. 22, no. 4, pp. 469–483, 1996.

[BF09] F. S. V. Bazan and J. B. Francisco, “An improved fixed-point algorithm for determining a tikhonov regularization parameter,” *Inverse Problems*, vol. 25, no. 4, p. 045007, 2009.

[BH06] T. F. Brooks and W. M. Humphreys, “A deconvolution approach for the mapping of acoustic sources (damas) determined from phased microphone arrays,” *Journal of Sound and Vibration*, vol. 294, no. 4-5, pp. 856 – 879, 2006.

[BK76] J. Billingsley and R. Kinns, “The acoustic telescope,” *Journal of Sound and Vibration*, vol. 48, no. 4, pp. 485 – 510, 1976.

[BK98] B.-K. Bae and K.-J. Kim, “A hilbert transform approach in source identification via multiple-input single-output modeling for correlated inputs,” *Mechanical Systems and Signal Processing*, vol. 12, no. 4, pp. 501 – 513, 1998.

[BL11] F. Bauer and M. A. Lukas, “Comparing parameter choice methods for regularization of ill-posed problems,” *Mathematics and Computers in Simulation*, vol. 81, no. 9, pp. 1795 – 1841, 2011.

[BR07] I. Balmages and B. Rafaely, “Open-sphere designs for spherical microphone arrays,” *Audio, Speech, and Language Processing, IEEE Transactions on*, vol. 15, no. 2, pp. 727 –732, feb. 2007.

[Bra83] D. H. Brandwood, “A complex gradient operator and its application in adaptive array theory,” *Communications, Radar and Signal Processing, IEE Proceedings F*, vol. 130, no. 1, pp. 11–16, 1983.

[CDP+12] G. Chardon, L. Daudet, A. Peillot, F. Ollivier, N. Bertin, and R. Gribonval, “Near-field acoustic holography using sparse regularization and compressive sampling principles,” *The Journal of the Acoustical Society of America*, vol. 132, no. 3, pp. 1521–1534, 2012.

[CDPL12] C. Cariou, O. Delverdier, S. Paillasseur, and L. Lamotte, “Tool for interior noise sources detection in aircraft with comparison of configurations,” in *Proceedings of BeBeC-2012. February*, 2012.

[CG11] G. Cerrato and P. Goodes, “Practical approaches to solving noise and vibration problems,” *Sound and Vibration*, vol. 45, no. 4, p. 18, 2011.

[CLG10] J.-L. L. Carrou, Q. Leclère, and F. Gautier, “Some characteristics of the concert harp’s acoustic radiation,” *The Journal of the Acoustical Society of America*, vol. 127, no. 5, pp. 3203–3211, 2010.

[CMDP13] N. Chu, A. Mohammad-Djafari, and J. Picheral, “Robust bayesian super-resolution approach via sparsity enforcing a priori for near-field aeroacoustic source imaging,” *Journal of Sound and Vibration*, vol. http://dx.doi.org/10.1016/j.jsv.2013.02.037i, no. 0, 2013.

[CPMD11] N. Chu, J. Picheral, and A. Mohammad-Djafari, “A robust super-resolution approach with sparsity constraint for near-field wideband acoustic imaging,” in *Signal Processing and Information Technology (ISSPIT), 2011 IEEE International Symposium on*, 2011, pp. 310–315.

[Cra46] H. Cramer, *Mathematical methods of statistics.* Princeton University Press, 1946.

[CS08] D. Calvetti and E. Somersalo, *Introduction to Bayesian Scientific Computing*, ser. Surveys and Tutorials in the Applied Mathematical Sciences. Springer Science+Business Media, 2008.

[CS10] P. Castellini and A. Sassaroli, “Acoustic source localization in a reverberant environment by average beamforming,” *Mechanical Systems and Signal Processing*, vol. 24, no. 3, pp. 796 – 808, 2010.

[CSP+13] P. Castellini, A. Sassaroli, A. Paonessa, A. Peiffer, and A. Roeder, “Average beamforming in reverberant fields: Application on helicopter and airplane cockpits,” *Applied Acoustics*, vol. 74, no. 1, pp. 198 – 210, 2013.

[CTT07] H. G. Choi, A. N. Thite, and D. J. Thompson, “Comparison of methods for parameter selection in tikhonov regularization with application to inverse force determination,” *Journal of Sound and Vibration*, vol. 304, no. 3-5, pp. 894 – 917, 2007.

[dat] http://lva.insa-lyon.fr/data-jsv-2013-pereira.

[dB03] H.-E. de Bree, “The microflown: An acoustic particle velocity sensor,” *Acoustics Australia*, vol. 31, no. 3, pp. 91–94, 2003.

[dBB08] H. de Bree and T. Basten, “Microflown based monopole sound sources for reciprocal measurements,” *SAE Technical Paper*, vol. 2008-36-0503, 2008.

[DBHW95] S. Dumbacher, J. Blough, D. Hallman, and P. Wang, "Source identification using acoustic array techniques," *SAE Noise and Vibration Conference*, vol. 2, pp. 1023–1035, May 1995.

[del] http://en.wikipedia.org/wiki/Delaunay_triangulation.

[DM98] R. O. Duda and W. L. Martens, "Range dependence of the response of a spherical head model," *The Journal of the Acoustical Society of America*, vol. 104, no. 5, pp. 3048–3058, 1998.

[Fah00] F. Fahy, *Foundations of engineering acoustics.* Academic Press, 2000, chap. 6, pp. 129-134.

[Fen09] B. A. Fenech, "Accurate aeroacoustic measurements in closed-section hard-walled wind tunnels," Ph.D. dissertation, University of Southampton, June 2009.

[FGJ11] E. Fernandez-Grande and F. Jacobsen, "Sound field separation with a double layer velocity transducer array (l)," *The Journal of the Acoustical Society of America*, vol. 130, no. 1, pp. 5–8, 2011.

[FGJL12] E. Fernandez-Grande, F. Jacobsen, and Q. Leclere, "Sound field separation with sound pressure and particle velocity measurements," *The Journal of the Acoustical Society of America*, vol. 132, no. 6, pp. 3818–3825, 2012.

[FM99] J. Fliege and U. Maier, "The distribution of points on the sphere and corresponding cubature formulae," *IMA Journal of Numerical Analysis*, vol. 19, no. 2, pp. 317–334, 1999.

[GB88] B. Gardner and R. Bernhard, "A noise source identification technique using an inverse helmholtz integral equation method," *Journal of Vibration Acoustics Stress and Reliability in Design*, vol. 110, p. 84, 1988.

[GBL$^+$12] A. Garcia, Y. Braikia, C. Langrenne, E. Bavu, M. Melon, and G. Visible, "Source identification in small spaces using field separation method: application to a car trunk," *Proceedings of Acoustics 2012, Nantes, France*, 2012.

[GCP$^+$11] P.-A. Gauthier, C. Camier, Y. Pasco, A. Berry, E. Chambatte, R. Lapointe, and M.-A. Delalay, "Beamforming regularization matrix and inverse problems applied to sound field measurement and extrapolation using microphone array," *Journal of Sound and Vibration*, vol. 330, no. 24, pp. 5852 – 5877, 2011.

[GD01] N. Gumerov and R. Duraiswami, “Modeling the effect of a nearby boundary on the hrtf,” in *Acoustics, Speech, and Signal Processing, 2001. Proceedings. (ICASSP ’01). 2001 IEEE International Conference on*, vol. 5, 2001, pp. 3337–3340 vol.5.

[GD05] N. Gumerov and R. Duraiswami, *Fast Multipole Methods for the Helmholtz Equation in Three Dimensions*, ser. Elsevier Series in Electromagnetism. Elsevier Science, 2005.

[GH08] J. Gomes and P. Hansen, “A study on regularization parameter choice in near-field acoustical holography,” in *Proceedings of Acoustics’08, Paris, France*, 2008.

[GHW79] G. H. Golub, M. Heath, and G. Wahba, “Generalized cross-validation as a method for choosing a good ridge parameter,” *Technometrics*, vol. 21, no. 2, pp. 215–223, 1979.

[Gom08] J. Gomes, “A study on regularization parameter choice in near-field acoustical holography,” *The Journal of the Acoustical Society of America*, vol. 123, no. 5, pp. 3385–3385, 2008.

[Hal06] J. Hald, “Patch holography in cabin environments using a two-layer handheld array with an extended sonah algorithm,” in *Proceedings of Euronoise 2006 (Tampere, Finland).*, 2006.

[Hal09] J. Hald, “Basic theory and properties of statistically optimized near-field acoustical holography,” *The Journal of the Acoustical Society of America*, vol. 125, no. 4, pp. 2105–2120, 2009.

[Han90] P. C. Hansen, “The discrete picard condition for discrete ill-posed problems,” *BIT*, vol. 30, no. 4, pp. 658–672, 1990.

[Han92] P. C. Hansen, “Analysis of discrete ill-posed problems by means of the l-curve,” *SIAM Rev.*, vol. 34, no. 4, pp. 561–580, Dec. 1992.

[Han98] P. Hansen, *Rank-Deficient and Discrete Ill-Posed Problems.* Philadephia, PA: Society for Industrial and Applied Mathematics, 1998.

[Han10] P. Hansen, *Discrete Inverse Problems: Insight and Algorithms*, ser. Fundamentals of algorithms. Society for Industrial and Applied Mathematics (SIAM, 3600 Market Street, Floor 6, Philadelphia, PA 19104), 2010.

[HBD⁺94] D. Hallman, J. Bolton, S. Dumbacher, D. Brown, B. Libbey, and M. Lally, "Acoustic source location in vehicle cabins and free-field with nearfield acoustical holography via acoustic arrays," in *Proc. of the 19th International Seminar on Modal Analysis, Leuven, Belgium, September 1994*, 1994.

[HH08] K. Haddad and J. Hald, "3d localization of acoustic sources with a spherical array," in *Proceedings of Acoustics'08, Paris, France*, 2008.

[Hjø11] A. Hjørungnes, *Complex-valued matrix derivatives: with applications in signal processing and communications.* Cambridge University Press, 2011.

[HKK06] P. C. Hansen, M. E. Kilmer, and R. H. Kjeldsen, "Exploiting residual information in the parameter choice for discrete ill-posed problems," *BIT Numerical Mathematics*, vol. 46, pp. 41–59, 2006.

[HN03] K. Holland and P. Nelson, "Sound source characterisation: The focussed beamformer vs the inverse method," in *Tenth International Congress on Sound and Vibration*, 2003.

[HN12] K. Holland and P. Nelson, "An experimental comparison of the focused beamformer and the inverse method for the characterisation of acoustic sources in ideal and non-ideal acoustic environments," *Journal of Sound and Vibration*, vol. 331, no. 20, pp. 4425 – 4437, 2012.

[HO93] P. C. Hansen and D. P. O'Leary, "The use of the l-curve in the regularization of discrete ill-posed problems," *SIAM J. Sci. Comput.*, vol. 14, pp. 1487–1503, November 1993.

[HR12] M. E. Hochstenbach and L. Reichel, "Combining approximate solutions for linear discrete ill-posed problems," *Journal of Computational and Applied Mathematics*, vol. 236, no. 8, pp. 2179 – 2185, 2012.

[HS96] R. Hardin and N. J. A. Sloane, "Mclaren's improved snub cube and other new spherical designs in three dimensions," *Discrete & Computational Geometry*, vol. 15, no. 4, pp. 429–441, 1996.

[JD93] D. H. Johnson and D. E. Dudgeon, *Array Signal Processing: Concepts and Techniques*, facsimile ed. Prentice Hall, Feb. 1993.

[JEBGB98] M. E. Johnson, S. J. Elliott, K.-H. Baek, and J. Garcia-Bonito, "An equivalent source technique for calculating the sound field inside an enclosure containing scattering objects," *The Journal of the Acoustical Society of America*, vol. 104, no. 3, pp. 1221–1231, 1998.

[JJ07] F. Jacobsen and V. Jaud, “Statistically optimized near field acoustic holography using an array of pressure-velocity probes,” *The Journal of the Acoustical Society of America*, vol. 121, no. 3, pp. 1550–1558, 2007.

[JM92] R. Jeans and I. C. Mathews, “The wave superposition method as a robust technique for computing acoustic fields,” *The Journal of the Acoustical Society of America*, vol. 92, no. 2, pp. 1156–1166, 1992.

[Kam92] D. C. Kammer, “Effects of noise on sensor placement for on-orbit modal identification of large space structures,” *Journal of dynamic systems, measurement, and control*, vol. 114, no. 3, pp. 436–443, 1992.

[KI96] B.-K. Kim and J.-G. Ih, “On the reconstruction of the vibro-acoustic field over the surface enclosing an interior space using the boundary element method,” *The Journal of the Acoustical Society of America*, vol. 100, no. 5, pp. 3003–3016, 1996.

[KN04] Y. Kim and P. A. Nelson, “Optimal regularisation for acoustic source reconstruction by inverse methods,” *Journal of Sound and Vibration*, vol. 275, no. 3-5, pp. 463 – 487, 2004.

[KSF89] G. H. Koopmann, L. Song, and J. B. Fahnline, “A method for computing acoustic fields based on the principle of wave superposition,” *The Journal of the Acoustical Society of America*, vol. 86, no. 6, pp. 2433–2438, 1989.

[LD07] Z. Li and R. Duraiswami, “Flexible and optimal design of spherical microphone arrays for beamforming,” *Audio, Speech, and Language Processing, IEEE Transactions on*, vol. 15, no. 2, pp. 702–714, 2007.

[Lec09] Q. Leclère, “Acoustic imaging using under-determined inverse approaches: Frequency limitations and optimal regularization,” *Journal of Sound and Vibration*, vol. 321, no. 3-5, pp. 605 – 619, 2009.

[Les88] C. Lesueur, *Rayonnement acoustique des structures: vibroacoustique, interactions fluide-structure*, ser. Collection de la Direction des études et recherches d’Électricité de France. Eyrolles, 1988.

[LL10] X. Li and S. Law, “Adaptive tikhonov regularization for damage detection based on nonlinear model updating,” *Mechanical Systems and Signal Processing*, vol. 24, no. 6, pp. 1646 – 1664, 2010.

[LMG07] C. Langrenne, M. Melon, and A. Garcia, “Boundary element method for the acoustic characterization of a machine in bounded noisy environment,” *The*

Journal of the Acoustical Society of America, vol. 121, no. 5, pp. 2750–2757, 2007.

[LMG09] C. Langrenne, M. Melon, and A. Garcia, “Measurement of confined acoustic sources using near-field acoustic holography,” *The Journal of the Acoustical Society of America*, vol. 126, no. 3, pp. 1250–1256, 2009.

[LPLP05] Q. Leclère, C. Pézerat, B. Laulagnet, and L. Polac, “Application of multi-channel spectral analysis to identify the source of a noise amplitude modulation in a diesel engine operating at idle,” *Applied Acoustics*, vol. 66, no. 7, pp. 779 – 798, 2005.

[MD06] A. Meyer and D. Döbler, “Noise source localization within a car interior using 3d-microphone arrays,” in *Berlin Beamforming Conference, Berlin, Germany*, 2006.

[Mic06] U. Michel, “History of acoustic beamforming,” in *Proceedings of BeBeC-2006*, 2006.

[MNA84] V. A. Morozov, Z. Nashed, and A. Aries, *Methods for solving incorrectly posed problems.* Springer-Verlag New York, 1984.

[MT04] M. B. S. Magalhaes and R. A. Tenenbaum, “Sound sources reconstruction techniques: A review of their evolution and new trends,” *Acta Acustica united with Acustica*, vol. 90, no. 2, pp. 199–220, 2004.

[MW02] M. Moondra and S. F. Wu, “Visualization of vehicle interior noise using hels based nah,” in *Proceedings of INTER-NOISE 2002, Dearborn, USA*, 2002.

[MWL85] J. D. Maynard, E. G. Williams, and Y. Lee, “Nearfield acoustic holography: I. theory of generalized holography and the development of nah,” *The Journal of the Acoustical Society of America*, vol. 78, pp. 1395–1413, 1985.

[NY00] P. A. Nelson and S. H. Yoon, “Estimation of acoustic source strength by inverse methods: Part i, conditioning of the inverse problem,” *Journal of Sound and Vibration*, vol. 233, no. 4, pp. 639 – 664, 2000.

[Pei12] A. Peillot, “Imagerie acoustique par approximations parcimonieuses des sources,” Ph.D. dissertation, Université Pierre et Marie Curie-Paris VI, 2012.

[PL03] J.-C. Pascal and J.-F. Li, “On the use of double layer beamforming antenna for industrial applications,” in *Proceedings of Euronoise 2003 (Naples, Italy)*, 2003.

[PL06] J.-C. Pascal and J.-F. Li, “Use of double layer beamforming antenna to identify and locate noise sources in cabins,” in *Proceedings of Euronoise 2006 (Tampere, Finland)*, 2006.

[Plu05] J. Plunt, “Finding and fixing vehicle nvh problems with transfer path analysis,” *Sound and Vibration*, vol. 39, no. 11, pp. 12–17, 2005.

[Pre05] S. Press, *Applied Multivariate Analysis: Using Bayesian And Frequentist Methods Of Inference*, ser. Dover Books on Mathematics Series. Dover Publications, 2005.

[Raf05] B. Rafaely, “Analysis and design of spherical microphone arrays,” *Speech and Audio Processing, IEEE Transactions on*, vol. 13, no. 1, pp. 135 – 143, jan. 2005.

[RO08] B. W. Rust and D. P. O’Leary, “Residual periodograms for choosing regularization parameters for ill-posed problems,” *Inverse Problems*, vol. 24, no. 3, p. 034005, 2008.

[Rob01] C. Robert, *The Bayesian Choice: From Decision-Theoretic Foundations to Computational Implementation*, ser. Springer Texts in Statistics. Springer, 2001.

[RWB07] B. Rafaely, B. Weiss, and E. Bachmat, “Spatial aliasing in spherical microphone arrays,” *Signal Processing, IEEE Transactions on*, vol. 55, no. 3, pp. 1003 –1010, march 2007.

[SHRH03] A. Schuhmacher, J. Hald, K. B. Rasmussen, and P. C. Hansen, “Sound source reconstruction using inverse boundary element calculations,” *The Journal of the Acoustical Society of America*, vol. 113, no. 1, pp. 114–127, 2003.

[Sij07] P. Sijtsma, “Clean based on spatial source coherence,” in *AIAA paper 2007-3436*, 2007.

[SLD10] A. SCHMITT, L. LAMOTTE, and F. DEBLAUWE, “Source identification inside cabin using inverse methods,” in *Proceedings of BeBeC-2010*, 2010.

[TA77] A. Tikhonov and V. Arsenin, *Solutions of ill-posed problems*, ser. Scripta series in mathematics. Winston, 1977.

[Tam90] M. Tamura, “Spatial fourier transform method of measuring reflection coefficients at oblique incidence. i: Theory and numerical examples,” *The*

Journal of the Acoustical Society of America, vol. 88, no. 5, pp. 2259–2264, 1990.

[tru] http://en.wikipedia.org/wiki/Truncated_icosahedron.

[TT03] A. Thite and D. Thompson, “The quantification of structure-borne transmission paths by inverse methods. part 2: Use of regularization techniques,” *Journal of Sound and Vibration*, vol. 264, no. 2, pp. 433 – 451, 2003.

[VCR92] M. Villot, G. Chaveriat, and J. Roland, “Phonoscopy: An acoustical holography technique for plane structures radiating in enclosed spaces,” *The Journal of the Acoustical Society of America*, vol. 91, no. 1, pp. 187–195, 1992.

[Vig12] D. Vigoureux, “Déconfinement de sources acoustiques par utilisation d’une méthode holographique à double information,” Ph.D. dissertation, INSA de Lyon, 2012.

[VM89] W. A. Veronesi and J. D. Maynard, “Digital holographic reconstruction of sources with arbitrarily shaped surfaces,” *The Journal of the Acoustical Society of America*, vol. 85, no. 2, pp. 588–598, 1989.

[VTG10] D. Vigoureux, N. Totaro, and J.-L. Guyader, “Mesure de vitesse vibratoire par la méthode iptf: simulation et expérimentation,” *10ème Congrès Français d’Acoustique*, 2010.

[VWHH12] N. P. Valdivia, E. G. Williams, P. C. Herdic, and B. Houston, “Surface decomposition method for near-field acoustic holography,” *The Journal of the Acoustical Society of America*, vol. 132, no. 1, pp. 186–196, 2012.

[WA04] H. Weber and G. Arfken, *Essential Mathematical Methods for Physicists.* Academic Press, 2004.

[Wil99] E. G. Williams, *Fourier acoustics : Sound Radiation and Nearfield Acoustical Holography.* Academic Press, June 1999.

[Wil01] E. G. Williams, “Regularization methods for near-field acoustical holography,” *The Journal of the Acoustical Society of America*, vol. 110, no. 4, pp. 1976–1988, 2001.

[WT10] E. G. Williams and K. Takashima, “Vector intensity reconstructions in a volume surrounding a rigid spherical microphone array,” *The Journal of the Acoustical Society of America*, vol. 127, no. 2, pp. 773–783, 2010.

[Wu04] S. F. Wu, “Hybrid near-field acoustic holography,” *The Journal of the Acoustical Society of America*, vol. 115, no. 1, pp. 207–217, 2004.

[WVHK06] E. G. Williams, N. Valdivia, P. C. Herdic, and J. Klos, “Volumetric acoustic vector intensity imager,” *The Journal of the Acoustical Society of America*, vol. 120, p. 1887, 2006.

[WW97] Z. Wang and S. F. Wu, “Helmholtz equation–least-squares method for reconstructing the acoustic pressure field,” *The Journal of the Acoustical Society of America*, vol. 102, no. 4, pp. 2020–2032, 1997.

[WY98] S. F. Wu and J. Yu, “Reconstructing interior acoustic pressure fields via helmholtz equation least-squares method,” *The Journal of the Acoustical Society of America*, vol. 104, no. 4, pp. 2054–2060, 1998.

[YN00] S. H. Yoon and P. A. Nelson, “Estimation of acoustic source strength by inverse methods: Part ii, experimental investigation of methods for choosing regularization parameters,” *Journal of Sound and Vibration*, vol. 233, no. 4, pp. 665 – 701, 2000.

[ZJBC09] Y.-B. Zhang, F. Jacobsen, C.-X. Bi, and X.-Z. Chen, “Near field acoustic holography based on the equivalent source method and pressure-velocity transducers,” *The Journal of the Acoustical Society of America*, vol. 126, pp. 1257–1263, 2009.

[Zot09] F. Zotter, “Sampling strategies for acoustic holography/holophony on the sphere,” *NAG-DAGA, Rotterdam*, 2009.